Capacité d'auto-cicatrisation des matériaux cimentaires : Amélioration avec des agents expansifs et des additions minérales

Lina Ammar

DOCTORAT BRETAGNE LOIRE SCIENCES POUR L'INGENIEUR

INSA RENNES

THESE DE DOCTORAT DE

L'INSTITUT NATIONAL DES SCIENCES APPLIQUEES RENNES

ECOLE DOCTORALE N° 602
Sciences pour l'Ingénieur
Spécialité : « *Génie Civil* »

Par

Lina AMMAR

Self-healing capacity of cementitious materials: Enhancement with expansive agents and mineral additions

Thèse présentée et soutenue à Rennes, le 10/02/2022
Unité de recherche : LGCGM
Thèse N° : 22ISAR 02 / D22-02

Composition du Jury :

Président :	Richard Gagné	Professeur des Universités	Université de Sherbrooke, Canada
Rapporteurs :	Farid Benboudjema	Professeur des Universités	ENS Paris-Saclay, France
	Luc Courard	Professeur des Universités	Université de Liège, Belgique
Examinateur :	William Prince Agbodjan	Professeur des Universités	INSA Rennes, France
Dir. de thèse :	Aveline Darquennes	Professeure des Universités	INSA Rennes, France
Co-Enc. de thèse :	Kinda Hannawi	Maître de conférences	INSA Rennes, France
Invité :	Denis Bézard	Project Manager	NEWCHEM company, Austria

Remerciements

First and foremost, I must acknowledge and thank The Almighty Allah for blessing, protecting and guiding me throughout this period.

I would like to express my gratitude to my supervisor Professor Aveline Darquennes for her useful comments, remarks and engagement through the learning process of this PhD thesis. Prof. Darquennes encouraged and guided me from the initial to the final level in developing a deep under-standing of the subject. Her instructive comments and evaluation guided and challenged my thinking, substantially improving the thesis outcome. I would like also thank my co-advisor, Doctor Kinda Hannawi for her useful remarks through these three years, as well as her encouragements and beautiful words.

I am also grateful for the valuable advices and constructive criticisms were given by the jury members. Many thanks go to Professor Richard Gagné for agreeing to chair the thesis jury. I would like to thank also Professor Farid Benboudjema, Professor Luc Courard and Professor William Prince-Agbodjan for their constructive comments and advices on the manuscript.

A big thanks go to Eng. Christian Garand for his precious time in helping me for running the experiments. I would also like to thank Franck Pavoine, Raphael Leon, Jean-Yves Brossault and Jean-Luc Métayer for their help in the laboratory.

I would like to extend my gratitude to my parents who provided me with moral support and bared my stress during the whole period, and to my friends who always stand by my side. I really cannot thank them enough and I pray God to preserve them for me.

My endless gratitude goes to my husband "Hussein" who has carried me throughout this journey and has helped and supported me on many occasions. Nothing could be accomplished without his support, his beautiful smiles and his patience.

Abstract

As the reinforced concrete structures are aging, they require more and more maintenance and repair works. Having a limited life span, repair materials may also show an early cracking due to environmental factors, deformational and physico-chemical incompatibilities between the repair material and the substrate, etc. In the context of sustainable development, it becomes essential to avoid costly maintenance and repair operations and to develop more durable and environmentally-friendly materials. The repair of structures using a self-healing mortar appears to be a solution in favor of this approach. This mortar will be able to heal autonomously its cracks. To achieve this objective, a large experimental campaign was performed to evaluate the effect of the addition of expansive agents at different contents and mineral additions on the mechanical behavior and self-healing capacity of mortars. The experimental results show that the addition of an expansive agent type MGO or CSA leads to a significant decrease of the autogenous shrinkage due to the formation of additional products in the pore network, leading to crystallization pressures and a matrix swelling at macroscopic scale. This expansion accelerates crack closure and therefore increases the autonomous healing potential of mortars. A partial substitution of cement by blast furnace slag is also beneficial to reduce autogenous shrinkage, and in the presence of MGO to increase the autonomous healing capacity of cracks. Moreover, the proposed repair mortars limit the cracking sensibility in a restricted autogenous condition and ensure mechanical resistances adapted to the repair requirements.

Key words: Blast furnace slag, cementitious materials, expansive agents, repair mortar, self-healing, swelling

Résumé

Suite à leur vieillissement, les structures actuelles en béton armé nécessitent de plus en plus de travaux de maintenance et de réparation. Ayant une durée de vie limitée, les matériaux de réparation peuvent également présenter précocement des fissures dues à des facteurs environnementaux, à des incompatibilités déformationnelles et physico-chimiques entre le matériau de réparation et le substrat, etc. Dans le cadre du développement durable, il devient essentiel d'éviter les opérations de maintenance et de réparation coûteuses, et de développer des matériaux plus durables et plus respectueux de l'environnement. La réparation de structures à l'aide d'un mortier auto-cicatrisant apparaît comme une solution s'inscrivant pleinement dans cette démarche. Ce mortier présentera la capacité de cicatriser ses propres fissures de manière autonome. Pour atteindre cet objectif, une large campagne expérimentale a été mise en œuvre afin d'évaluer l'impact de l'ajout d'additifs expansifs à différents pourcentages et d'additions minérales sur le comportement mécanique et la capacité d'auto-cicatrisation de mortiers. Les résultats expérimentaux montrent que l'ajout d'un additif expansif de type MgO ou CSA entraîne une diminution significative du retrait endogène en raison de la formation de produits supplémentaires dans le réseau poral, générant des pressions de cristallisation et un gonflement de la matrice à l'échelle macroscopique. Cette expansion permet d'accélérer la fermeture des fissures et augmente ainsi le potentiel de cicatrisation autonome des mortiers. Une substitution partielle du ciment par du laitier de haut-fourneau est également bénéfique pour réduire le retrait endogène, et en présence de MgO pour augmenter la capacité de cicatrisation autonome des fissures. De plus, les mortiers de réparation proposés limitent la sensibilité à la fissuration dans une condition endogène restreinte et assurent des résistances mécaniques adaptées aux exigences de la réparation.

Mots clés: Agents expansifs, cicatrisation, gonflement, laitier de haut fourneau, matériaux cimentaires, mortier de réparation

Résumé Etendu en Français

Introduction

De nombreux risques affectant les structures de génie civil sont généralement traités par les ingénieurs. Les règles et les normes utilisées pour la conception et la construction offrent généralement une sécurité suffisante. Toutefois, des risques non prévus peuvent survenir en raison de conditions environnementales, mécaniques, etc [1,2]. Par ailleurs, les matériaux à base de ciment présentent des variations volumétriques dues à leur évolution chimique, thermique, microstructurale et à leurs interactions avec leur environnement, dès qu'ils sont en contact avec l'eau [3, 4]. Ces déformations peuvent éventuellement provoquer des fissures dans les structures en béton. Cette fissuration modifie localement les paramètres de transfert du béton. L'eau et les agents agressifs (ions chlorure, dioxyde de carbone, etc.) pénètrent plus facilement dans le matériau, endommagent la matrice cimentaire et affectent ainsi la durabilité de la structure. Ainsi, tous ces problèmes peuvent entraîner des coûts de réparation élevés, ainsi que des impacts socio-économiques (fermeture de routes) et environnementaux (bruit, émissions de CO_2). Pour cette raison, il est nécessaire de trouver une solution de réparation plus respectueuse à l'environnement et ayant une durée de vie suffisante.

Dans le domaine du génie civil, certaines solutions peuvent être mises en œuvre pour réduire la formation de fissures dans une telle structure. L'une de ces approches, a récemment attiré l'attention, est l'utilisation de matériaux auto-cicatrisants [1, 5]. Le processus d'auto-cicatrisation est un processus intéressant qui a été élaboré dans de nombreuses études. Un matériau est défini comme auto-cicatrisant lorsqu'il est capable de réparer ses propres fissures au cours du temps. Deux mécanismes principaux d'auto-cicatrisation sont élaborés dans les études : la cicatrisation endogène et la cicatrisation autonome. Le premier mécanisme a lieu par l'hydratation des grains anhydres, ou par la carbonatation des produits d'hydratation. Le second mécanisme consiste à ajouter des matériaux spécifiques (agents expansifs par exemple) à la formulation initiale afin d'améliorer la capacité d'auto-cicatrisation des fissures. Les Agents Expansifs "AE' sont généralement utilisés dans les mélanges de béton, les mortiers, etc. pour réduire leur retrait. Ils ont récemment suscité un intérêt dans le domaine de l'auto-cicatrisation en raison de leur mécanisme de réaction qui peut former des produits d'hydratation expansifs et

ainsi produire une expansion de la matrice cimentaire. Les formulations avec AE (comme MgO ou CSA) ont montré des propriétés d'auto-cicatrisation des fissures dans certaines études. En revanche, la plupart de ces études ont examiné le processus d'auto-cicatrisation d'échantillons pré-fissurés à un âge précoce (par exemple, 1 jour) [6, 7], et l'ouverture initiale de la fissure était inférieure à 170 μm [7–9]. Il est important de mentionner que l'auto-cicatrisation à un jeune âge peut être améliorée même sans l'utilisation d'AE. En effet, la présence de particules non hydratées dans la fissure est plus importante au jeune âge, ce qui favorise le phénomène de cicatrisation. En plus, les capacités de cicatrisation démontrées par ces travaux sont limitées à la cicatrisation endogène (formation de produits de cicatrisation dans les fissures) alors qu'aucune cicatrisation autonome (expansion de la matrice) n'a été vérifiée dans leurs études. Ainsi, l'accent est mis sur l'utilisation de MgO et de CSA et l'évaluation de leurs limites de cicatrisation endogène et autonome.

Objectifs et contributions

Dans le cadre du développement durable, il devient essentiel d'éviter les opérations de maintenance et de réparation coûteuses ou difficiles, et de développer des matériaux durables et respectueux à l'environnement. Cela implique de réparer la structure endommagée avec un mortier de réparation. Cependant, ce mortier peut également conduire à des problèmes de fissuration dans le temps accélérant à nouveau la dégradation de la structure. Le présent projet vise à concevoir un mortier de réparation caractérisé par une capacité d'auto-cicatrisation de ses fissures pendant la durée de vie de la structure réparée.

Un matériau traditionnel (Figure 1), sans propriétés d'auto-cicatrisation, présente une durée de vie limitée. En comparaison, un mortier de réparation auto-cicatrisant serait idéalement capable de se cicatriser à l'infini et de retrouver ses performances initiales. Ainsi, les structures intégrant des matériaux auto-cicatrisants permettraient d'allonger leur durée de vie et de réduire les coûts de maintenance. Le présent travail de recherche se concentre sur la capacité de cicatrisation autonome des fissures des mortiers caractérisés par un comportement expansif. Cette expansion pourrait accélérer la fermeture des fissures qui peuvent se former en fonction du temps, tout en compensant le retrait du mortier. De plus, le mortier de réparation doit posséder de bonnes performances mécaniques, physiques et de transfert. Pour atteindre ces buts, cette étude présente les objectifs suivants:

1. Fournir un état de l'art sur le phénomène d'autocicatrisation et les paramètres affectant ce processus, ainsi que sur l'autocicatrisation en utilisant des agents expansifs. Il s'agit également d'une étude approfondie sur les effets des agents expansifs sur les différentes propriétés du matériau, notamment les propriétés mécaniques (résistances mécaniques

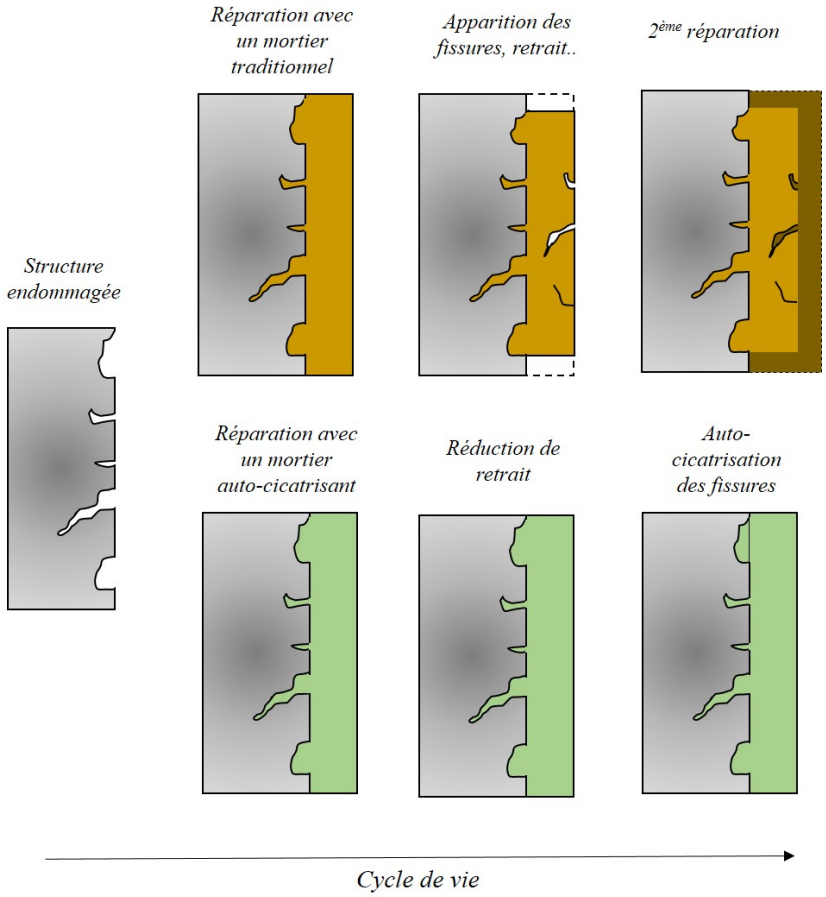

Figure 1 – Réparation traditionnelle vs réparation avec des matériaux auto-cicatrisants.

et déformations). Cela permet de faire le choix des additions qui peuvent apporter un potentiel de cicatrisation autonome grâce à leur comportement expansif (*Chapitre 1*).

2. Examiner, à partir de la littérature, les différentes méthodologies d'évaluation du processus d'autocicatrisation (*Chapitre 1*). En complément, évaluer expérimentalement la capacité et la cinétique d'autocicatrisation des formulations de béton dans le cadre du Round Robin Test (RRT) (*Chapitre 2*) afin de proposer nos propres méthodologies expérimentales.

3. Concevoir les mélanges de mortier de réparation et proposer la campagne expérimentale pour atteindre nos objectifs (*Chapitre 3*).

4. Évaluer l'impact des additions minérales et de l'AE sur les résistances en compression des mélanges de mortier de ciment afin d'assurer leur conformité aux normes de réparation (EN1504-3), ainsi que plusieurs paramètres des matériaux affectant la sensibilité à la fissuration du mortier de réparation lorsque ses déformations différées sont retenues par un support, par exemple la résistance à la flexion, le module d'Young dynamique et les déformations différées (*Chapitre 4 & 5*).

5. Évaluer le processus de cicatrisation et la cinétique des éprouvettes fissurées pour tous les mélanges de mortier proposés, ainsi que les limites de la cicatrisation autonome (*Chapitre 4 & 5*).

Principaux résultats et conclusions de la thèse

Choix de la technique expérimentale pour l'évaluation de l'auto-cicatrisation:

Tout d'abord, nous avons étudié l'effet des additions minérales et additions cristallines sur la capacité de cicatrisation des fissures de béton par le biais de deux essais expérimentaux: la perméabilité à l'eau et l'absorption d'eau. Ces essais ont été réalisés dans le cadre du Round Robin Test (RRT1 et RRT3) afin d'évaluer la capacité et la cinétique d'auto-cicatrisation du béton, ainsi que la viabilité des deux essais proposés. Pour RRT1, deux compositions de béton sont étudiés : le béton de référence " REF1 " et le " SLAG " qui contient 20% de laitier (en poids de ciment). De même, pour RRT3: le béton de référence "REF2" et le "CA" qui contient 1% d'addition cristalline (en poids de ciment).

Les essais de perméabilité à l'eau et d'absorption d'eau sont lancés après la préfissuration des éprouvettes par des essais de fendage et de flexion trois points respectivement. Les éprouvettes sont soumises à une cure sous eau, chaque composition étant placée dans un récipient séparé. Les tests sont effectués à 4 intervalles de temps : après la préfissuration (0M), 1 mois (1M), 3 mois (3M) et 6 mois (6M). Ainsi, le taux de cicatrisation des éprouvettes fissurées est déterminée par trois mesures principales après chaque test: la largeur de la fissure, le débit d'eau et le coefficient de sorption. Elles correspondent respectivement au suivi de la largeur de la fissure pour tous les échantillons fissurés, aux tests de perméabilité à l'eau et aux tests d'absorption d'eau effectués sur les échantillons. Les résultats expérimentaux ont montré que le suivi de la largeur des fissures est une technique qui ne fournit qu'une observation visuelle (2D) de la cicatrisation. Ainsi, cela ne prend pas en compte la cicatrisation interne de la fissure. A partir des tests d'absorption d'eau, le coefficient de sorption est déterminé pour les échantillons fissurés et non fissurés. Cette technique permet de calculer le taux de cicatrisation en prenant en compte la cicatrisation des fissures et la réduction de la porosité de la matrice saine liée à l'avancement de l'hydratation. Cependant, de cette manière, ce test nécessite des échantillons supplémentaires qui compliquent le calcul et ne permettent pas d'obtenir un taux de cicatrisation précis. Alors qu'avec le test de perméabilité à l'eau, le débit d'eau estime correctement la cinétique de la cicatrisation interne de la fissure, ce qui fournit un taux de cicatrisation plus précis.

Ainsi, cette étude a fourni une approche intéressante pour évaluer le processus d'auto-cicatrisation des mélanges, et a effectivement servi de support utile pour nos prochaines travaux.

Campagnes expérimentales et préparation des échantillons:

Par la suite, nous avons évalué l'effet de l'AE sur deux types de mortiers: un mortier de ciment Portland (campagne expérimentale n°I) et un mortier mélangé avec 50% de BFS (en poids de liant) (campagne expérimentale n°II). La première campagne consiste à comprendre l'impact de l'AE sur le mortier à base de ciment dans deux états, sain et fissuré, afin de proposer un mortier de réparation ayant une capacité de cicatrisation autonome intéressante. Ensuite, il s'agit de comprendre l'impact de l'AE sur la matrice cimentaire avec des additions minérales (laitier de haut fourneau) et ainsi proposer un mortier de réparation innovant ayant une capacité de cicatrisation intéressante. Deux types différents d'AE sont choisis : un à base d'oxyde de magnésium et sera nommé par la suite "MGO" et un à base de sulfoaluminate de calcium et sera nommé par la suite "CSA". Selon des mesures de calorimétrie isotherme, le CSA réagit plus rapidement que le MGO.

Des mortiers avec trois teneurs en AE sont testés : 0%, 5% et 10% (du poids du liant). Les mortiers de référence des campagnes I et II (respectivement REF et BFS) sont comparés aux mortiers contenant du MGO (respectivement MG5, MG10 et BM5, BM10), et aux mortiers contenant du CSA (respectivement CSA5, CSA10 et BC5, BC10). Pour les deux campagnes, les rapports Eau/Liant et Sable/Liant sont égaux à 0,45 et 2 respectivement. Toutes les éprouvettes préparées sont condionnées dans la salle humide (95% HR et 20°C). Les éprouvettes utilisées pour l'évaluation de l'auto-cicatrisation sont pré-fissurées à l'âge de 28 jours. Au délà, elles sont mises dans deux conditions de cure: sous eau à 20°C (WC), et sous des cycles eau/salle humide chaque 3 jours (CC).

Effet des AE sur le mortier à base de ciment Portland:

Ce chapitre détaille l'avantage de l'ajout des AE (MGO et CSA) sur les propriétés des mortiers sains et leur capacité d'auto-cicatrisation.

Les résultats expérimentaux montrent que l'ajout d'un agent expansif de type MGO ou CSA conduit à une diminution significative du retrait endogène et total due à la formation de produits supplémentaires dans le réseau de pores, conduisant à des pressions de cristallisation et à un gonflement de la matrice à l'échelle macroscopique. Cette expansion accélère la fermeture des fissures et augmente donc le potentiel de cicatrisation autonome des mortiers. Ces comportements sont plus importants en augmentant la teneur en AE dans le mélange. D'autre part, la substitution partielle de la masse de ciment par de l'AE diminue les résistances mécaniques (flexion et compression) au jeune âge et à long terme en raison de la diminution des gels C-S-H produits. Cette réduction est plus faible en présence de CSA que dans le MGO, en raison de l'hydratation de la CSA qui est achevée au jeune âge. Malgré cette diminution de résistance, tous les mortiers proposés présentent des résistances à la compression élevées à 28

jours. Cela confirme donc leur conformité aux exigences de la norme de réparation (EN 1504-3) pour la résistance en compression. Enfin, l'ajout d'AE réduit significativement la sensibilité du mortier à la fissuration en condition endogène restreinte. La présence de MGO dans le mélange augmente ce comportement en raison du gonflement modéré de la matrice.

Par conséquent, ce chapitre propose des mélanges à base de ciment incorporant de l'AE comme mortiers intéressants pouvant pour des applications de réparation, limitant la sensibilité à la fissuration et caractérisés par des capacités de cicatrisation endogènes et autonomes intéressantes.

Effet des AE sur le mortier à base de ciment Portland mélangé avec 50% de laitier de haut fourneau:

Ce chapitre détaille l'intérêt du couplage des additions minérales et des AE (MGO et CSA) sur les propriétés des mortiers sains et leur capacité d'autocicatrisation.

Les résultats expérimentaux montrent que l'ajout d'un agent expansif de type MGO ou CSA conduit à une diminution significative du retrait endogène et total due à la formation de produits supplémentaires dans le réseau poreux, conduisant à des pressions de cristallisation et à un gonflement de la matrice à l'échelle macroscopique. Cette expansion accélère la fermeture des fissures et augmente donc le potentiel de cicatrisation autonome des mortiers. On observe que ces comportements sont plus importants en présence de MGO en raison de son hydratation lente qui se poursuit à long terme. De plus, il augmente la formation de produits supplémentaires à l'intérieur de la fissure par cicatrisation endogène. D'autre part, la substitution partielle de la masse cimentaire par de l'AE diminue les résistances mécaniques (flexion et compression) au jeune âge et à long terme en raison de la diminution des gels C-A-S-H produits. Cette réduction est plus faible en présence de CSA que dans le MGO, en raison de l'hydratation de la CSA qui est achevée au jeune âge. Malgré cette diminution de résistance, tous les mortiers proposés présentent des résistances à la compression élevées à 28 jours. Cela confirme donc leur conformité aux exigences de la norme de réparation (EN 1504-3) en résistance en compression. Enfin, l'ajout d'AE réduit significativement la sensibilité du mortier à la fissuration en condition endogène restreinte.

Par conséquent, ce chapitre propose un mélange ternaire de ciment-laitier de haut-fourneau-AE comme mortiers très intéressants pour des applications de réparation, limitant la sensibilité à la fissuration et caractérisés par des capacités de cicatrisation endogènes et autonomes intéressantes.

Perspectives

Bien que ce travail ait permis de mieux comprendre l'impact de l'EA sur le phénomène d'auto-cicatrisation, de nombreuses remarques peuvent être soulevées, que nous citons ci-dessous:

- Développement d'une approche statistique pour l'essai de perméabilité à l'eau afin de prendre en compte la variabilité de la géométrie initiale des fissures des échantillons. Cela permettra d'obtenir des résultats de flux d'eau plus fiables et comparables entre les échantillons.
- Amélioration du test de perméabilité à l'eau par le développement d'un système qui maintient une pression d'eau constante au-dessus de l'échantillon pendant le test.
- Évaluation de la porosité du mortier à l'échelle des micropores. Cela permettra de mieux comprendre le comportement de gonflement du MGO et du CSA s'il est lié à une plus petite porosité remplie par les produits d'hydratation supplémentaires par exemple.
- Réalisation d'images de tomographie à rayons X pour fournir des informations concernant la connectivité, la tortuosité ou la perméabilité associées à un réseau de pores (analyse 3D). Cela permettra de vérifier si le mécanisme de gonflement des mélanges contenant de l'AE peut conduire à des microfissures.
- Suivi du processus d'hydratation par analyse DRX et quantification des produits d'hydratation dans le temps. Cela permet de mieux comprendre l'effet de l'AE sur l'avancement de l'hydratation, et la stabilité des produits d'hydratation formés au cours du temps.

Contents

List of Figures

List of Tables

List of Symbols

Acronyms and abbreviations

3pbt	*three points bending test*
4pbt	*four point bending test*
btbw	*by the binder weight*
btcw	*by the cement weight*
ECC	*Engineered Cementitious Composites*
HPC	*High Performance Concrete*
SHCC	*Strain Hardening Cementitious Composites*
UHPC	*Ultra High Performance Concrete*

Chapter 1

General Introduction

People generally feels secure towards the structures in which they live and work. This feeling results from the fact that a large part of the risks affecting the structures have been correctly predicted and treated by the engineers. The rules and standards used for the design and construction usually ensure sufficient safety. However, risks are then only recognized when accidents or serious non-predicted failures occur [1]. The causes of damage differ from one structure to another by the source and type of deterioration. They can be divided into four main causes that are mentioned below [1, 2]:

1. *Natural causes* due to the environmental conditions such as temperature and humidity, wind, snowfall, etc.,
2. *Structural causes* linked to a structure anomaly such as an embedding effect, redistribution of the moments due to creep and shrinkage , etc.,
3. *Accidental causes* such as shocks, earthquakes, explosions, fire, etc.,
4. *Structure aging* directly linked to the building/construction use.

In addition, cement-based materials show volumetric variations due to their chemical, thermal and microstructural evolution and to their interactions with their environment, as soon as they get in contact with water [3, 4]. These deformations can sometimes induce tensile stresses due to their restriction (e.g. concrete support for a repair mortar) and cracks into concrete structures [4] (Figure 1.1). This cracking modifies locally the transfer parameters of concrete. Water and aggressive agents (chloride ions, carbone dioxide, etc.) penetrate easier into the material, damaging the cement matrix and the steel reinforcements (Figure 1.2). The ions transfer (especially chlorides) accelerates the initiation of corrosion in the reinforcement, thereby impairing the structure durability.

The deteriorations of concrete structures imply often expensive repair costs, as well as socio-economic impacts (road closure) and environmental impacts (noise, CO_2 emissions). For this reason, it is necessary to find a repair solution more respectful of the environment and characterized by a sufficient lifespan.

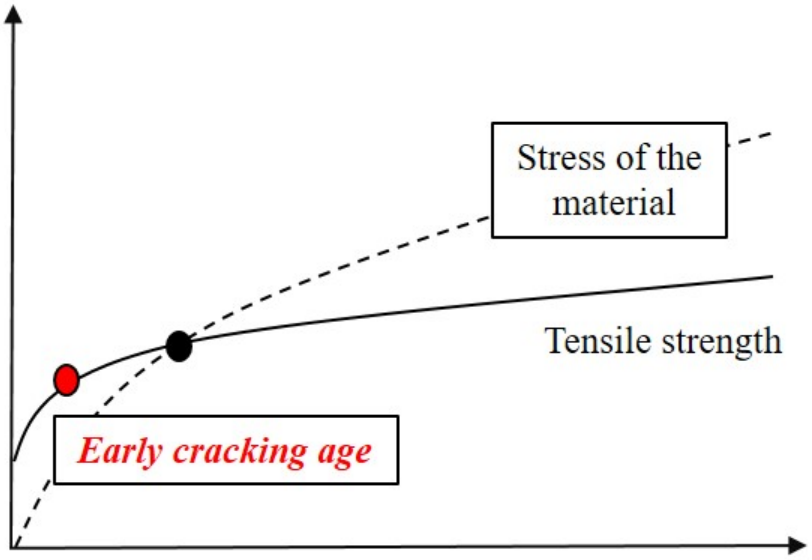

Figure 1.1 – Cracking risk as a function of time.

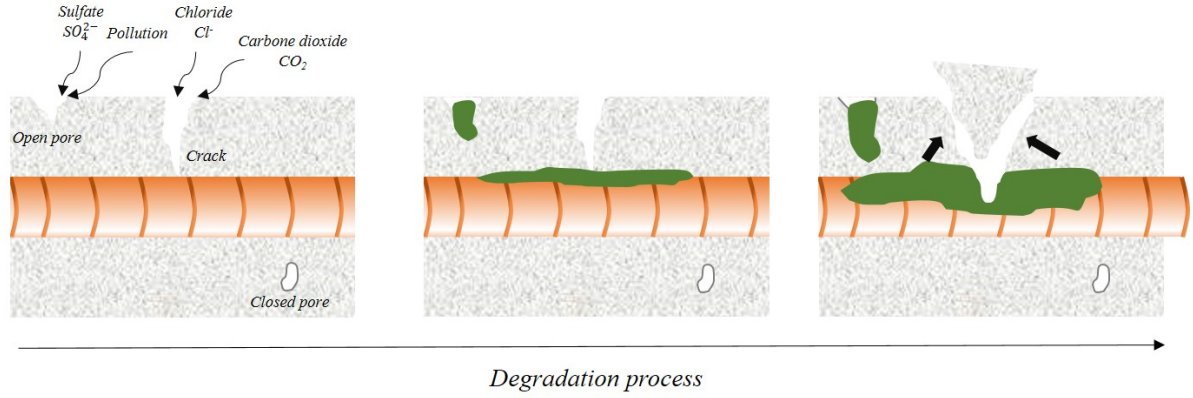

Figure 1.2 – Degradation process of the reinforced concrete structure due to penetration of aggressive agents.

Objectives of the present research project

In the context of sustainable development, it becomes essential to optimize costly or difficult maintenance and repair operations, and to develop sustainable and environmentally friendly materials. The use of a traditional repair mortar can lead to cracking problems over time, accelerating the degradation of the structure (Figure 1.3). In this context, this project aims to design a Self-Healing Repair Mortar (SHRM) able to heal itself infinitely and regain its initial

performances. Thus, structures repaired with these materials would extend their service life and reduce maintenance costs. The present research work focuses on autonomous healing capacity of mortars characterized by an expansive behavior. The mortar's expansion could in the short term limit the shrinkage and the incompatibilities of the repair mortar with its support, and in the long term accelerate the closure of cracks and the healing process. Moreover, the repair mortar should possess good mechanical performances adapted to the repair requirements (EN 1504-3) [10]. So, this study presents the following objectives:

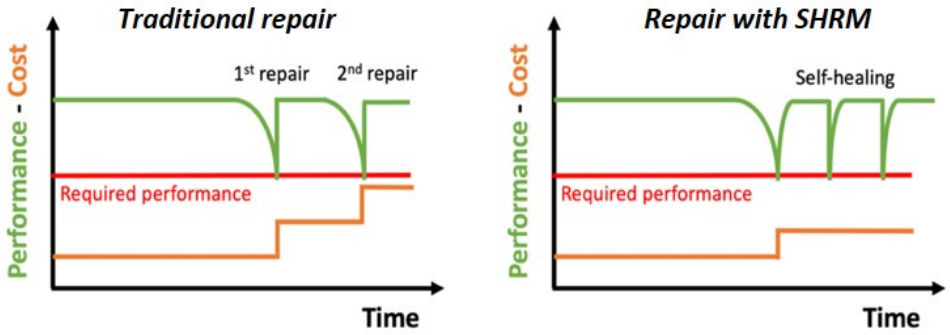

Figure 1.3 – Traditional repair vs repair with SHRM [11]

- Propose a repair mortar with autonomous healing capacities by using Expansive Agents (EA) in the cement-based mortar mixtures.
- Propose an innovative repair mortar with autonomous healing capacities by using more environmentally-friendly materials (e.g. blast furnace slag) and Expansive Agents (EA).

To achieve these goals, the methodology used can be divided into several parts:

1. Provide a state of the art on self-healing, in particular on the research about the autonomous healing for materials having a special type of admixture: expansive agents. It also includes a review of the effect of expansive agents on the mechanical properties of sound materials (*Chapter 1*).
2. Review from the literature the experimental methodologies to evaluate the self-healing (*Chapter 1*) and compare several methodologies to monitor self-healing in the frame work of Round Robin Test (RRT) (*Chapter 2*) in order to propose our own experimental methodology.
3. Design the repair mortar mixtures and propose the experimental campaign to achieve our goals (*Chapter 3*).
4. Evaluate the impact of mineral additions and EA on the compressive strengths of cement mortar mixtures to ensure their compliance with repair standards (EN1504-3), as well as several material parameters affecting the sensitivity to cracking of the repair mortar

when its delayed deformations are restrained by a support, e.g. flexural strength, dynamic Young's modulus and delayed deformations (*Chapter 4 & 5*).

5. Evaluate the impact of mineral additions and EA on the self-healing process, as well as the time and conditions necessary for a reasonable healing response (*Chapter 4 & 5*).

Chapter 2

State of the art

Contents

2.1 Introduction

This chapter is divided into 3 main parts. The first part (§2.2) introduces the self-healing phenomenon and the parameters influencing its potential. The second part (§2.3) deals with five different types of Expansive Agents "EA", their hydration, expansion mechanisms and impact on the cement matrix. It also discusses the works carried out on autonomous healing using EA. The third part (§2.4) reviews the mostly related self-healing techniques to our work, especially, the water permeability test. The last part (§2.5) summarizes the main points in order to establish our research program.

2.2 Reducing the crack formation: Self-healing materials

In the civil engineering field, many solutions are proposed in order to limit the crack formation in a structure. Although it is often difficult to overcome this problem, but some solutions can be implemented to reduce the cracks and to improve the mechanical, physical and transfer properties of the material. Different materials can be used in the mixtures such as: Supplementary Cementitious Materials “SCM”, different types of aggregates or fibers, shrinkage reducing agents or expansive agents [12]. Another approach, which has lately gained attention, is the use of self-healing materials [1, 13]. The self-healing mechanism is an interesting process that has been elaborated in many studies. Thus, more details about this process are presented in the following sections

2.2.1 Definition of the Self-healing process

RILEM TC 221-SHC [14] defines the self-healing process as “Any process by the material itself involving the recovery and hence improvement of a performance after an earlier action that had reduced the performance of the material”. The material is therefore described as being self-healing when it is able to repair its own cracks over time. Three different terms of healing are used nowadays. We distinguish: autogenous (1 and 2 on Figure 2.1) and autonomous healing (3 on Figure 2.1), and activated repairing. The last mechanism is also called "smart healing" and consists in the use of some artificial devices like micro-capsules. In this study, we elaborate only the first two mechanisms.

2.2.1.1 Autogenous healing

“The self-healing process is autogenic when the recovery process uses materials components that could otherwise also be present when not specifically designed for self-healing (own generic materials)”, as mentioned by RILEM TC 221-SHC [14]. This type of healing is also called

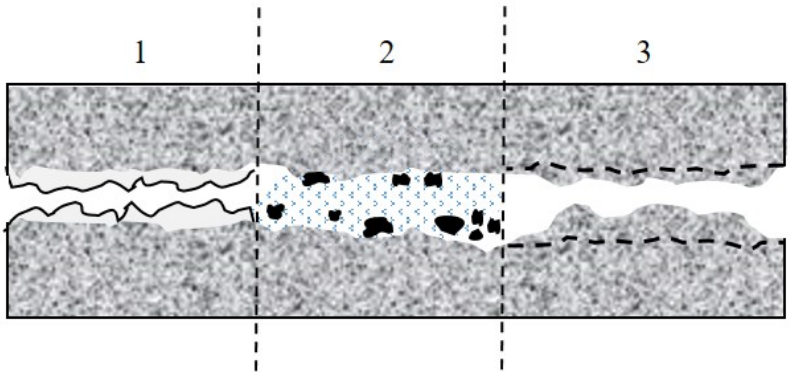

Figure 2.1 – Mechanisms of Self-Healing: **1** & **2:** *Autogenous healing*; **3:** *Autonomous healing.*

"natural healing". It takes place by hydration of the anhydrous grains in concrete at young age, or by carbonation of the hydration products, as explained hereafter.

– **Continuous hydration:** In most concretes, from 20 to 30% of the cement grains remain anhydrous in the cement matrix [15]. Their contact with free water (capillary water or water coming from outside) leads to the formation of additional hydration products such as portlandite [16], ettringite or C-S-H [17, 18]. They could fill the cracks [17].

– **Carbonation:** When the crack is in contact with air and water, the portlandite and the C-S-H located around the crack dissolve [19]. This will increase the amount of Ca^{2+} ions in the interstitial solution and thereby increase its pH. The increase in pH leads to the dissolution of atmospheric carbon dioxide in water and the formation of bicarbonate HCO_3^- then carbonate ions CO_3^{2-} (Eq. 2.1) [19]. The latter will react with Ca^{2+} ions to form calcium carbonate according to Eq. 2.2 and 2.3.

It is also worth noting that $CaCO_3$ can be found in different forms due to the various types of ions existing in the interstitial solution and coming from the matrix. It also depends on the pH of the solution, the temperature and the saturation degree of carbonate ions. Thus, calcium carbonate can exist in six different forms: calcite, aragonite, vaterite, monohydrocalcite, ikaite and amorphous $CaCO_3$ [20].

$$CO_2 + H_2O \leftrightarrow H_2CO_3 \leftrightarrow H^+ + HCO_3^- \leftrightarrow 2H^+ + CO_3^{2-} \tag{2.1}$$

$$Ca^{2+} + CO_3^{2-} \rightarrow CaCO_3 \qquad (pH > 8) \tag{2.2}$$

$$Ca^{2+} + HCO_3^- \rightarrow CaCO_3 + H^+ \qquad (pH < 8) \tag{2.3}$$

Autogenous healing is considered as an unreliable phenomenon to achieve significant healing effects [5]. Neville [16] reported that autogenous healing is limited to crack widths of 300 μm. For this reason, interest has been shown in autonomous healing. However, in both cases, the phenomenon is a function of several parameters that influence the healing potential (§2.2.2).

2.2.1.2 Autonomous healing

« The self-healing process is autonomic when the recovery process uses materials components that would otherwise not be found in the material (engineered additions)", as mentioned by RILEM TC 221-SHC [14]. This type of healing, for which specific materials are added into the initial mixture, is also called "engineered healing". These materials can be supplementary cementitious materials [21], superabsorbent polymers [22], bacteria [23], special expansive agents [24], etc. They can be used in mortar or concrete formulations in order to improve crack self-healing ability [14].

2.2.2 Influence parameters on the self-healing

Various parameters can influence the potential of autogenous and autonomous healing. They are succinctly described below.

(i) **Crack width:** The maximum crack width likely to be completely healed is different in each study as shown in Figure 2.2. In addition, Gagné et Argouges [25] found that the kinetics of crack healing were fast for large cracks. For fine cracks (50 μm), the self-healing rate was slow (5-10 $\mu m/month$). In contrast, for cracks larger than 200 μm, the self-healing rate was faster (15-30 $\mu m/month$). The authors attributed this to the fact that in a large crack, more space is available to form healing products due to sufficient external CO_2 and water supply [25]. This observation is in agreement with Kan et al. [26] who noted that C-S-H was observed in very fine cracks while larger cracks were filled with calcite.

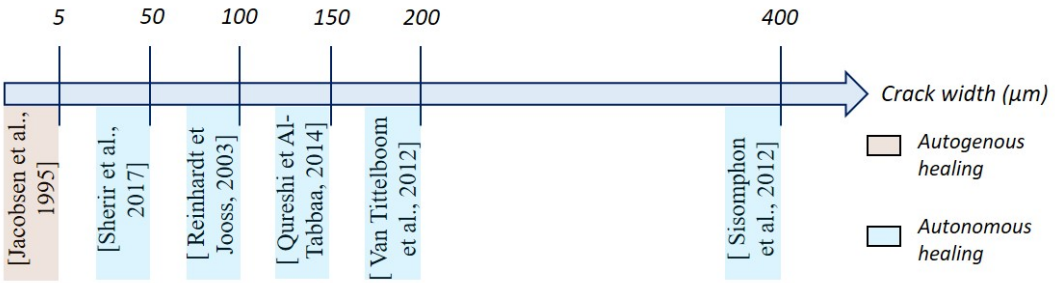

Figure 2.2 – Healing of crack as a function of their width in different studies; from left to right: [18], [9], [27], [6], [21], [24].

(ii) **Crack age:** At early age, the large content of anhydrous grains in the crack promotes further hydration and crack healing. Therefore, cracking at long-term could decrease the healing capacity [19, 28, 29]. Jiang et al. [29] observed that the permeability of mortars cracked at 7 days decreases faster than those cracked at 28 days. This is due to crack healing, which was observed to be fast for the mortars cracked at early ages. In addition, mechanical properties such as flexural and tensile strength, can be partially recovered if the crack appears at early age [30, 31]. In opposite, Gagné et Argouges [25] found that the crack age has a minor role in the kinetics of crack healing.

(iii) **Crack location:** The crack location can partially affect its healing efficiency. Roig-Flores [13] found that when the cracked specimens were placed as shown in Figure 2.3, the lateral cracks remain open, while the top crack accumulates precipitates in its whole surface. This is probably related to the location of the top crack, which allows for more stable accumulation of healing products than in the lateral crack.

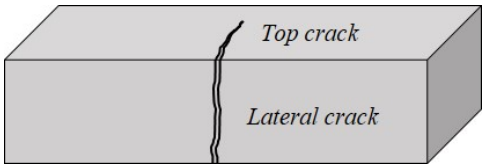

Figure 2.3 – Position of the specimen in the container during the healing period; [13].

(iv) **Curing condition:** The curing condition is an essential parameter in the self-healing process. Several researches [5, 15, 24, 32, 33] agree that water curing is more favorable to the crack healing process, because it promotes the formation of new hydration products. In contrast, cracked specimens exposed to ambient air ($20 \pm 2°C$ and $\leq 60\%$ RH) do not show signs of healing over time [5, 15, 32, 34]. Sisomphon et al. [34] evaluated the healing rate of cracks characterized by an initial width equal to 300 μm under 4 curing conditions: Water Immersion (WI), Regularly refreshed Water (RW), Water/Air cycles (W/A) and Air Exposure (AE). After 28 days of curing, the cracked specimens cured in RW and W/A conditions presented a more important crack healing (Figure 2.4). This was related to the formation of additional calcium carbonate on the crack surface resulting from the regular interaction between fresh water - CO_2 – crack surfaces. Moreover, the distribution of $CaCO_3$ in the crack was not uniform as explained in Figure 2.5. The authors [24] claimed that the water in the interstitial solution contains a high concentration of Ca^{2+} ions, while less concentration exists in the curing water. On the contrary, the carbonate ions in the interstitial solution are lower than those existing in the curing water. Therefore, the crack surface is the only area that has significant amounts of both calcium and carbonate ions. Consequently, more $CaCO_3$ precipitation was observed on the crack surface, and less precipitation was observed at other locations (Figure 2.5).

Roig-Flores et al. [5, 33] evaluated the healing rate of cracks characterized by an initial width equal to 300 μm, undergone several curing conditions: Water Contact (WC: only 2 cm of the specimens were in contact with water), Humid Chamber (HC) at 20°C and 95% RH, WI and AE. After 42 days, cracks exposed to water (WC and WI) are completely healed. It is not the case for cracks exposed to the other conditions (HC and AE) (Figure 2.6). Similar results were found in another research work [15].

The chemical composition of the curing water also influences the self-healing process. For example, when the cracked specimen was cured in water rich in magnesium ions Mg^{2+} and having a low pH (< 7.8), the formation of aragonite was favored into the crack [20]. The growth rate of aragonite is generally slower than that of calcite. This leads to a slower healing rate for this specimen due to the formation of aragonite in the crack instead of calcite.

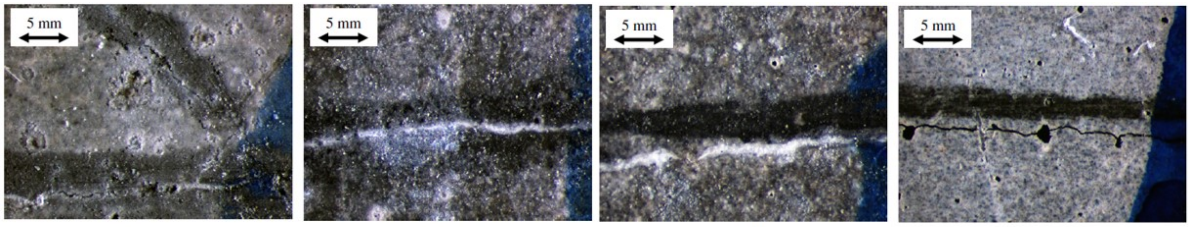

Figure 2.4 – Crack closure results after 28 days of curing in 4 different exposures: Water Immersion (WI), Regularly refreshed Water (RW), Water/Air cycles (W/A) and Air Exposure (AE); [34].

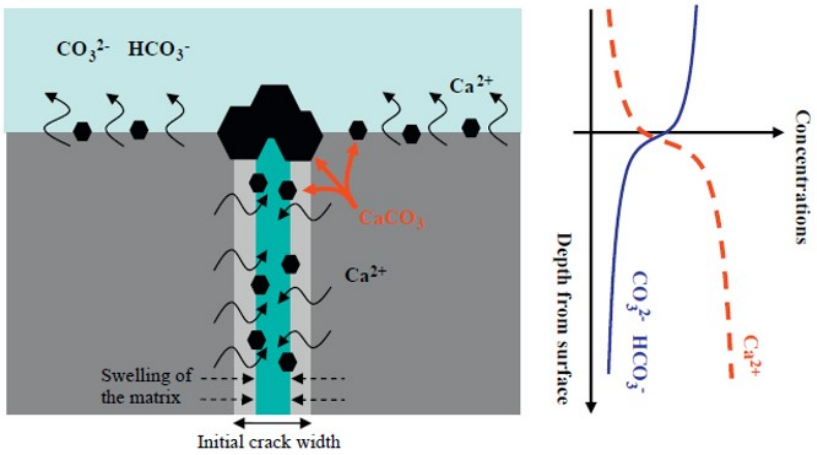

Figure 2.5 – Schematic of precipitation of calcium carbonate; [24].

(v) **Type of materials:** As explained previously, autogenous healing is not always sufficient to heal large cracks (over 300 μm) [16]. For this reason, autonomous healing has been the focus of many studies [19, 21–23, 35–37].

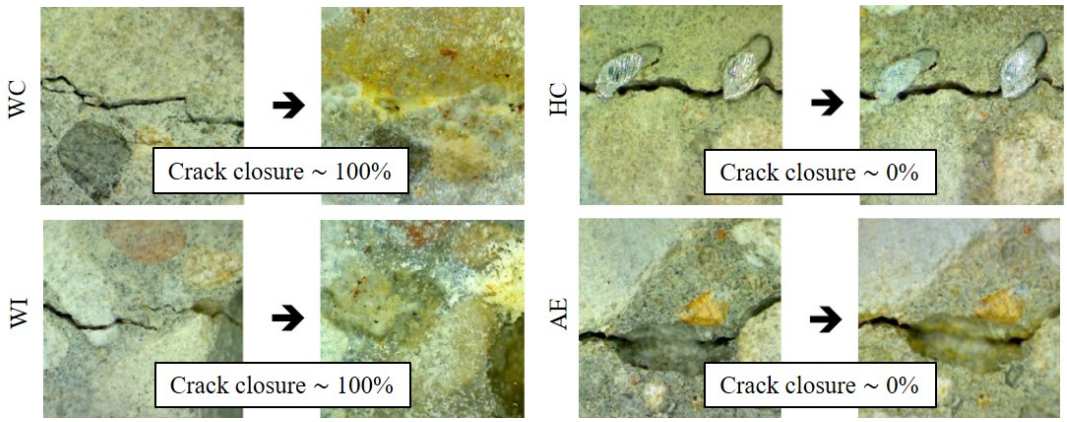

Figure 2.6 – Crack closure results after 42 days of curing in 4 different exposures: Water Contact (WC), Humid Chamber (HC), Water Immersion (WI) and Air Exposure (AE); [5].

Several researchers have worked on the self-healing capacities of cementitious materials more environmentally friendly, such as fly ash and blast furnace slag. Their interest for the self-healing is based on the fact that their hydration is slower than that of cement. At a given age, a large quantity of anhydrous particles can exist on the crack surfaces. This helps to promote further hydration and so, the healing process at long-term [21,35,37–39]. The addition of fly ash increases the self-healing capacity according to Sahmaran et al. [38] and Termkhajornkit et al. [37]. Sahmaran et al. [38] studied the self-healing of concretes with fly ash replacement ratios of 0%, 35%, and 55%. Their water/binder ratio was equal to 0.35 and the specimens were loaded at 28 days to 90% of their ultimate compressive strength. Concretes with fly ashes lost initially 27% of their strength while this lost was 19% for the reference concrete. However, after 30 days of water curing, the strength loss of concrete with fly ashes is reduced to only 7%, while it was higher for the reference concrete (13%). This compressive recovery was attributed to the progressive filling of the crack by new C-S-H gels due to the pozzolanic reaction of unhydrated fly ashes. Similar observations were made by Termkhajornkit et al. [37]: after 28 days, the C-S-H content increases with the fly ashes content.

Tittelboom et al. [21] compared the self-healing capacity of a Portland cement mortar (CEM I) and mortars containing 50% of blast furnace slag (50-BFS) and 50% fly ashes (50-FA). The prismatic mortars were cracked by 3pbt and stored under water. Microscopic analysis showed that cracks smaller than 200 μm are completely closed after 42 days due to $CaCO_3$ precipitation (Figure 2.7). But no significant difference on the crack healing kinetics was noted between the studied mixes (Figure 2.7). The mortars were reloaded 71 days after cracking. The recovery of their flexural strengths is rather low (almost 20% for CEM I and 50-BFS and 13% for 50-FA). The comparaison between the two alternative binders shows that the mortar with blast furnace slag presents the best self-healing properties at 71 days. Hung et al. [35] evaluated the self-healing performance

of SHCCs incorporating high volumes of blast furnace slag and fly ashes and pre-cracked at 180 days old. They found that SHCCs with a mix of blast furnace slag and fly ashes had better self-healing performances compared to SHCCs containing only fly ashes. The SHCC with blast furnace slag and fly ash healed totally cracks characterized by an initial width of 70 μm after 90 days of water curing due to the formation of $CaCO_3$ and C-S-H into the cracks.

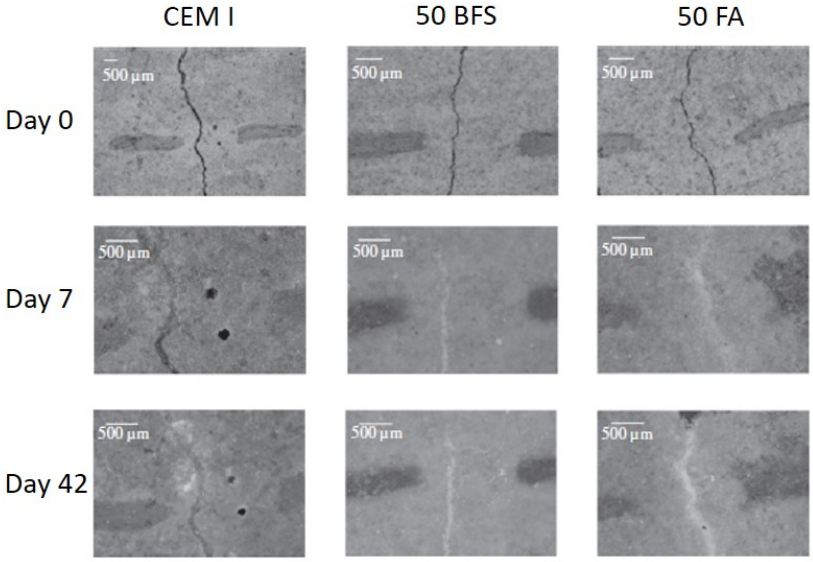

Figure 2.7 – Evolution of the crack width after 0, 7 and 42 days of water curing; [21].

Several studies also aimed to use other materials like superabsorbent polymers [22] and bacteria [23] in the mixtures. Deng and Liao [22] investigated the self-healing ability of ECC mixtures with 2 contents (2% and 4%) of SAP of two different sizes (75 and 550 μm). The authors found that the ECC mixture with 4% SAP of 550 μm was the best mixture to recover its mechanical performances. In addition, cracks below 30 μm were completely filled with calcium carbonate after 6 days. The self-healing process of ECC was accelerated by the help of SAPs which can absorb H_2O under high relative humidity conditions and release H_2O under low relative humidity conditions. The encapsulated bacteria technique could be classified as a smart healing agent [14]. The bacteria wake up when water reaches its position through the crack in order to form calcite into the crack [14, 23]. However, there are several challenges that are not suitable for bacterial life, such as high alkalinity (pH up to 13), high temperatures during manufacturing processes, limited oxygen supply, as well as many biological factors. These factors remain unclear and affect the life and efficiency of the bacteria [23].

As the present research project focuses on the healing capacity of cementitious materials containing Expansive Agents "EA", the effect of these admixtures on the healing process will be presented and discussed in a specific section (§2.3).

(vi) **Water/Binder ratio:** As explained in the previous paragraph (§(v)), further hydration should preferentially occur with a more important content of anhydrous particles into the cementitious matrix [19, 21, 28]. A small W/B ratio favors the presence of a larger content of anhydrous particles at the cracking age [19]. This promotes crack healing by further hydration. Thus, the efficiency of self-healing by the ongoing hydration decreases with the increase of the W/B ratio [21].

2.3 Expansive Agents

Expansive agents "EA" are generally used in mixtures to reduce their shrinkage. They have recently gained interest in the field of self-healing because of their reaction mechanisms that can generate supplementary products and an expansion of the cementitious the matrix. Subsequently, it can lead to a reduction in the crack size (Figure 2.1). First, the expansion mechanism of EA is explained hereafter. Then, the effect of EA on the sound and cracked material is described according to the literature.

2.3.1 Mechanism of expansion

The EA are characterized by their expansive behavior in the matrix. As shown in Figure 2.8, the hydration process of EA is divided into three main phases [12]:

1. **Formation of crystals:** An initial connection forms between the aggregates in the matrix as soon as they get in contact with water. Meanwhile, EA start to form crystals.

2. **Growth of crystals:** The crystals grow progressively in the microstructure. Then, they break the initial connections between the aggregates and consequently form new connections.

3. **Volume expansion:** The crystals generate crystallization pressures as they grow. These pressures become swelling pressures when there is no more space in the pores for the new crystals. This contributes to reduce the shrinkage of the cementitious material thanks to an expansion of the matrix.

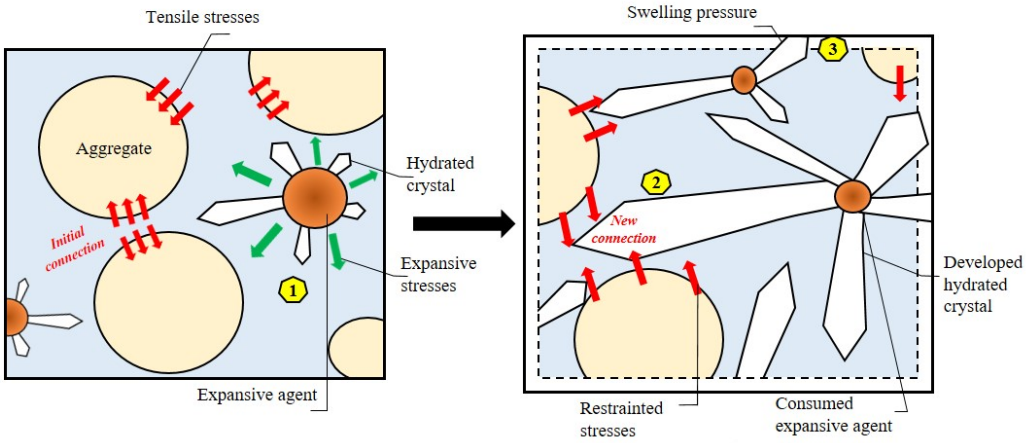

Figure 2.8 – Schematic of the EA expansion in the microstructure; **1:** Fromation of crystals - **2:** Growth of crystals - **3:** Volume expansion.

2.3.2 Types of EA

Several types of EA exist in the market, such as iron and alumina powders, calcium oxide, magnesium oxide and calcium sulfo-aluminate [12]. These three lasts are the most popular. The main characteristics of the five EA are detailed in the coming paragraphs.

2.3.2.1 Iron Powder (IP):

Iron Powder "IP" is an industrial by-product resulting from the grinding, cutting and milling of finished iron products [40]. This by-product is generated in huge quantities in the form of powder by workshops, steel mills and factories [41].

(i) **Hydration of IP:** Iron oxide has several chemical forms like FeO, Fe_2O_3, and Fe_3O_4 [42]. Fe_2O_3 has attracted the most attention because of its high potential to react with portlandite ($Ca(OH)_2$). The reaction of IP produces compacted C-S-H, which are responsible for enhancing the strength of the material [43].

(ii) **Effect on the sound material:** Most studies have focused on the replacement of sand with IP in the size range of fine aggregates (0-4 mm) in mixtures and its effect on the mechanical properties [40, 44, 45]. They showed that IP can be used as a partial replacement of natural sand in concrete mixtures. 20% of the sand can be replaced by IP without compromising the concrete compressive and flexural strength [40]. Ismail et Al-Hashmi [44] noted an increase in compressive (by 17%) and flexural strength (by 28%) when 20% of the sand was replaced by IP in concrete mixtures. When the sand replacement was equal to 30%, the mortar compressive, tensile and flexural strength have increased by 30%, 18% and 47% respectively at 28 days, compared to the mortar made

with 100% sand [40]. Other researchers found that the concrete compressive strength made with 100% IP was about 26% higher than concrete made with 100% natural sand [45].

Kiamahalleh et al. [43] performed a recent study on the physico-chemical properties of cement-based mortars containing IP nanoparticles (0%, 2%, 2.5%, and 3% by weight of cement). They found that 2.5% IP is the perfect content for the mechanical performances: increase in compressive (12%) and flexural (2%) strength at 28 days. It has a more compact microstructure compared to the mortar with 0% IP [43]. In addition, the hydration degree of the mortar with 2.5% IP is 32% higher than that of the ordinary mortar. IP can improve the formation of C-S-H gels resulting in faster hydration, and acts as a nano filler in the pore structure resulting in a denser material with good mechanical strengths [40, 43].

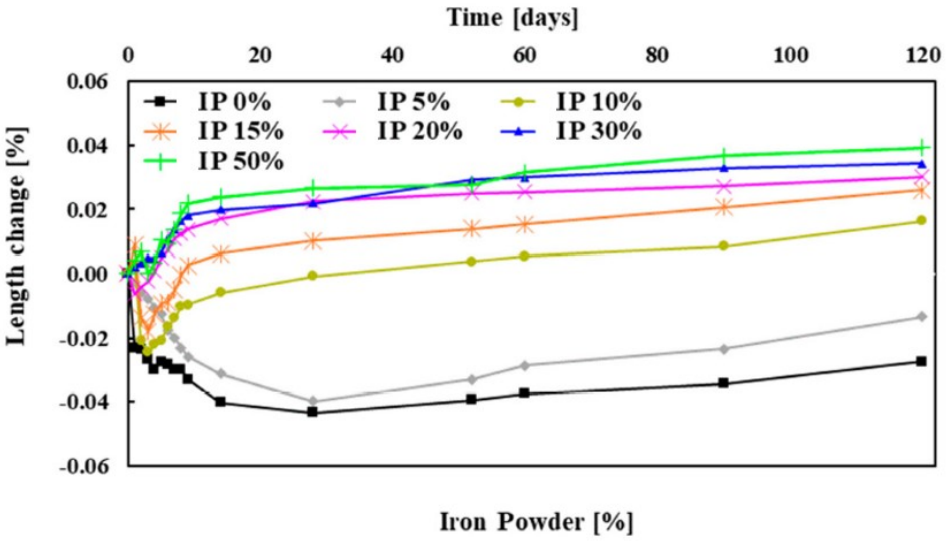

Figure 2.9 – Length change of mortars containing 0%, 5%, 10%, 15%, 20%, 30% and 50% of IP; [40].

The free shrinkage of cement-based mortars incorporating IP (0%, 5%, 10%, 15%, 20%, 30% and 50% by sand replacement) under water curing has been recently investigated [40]. As shown in Figure 2.9, mortars with low IP content (0% and 5%) show more significant free shrinkage. While mortars with 10%, 15%, and 20% IP shrink during the first week, but their shrinkages are rapidly offset with the matrix expansion. Their swelling reach a length change between 0.01% and 0.02% after 120 days of water curing. With a higher IP content (30% and 50%), matrix expansion occurs directly from the first day, and reaches about 0.04% after 120 days of water curing.

2.3.2.2 Alumina Powder (AP):

Alumina Powder "AP" is mainly extracted from two main resources: clays and coal fly ash [46]. Clay (e.g. kaoline) is a natural mineral that is widely used to produce nano alumina due to its sufficient availability and low cost. Alumina powder (Al_2O_3) has a high density, high melting point and good chemical stability [47].

(i) **Hydration of AP:** AP has a high chemical reactivity [47, 48]. It behaves as an activator that promotes the pozzolanic reaction and reacts with the portlandite. This reaction contributes to the formation of additional C-S-H which further densifies the matrix as reported by several authors (Eq. 2.4) [47–49]. Thus, similar to IP, the increase in compressive strength of mixture containing AP is due to the formation of the secondary C-S-H gel (or C-A-S-H gel).

$$Al_2O_3 + Ca(OH)_2 \rightarrow C - A - S - H \tag{2.4}$$

(ii) **Effect on the sound material:** Farzardnia et al. [49] noted that the addition of 1% AP nanoparticles (by cement weight) to cement-based mortar with 5% silica fume improveS its compressive strength by 16% at 28 days. It is due to the filler effect of the nanoparticles. It was also confirmed by other research works [50–52]. Szymanowski and Sadowski [53] showed that cement mortar with 0.5% of AP nanoparticles reduced its total porosity from 18.5% to 11.2% at 28 days.

Recently, Abdel-Gawwad et al. [54] studied the effect of AP nanoparticles on alkali activated slag pastes. The authors found that the drying shrinkage of paste containing 2% of AP is lower than the deformation observed for the slag paste without AP (drying shrinkage reduction of 49% at 28 days). Moreover, XRD analysis confirmed the formation of expansive strätlingite phases in parallel with C-S-H and C-A-S-H in the microstructure of the mixture containing AP, which were responsible for to the reduction of drying shrinkage.

2.3.2.3 Calcium Oxide (CaO):

The production of Calcium Oxide “CaO” from limestone is one of the oldest chemical transformations. Calcium oxide is a white crystalline solid. It is made by heating limestone, chalk, shells or coral containing mainly calcium carbonate ($CaCO_3$) [55]. At a certain temperature [750-900]°C, $CaCO_3$ is heated to produce CaO. The reactivity of CaO is strongly influenced by the calcination temperature of $CaCO_3$ as shown in Table 2.1. In this study, limestone particles of 200 μm diameter are calcined at different temperatures (750 °C, 850 °C and 900 °C) maintained constant during 3600 or 5000 seconds [55]. The specific surface area decreases when

the calcination temperature increases (Table 2.1). As the CaO reactivity is proportional to its specific surface area, the increase in $CaCO_3$ calcination temperature reduces the reactivity of CaO [56, 57]. The CaO-based EA will be referred to as CaO hereafter.

Duration (s)	Calcination temperature ($°C$)	Specific surface area (m^2/g)
3600	750	37.1
3600	850	25.4
3600	900	6.6
5000	850	25.7
5000	900	5.3

Table 2.1 – Specific surface area of CaO determined by the BET method as a function of the calcination temperature of $CaCO_3$ and its duration; [55].

(i) **Hydration of CaO:** Portlandite is the product resulting from the reaction of calcium oxide with water (Eq. 2.5). The portlandite turns into crystals which grow progressively and cause pressures on the paste matrix [58]. The delayed formation of portlandite in a constrained space lead to expansion in the matrix [58, 59].

$$CaO + H_2O \rightarrow Ca(OH)_2 \tag{2.5}$$

(ii) **Effect on the sound material:** Several studies have investigated the effect of CaO addition on the mechanical properties of cementitious materials. The main results are summarized in the following paragraphs:

Mechanical strength:

The addition of 15% CaO (by cement mass replacement) decreases the mortar compressive strength by 47.77% within the first day in case of a curing at 30°C and 60% RH [60]. In the same curing conditions [61], a decrease in the mortar compressive strength is also observed at 28 days when the CaO content increases from 3% to 5%. On the other hand, cement mortars with 3% CaO shows a very slight increase in their compressive strengths at 2, 7 and 21 days [62].

Shrinkage:

Zhang et al. [63] studied the shrinkage behavior of concrete specimens with 10% CaO stored at 20°C in three different curing conditions: sealed, water and 65% RH. The aim was to follow the autogenous shrinkage, expansion and drying shrinkage respectively. For the three types of curing, the shrinkage of specimen with 10% CaO is eliminated at early age (Figure 2.10). This is due to the matrix expansion occurred between the first and the fifth day. The phenomenon is more accentuated with the water curing (Figure 2.10(b)). It favors the hydration of CaO and the formation of $Ca(OH)_2$.

Similarly, the autogenous shrinkage of HPC with 10% CaO is reduced by 68% after 50 days compared to the ordinary HPC [59]. Gruszczyński and Bajorek [62] used 1% and 3% CaO (by cement mass replacement) in cement-based mortars. After 120 days, the drying shrinkage decreases by 30% and 60% respectively. Likewise, mortars of a ternary blend (cement-blast furnace slag-silica fume) with 3% and 5% CaO present a lower autogenous shrinkage at 28 days than the ordinary mortar due to matrix expansion [61]. The authors attributed this expansion to the growth of $Ca(OH)_2$ crystals that filled the pores and reduced capillary depressions.

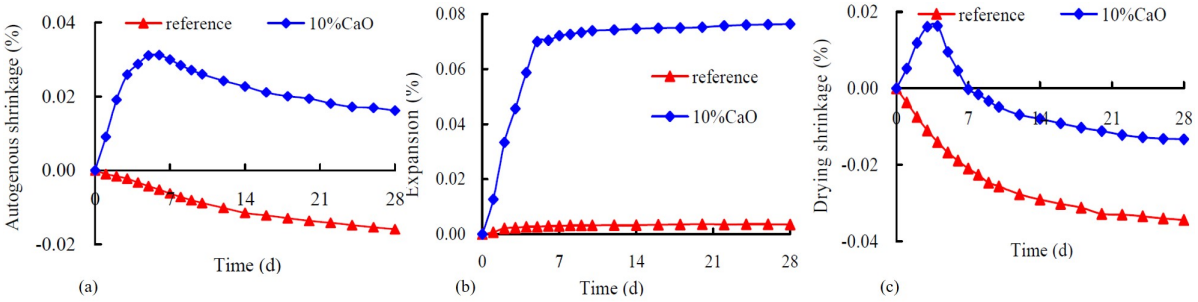

Figure 2.10 – Autogenous shrinkage (a), expansion (b) and drying shrinkage (c) of concrete with/out 10% CaO; [63].

In several studies [59, 60, 62, 64], combination of shrinkage reducing agents (e.g. glycol, polyoxyalkylene alkyl ether and propyleneglycol ether type) and CaO (1% to 10%) are tested and appear to be favored to limit the shrinkage (plastic, autogenous and total) thanks to the formation of large crystals $Ca(OH)_2$ responsible of the matrix expansion.

2.3.2.4 Magnesium oxide (MgO):

The MgO-based EA is generally calcined from magnesium carbonate minerals. It can also be synthesized from sea water or brine obtained as waste from the desalination process [8]. Thus, it can be an industrial by-product being environmentally friendly [65]. MgO-based EA has gained a great interest lately. It is being used more and more in various constructions, especially in China thanks to its expansive behavior related to its hydration mechanism [65]. The MgO-based EA will be referred to as MgO hereafter.

The reactivity of MgO can be easily controlled by the calcination conditions such as temperature and time of calcination [65–67]. These calcination conditions affect directly the surface area and the fraction volume of MgO grains (crystal lattice distortion) [66, 68], the two main factors controlling its reactivity and thus, its hydration rate and expansive behavior.

Two types of MgO can be defined: Light Burned MgO (LBM) and Dead Burned MgO (DBM) [67]. LBM, also called "reactive MgO", is calcined at [700 - 1000]°C to the formation of small crystals characterized by a large specific surface area and thus a higher hydration

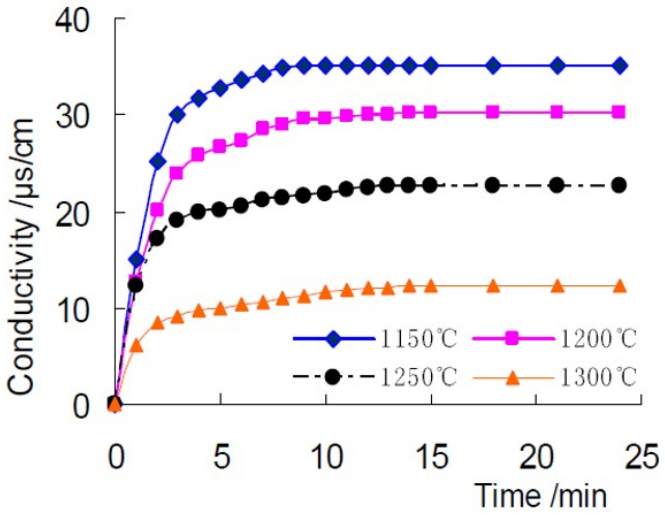

Figure 2.11 – Influence of calcination temperature on the MgO conductivity; [68].

reactivity [67,69]. LBM produces generally a fast and large expansion at early age, but slow and small expansion at later age [67]. On the contrary, DBM, also called " overburned MgO ", is calcined in a higher temperature range of [1100 - 1500]°C. It therefore hydrates extremely slowly at early age due to its lower reactivity [67,69]. As shown in Figure 2.11, the conductivity of 0.2 g MgO with 100 ml water decreases when increasing the calcination temperature of magnesium oxide, which confirms that this last influence the reactivity of MgO [68].

(i) **Hydration of MgO:** The hydration of MgO occurs as follows:

$$MgO + H_2O \rightarrow Mg(OH)_2 \tag{2.6}$$

Initially, MgO dissolves and increases the concentrations of Mg^{2+} ions in the interstitial solution. The brucite crystals formation is driven by the supersaturation of Mg^{2+} in the interstitial solution [69]. When the ionic concentration becomes high enough for brucite formation, this product forms near the MgO particles and grow continuously [8,65]. The brucite crystal growth is limited by the porous network of the matrix. It undergoes crystalline pressures that enlarge the spaces within the matrix, and thus generates expansion [69]. The rate of expansion is related to the reactivity of MgO: higher reactivity will produce rapid and large expansion at early age, and tends to be constant after 70 days. Lower reactivity will produce slow and small expansion at early age, but faster and larger expansion at late age [70]. In addition, the brucite is characterized by its perfect thermal stability and relatively controllable forming speed [8,69,71]. MgO is usually used in ordinary concrete to compensate for its shrinkage [69]. It is also used to activate blast furnace slag-based matrices [72,73]. Many types of hydration products can be identified in the MgO-activated slag system such as: C-A-S-H gel, hydrotalcite, brucite, ettringite

and monosulfate [73]. A higher dosage of MgO increases the degree of blast furnace slag reaction, and the formation of hydration products [73].

(ii) **Effect on the sound material:** The effect of MgO addition on the mechanical properties was investigated in several studies and the main results are summarized hereafter:

Mechanical strength:

Cao et al. [65] reported a slight decrease in the compressive and flexural strengths of mortars containing 10% MgO and cured under water at 7 and 28 days. Similarly, the compressive strengths of mortars containing 5% and 8% MgO are decreased by 8.5 MPa and 12.2 MPa respectively at 90 days [74]. This decrease in strength is mainly attributed to the reduced formation of C-S-H gel due to the partial replacement of Portland cement by MgO [74].

Shrinkage:

Mo et al. [74] examined the autogenous shrinkage of cement pastes containing MgO. The cement pastes with 5% MgO compensate their shrinkage and expand after 55 days, while the one with 8% MgO starts to expand after 21 days. On the other hand, when 8% MgO is added to the concrete mixture cured in water (at 20°C), the matrix starts to expand very quickly and compensates its shrinkage after only 7 days and its concrete expansion continues after 28 days [68]. The authors claimed that water curing activates the hydration of MgO, accelerates the expansion rate of the matrix and might cause excessive expansion at later ages [68].

Indeed, as shown in Figure 2.12(a), the cement paste with 8% MgO agent was cured in sealed condition for 160 days. It can be seen that the growth of $Mg(OH)_2$ crystals was limited by the lack of water. Therefore, it was difficult to generate expansive forces in the paste. The lack of water do not facilitate the crystallization of $Mg(OH)_2$. In contrast, for the water-cured cement paste for 160 days (Figure 2.12(b)), the supply of water promotes the crystallization of $Mg(OH)_2$ into large and dense crystals. Consequently, the crystals crowd together to push the hardened paste and generate expansion. Moreover, when sufficient water is provided, even after the MgO is completely hydrated, the expansion of the paste continued due to the re-crystallization of $Mg(OH)_2$ [69].

In addition, several works attempted to combine the use of MgO with CaO [71, 75–77]. After 28 days, cement concretes with 2% and 4% of (MgO:CaO = 1:1) reduced their autogenous shrinkage by 50% and 94.5% respectively. This is explained by the internal relative humidity which is higher by 7.81% and 13.41% respectively than the concrete without EA at 28 days. It is in agreement with other study [77], that report that concrete containing CaO and MgO expansive agents can produce remarkable expansion that increases with increasing CaO:MgO content.

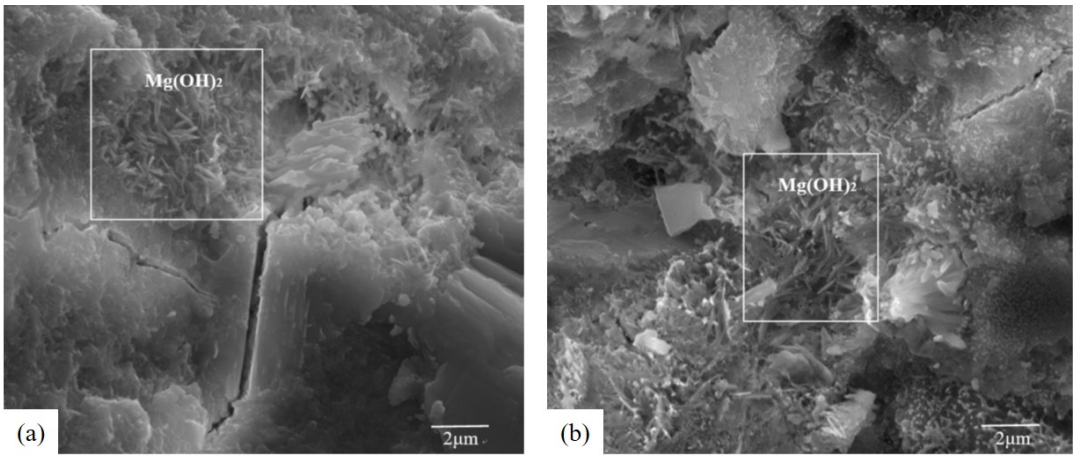

Figure 2.12 – Brucite crystals formation at 160 days in sealed (a) and water curing (b); [69].

2.3.2.5 Calcium Sulfo-Aluminate (CSA):

Calcium Sulfo-Aluminate "CSA" is an expansive agent that can be prepared from industrial by-products. It is commonly a ternary blend of Hauyne ($C_4A_3\underline{S}$), free lime (C) and anhydrite ($C\underline{S}$) as shown in Figure 2.13. CSA-based EA can be produced from natural calcite and industrial by-products and wastes, such as $Al(OH)_3, CaSO_4.2H_2O$ [78]. The raw materials are mixed and heated at 20, 400, 600 and 1200°C for 1 hour and cooled rapidly in air. The CSA-based EA is generally used in concrete mixtures to compensate for shrinkage. It will be referred to as CSA hereafter.

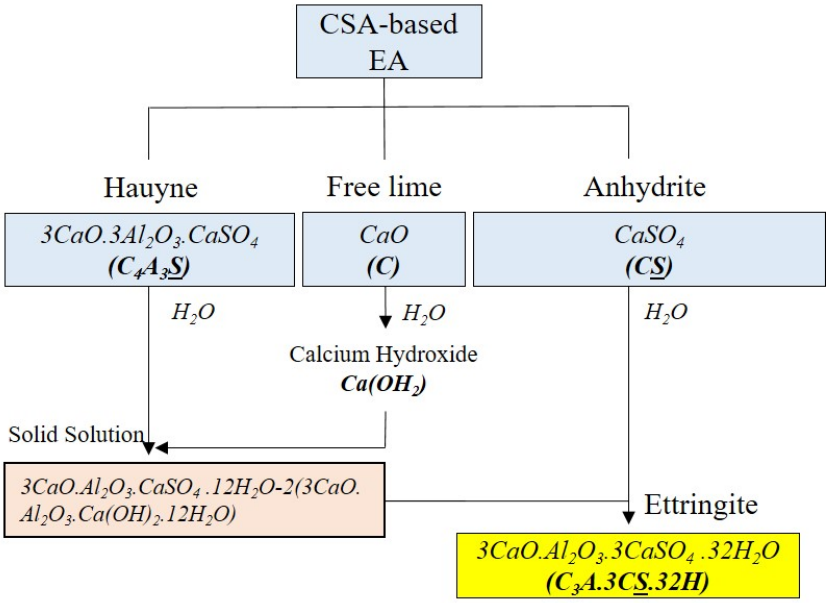

Figure 2.13 – Schematic of the hydration of CSA and the ettringite formation.

(i) **Hydration of CSA:** The CSA hydration is described in Figure 2.13. On contact with water, hauyne reacts with $Ca(OH)_2$ from the free lime hydration and/or the matrix [79,80]. They form a solid solution that reacts with anhydrite to form ettringite (Figure 2.13). A simplified hydration process is shown in Eq. 2.7. Several researchers claim that ettringite formation is responsible for matrix expansion, which results in shrinkage compensation.

$$C_4A_3\underline{S} + 8C\underline{S} + 6C + 96H \rightarrow 3(C_3A.3C\underline{S}.32H) \tag{2.7}$$

(ii) **Effect on the sound material:** The effect of CSA addition on the mechanical properties was investigated in several studies and the main results are summarized hereafter:

Compressive strength:

The effect of CSA on the mechanical strength is still not clear. The addition of CSA content equal to 2%, 4%, 6%, and 8% in UHPC improves its compressive strength in a range of 10-22% compared to control UHPC at 2 days old [81]. Similarly, the addition of 10% CSA increases the mortar compressive strength by more than 6% at 7, 28, and 90 days [82]. Other research works does not support the fact that the addition of CSA improves the mechanical strengths of the material. Guo et al. [83] reports a decrease of 9.3% and 7.9% of the concrete's compressive and tensile strengths respectively at 14 days, when 10% CSA is added. They attributed the reduction in strength to the excessive CSA content leading to the formation of an excessive ettringite content at early age, as shown in Figure 2.14(a). This caused the formation of micro-cracks in the microstructure. Other authors [84,85] also proved that the compressive strengths decreases by adding more than 5% CSA.

Furthermore, according to [83,86], the addition of CSA combined with MgO is beneficial to the mechanical strength of concrete. The cracking resistance of concrete with 10% CSA (by the cement weight) at 60 days is improved by 49.2% compared to ordinary concrete [83]. With 10% of the combination of (CSA:MgO = 2:1), the cracking resistance of concrete is further improved by more than 97% compared to concrete with 10% CSA [83].

Shrinkage:

Guo et al. [83] evaluated the drying shrinkage of concrete containing 10% CSA at 14, 28 and 60 days. The drying shrinkage was reduced by 35% after 14 days. However, no further improvement in drying shrinkage was observed at 28 and 60 days. This is explained by XRD analysis, where the intensity of ettringite peak is not changed obviously after 14 days (Figure 2.14(b)). This means that ettringite formation is almost finished at this period, and do not participate to a shrinkage reduction beyond 14 days. Yoo et al. [81] reported that at least 6% CSA (by weight of cement) should be added to the UHPC mixture to compensate for its drying shrinkage. Most authors [81,83,84,86] agreed that CSA is characterized by a rapid setting and shrinkage compensation properties due to

the rapid reaction of C_4A_3S and the expansive nature of ettringite. In addition, the expansion of the matrix increases with the increase of CSA content [84, 87].

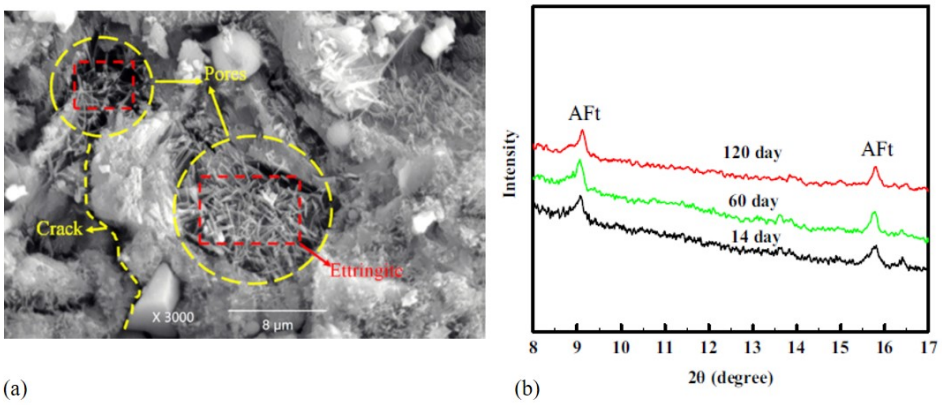

Figure 2.14 – SEM image of concrete at 14 days (a), XRD analysis showing AFt formation at 14, 60 and 140 days (b); [83].

2.3.3 Autonomous healing using EA

As shown previously, the effect of EA on the sound material properties was studied in several studies, but only a few studies look on the effect of EA on the behavior of cracked material and more particularly the self-healing capacities of mixtures containing MgO [6, 7, 9, 88–90] and CSA [24, 34, 91]. The following paragraphs summarize these research works.

Cement-based mortars incorporated 10% CSA were tested by Sisomphon et al. [24]. The objective was to evaluate the self-healing capacities of the mortars. The study was conducted via a water permeability test on pre-cracked specimens at 28 days old with an initial crack width from 100 to 400 μm. The height of water above the specimen was set at 100 ± 5 mm. The water flow rates were measured at different ages. Also, the specimens were cured in water after each test, which was renewed every 7 days. After 28 days of water curing, the mortar with 10% CSA shows a crack sealing rate superior to 80%. For the reference mortar, it is equal to 70%. In addition, the water flow rate is reduced by more than 90% in the presence of CSA.

Some research works have also shown that MgO has some self-healing capacities. Qureshi and Al-Tabbaa [6] evaluated the self-healing of cement pastes by measuring the mechanical strength recovery of cracked specimens. The one-day old specimens were cracked through a 3pbt and then cured under water. The initial crack widths ranged between 100 to 500 μm. The specimens were cracked again after a curing period of 14, 28, and 150 days. At these intervals, mixture with 5% MgO achieved 24%, 35%, and 8% strength recovery, respectively, compared to mixture with 10% MgO (14%, 13%, and 2%, respectively), and the reference mixture (4%, 6%, and 9%, respectively). The reduction in strength recovery when using 10% MgO is attributed

to the high MgO content in the cement paste leading to a high expansion. It is in agreement with the results Zhang et al. [8]. The 28 days old cement-pastes was pre-cracked by a 4pbt and the crack widths were smaller than 100 μm. After 90 days of water curing, the cement paste with 5% MgO reaches a crack sealing rate equal to 82% (Figure 2.15). This rate is smaller for the paste with 10% MgO - it is around 70%. According to the authors, the increase of MgO content to 10% causes an excessive expansion of the paste, which is responsible for a poor volume stability and poor self-healing of the cracks [8].

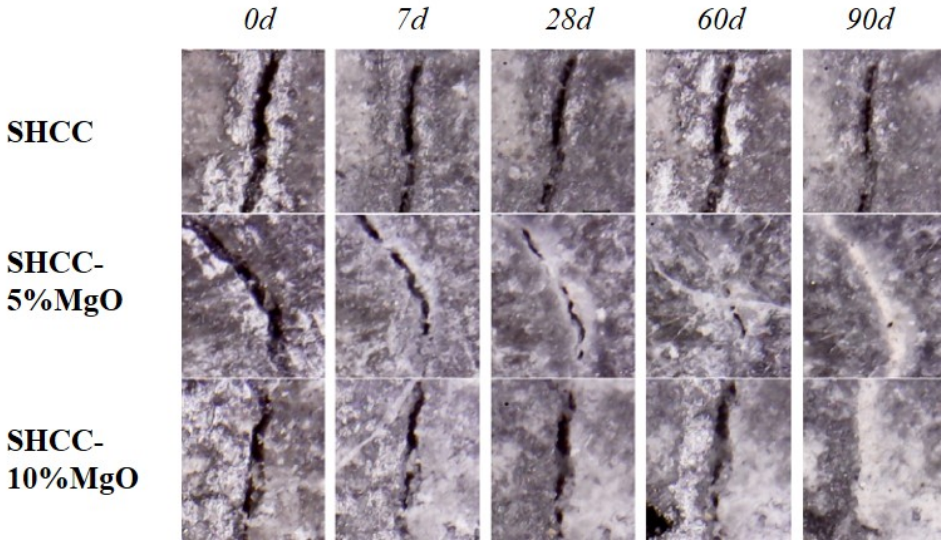

Figure 2.15 – The evolution of the cracks in water curing [8].

Similarly, Qureshi et al. [7] studied the healing performance of cement pastes incorporating four contents of MgO (0%, 2.5%, 5% and 10%). The specimens were pre-cracked at one day old until a crack width of 170 μm and then cured under water. The healing performance was estimated by visual observations of crack and measurement of strength recovery. The optimal mixture is the one containing 5% MgO (PC95M5 - Figure 2.16) whose the cracks were the most reduced during the 28-first days (Figure 2.17). The healing products in the crack of the cement paste (PC100) and the one with 5% MgO (PC95M5) showed calcite, portlandite, ettringite and C-S-H. Moreover, the addition of MgO in $PC95M5$ promoted the formation of brucite and other magnesium hydro-carbonate products [7].

Also, Sherir et al [9, 89, 90] performed several works to design a self-healing system of ECC containing MgO, such as cement-based mortars containing 50% fly ash and 5% MgO. The evaluation of self-healing was done by strength development and recovery via a compressive test. The results confirmed that the ECC with 5% MgO developes and recovers more compressive strength than the control ECC, especially after a long water curing period (more than 300 days in water and natural curing -Canada). In addition, the ECC-MgO system showed a good ability to self-heal micro-cracks (less than 60 μm) compared to ECC.

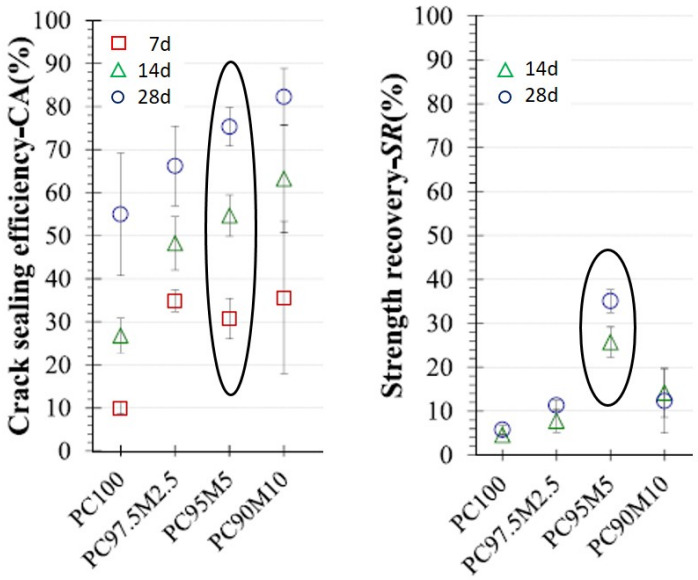

Figure 2.16 – Crack sealing efficiency and strength recovery of cement pastes under water curing [7].

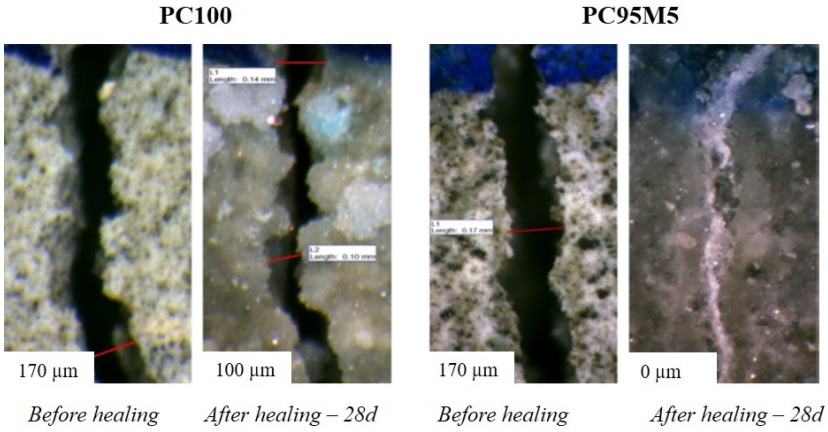

Figure 2.17 – Evolution of the cracks in water curing [7].

2.3.4 Overview on the EA

Many types of expansive agents exist in the commercial market. Their effect on the mechanical and healing properties of cementitious material depends on their content, their chemical composition, their reactivity and their curing condition. Table 2.2 summarizes the main characteristics of the five EAs found in the literature.

As shown in Table 2.2, the addition of IP and AP is mainly studied to improve the compressive strength of the material. They are not treated in the field of self-healing. Their hydration leads to the formation of a C-S-H/C-S-A-H gel by the pozzolanic reaction. IP and AP are poorly treated in the literature, providing a lack of context for their expansive behavior that might be interesting for the autonomous healing.

CaO and MgO receive good attention because of their hydration reaction and the thermal stability of their hydration products (portlandite and brucite respectively). The addition of CaO and MgO to the mixtures decreases the compressive strength but effectively reduces the autogenous, drying and free shrinkage. It can also offset the shrinkage at early age when cured in water and induces matrix expansion. But, the expansion of mixture with CaO could be constant after 7 days, while for mixture with MgO, it might continues to the long-term. Moreover, the portlandite can be consumed by topochemical reaction, especially when mineral additions are used in the mixtures. This can be an undesirable condition for the self-healing process. While mixture with MgO show good ability to heal cracks created at early age. Mixtures with CSA show also good ability to heal cracks created at 28 days. Moreover, the early ettringite formation due to CSA addition densifies the matrix and decreases its drying shrinkage.

However, there is still a lack of knowledge for the expansive behavior of MgO and CSA which could be interesting for the autonomous healing. Moreover, even though MgO and CSA are treated for self-healing purpose, most of the studies pre-cracked the specimens at an early age (e.g., 1 day) [6, 7], and the cracks were less than 170 μm [7–9]. It is worth mentioning that the self-healing process at a young age could be improved even without the use of EA in the mixtures. More anhydrous particles can be found at this stage which improves the healing of the crack. In addition, matrix expansion using these two EAs was not considered in the self-healing evaluation, so no autonomous healing was checked by these different works. So, in this work, the main attention is given on MgO and CSA expansive agents. But, other tests and analyses must be considered to correctly evaluate the effect of MgO and CSA on the mortar properties and its healing capacity.

EA	Origin	Main hydration product	Content in the mixture	Main effect on the		Hydration	
				sound material	cracked material	Advantages	Disadvantages
IP	Steel products [41]	C-S-H [43]	- 5% to 50% of sand weight [40] - 2% to 3% of cement weight [43]	- Increases the compressive strength (more than 12%) [40] - Decreases the free shrinkage [40]	-	-	-
AP	Clay [47]	C-S-A-H [48]	0.5% to 2% [49,53,54]	- Increases the compressive strength [49–53] - Decreases the drying shrinkage (more than 49%) [54]	-	-	-
CaO	Limestone [55]	$Ca(OH)_2$ [58]	1% to 10% [59,61–63]	- Decreases the compressive strength [60,61] - Decreases the drying and autogenous shrinkage [59,61–63] - Causes matrix expansion up to 7 days [63]	-	- Needs little water to hydrate (1 mole of H_2O) [Eq.2.5] - Produces portlandite which is a thermal stable hydration product (decomposes at 450°C) [92]	- Produces portlandite that can be consumed by topochemical reaction [93]
MgO	Magnesium carbonate [8]	$Mg(OH)_2$ [8]	5% to 10% [6,7,65,68,74]	- Decreases the compressive strength [65,74] - Reduces the autogenous and free shrinkage [68,74] - Causes matrix expansion that continued after 28 days [68]	- Shows good ability to heal cracks created at early age [6,7] - Increases the strength recovery of the cracked material [6,7]	- Needs little water to hydrate (1 mole of H_2O) [Eq.2.6] - Produces brucite which is a thermal stable hydration product (decomposes at 400°C) [94]	- Can cause excessive expansion due to continuous formation of brucite [69]
CSA	Industrial wastes [78]	AF_t [79,80]	2% to 10% [81–83]	- Decreases the drying shrinkage till 14 days [83] - Increases the compressive strength (more than 6%) [81,82]	- Shows good ability to heal cracks created at 28 days [24]	- Rapidly produces ettringite at early age which densifies the matrix [83]	- Requires a lot of water to hydrate (32 moles of H_2O) [Eq.2.7] - Produces ettringite which is not a thermal stable hydration product (decomposes at 80°C) [92,95]

Table 2.2 – Summary table of the main criteria of Expansive Agents.

2.4 Experimental methodology for self-healing monitoring

The evaluation of the self-healing process requires accurate and, most importantly, multi-time reproducible test methods. Several methods have been proposed in the last years [14]. Generally, the methodology for monitoring self-healing can be divided in five steps (Figure 2.18) : (1) casting and preparation of the specimen; (2) cracking of the specimen; (3) measurement of the required property/state; (4) curing type and duration; (5) evaluation of the recovery of the same property/state measured at the third step. This paragraph focuses on the third step and present the main methodologies used recently in the literature for the self-healing evaluation.

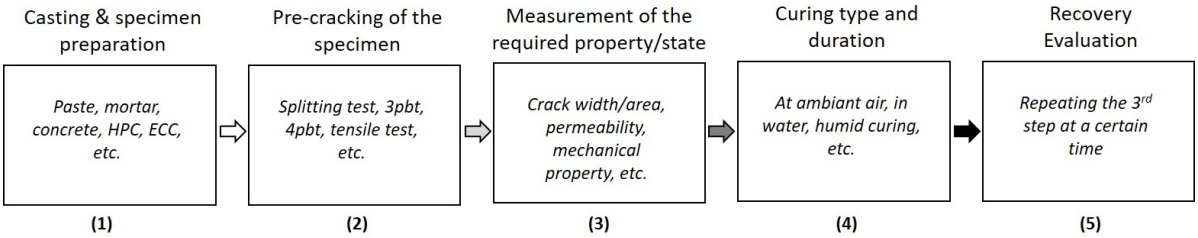

Figure 2.18 – Methodoloy for the self-healing evaluation.

2.4.1 Measurement of the crack dimensions

Crack surface measurement is the most commonly method used for monitoring self-healing process. It has also been frequently used as a secondary method to support the results of other tests [5–7,24,33,34,88]. The most popular used equipment for this analysis is the optical microscope, which is easy to use for crack width measurement. The crack area is usually determined by image processing using a software [7,15]. The measurement points must be determined along the crack to measure the initial crack dimension (width/area). Then, after a

certain healing period (at time t), it is necessary to compare the crack dimension (width/area) with its initial value. So, the Crack closing Ratio "CR(t)" is calculated using Eq. 2.8 [7,33].

$$CR(t) = \frac{W_i - W_f(t)}{W_i} * 100 \tag{2.8}$$

Where W_i and $W_f(t)$ are the initial and final crack width/area.

This technique can be very time consuming, as a large number of points are required to measure the crack width along its length, in order to obtain a better estimation of self-healing. Moreover, no information is given by this method on the internal healing process into the crack because it is limited on the surface. While X-ray tomography can monitor the self-healing evolution and the healing products into the crack [96]. It is also an nondestructive technique, does not require a sample preparation, and it is often used to produce 3D images of cementitious materials with and without mechanical loading [96]. But, it could be very expensive.

2.4.2 Recovery of mechanical properties

The self-healing of the crack should not only seal the crack, but also recover the mechanical properties of the damaged specimens. Different test setups have been proposed in the literature: three-point bending test (single crack) [7,88] or four-point bending test (multiple cracks) [8,9] (Figure 2.19), compressive [9] and tensile strength test [97]. During these tests, specimens are loaded until a defined crack width or strength level. After, specimens are cured to heal under specific conditions according to the self-healing mechanism investigated by the authors. Regularly, specimens are tested with the same initial test to evaluate the recovery of the mechanical property and the healing kinetics.

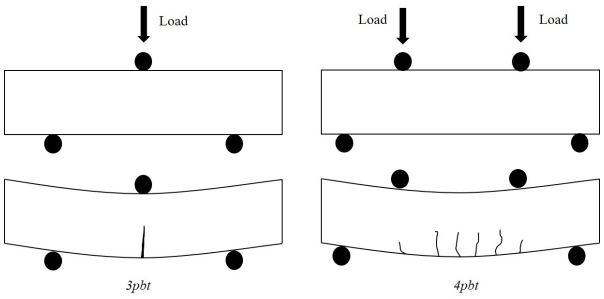

Figure 2.19 – Schematic of the pre-crackinf using 3pbt and 4pbt.

These techniques sometimes require reinforced concrete specimens to control the desired crack width. Therefore, the size of the specimen can be very large, making the test difficult to perform [15,20]. In addition, the evaluation of self-healing can be complicated to interpret due to the presence of the reinforcement. The bond between the concrete matrix and the reinforcement and its evolution during the maturation of the concrete will change the stiffness of

the element, which may inhibit small healing effects as part of the natural change in properties that occurs in normal concrete [13].

2.4.3 Recovery of transfer properties

One of the main goals of crack healing is to improve the durability of the material. Therefore, self-healing studies based on the transport properties are of great importance. Different water permeability test methods are proposed in the literature in order to evaluate the self-healing [13, 14, 24, 98, 99].

Sisomphon, et al. [24] used a simple water permeability test made by a plastic cylinder and a PVC ring sealed with silicone to prevent water leakage (Figure 2.20(a)). The water level above the specimen was maintained at 100 ± 5 mm (Figure 2.20(b)). The amount of water passing through the crack was measured during a 10-min test duration only, and the specimen was pre-cracked by a splitting test till a residual crack width equal to [100-400] µm. Another water permeability test setup is used by Park et Choi [98] (Figure 2.20(c)). The test was performed with a water level of 135 mm above the specimen, and the water flow was measured for only 1 minute during each measurement. The specimen was pre-cracked by a splitting test till a residual crack width equal to [200-300] µm. Roig-Flores [13] used a method consistent with the permeability test described in UNE-EN 12390-8, but measuring the water flow instead of the water penetration depth. In addition, to prevent water leakage from the lateral surface, these areas were sealed with epoxy resin as shown in Figure 2.20(d). The test was performed with a head water pressure equal to 2 ± 0.05 bar. However, due to the capacity limits of the containers collecting the water, the duration of the test was limited to 5 minutes for small cracks ([100-200] µm) and 1 minute for large cracks ([300-400] µm). The tests listed above show some scattered results related to the wide range of crack width of the tested specimen and the small duration of the test.

Escoffres [99] used a permeability device coupled to a hydraulic press that simultaneously: applies uniaxial tensile loading to the specimen and measures crack openings and water permeability (Figure 2.21). The specimen used was reinforced concrete and was pre-cracked by a four point bending test. The average obtained crack widths measured 200 µm. As shown in Figure 2.21, two lateral faces of the specimen are covered with a waterproof layer where displacement sensors are placed. These sensors allow real-time measurement of crack openings during the loading. The other two lateral faces are exposed to water through small tanks filled with water and connected to big cylinders. While the specimen is loaded, a pressure gradient is created between the front and the back of the specimen in order to induce a unidirectional movement of the water. The initial pressure gradient was 50 kPa, equivalent to a water head of 5 meters. Finally, in order to obtain the inlet and outlet flow rates of the specimen, differential height sensors are installed at the base of the cylinders to measure the volume of water passing

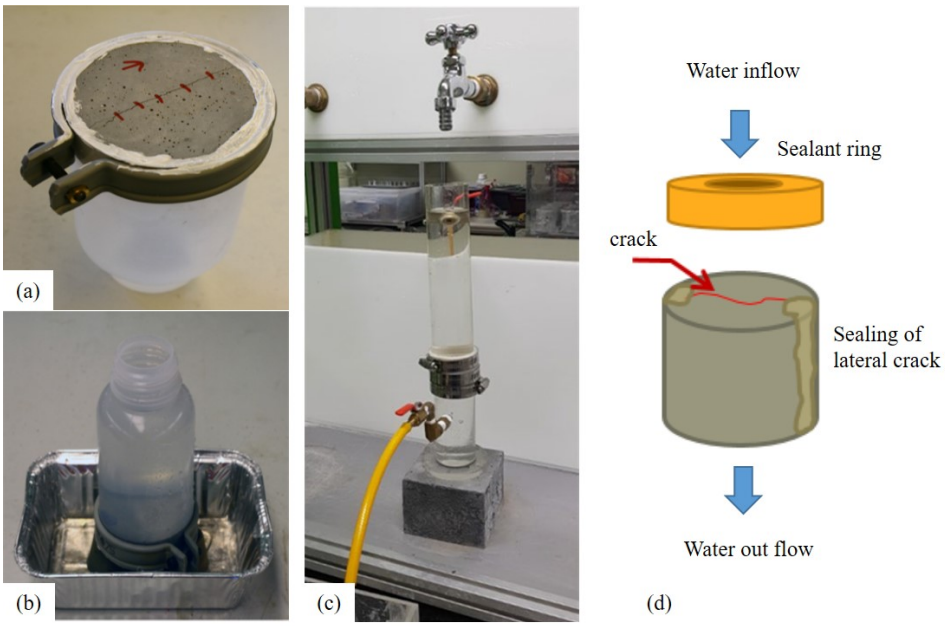

Figure 2.20 – Water permeability tests implemented in several research works: Sisomphon et al. [24] (a & b); Park et Choi (c) [98]; Roig-Flores [13] (d).

through the specimen. This test setup is very complicated and requires large reinforced concrete specimens (550x150x150 mm^3).

The University of Ghent developed a water permeability setup as shown in Figure 2.22 [14]. The specimen glued in a PVC ring is mounted between two transparent cylinders. To prevent water leakage, white rubber joints are used between the PVC ring and the transparent cylinders. Each cylinder is covered at its outer ends by a plate with two openings. In the upper opening of the plate a pipette is placed and covered to avoid evaporation during the test. The glass pipette has an inner diameter of 10 mm and was graduated to measure the water level during the test. In the lower opening of the plate, a rubber tube is attached and goes up to the specimen. The other two openings are used to fill water into the cylinders, the pipette and the rubber tube. Thus, the water passing through the crack is measured by the water level in the pipette at regular intervals, normally once a day. However, the test may last several days until a steady water flow is achieved.

2.4.4 Overview on the self-healing evaluation

The interesting experimental techniques for the evaluation of self-healing are reviewed. Table 2.3 summarizes the main advantages and disadvantages of the different techniques used in the literature, including their test limits. The monitoring of the crack dimensions is the most frequently used method for evaluating self-healing, due to the simplicity of the test and the accessibility of the necessary equipment. But, as it is performed on the crack surface, it

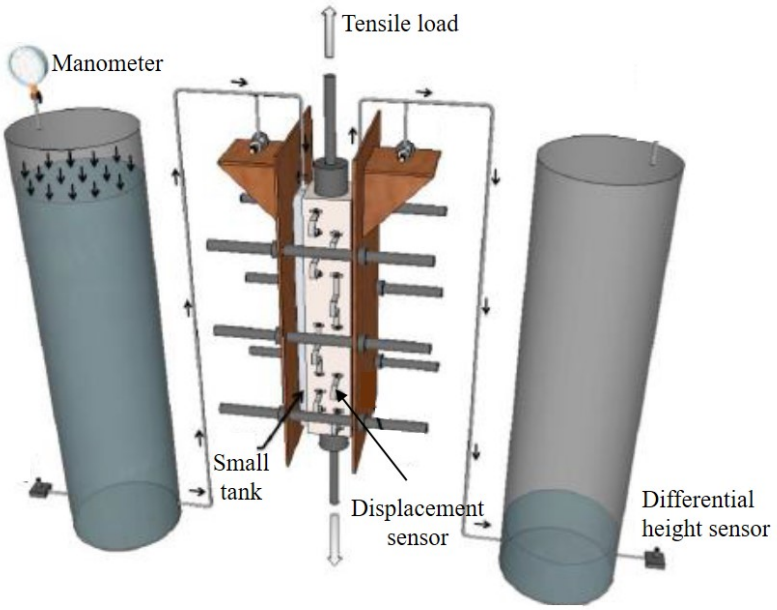

Figure 2.21 – Water permeability test implemented by Ecoffres [99].

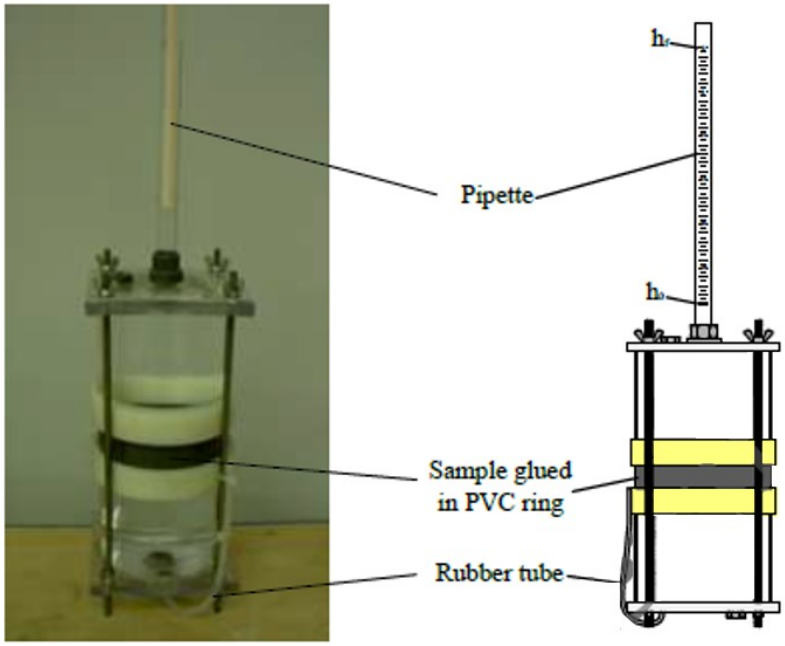

Figure 2.22 – WP test used implemented by the University of Ghent [14].

presents a limited evaluation of crack healing. Mechanical property monitoring could present a complicated analysis related to the large reinforced specimens required for analysis. While monitoring the transfer properties through a water permeability test provides a good assessment of the healing capacity and kinetics. This test differs among studies with regards to the tested specimen, the water pressure above the specimen, and the duration of the test. Most of the works aimed to monitor the water flow for less than 10 minutes. This is insufficient for a healed specimen, as it is not possible to compare results when specimens are partially or fully healed over a limited test duration. So, in this work, the main attention is given for the water permeability test. Nevertheless, some improvements regarding the test duration and the specimen's initial crack width should be considered to properly evaluate the self-healing process.

Self-healing evaluation	Advantages	Disadvantages	Research work	Test limit		
Measurement of crack dimensions	- Supports other results - Monitors the crack dimensions over time - Its equipment is affordable and easy to implement	- Does not quantify the internal dimensions and healing of the crack - It could be a time consuming	[5–7, 24, 33, 34, 88]	- Limited on the crack surface (2D monitoring)		
Recovery of mechanical properties	- Provides a direct measurement of the mechanical property of the tested specimen	- It can make the self-healing evaluation hard to interpret due to the presence of the reinforcement	[15, 20]	- Large specimens		
				Studied crack width (µm)	Water pressure	Test duration
Recovery of transfer properties	- Provides a good approach for the durability of the material - Evaluates the internal crack healing capacity	- It could be complicated to setup - It can present scattered results related to the initial crack width of the specimen	[24]	[100-400]	100 ± 5 mm	10 minutes
			[98]	[200-300]	135 mm	1 minute
			[13]	[100-200] [300-400]	2 ± 0.05 bar	5 minutes 1 minute
			[99]	[200]	5000 mm	-
			[14]	-	-	Several days until a steady flow

Table 2.3 – Summary table of the experimental procedures for self-healing evaluation.

2.5 Conclusion

The self-healing of cementitious materials, the different mechanisms and the parameters influencing their potential were discussed in this literature review. Two types of healing are responsible for crack closure: autogenous healing and autonomous healing. The potential of autogenous healing is limited. Therefore, the latest research focuses on autonomous healing using different materials and experimental techniques. However, most of the studies conducted so far identify possible causes of the autonomous healing phenomenon, such as hydration of anhydrous particles left in the crack and carbonation. While other mechanisms could accelerate this process, e.g. matrix expansion. This mechanism can be achieved by the use of an Expansive Agent "EA" in the mixture. Therefore, this chapter examined five different EA's: iron powder, alumina powder, calcium oxide, magnesium oxide and calcium sulfoaluminate. Their effect on the mechanical properties of the cementitious material depends on their content, chemical composition, reactivity and curing conditions. However, there is a lack of knowledge about the autonomous healing of the material in the presence of EA. Therefore, further tests and analyses must be considered to properly evaluate the effect of EA on the mortar properties and its healing capacity.

The techniques used to monitor the self-healing process vary among studies. Monitoring of crack dimensions is the most frequently used method for evaluating self-healing. However, it can be used as a supplementary study for other tests and to explain the results. Monitoring of transfer properties by a water permeability test provides a good assessment of healing capacity and kinetics. Nevertheless, some improvements (e.g. test duration, initial crack width of the tested specimens, etc.) should be considered to properly evaluate the self-healing process.

Chapter 3

Monitoring of self-healing: Round Robin Tests

Contents

3.1 Introduction

The Round Robin Test (RRT) is an interlaboratory test (measurement, analysis or experiment) performed similarly in different laboratories. In the civil engineering field, the goal of the RRT is to identify and validate methodologies for testing the durability of cement-based concrete. Thus, several independent researchers conduct tests using the same methods proposed by the RRT program. SARCOS COST Action (https://www.sarcos.eng.cam.ac.uk) is leaded by research institutions searching on different self-healing technologies and repair solutions for extending service life of new and existing concrete structures.

This chapter focuses on evaluating the experimental methodologies provided by the RRT program within the framework of SARCOS Cost Action for the self-healing, since there is a lack of standard test procedures in this topic. Two projects are decided to work on, among five projects. One of the main objectives of this RRT is to evaluate several methodology to monitor the healing process by adding in the concrete mixtures mineral addition, expansive admixture, crystalline admixture, or encapsulating bacteria. In the present work, the tests are conducted within the framework of RRT1 and RRT3 which respectively focus on the use of mineral addition and crystalline admixture. RRT1 program is provided by the Aristotle University of Thessaloniki (AUTH), directed by Prof. Stefanidou Maria and Dr. Tsampali Evangelia [100]. RRT3 program is provided by the Polytechnic University of Valencia, directed by Prof. Pedro Serna and Dr. Marta Roig-Flores [101]. The healing process is monitored using two different tests: water permeability and water absorption

3.2 Materials and mixtures proportions

For each RRT, two concrete mixtures are tested: a Portland cement concrete, the reference and a concrete with mineral additions for RRT1 or an expansive admixture for RRT3.

3.2.1 RRT1's mixtures

Two fiber concrete compositions were proposed by the Aristotle University of Thessaloniki (AUTH) and designed by Kaunas University of Technology (KTU) in Lithuania. The first, named "REF", is the reference concrete and the second named "SLAG" contains 20% of Ladle Furnace Slag (LFS). This LFS is used to produce CEM III/B 32,5 N-LH/SR in the factory AB "Naujoji Akmene". Its chemical composition is given in Table 3.1. These mixtures contain 30 kg/m^3 of steel fibers HENDIX PRIME 60/32 (32 mm length and 0.53 mm diameter). The mixtures proportions are given in Table 3.2. The used cement is CEM I 42.5 N and the aggregates are dolomite coarse aggregates with a maximum size of 16 mm. The water/binder ratio is equal to 0.55. The used superplasticizer is Sika ViscoCrete D418, with a content varying

from 3 to 3.5% by cement weight.
Six beams (100x100x400 mm^3) for water absorption tests and four cylinders (Ø100xH200 mm^3) for water permeability tests are received for each concrete composition.

Al_2O_3	SiO_2	K_2O	Na_2O	MgO	CaO	Fe_2O_3	SO_3
6.33	35.48	0.45	0.29	5.36	48.88	1.11	1.99

Table 3.1 – Chemical compositions of ladle furnace slag (%).

kg/m^3	REF	SLAG
Cement I 42.5 N	300	240
Ladle furnace slag	-	60
Water	165	165
Dolomite sand	975	975
Dolomite coarse aggregates	975	975
Steel fibers	30	30
Superplasticizer l/m^3	3	3-3.5

Table 3.2 – Mixture proportions (kg/m^3) -for RRT1.

3.2.2 RRT3's mixtures

Two fiber concrete compositions are proposed and prepared by the Polytechnic University of Valencia. The first, named "REF" is the reference concrete and the second named "CA" contains 1% (btcw) of Crystalline Admixture "CA". The CA used is provided by "Penetron company". The mixture proportions are shown in Table 3.3. These mixtures contain 40 kg/m^3 of steel fibers Dramix 65/35 (35 mm length and 0.53 mm diameter). The cement used is CEM I 42.5 R SR5. Natural sand and calcareous aggregates with a maximum size of 12 mm are used in the mixtures. The water/binder ratio is equal to 0.5.
Seven beams (60x60x300 mm^3) for the water absorption tests and four cylinders (Ø100xH200 mm^3) for water permeability tests are received for each concrete composition.

3.3 Experimental methodologies

All specimens were stored in a humidity room at 20°C and 95 ± 5% RH until the testing age corresponding to 70 days old and 260 days old respectively for RRT1 and RRT3. For both RRTs, the concrete specimens are tested by means of two tests: water permeability and water absorption. The experimental procedures are similar for the both RRTs and are described in the following paragraphs.

kg/m^3	REF	CA
Cement I 42.5 R	350	350
CA	-	3.5
Water	192	192
Natural sand	950	950
Limestone filler	60	60
Aggregate 4/7	300	300
Aggregate 7/12	600	600
Steel fibers	40	40
Plasticizer Sika 5780	0.7	0.7

Table 3.3 – Mixtures proportions (kg/m^3) -for RRT3.

3.3.1 Water permeability test

I - Specimens preparation

Three days before the water permeability test, the four cylindrical specimens for each RRT are cut each into 3 disks (Ø100xH50 mm^3) as shown in Figure 3.1(a) (12 disks/composition). To prevent the disks slipping during the splitting test and to keep both disk pieces together, the disks are surrounded with a glued tape (Figure 3.1(b)). At 70 days old for RRT1 and 260 days for RRT3, all the disks are pre-cracked using a splitting test to obtain a crack width equal to 200 ± 50 mm. The loading speed is fixed at 0.05 mm/min. Under loading, a maximal crack opening equal to 300 μm is reached in order to obtain a residual crack width equal to 200 ± 50 μm. During the splitting test, the crack opening is visually monitored using a specific ruler as shown in Figure 3.2(a). After the test, the average crack width is measured using a reflective microscope (§II).

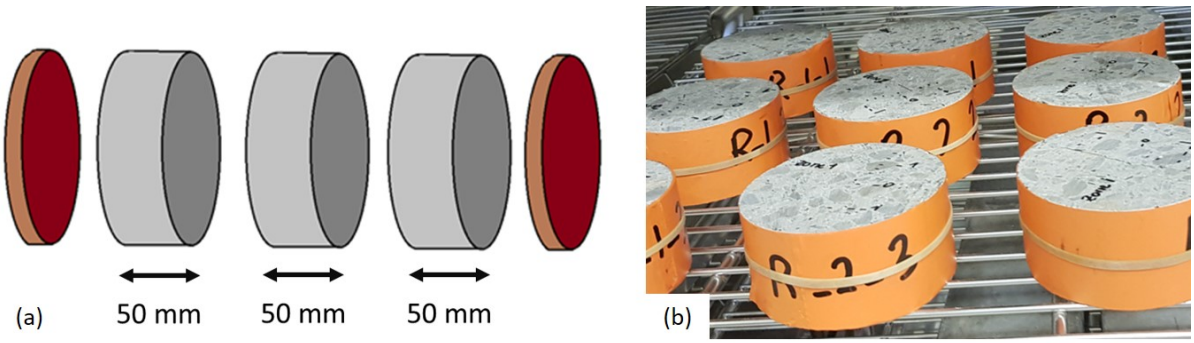

Figure 3.1 – Cylindrical specimen cut into three disks (a); Disks surrounded with a glued tape (b).

II - Crack width measurement

In parallel to water permeability measurements giving a 3D information on the crack, crack width measurements are performed on both disk surfaces. To determine correctly the geometrical crack parameters, measurements are performed on areas being representative to the global crack,

i.e. without defects, such as missing pieces of the cementitious matrix, parallel cracks, inclined crack path, etc, as recommended by [102]. In this study, the crack width is measured using a reflective microscope (Automatic HD Crack Width Meter ZBL-F130) having an accuracy of 0.025 mm. The measurements are performed beyond 1 cm from the disk edges on several points (from 3 to 10) over a 50 mm long area (Figure 3.2(b)). Particularly, three locations are investigated: center of the disk and two 25 mm long areas around the center (Figure 3.2(b)). Furthermore, the crack width measurements are uniformly distributed, and marked using waterproof markers to insure their repeatability during all the test duration. Finally, the average crack width is calculated and used to interpret the water permeability results.

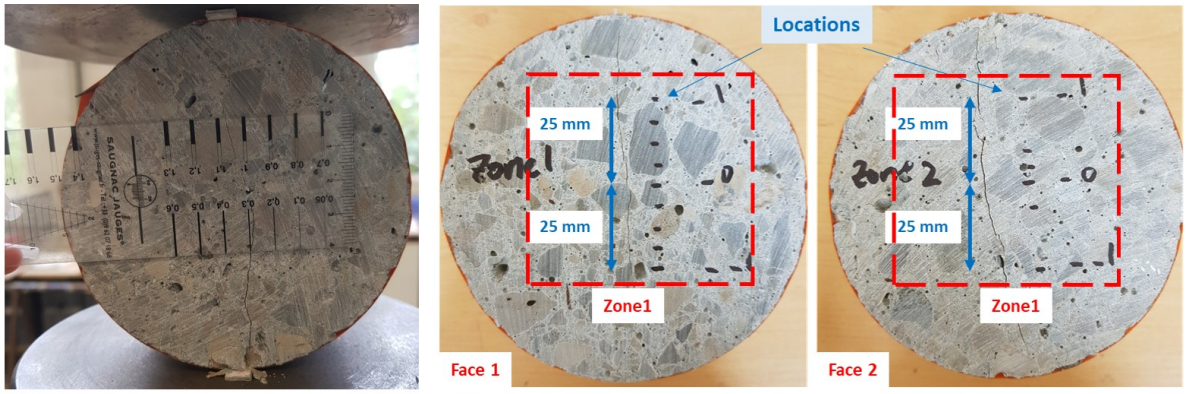

Figure 3.2 – Crack width controlled with a ruler during the splitting test (a); Locations for the crack width measurements on the specimen surfaces (b).

III - Test protocol

After crack width measurements, all specimens are stored at 40°C and 20% R.H. during 24 hours. This curing is applied to dry lightly concrete disks to ensure a good adhesion of the PVC tubes (ϕ_{inner} = 190 mm, H = 200 mm) glued on their top. As concrete is older than 28 days old, this curing does not affect significantly the concrete microstructure.

The concrete disks mass is measured before and after the drying process. Then, the disks are stored at 20 ± 2°C and 60 ± 5% RH during 24 hours to let dry the glue before the water permeability test. Notice that the PVC transparent tubes are previously graduated (Figure 3.3(a)). For the water permeability test, the PVC tubes are filled with 1.27 liters of tap water (tube's capacity = $\pi(90/2)^2$x200 mm^3). To monitor the water quantity flowed through the crack, the tested specimens are placed on a support above a balance (precision of 100 mg) (Figure 3.3(b)). The water level variation is monitored during 3 hours, as well as the flowed water quantity after 5, 10, 15, 20, 25 and 30 minutes. From these measurements, a water flow (Liter/minute) is calculated. After removing the PVC tubes, the specimens mass is measured again and all disks are stored vertically (parallel to the crack) in a tap water container until

the next measurement. The concrete specimens of RRT1 and RRT3 are stored in two different containers.

Four measurements of water permeability test are made: just after the cracking (0M), after a water curing of 1 month (1M), 3 months (3M) and 6 months (6M) (Figure 3.4). The water is renewed every month. From each test, a Healing Rate ($HR_{WP}(t)$) is calculated according to Eq. 3.1.

$$HR_{WP}(t) = \frac{W_{unhealed}(0M) - W_{healing}(t)}{W_{unhealed}(0M)} * 100 \tag{3.1}$$

Where:

- $HR_{WP}(t)$ is the Healing Rate at time t determined from the Water Permeability test (%)
- $W_{unhealed}(0M)$ is the initial water flow just after the cracking at time 0M (L/min)
- $W_{healing}(t)$ is the water flow after a water curing period at time t (L/min)

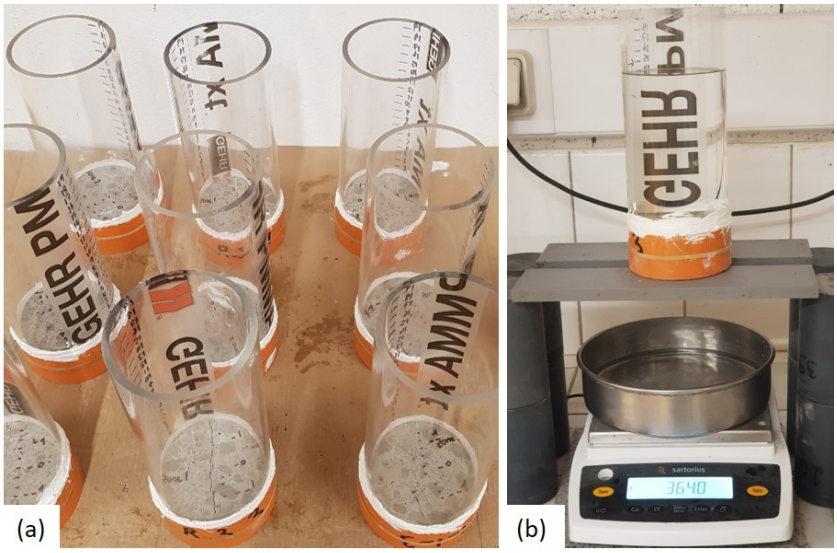

Figure 3.3 – PVC tubes glued on the top of the disks using SIKADUR 31 (a); Water permeability test (b).

3.3.2 Water absorption test

I - Specimens preparation

As the water permeability test, the water absorption test gives a 3D crack description and its healing process. This test is performed on notched prismatic specimens. The notch dimensions are 10 mm high and 2.6 mm wide. It is located in the middle of the specimen and it is made three days before cracking. Three -70 and 260 days old- prisms are cracked using a three-point

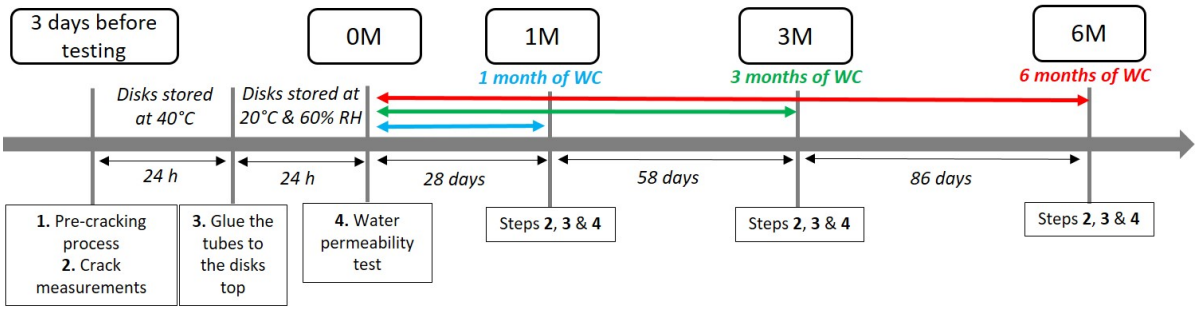

Figure 3.4 – Timeline of the water permeability tests.

bending test (Figure 3.5) for RRT1 and RRT3 respectively. The loading speed is fixed at 0.06 mm/min. The test is stopped when a crack width equal to 300 μm is reached to ensure a residual crack width equal to 200 $\pm$ 50 μm. The evolution of the crack width is monitored using a crack opening sensor having a precision of 0.05 mm and placed over the mid-span of the specimen's notched side (Figure 3.5). After the test, the average crack width is measured using a reflective microscope (§II).

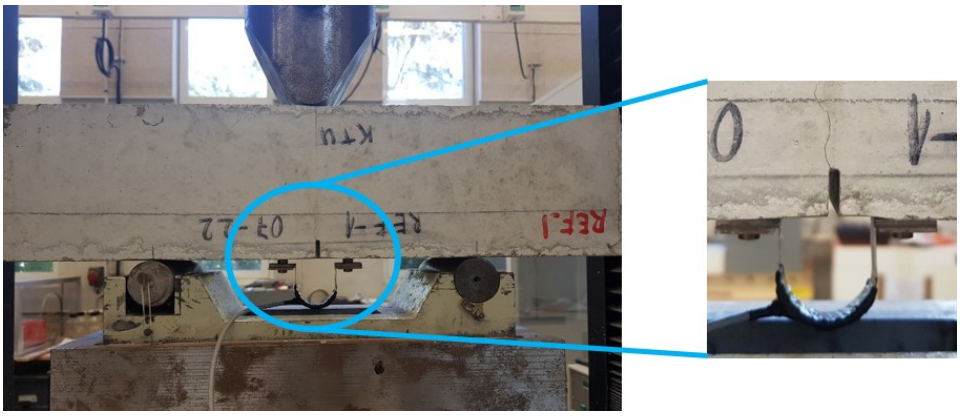

Figure 3.5 – Three-point bending test (beam span = 210 mm) on a prismatic specimen with a crack opening sensor controlling the crack width.

II - Crack width measurement

The crack width is measured using the reflective microscope at several points located on the lateral surfaces: two 20 mm long zones on the smooth lateral surface and one zone 20 mm long zone on the irregular lateral surface (Figure 3.6). For each zone, three to six measurements are performed following the process described previously (§3.3.1-II). From all these measurements, an average crack width is calculated.

III - Test protocol

The water absorption test is performed on 3 cracked and 3 uncracked prismatic specimens for RRT1, and on 4 cracked and 3 uncracked prismatic specimens for RRT3. Before the first measurement, a coating of transparent silicone (Mastic Silicone Rubson SP2) is applied on the

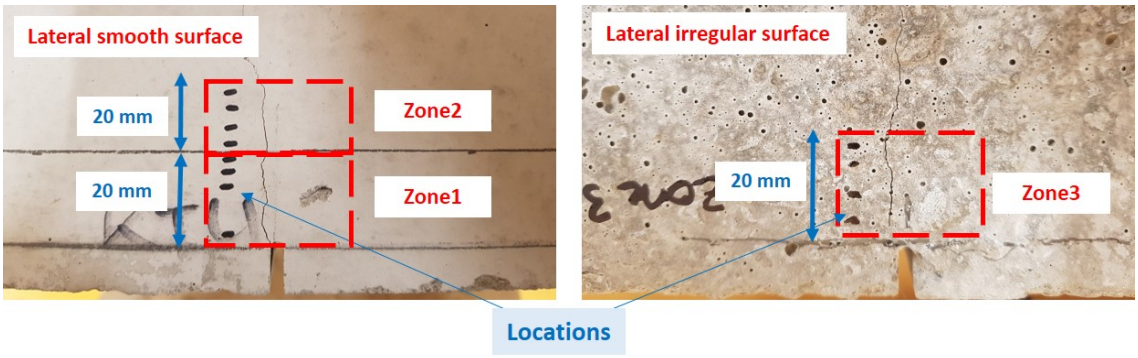

Figure 3.6 – Locations for the crack width measurements.

inferior surface and the lateral surfaces up to a height of 30 mm to isolate the crack (Figure 3.7(a)). Only a 14 mm wide area around the crack is in contact with water. This process allows limiting the water absorption at the crack. In order to determine the water absorption capacity related to the concrete matrix, this process is also applied on uncracked specimens. The specimens are stored during 24 hours in the laboratory environment (20 ± 2°C and 60 ± 5% R.H.) to let drying the silicone coating. Then, as the saturation degree of specimens affects their water absorption capacity, it is important to have a constant weight before starting the adsorption test. So, they are put in a climatic chamber (40°C and 20% R.H.) until the moment that the weight variation between two measurements -made with 2-hour intervals- is inferior to 0.2%. This weight variation is chosen to ensure sufficient drying of the specimens during a short duration ($\leq$ 14 days) limiting the effect on the crack width (because drying can cause desiccation shrinkage and carbonation). Before the test beginning, specimens are stored in the laboratory environment (20°C and 60% R.H.) – similar to the test conditions during 24 hours. During the tests, the specimens are placed with the crack downwards in the containers filled with water up to 3 mm higher than the notch (Figure 3.7(b)). The containers are closed to limit the water evaporation. The specimens are weighed after 0, 1, 16, 36, 49, 64, 81, 100, 121, 144, 169, 196, 225, 256, 289, 324 minutes, 8 and 24 hours. Before each measurement, the wet specimen surfaces are wiped with a moistened tissue. Based on the slope of the Sorption Coefficient (SC) evolution as function of time, SC is calculated for each specimen using a linear regression method. After the test, specimens are stored horizontally with the crack downwards in containers filled of tap water renewed every month. Each composition is stored in a separate container. This test is made after the cracking (0M) and 1 month (1M), 3 months (3M) and 6 months (6M) of water curing (Figure 3.8).

Finally, a Healing Rate ($HR_{WA}(t)$) is calculated according to Eq. 3.2. In this relation, the evolution of SC for the uncracked specimens is used to limit the effect of concrete microstructure and its evolution as function of time on the HR calculation and to focus only on the crack healing.

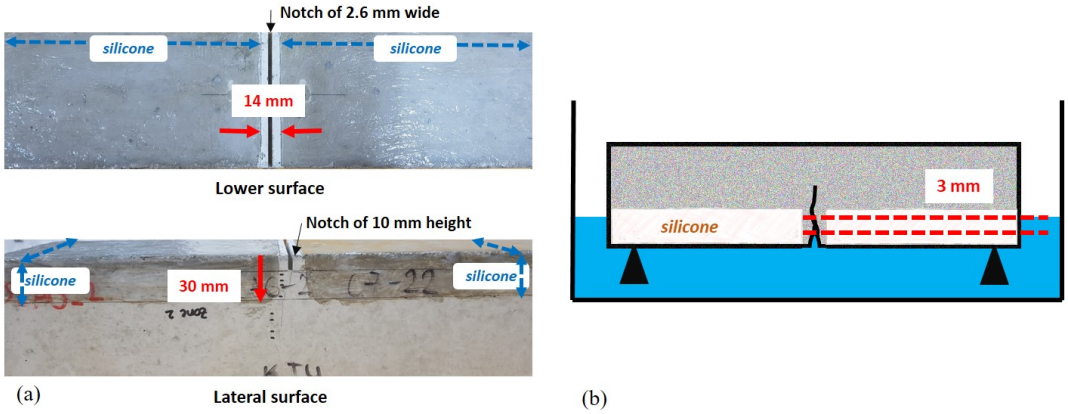

Figure 3.7 – Lateral and inferior surfaces of the notched specimen coated with silicone (a); Position of the specimen in the container during the water absorption test (b).

$$HR_{WA}(t) = \frac{[SC_{unhealed}(0M) - SC_{uncracked}(0M)] - [SC_{healing}(t) - SC_{uncracked}(t)]}{[SC_{unhealed}(0M) - SC_{uncracked}(0M)]} * 100 \tag{3.2}$$

Where:

- $HR_{WA}(t)$ is the Healing Rate determined with the Water Absorption test at time t (%)
- $SC_{unhealed}(0M)$ is the initial Sorption Coefficient of the cracked specimens before starting the healing period (at time 0M) (kg/m^2)
- $SC_{uncracked}(0M)$ is the initial Sorption Coefficient of the uncracked specimens before starting the healing period (at time 0M) (kg/m^2)
- $SC_{healing}(t)$ is the Sorption Coefficient of the cracked specimen after a healing period (at time t) (kg/m^2)
- $SC_{uncracked}(t)$ is the Sorption Coefficient of the uncracked specimens after a healing period (at time t) (kg/m^2)

The sorption coefficient $SC_x(t)$ is defined as follows:

$$SC_x(t) = \frac{M(t) - M(0)}{A} \tag{3.3}$$

Where:

- $M(t)$ is the mass of the specimen at time t (kg)
- $M(0)$ is the initial mass of the specimen at each test (kg)

- A is the specimen surface in contact with water (m^2)

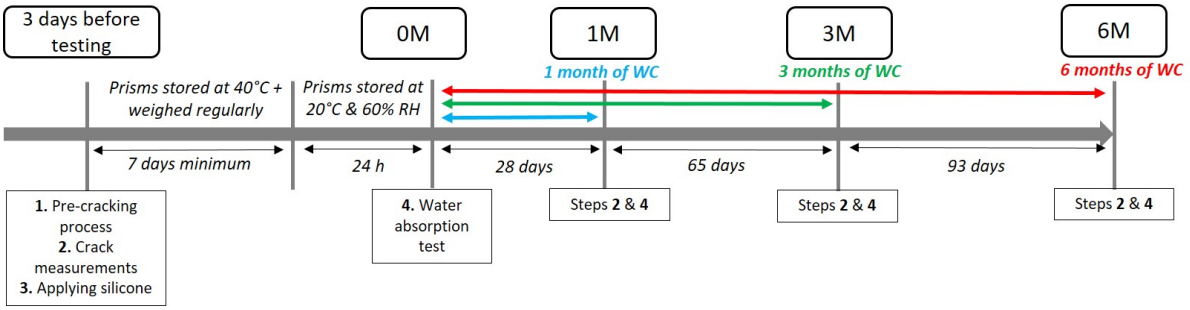

Figure 3.8 – Timeline of the water absorption tests.

3.4 RRT1: Effect of mineral addition on concrete self-healing

RRT1 focuses on the role of mineral additions on the self-healing of cracked concrete. The experimental results of water permeability and water absorption tests at different ages are presented in this section.

3.4.1 Water permeability results

I - Water flow

Although a crack width about 300 μm is obtained during the loading, the residual crack width presents a variability between the specimens. For REF, it varies from 87 μm to 200 μm except for one specimen characterized by a crack width equal to 357 μm. For SLAG, it varies from 200 μm to 300 μm. So, the average crack width of REF (173 μm) is inferior than that of SLAG (247 μm) (Figure 3.9). The Water Flow (WF) presented in Figure 3.9 is calculated using the water quantity flowed through the crack after 30 minutes (only the WF of the specimen with a crack width of 357 μm is calculated after 20 minutes because the water flow has stopped at this time). The water flow increases with the crack width. Thus, a higher water flow (around 0.04 l/min) is measured for the largest cracks (more than 200 μm). But a variability of the water flow is observed for some specimens characterized by similar crack widths, especially for crack widths between 150 μm to 250 μm. As explained previously, the crack width shown on Figure 3.9 is an average of measurements made on the two specimen faces. However, this approach does not consider the crack tortuosity and connectivity, i.e. parameters affecting the water flow.

The water flow evolution for a test duration equal to 180 minutes is shown in Figure 3.10 for each specimen (R1 to R9 for REF and S1 to S9 for SLAG) at different curing duration (0M, 1M, 3M and 6M). The specimens are numbered according to the smallest to the largest crack width. During the water permeability test, the water flow decrease due to the variation of the

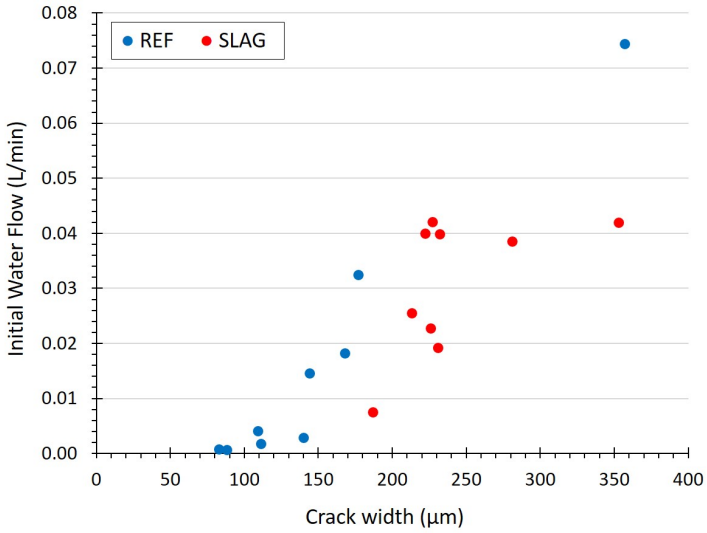

Figure 3.9 – Water Flow as function of the average crack width at 0M for each tested specimen.

water height in the PVC cylinder for all the tested specimens (REF and SLAG). Moreover, the water flow decreases with the curing duration due to the reduction of crack width. Figure 3.11 shows the evolution of the average Water Flow (WF). Its initial value is higher for SLAG (0.031 l/min) - it is equal to 0.016 l/min for REF. This difference of behaviour is mainly due to their initial crack width that it is more important for SLAG (Figure 3.9). Then, the WF decreases with time for the two studied mixtures, but this reduction is more important for REF (Figure 3.11). Indeed, the WF reduction is equal to 48%, 79% and 84% for REF at 1M, 3M and 6M respectively, while it is equal to 31%, 47% and 64% for SLAG at 1M, 3M and 6M respectively.

II - Healing rate

Figure 3.12 shows the evolution of the Healing Rate (HR) determined from the Crack Width (CW) measurements on the specimen surfaces. The number of specimens used to calculate HR is indicated below each crack width. For each crack width, the standard deviations are calculated by this relation: $(|HR_{average} - HR_{obtained}|/HR_{average})$.

For REF (Figure 3.12(a)), HR increases rapidly as function of time. Specimens characterized by an initial crack width varying from 50 to 150 μm are healed by 88% after only 1 month. Moreover, their HRs increase rapidly to more than 95% after 3 months of water curing till achieving a complete healing (HR=100%) at 6M. REF and SLAG' specimens characterized by an initial crack width between 150 and 200 μm present a close HR value at 1M (55% and 43% respectively). At 3M, this value increases faster for SLAG (by 50%) than for REF (by 38%). However, the healing behavior continues more significantly for REF reaching a HR equal to 91% at 6M compared to SLAG (HR = 72%). Similar observation is also drawn for specimens having a crack width between 300 to 400 μm. Thus, it appears that SLAG exhibits faster healing capacity at 3M than at 6M and compared to REF. But, the HR calculated from CW

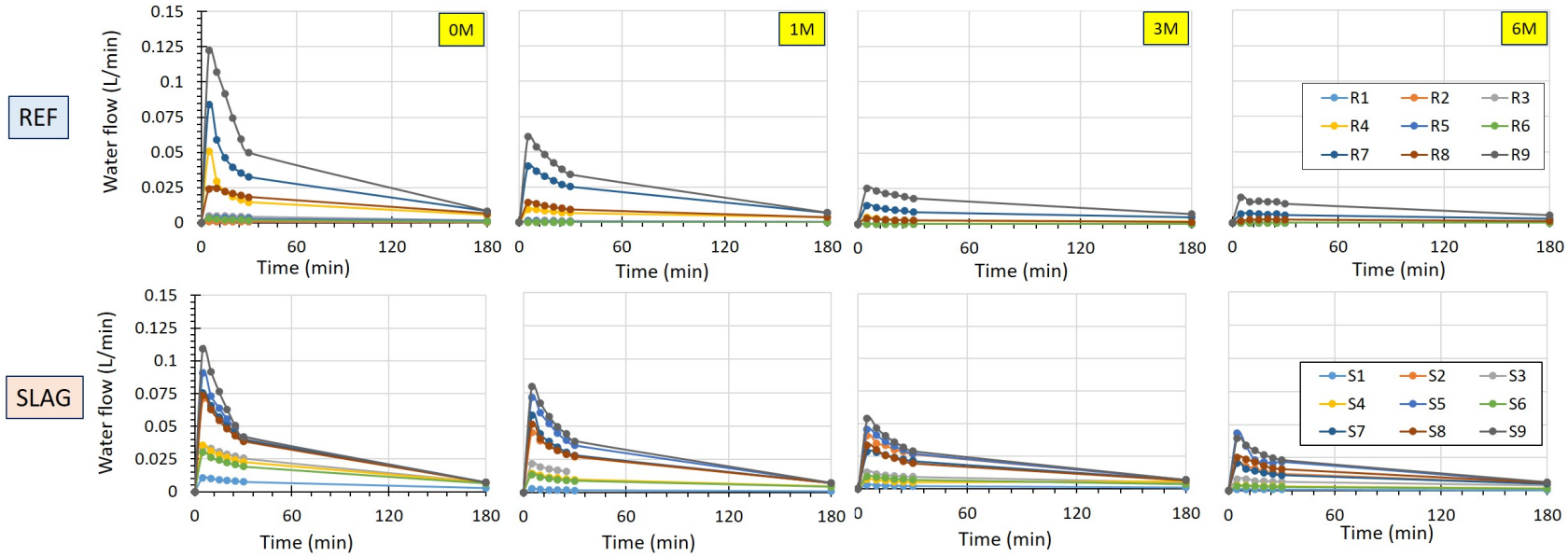

Figure 3.10 – Water flow evolution up to 180 minutes for each specimen (R1 to R9 for REF and S1 to S9 for SLAG) at different curing duration (0M, 1M, 3M and 6M).

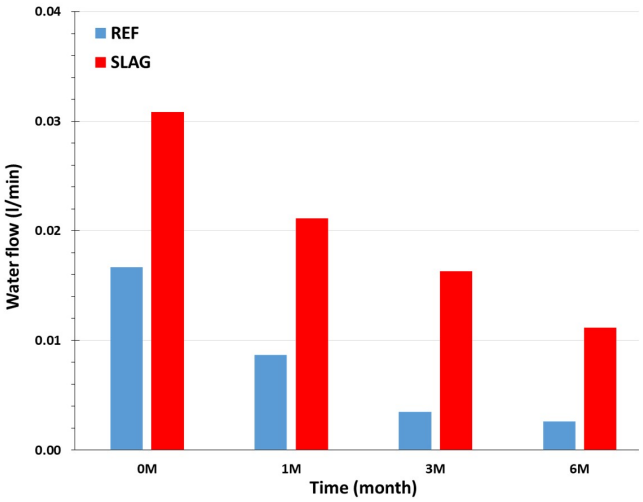

Figure 3.11 – Evolution of the average water flow (9 specimens/composition) after each test.

measurements gives only a 2D information on the crack healing process. With this method, it is not possible to estimate the healing process inside the crack. So, HR is also determined from the Water Permeability results taking into account the crack's internal healing (Figure 3.13).

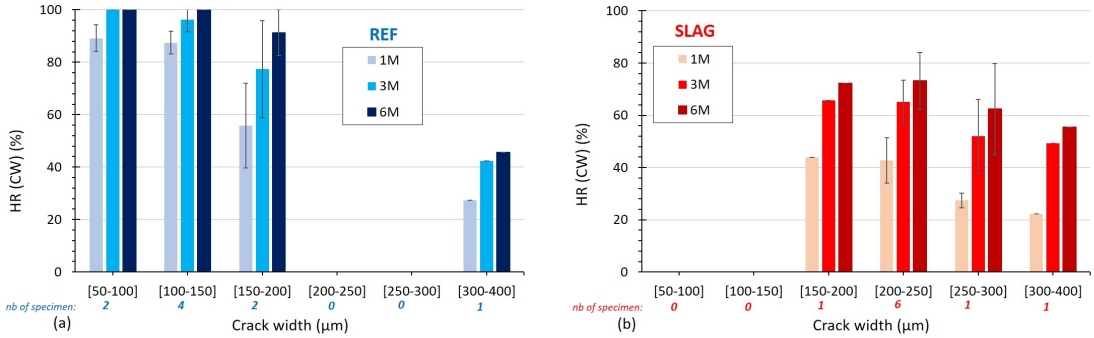

Figure 3.12 – Healing Rate (HR) determined from the Crack width (CW) measurement as function of the initial crack width at 1M, 3M and 6M for REF (a) and SLAG (b).

The HR values differ as function of the used method. But, the same trends can be globally observed: an increase of HR as function of time as well as a complete healing for REF's specimens with an initial crack width between 50 to 150 μm (Figure 3.13(a)). While when the crack width increases ([150-200] μm), it appears that REF present a faster healing behavior at 3M (HR = 80%, Figure 3.13(a)) than SLAG (HR = 73%, Figure 3.13(b)). However, both mixtures reach around 85% HR at 6M in this case. For SLAG specimens having a crack width between 200 to 300 μm, the HR values are always inferior to 71%. Finally, when the crack width is between 300 to 400 μm, the rate of increase of the HR between 3M and 6M is more important for SLAG (76%) than for REF (54%). Based on these observations, it appears that no specific conclusions can be drawn. This is due to the classification of the specimens according

to the initial CW that does not take into account the tortuosity of the internal crack. However, this can be done by classifying the specimens according to their initial WF. Indeed, Figure 3.14 compares the HR of the specimens characterized by a similar intial WF: [0.001-0.025] l/min, [0.025-0.04] l/min and [0.04-0.07] l/min.

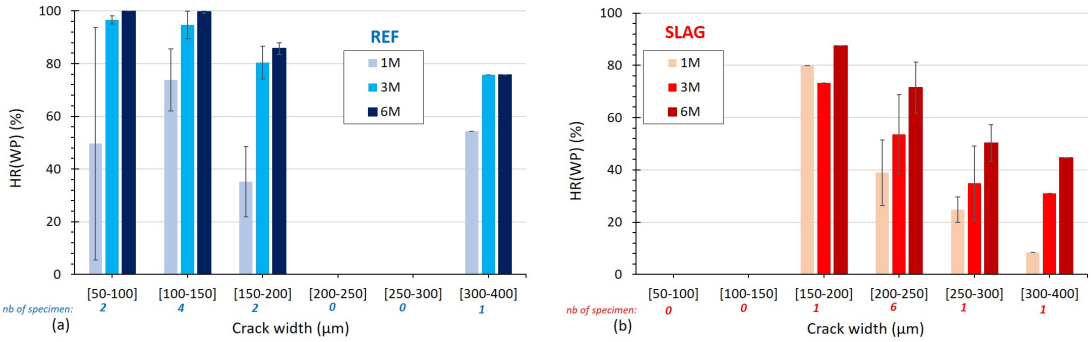

Figure 3.13 – Healing Rate (HR) determined from the Water Permeability (WP) measurement as function of the initial crack width at 1M, 3M and 6M for REF (a) and SLAG (b).

For a WF = [0.001-0.025] l/min, REF and SLAG show similar initial HR (60% at 1M) which increases more rapidly for REF (by 54%) than for SLAG (by 19%) after 3 months of water curing. However, the healing behavior of REF does not improve significantly at 6M of which its HR increases by 4% only after 3M, while that of SLAG continues to increase at this time (by 19% after 3M). The same observation can be found for the large initial WFs ([0.025-0.04] l/min & [0.04-0.07] l/min). In these cases, the HR of REF is higher than that of SLAG at 1M and increases more rapidly after 3 months of water curing. However, REF's healing capacity tends to be constant after this time. Whereas SLAG shows slow healing behavior at 1M and 3M, but continues significantly over the long term (up to 6 months). Thus, with this method, conclusions are more evident to draw.

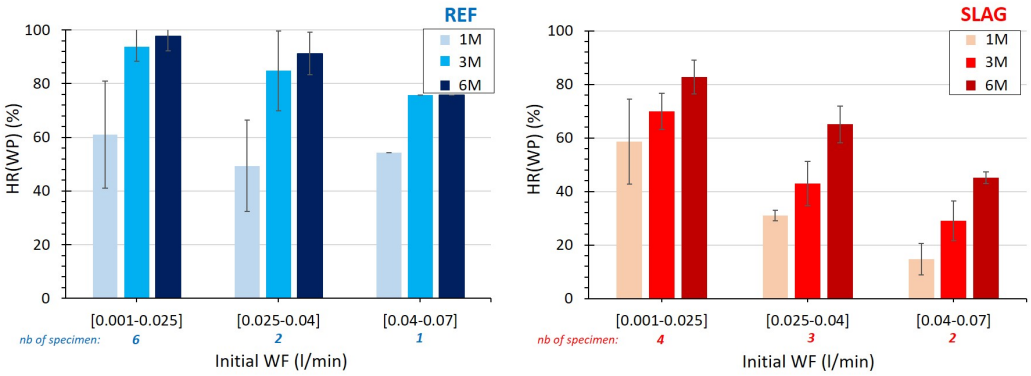

Figure 3.14 – Healing Rate (HR) determined from the Water Permeability (WP) measurement as function of the initial water flow at 1M, 3M and 6M for REF (a) and SLAG (b).

Based on the average Healing Rate for REF and SLAG at 1M, 3M and 6M (Figure 3.15), it is seen that the HR is more important for REF than for SLAG after each test. This difference of behaviour is partially related to the initial crack width of the specimens. However, the rate of healing from 3M to 6M is more important for SLAG (33%) than for REF (3%). It could be related to the delayed hydration of slag that appears at a long term.

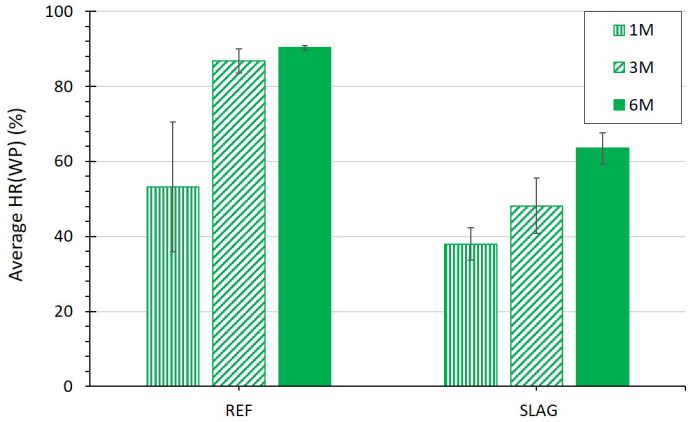

Figure 3.15 – Average Healing Rate for REF and SLAG (9 specimens/composition).

3.4.2 Water absorption results

I - Sorption coefficient

As for the water permeability test, the initial cracks widths is smaller for REF than for SLAG. The initial crack width measured on the specimens' lateral faces varies from 100 to 122 μm for REF and from 93 to 222 μm for SLAG. So, the average crack width is equal to 115 μm and 155 μm for REF and SLAG respectively.

For both compositions, the evolution of the Sorption Coefficient (SC) is presented at 0M, 1M, 3M and 6M for the cracked (Figure 3.16(a & b)) and uncracked specimens (Figure 3.16(c & d)). The SC increases more rapidly for cracked specimens than for uncracked specimens during the test period. At 0M, SC of uncracked specimens presents a maximal value equal to 4 kg/m^2 at 24h (Figure 3.16(d)). For the cracked specimens, it is around 8 kg/m^2 (Figure 3.16(b)). So, SC is lower for uncracked specimens. Indeed, these specimens present a smaller surfaces in contact with water and no capillary effects related to the crack. When increasing the curing duration, SC decreases for all specimens especially at 1M. In the case of specimens with a similar crack width, Figure 3.16(a) shows that SC curves are very close for both studied compositions, especially at 0M – before the healing process. The SC evolution is also presented as a function of the square root of time for each composition in Figure B.2 in appendix B. The curves shows similar patterns as the SC evolution in Figure 3.16. To determine the mineral additions effect on SC during the healing process, the global sorption coefficient is presented in

Figure 3.17 for both compositions. It is determined from the slope curve of SC as function of the square root of time.

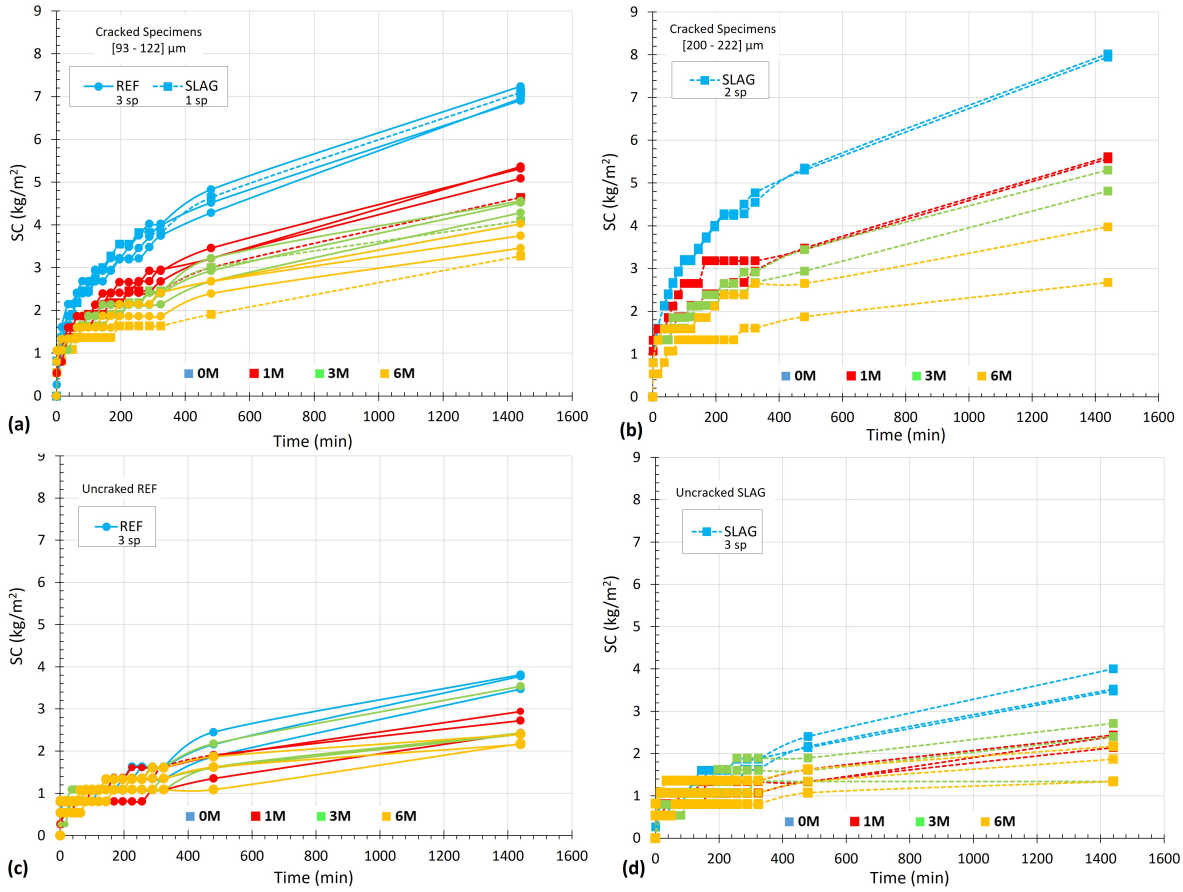

Figure 3.16 – Evolution of the sorption coefficient at 0M, 1M, 3M and 6M for cracked specimens (a & b) and uncracked specimens (b & c).

The cracked specimens of SLAG present a higher SC (0.3 kg/m^2) at the cracking age (at 0M) than cracked specimens of REF (0.26 kg/m^2). But, their reduction of SC over time is more important: 38%, 42% and 62% respectively at 1M, 3M and 6M. This reduction is equal to 27%, 43% and 52% respectively for cracked specimens of REF. This difference of behavior is also observed for the uncracked specimens: a more important SC reduction at 6M for SLAG (66%) compared to REF (38%). Two phenomena lead to the SC decrease for the cracked specimens: the crack healing and the porosity reduction of the sound matrix related to the hydration advancement. This last effect can be quantified with SC measured on the uncracked specimens to determine correctly the Healing Rate (HR) using (Eq. 3.2).

II - Healing rate

Figure 3.18 presents the evolution of HR calculated from the crack width measurements on the specimen lateral surfaces. The number of specimens used to calculate HR is indicated for

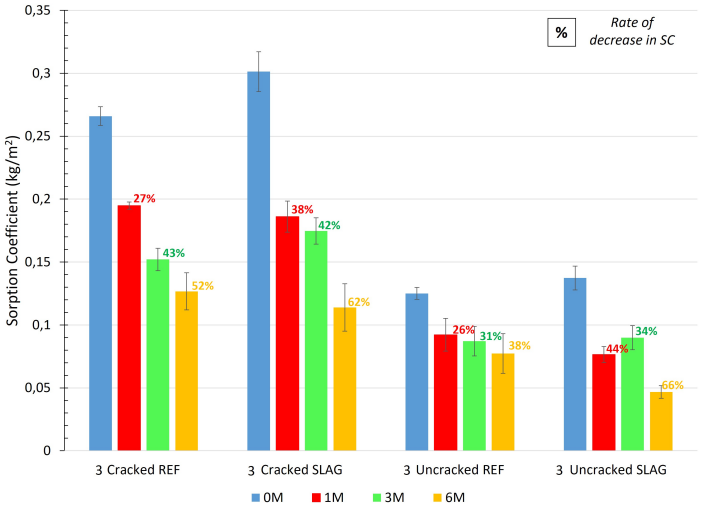

Figure 3.17 – Global sorption coefficient for REF and SLAG after each test.

each crack width. From these diagrams, it appears that REF and SLAG have a similar healing behavior: HR values are always higher than 90% at 1M, 3M and 6M. As observed for the specimens used for the WP, the monitoring of the healing process using specimen's crack width does not quantify an appropriate HR. So, Figure 3.19 shows the evolution of the Healing Rate (HR) calculated with the Water Absorption (WA) results for the several crack width ranges.

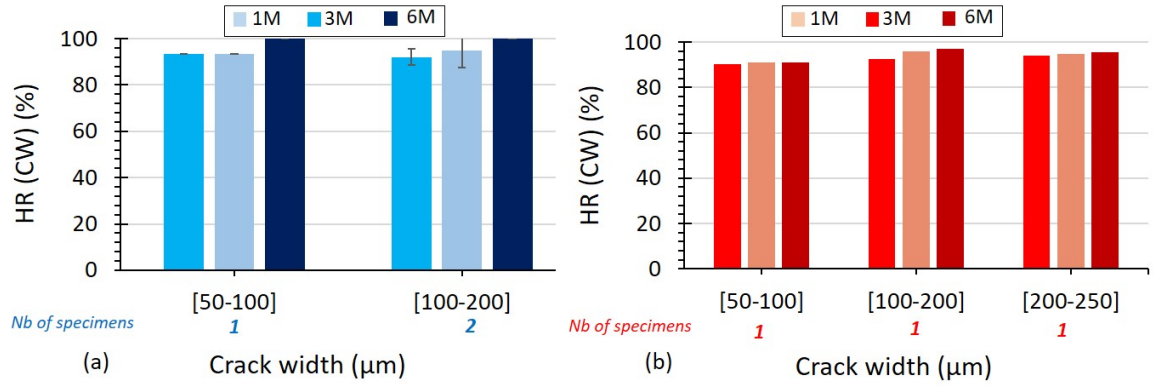

Figure 3.18 – Average Healing Rate (HR) based on the Crack Width (CW) results as function of the initial crack width for REF (a) and SLAG (b).

The HR after 1 month is always higher for SLAG than for REF. It is about 35% for all crack ranges (Figure 3.19(b)), while it is about 25% for REF (Figure 3.19(a)). However, the rate of increase in HR for REF is faster (over 80%) than that for SLAG (about 32%) from 1M to 3M for specimens characterized by an initial crack width between 50 and 200 μm. After that, HR increases continuously for SLAG in comparison to REF. SLAG also shows significant healing behavior when the initial crack width is large ([200-250] μm) after 6 months. Thus, it appears that SLAG exhibits better long-term healing behavior (at 6 months) than REF.

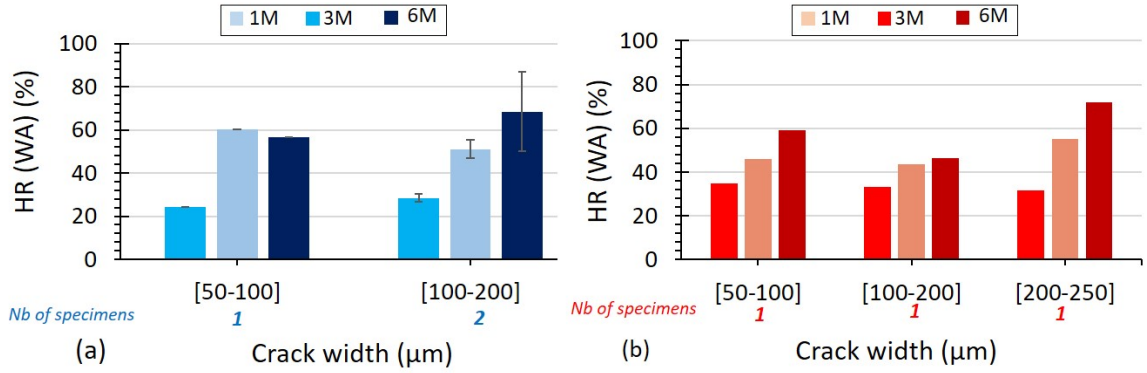

Figure 3.19 – Average Healing Rate (HR) based on the Water Absorption (WA) results as function of the initial crack width for REF (a) and SLAG (b).

Based on the average Healing Rate for REF and SLAG (Figure 3.20), it is showed that REF does not present a significant healing rate after 6 months of water curing. The average HR of REF is enhanced only by 10% while that of SLAG is enhanced by 23% from 3M to 6M. This confirms that SLAG presents delayed hydration due to the slag addition.

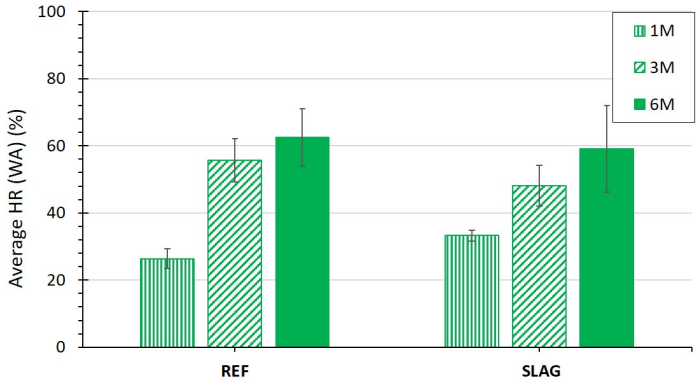

Figure 3.20 – Average Healing Rate for REF and SLAG (3 specimens/composition).

3.5 RRT3: Effect of cristalline admixture on the concrete self-healing

The RRT3 project focuses on the role of cristalline admixture on the self-healing of cracked concrete. The experimental results of water permeability and water absorption tests at different periods are presented in this section.

3.5.1 Water permeability results

I - Water flow

The residual crack widths obtained after the splitting test for RRT3 specimens are very similar between REF and CA and range from 140 μm to 310 μm (Figure 3.21). On average, REF and CA have a crack width of 220 μm. All the WFs shown in Figure 3.21 are calculated using the water quantity flowed through the crack after 30 minutes; except for the highest WF (0.125 l/min for REF and 0.09 l/min for CA). These WFs are calculated using the water quantity flowed through the crack after 20 minutes because the water flow has stopped at this time. Moreover, unlike RRT1 specimens, the majority of the initial WFs for RRT3 specimens are between 0.02 l/min and 0.04 l/min for specimens characterized by a crack width between 200 μm and 250 μm for REF and CA.

Theoretically, if the relationship between the water flow and the crack width is physical, this can lead to a cubic relationship (WF[l/min]=AxCW[µm], A is a constant value). However, this cannot be easily obtained in this case (Figure B.1 in Appendix B). This could suggest that this relationship is a chemical relationship related to the effect of the composition being studied; example: the formation of additional hydration products within the crack that will influence the water flow through the crack.

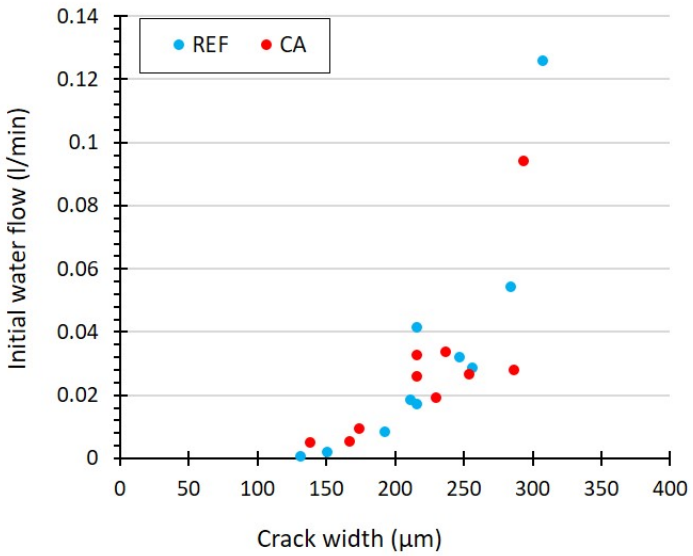

Figure 3.21 – Crack width of each tested specimen at 0M.

Figure 3.22 shows the evolution of the water flow for a test duration equal to 180 minutes for each specimen (R1 to R10 and C1 to C10) at different curing duration (0M, 1M, 3M and 6M). The specimens are numbered according to the smallest to the largest crack. For all the specimens (REF and CA), the water flow rate decreases due to the variation of water pressure

during the water permeability test. It also decreases with the curing age due to the reduction of the crack width.

Figure 3.23 shows the evolution of the average Water Flow (WF). Its initial value is slightly higher for REF (0.033 l/min) - it is equal to 0.028 l/min for CA. After 1 month of water curing, the WF decreases by 30% for both compositions. This reduction is greater for CA (by 79%) than for REF (by 63%) at 3M. However, REF continues the healing process until 6 months unlike CA until the same WF is reached for both composition at this time (0.005 l/min).

II - Healing rate

In this section, the HR results are determined from the Water Permeability (WP) results and presented as a function of the initial WF (Figure 3.24). The number of specimens used to calculate HR is indicated for each water flow.

For a WF = [0.001-0.01] l/min, CA present a significantly higher initial HR (65% at 1M) than REF (25% at 1M). This HR is enhanced by 48% after 3 months of water curing and does not show any increase after this time. However, the HR of REF is increased by more than 200% after 3 months of water curing until a complete healing at 6M. For large initial WFs ([0.01-0.05] l/min & [0.05-0.12] l/min), CA present a fast healing behavior after 3 months of water curing characterized by an HR equal to 79% and 73% respectively. However, its healing capacity does not increase significantly after this time (82% and 76% respectively at 6M). On the other hand, REF's healing behavior continues over the long-term till reaching a HR equal to 97% and 63% respectively at 6M. Based on these observations, it seems that CA composition admits a faster healing capacity than REF till 3 months, but remains constant after this duration.

Based on the average Healing Rate for REF and CA (Figure 3.15), CA exhibits a higher HR (41%) than REF (34%) at 1M. This HR increases rapidly for both mixtures from 1M to 3M by around 100%. However, REF's HR continues to increase till 6 months of water curing, while no significant change is observed for the CA's HR at this time. This difference of behavior may be related to the crystalline admixture that promotes additional hydration at early age and consumes its capacity within a short time.

3.5.2 Water absorption results

I - Sorption coefficient

The initial crack width measured on the specimens' lateral faces varies from 50 μm to 130 μm for REF and CA. On average, REF and CA cracked by 95 μm on the lateral face.

Figure 3.26 shows the evolution of the sorption coefficient calculated after each curing duration (0M, 1M, 3M and 6M). For all specimens, SC increases over the 24 hours, and its rate is faster for cracked specimens than for uncracked ones. At 0M, SC of uncracked specimens presents a maximal value equal to 7 kg/m^2 at 24h (Figure 3.26(c)). For the cracked specimens,

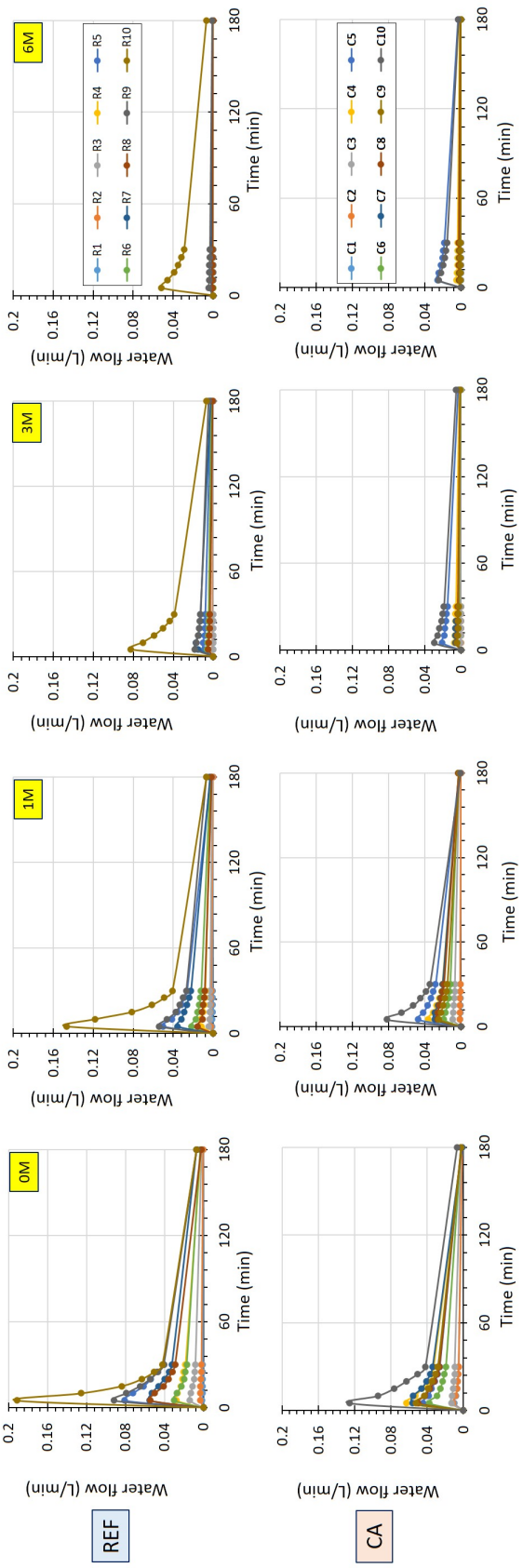

Figure 3.22 – Water flow evolution up to 180 minutes for each specimen (R1 to R10 for REF and C1 to C10 for CA) at different curing duration (0M, 1M, 3M and 6M).

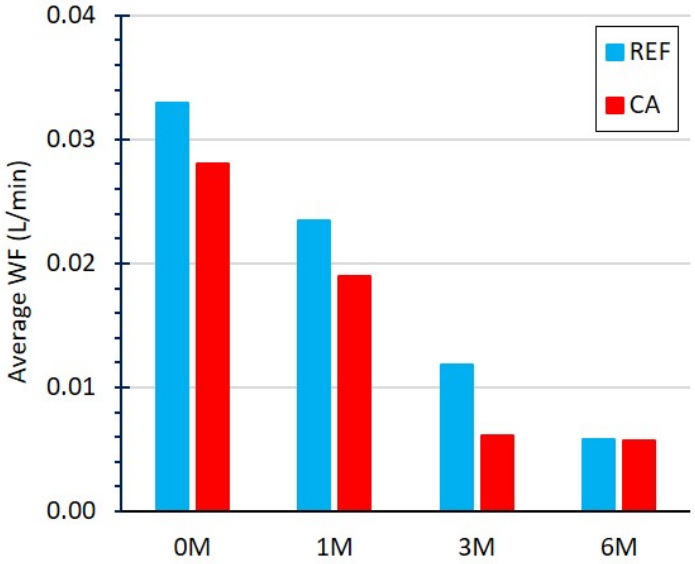

Figure 3.23 – Evolution of the average water flow after each test (10 specimens/composition).

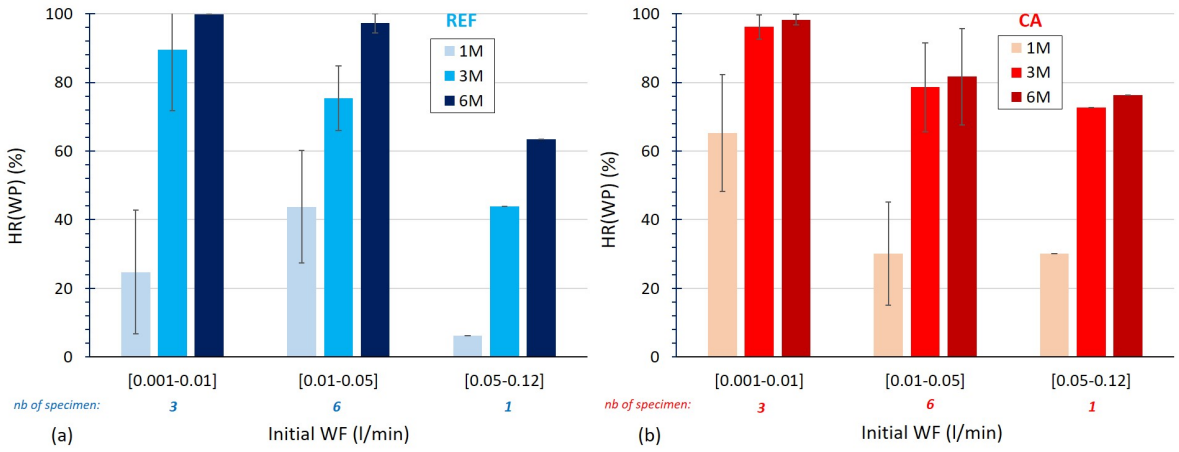

Figure 3.24 – Healing Rate (HR) determined from the Water Permeability (WP) results as function of the initial water flow for REF (a) and CA (b).

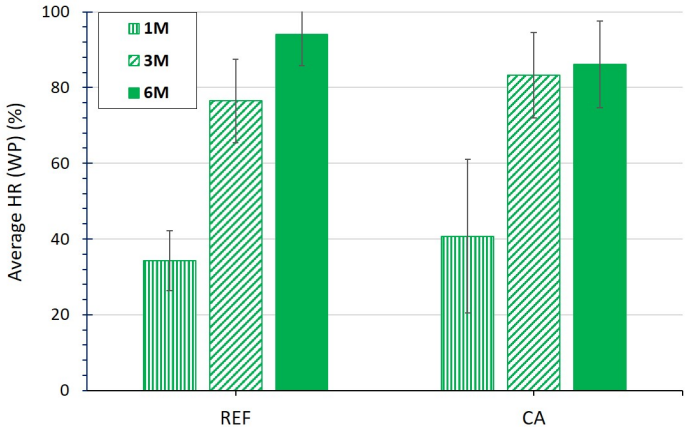

Figure 3.25 – Average Healing Rate for REF and CA (10 specimens/composition).

it is equal to 11 kg/m^2 (Figure 3.26(b)). So, SC is lower for uncracked specimens, where these specimens present a lower contact surfaces with water. In addition, the evolution of SC at 0M is similar between the specimens characterized by a crack width equal to [50-100] μm and [100-150] μm. Then, with the increase of the curing duration, SC is significantly reduced after 1 month of water curing (1M). The SC evolution is also presented as a function of the square root of time for each composition in Figure B.3 in appendix B. The curves shows similar patterns as the SC evolution in Figure 3.26. To better estimate this reduction and to determine the effect of crystalline admixture on SC during the healing process, the global SC is presented in Figure 3.27 for both mixtures.

The cracked specimens of CA present a higher global SC (0.37 kg/m^2) at the cracking age (at 0M) than cracked specimens of REF (0.31 kg/m^2). After one month of water curing (1M), their SC are reduced by 35% and 45% respectively. After this period, their SC continue to decrease by the same rate. The uncracked specimens also show a decrease in their SC as a function of time. But, the SC of uncracked specimens of REF is quite constant after 1M, while that of uncracked specimens of CA continues to decrease with time. As explained previously, two phenomena lead to the SC decrease for the cracked specimen. So, the Healing Rate (HR) is calculated using (Eq. 3.2) and presented hereafter.

II - Healing rate

The evolution of the Healing Rate (HR) based on the Water Absorption (WA) results is presented in Figure 3.28. For specimens characterized by a crack width equal to [50-100] μm, CA exhibits a slightly higher initial HR (34% t 1M) than REF (30% at 1M). However, this HR is increased by only 21% and 59% after 3 and 6 months of water curing respectively, whereas the HR of REF is increased by 47% and 67% respectively at these curing ages. Similar behavior is observed for specimens characterized by a crack width equal to [100-150] μm. After reaching 39% HR for the CA specimen, it appears that this composition has consumed its healing capacity at 1M because no improvement in its HR is shown after this time. In contrast,

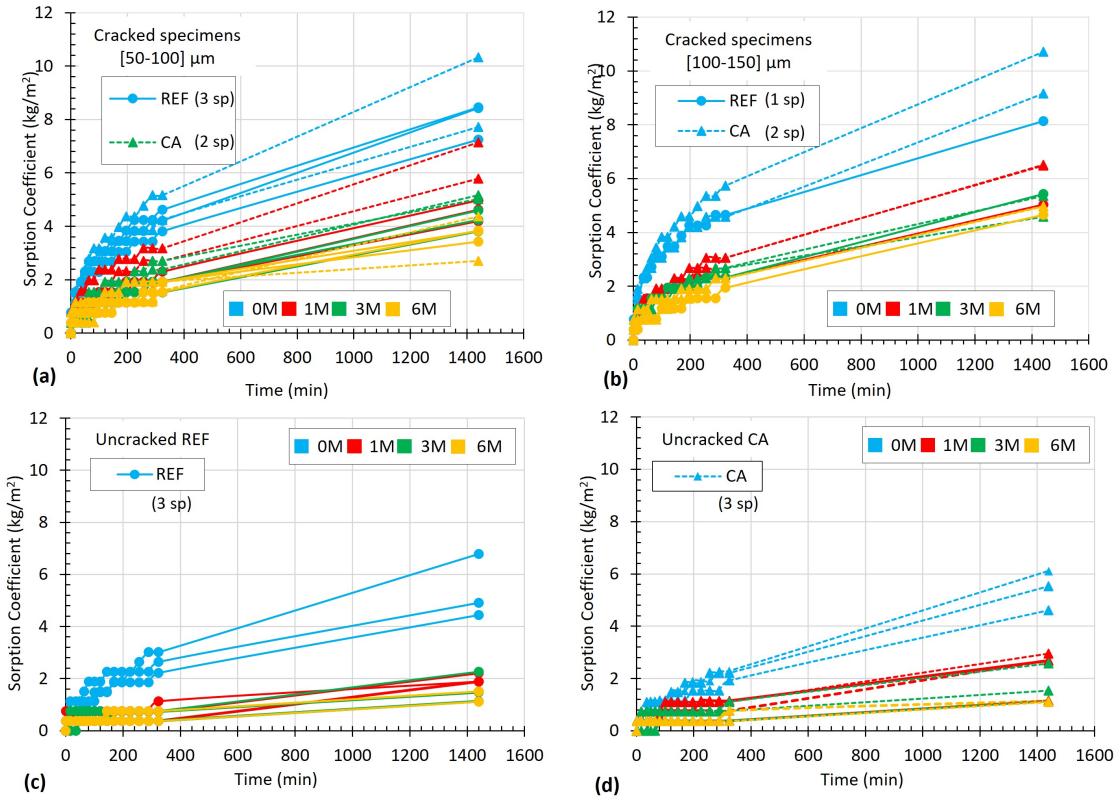

Figure 3.26 – SC evolution after each test for cracked specimens (a & b) and uncracked specimens (c & d).

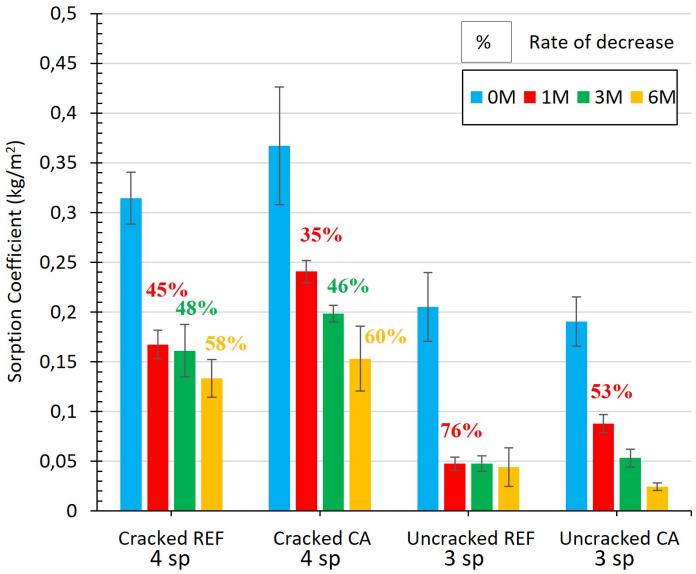

Figure 3.27 – Global sorption coefficient for REF and CA after each test.

although the HR of REF decreases by 25% at 3M, it increases significantly again (by 83%) after 6 months. Thus, CA exhibits faster healing behavior than REF at an early age, but weaker healing potential in the long term.

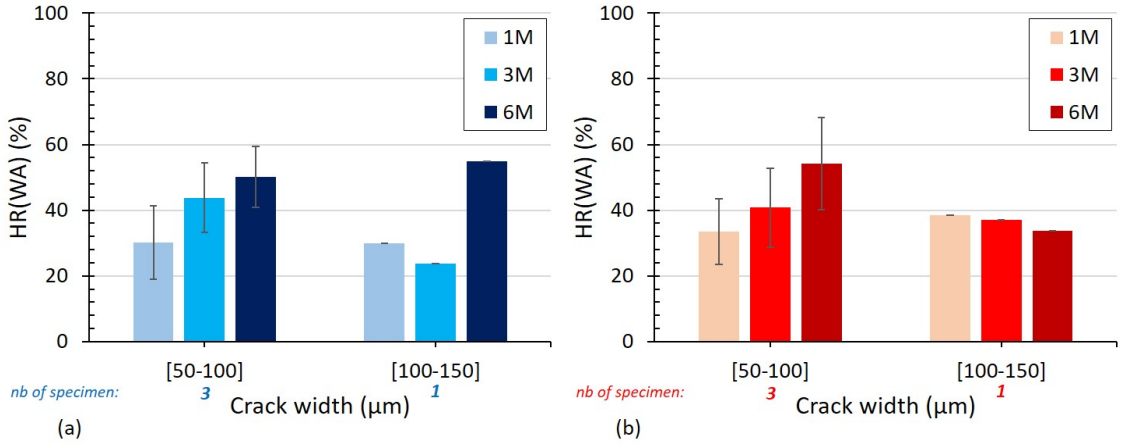

Figure 3.28 – Average Healing Rate (HR) based on the Water Absorption (WA) results as function of the initial crack width for REF (a) and CA (b).

Based on the average HR for REF and CA (Figure 3.29), it is showed CA present a high average HR value at 1M (around 40%), which does not improve significantly after this time (HR = 44% at 6M). On the contrary, REF presents a continuous healing rate till achieving around 55% HR after 6 months of water curing. This confirms that the addition of the crystalline admixture to the mixture improves the hydration process. This increases the healing capacity of the mixture at an early age more than the reference mixture without crystalline admixture.

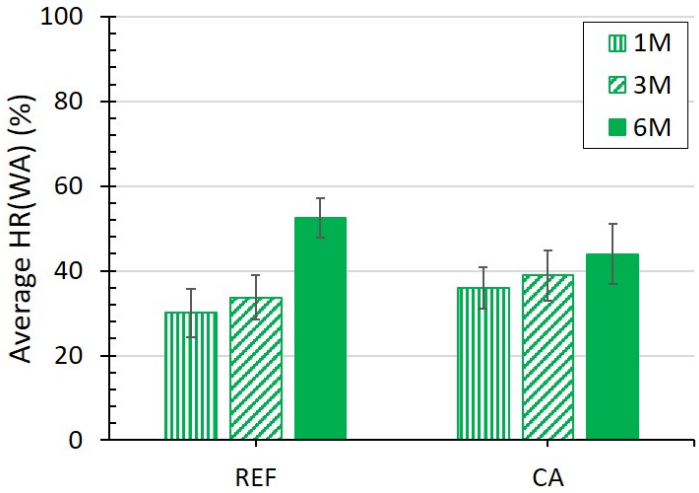

Figure 3.29 – Average Healing Rate for REF and CA (4 specimens/composition).

3.6 Discussion

In this study, we investigated the effect of a mineral addition and a crystalline admixture on the healing capacity of concrete by means of two different experimental tests: water permeability and water absorption. These tests were conducted as a part of the Round Robin Tests in order to evaluate the self-healing capacities and healing kinetics of the concrete compositions, as well as the viability of the proposed tests. Therefore, it is important to discuss these parameters in order to provide an outline conclusion and the purpose of this study.

3.6.1 Influence of the test method in self-healing evaluation

First, the crack width monitoring is a technique that provide only a visual observation of the crack healing. Despite this, this method can provide a complementary study to other tests for the evaluation of self-healing.

Table 3.4 lists the main advantages and disadvantages encountered when manipulating the WA and WP tests. For RRT1 and RRT3, the HR values of the WP test are higher than those of the WA test. With the latter test, the effect of matrix porosity is taken into account by using additional specimens. This does not seem to be a good approach for the evaluation of self-healing because it might ignore the additional hydration capacity related to the addition used in the mixture. This is the reason why no relevant difference was found between the HR of the four compositions using this method (Figure 3.30). Another reason is that when calculating the sorption coefficient (Eq 3.3), the surface in contact with water "A" does not take into account the internal surface of the crack. Therefore, the sorption coefficient was very close between the cracked specimens of each composition. It was also impossible to measure the crack width on the bottom face of the specimen because it exists inside the notch [103]. This is also seen in other studies that performed similar WA tests [13, 103]. The results obtained were highly scattered due to the crack width of the specimens, as well as the limited estimation of the sorption coefficient of the studied specimens.

On the other hand, with the WP test, the two reference concretes and the CA showed close healing behavior (Figure 3.30). Only the SLAG mixture showed small healing rates, which were mainly related to the disk crack width obtained at 0M. Therefore, it is challenging to control the crack opening of the disks during the splitting test. However, with the WP test, it is possible to compare and monitor the healing rate for specimens started with a similar water flow. It also takes into account the effect of crack tortuosity and connectivity on the water flow which provides a 3D approach to evaluate the self-healing kinetic of different compositions [13, 14].

In addition, for both tests, the drying procedures (at 40°C or 20°C), during the specimen preparation, can cause desiccation shrinkage as well as carbonation which will create severe conditions to restart the hydration and impact the crack width.

Test method	Advantages	Disadvantages
WA	- Easy to implement	- Uses aditionnal specimens - Does not provide accurate HR values - Ignores the effect of the internal and the bottom crack - May alter the crack opening during the manipulation of the specimens
WP	- Easy to implement - Monitors the self-healing kinetics - Takes into account the crack turtuosity and connectivity (3D approach)	- May lead to some scattered results related to uncontrolled crack openings

Table 3.4 – Advantages and disadvantages of the WA and WP tests.

3.6.2 Influence of the addition used on the concrete self-healing

First, the testing age differs between RRT1 (70 days) and RRT3 (260 days) specimens. This is one of the main parameters that may influence the self-healing potential of the compositions.

The difference in self-healing behavior between REF and SLAG is related to the addition of minerals used in the composition of SLAG. In the WP and the WA test, SLAG showed a small healing capacity than REF after 1 month of water curing (Figure 3.30). This healing capacity continued to increase progressively till 6 months of water curing, contrary to REF. This is related to the addition of slag into the mixtures that promotes delayed hydration at older ages [19, 104, 105], which resulted in a better healing process than REF at a long term. From RRT3 project, it is found an opposite observation: CA showed a higher HR values than REF after 1 month of water curing i both tests (Figure 3.30). This healing capacity decreased progressively with the curing age compared to continuous healing behavior presented by REF. These results highlight the crystalline admixture content (1%) in the CA composition which is likely to be small for a concrete mixture. This might lead to the consumption of the crystalline addition in the mixture at an early age of curing, and thus no further self-healing effect will be shown at later ages.

3.7 Conclusion

It is interesting to study the influence of different admixtures on the self-healing capacity of mixtures, using several techniques in order to choose the most appropriate method. From the above discussions, it is concluded that the water permeability test is a promising test to evaluate the healing kinetics of cracked specimens. The test provides an adequate calculation of the

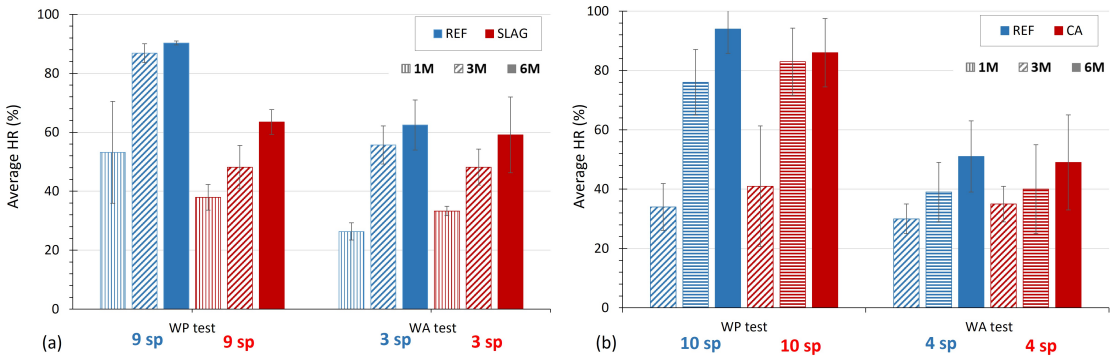

Figure 3.30 – Average HR for RRT1 (a) and RRT3 project (b) from WP and WA tests.

healing rate based on the water flow results. Furthermore, with this test, it is possible to take into account several crack characteristics, i.e. connectivity, tortuosity, geometric dimensions, variation of its opening along its length, etc. In this case, this approach allows a 3D assessment of the healing process. So, this study provided an interesting approach to evaluate the self-healing process of mixtures, and effectively served as a valuable basis for our next studies.

Chapter 4

Materials and experimental procedures

Contents

4.1 Introduction

To begin the research work, a characterization of the materials used in this work (Portland cement, blast furnace slag, EA and sand) is necessary to propose the mortar mixtures. Also, the different experimental procedures are explained to finally provide an overview of the research program followed in our study.

4.2 Materials and mixtures proportions

The effect of two expansive agents is studied for two types of mortars: one Portland cement "CEM I" mortar (experimental campaign n°I) and one blended mortar with 50% of Blast Furnace Slag "BFS" (by binder weight) (experimental campaign n°II). The first campaign consists in understanding the benefit of incorporating EA into cement-based mortars. The objective is to propose a cement-based repair mortar with an interesting autonomous healing capacity. Then, the benefit of incorporating EA into a more environmentally-friendly mortar (blended mortar with blast furnace slag) is investigated to propose an innovative mortar with interesting autonomous healing capacity.

4.2.1 Characterization of CEM I, BFS and sand

Ordinary Portland cement (CEM I 52.5 N) and Blast Furnace Slag (BFS) are used in mortar mixtures. Their chemical composition (given by the data sheet) is shown in Table 4.1. CEM I is mainly composed of lime (more than 60%) and silica (about 20%). Slag is less rich in lime (-23.8%), but has more silica (+14.3%), more aluminium (+5.7%) and more magnesium (+5.9%) compared to CEM I. From XRD analysis (copper source), CEM I shows mainly tricalcium silicate (PDF #31-301 & #49-442), dicalcium silicate (PDF #33-302 & #29-371) and gypsum (PDF #33-311) (Figure 4.1(a)). The blast furnace slag is amorphous having a broad peak at [25-35°] 2Θ (Figure 4.1(b)) [106]. Moreover, the results of TGA analysis show that CEM I contains a higher mass loss in the temperature range of [105-1000]°C than the BFS (Table 4.2). The corresponding DTG curves for CEM I and BFS are presented in Appendix (A). According to Table 4.2, CEM I contains a small contents of portlandite and calcite (0.9% and 1.9% respectively). While BFS contains a small content of calcite (0.9%). These results indicate that a small quantity of these raw materials has reacted with its environment (by hydration/carbonation).

The particle size distribution of CEM I and BFS is determined by laser granulometric analysis in ethanol solution (Figure 4.2(a)). As shown in Figure 4.2(a), BFS has more particles smaller than 10 µm compared to CEM I. Indeed, their median diameters are equal to 8.9 µm and 13.55 µm respectively. They are calculated from the particle size distribution curves.

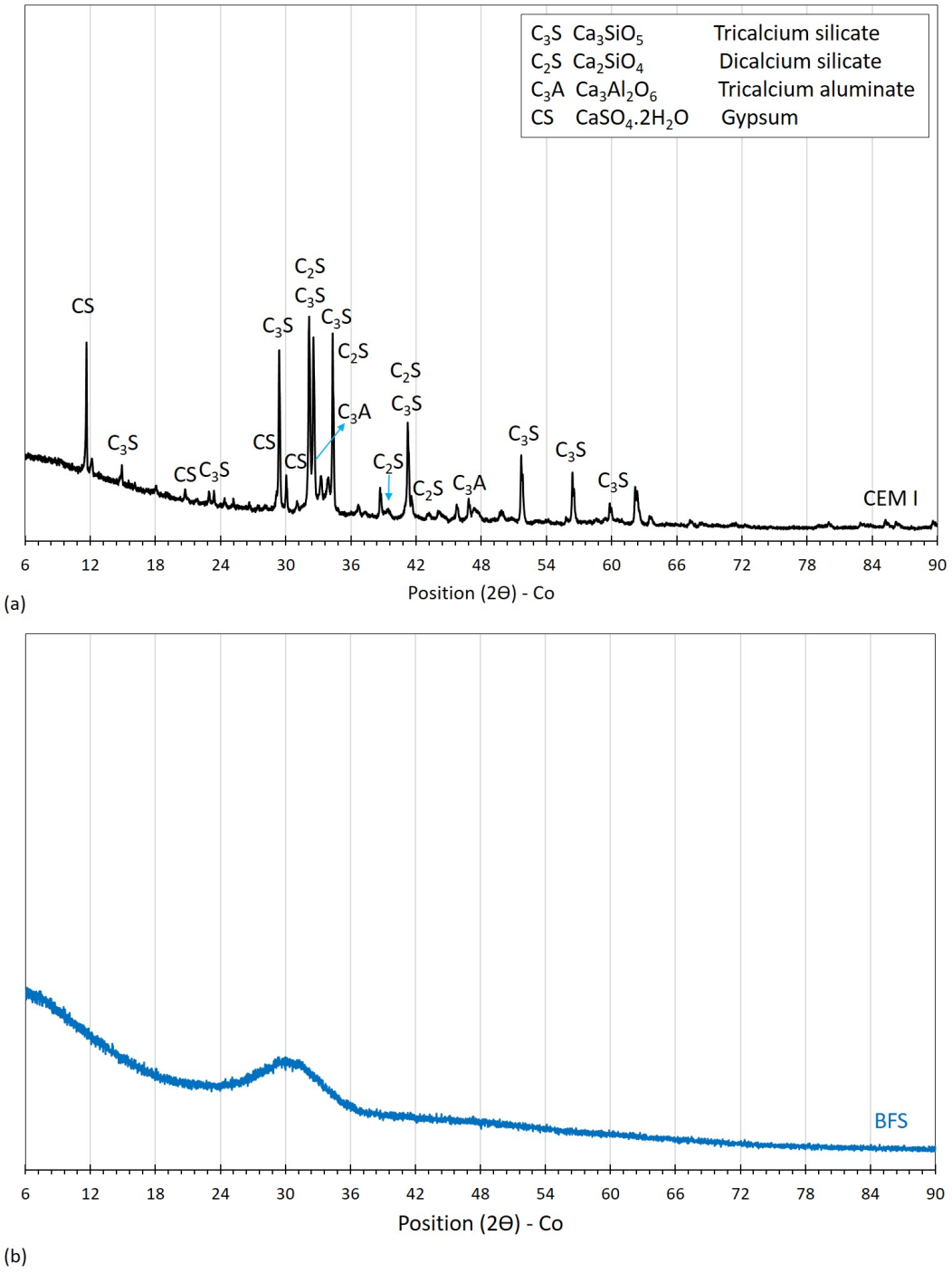

Figure 4.1 – XRD analysis for CEM I (a) and BFS (b).

	CaO	SiO_2	MgO	SO_3	Al_2O_3	Fe_2O_3	K_2O	Na_2O	TiO_2	D_{50} (µm)	S_{BET} (m^2/g)
CEM I	65.9	20.8	1.1	3.4	5.4	2.2	0.3	0.2	-	13.55	1.35
BFS	42.1	35.1	7.0	0.1	11.1	0.4	0.43	0.21	0.8	8.90	1.03

Table 4.1 – Chemical composition (given by the data sheets), median particle size and specific surface area (determined from laser granulometric and sorption analysis respectively) of CEM I and BFS.

Material	Δ_m between [105-1000]°C	Portlandite		Calcite	
		Δ_m	Content	Δ_m	Content
CEM I	2.1%	0.2%	0.9%	0.9%	1.9%
BFS	0.7%	-	-	0.4%	0.9%

Table 4.2 – Mass variation in the temperature range of [105-100]°C for the anhydrous CEM I and BFS - Mass variation and contents of portlandite and calcite.

Moreover, their specific surface areas determined by sorption analysis are equal to 1.03 m^2/g and 1.35 m^2/g respectively for BFS and CEM I (Table 4.1). CEM I has a higher specific surface area than BFS, but BFS contains more small particles than CEM I. This is contrary to the assumption that a material with a large specific surface area would lead to having fine particles. This could be related to the drying at 105°C during the sorption analysis, which could adversely affect the specific surface area results.

The particle size distribution of the sand is determined by sieving granulometry. The used sand is of silica source and its particle size are between [0-4] mm as shown in Figure 4.2(b).

4.2.2 Characterization of EA

Two types of expansive agents are chosen for this study: MgO and CSA, respectively Namex XA and CSA#20 Denka. Namex XA contains 80% magnesium oxide and a small content of calcium oxide (5%) as given by its data sheet (Table 4.3). While CSA#20 is composed mainly of calcium oxide (54%), sulfur trioxide (27%) and alumina (12%) as given by its data sheet (Table 4.3). So, the EA are respectively based on magnesium oxide and calcium sulfoaluminate. They will be referred as MGO and CSA respectively hereafter.

From XRD analysis (copper source) (Figure 4.3), MGO presents mainly magnesium oxide (PDF #45-946) and talc (PDF #13-558). The latter comes from the magnesian minerals used to prepare the MGO. A small peak of calcite (PDF #5-586) and dolomite (PDF #36-426) is also found in MGO. CSA shows ye'elimite (PDF #20-1157), anhydrite (PDF #37-1496) and free lime (PDF #37-1497) as confirmed by several studies [34, 78–80]. In addition, the results of TGA analysis show that MGO contains a small portlandite content (2.2%) and its high mass loss is due to brucite content (4.6%) and calcite content (7.0%). CSA also has a notable portlandite content (18.3%) and a small calcite content (1.3%). Their corresponding DTG curves are

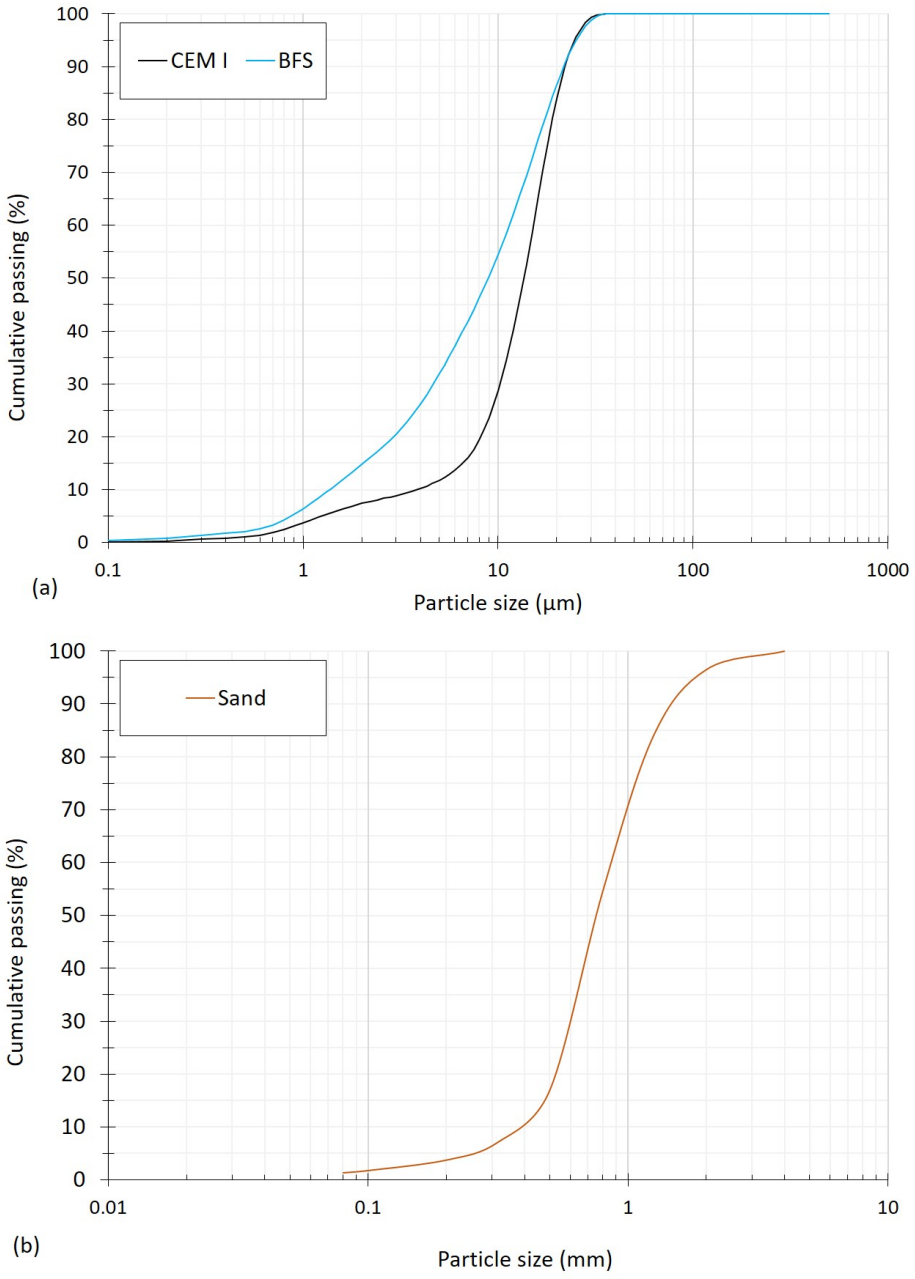

Figure 4.2 – Particle size distribution of CEM I & BFS (a) and sand (b).

presented in Appendix (A). These results indicate that the raw materials were slightly exposed to the ambient air.

	CaO	SiO_2	MgO	SO_3	Al_2O_3	Fe_2O_3	D_{50} (µm)	S_{BET} (m^2/g)
MGO	5.0	4.0	80.0	-	-	2.0	19.0	17.04
CSA	54.0	1.0	0.4	27.0	12.0	0.3	16.4	1.46

Table 4.3 – Chemical composition (given by the data sheets), median particle size and specific surface area (determined from laser granulometric and sorption analysis respectively) of MGO and CSA.

Material	Δ_m between [105-1000]°C	Brucite		Portlandite		Calcite	
		Δ_m	Content	Δ_m	Content	Δ_m	Content
MGO	6.3%	1.4%	4.6%	0.5%	2.2%	3.1%	7.0%
CSA	5.6%	-	-	4.5%	18.3%	0.6%	1.3%

Table 4.4 – Mass variation in the temperature range of [105-100]°C for the anhydrous MGO and CSA - Mass variation and contents of brucite, portlandite and calcite.

The particle size distribution of the EA is determined by laser granulometric analysis in ethanol solution (Figure 4.4). The results show that MGO is slightly coarser than CSA. It has more particles above 12 µm and less below. The median diameters obtained for these two EA are respectively equal to 19 µm and 16.4 µm (Table 4.3). Their S_{BET} determined by sorption analysis are equal to 17.04 m^2/g and 1.46 m^2/g respectively (Table 4.3). These values are close to what is found in the literature [65, 74].

4.2.3 Hydation process of EA

In order to measure the hydration rates of the EA, isothermal calorimetry is performed on pastes with proportion of EA: Water = 1:5. During the test, once the heat flow is close to zero, we stop it and measure the device's deviation. The results show that CSA reacts fast compared to MGO. Most hydration is achieved within a 7 day period for MGO and 3 day period for CSA (Figure 4.5(a)). The hydration of MGO produces brucite at a slower rate than ettringite production due to CSA hydration. In parallel, the hydration heat is fast and high for CSA due to ettringite production at early age (Figure 4.5(b)). This is in agreement with other studies [83, 86].

4.2.4 Mixtures proportions

Mortars with three EA contents are tested: 0%, 5% and 10% (of binder weight) (Table 4.5). The reference mortars in campaign I and II (REF and BFS respectively) are compared to mortars

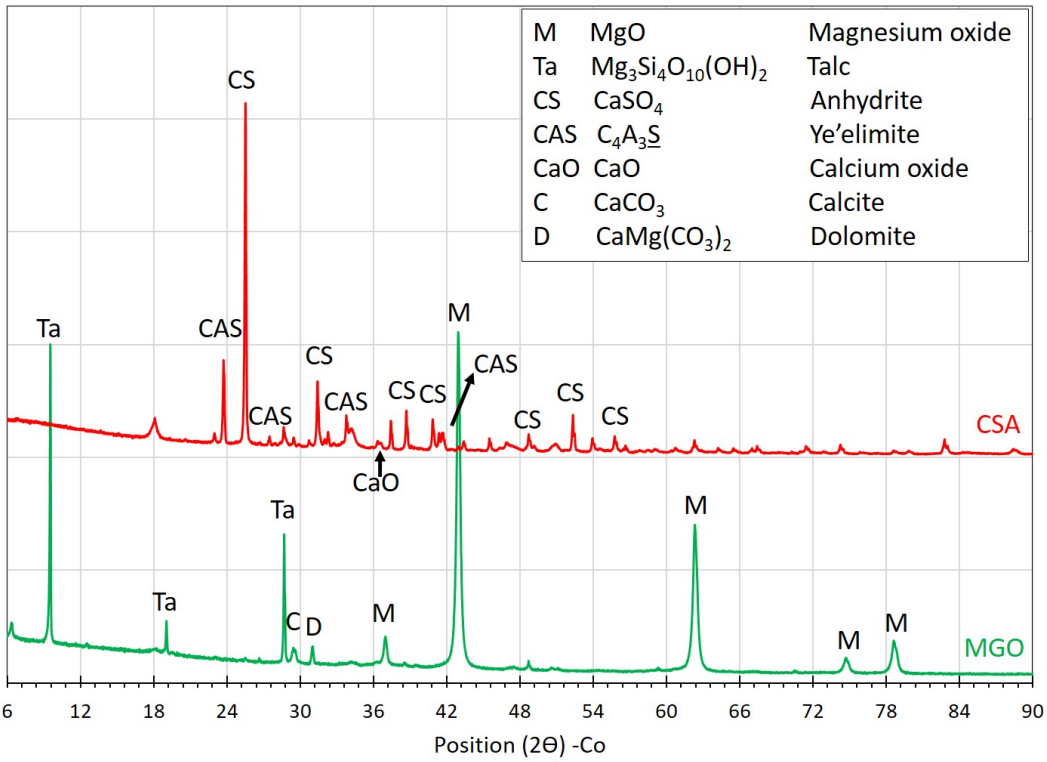

Figure 4.3 – XRD analysis for MGO and CSA.

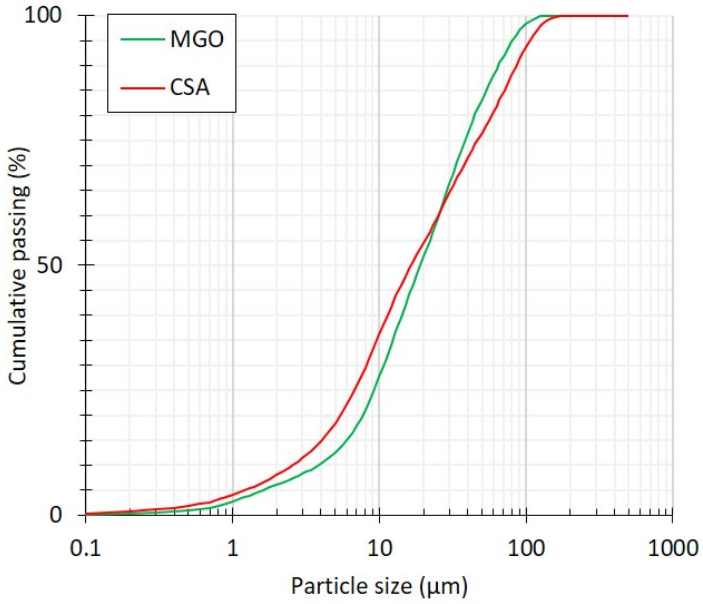

Figure 4.4 – Particle size distribution of MGO and CSA.

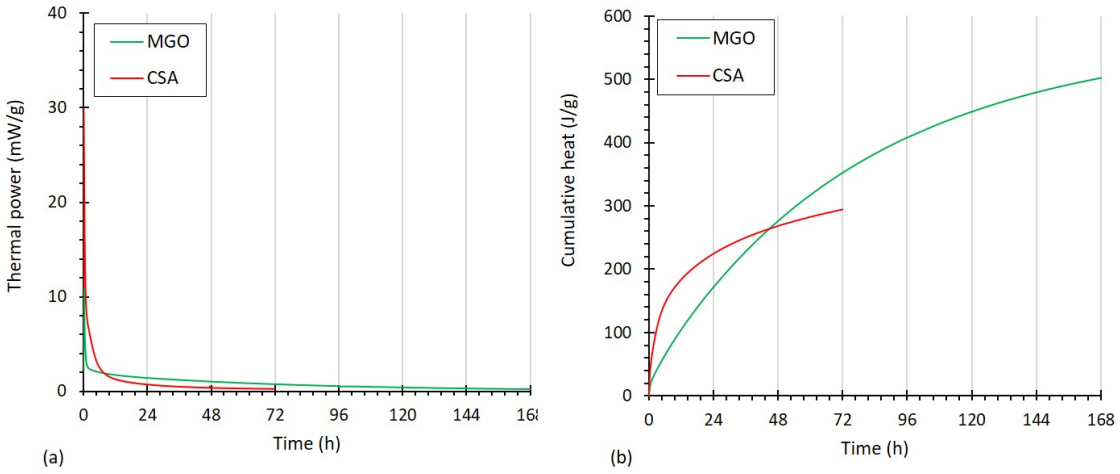

Figure 4.5 – (a): Thermal power and (b): Cumulative heat of MGO and CSA.

containing MGO (MG5, MG10 and BM5, BM10 respectively), and to mortars containing CSA (CSA5, CSA10 and BC5, BC10 respectively). For the mixtures: BFS, BM5, BM10, BC5 and BC10, 50% of the Portland cement is substituted by blast furnace slag. This substitution is chosen because cementitious materials with 50% blast furnace slag presented mechanical performances almost similar to those of matrices with 100% Portland cement [107, 108].

The Water/binder and Sand/Binder ratios are maintained constant and equal to 0.45 and 2 respectively. All mortar mixtures are characterized by a sufficient fluidity to be used in future repair applications. Hence, the superplasticizer -Sika ViskoFlow-800 Power- is used and its content is mentioned in Table 4.5 for each mixture (by binder weight). For the specimens used to monitor the healing process, steel fibers (50 kg/m^3) are added to better control the initial crack width. These fibers are characterized by a length of 25 mm and a diameter of 0.2 mm.

Campaign	I					II				
kg/m^3	REF	MG5	MG10	CSA5	CSA10	BFS	BM5	BM10	BC5	BC10
CEM I	650	619	588	616	582	322	307	292	305	289
BFS	-	-	-	-	-	322	307	292	305	289
EA	-	33	65	32	65	-	32	65	32	64
Sand	1299	1299	1299	1299	1299	1287	1287	1287	1287	1287
Water	291	292	292	290	289	289	290	291	289	289
SP (%)	0.3	0.3	0.3	0.3	0.3	0.13	0.13	0.20	0.10	0.08
Water/Binder	0.45	0.45	0.45	0.45	0.45	0.45	0.45	0.45	0.45	0.45
Water/(CEM I+BFS)	0.45	0.47	0.50	0.47	0.50	0.45	0.47	0.50	0.47	0.50
Average slump (cm)	11.5	11.0	11.0	12.0	12.0	10.4	9.0	8.5	10.7	10.5
Air content (%)	2.1	2.8	2.8	2.2	3.5	2.7	5.2	4.7	4.2	4.8

Table 4.5 – Mix proportions and fresh mortar properties of mortars.

4.3 Experimental procedures

Several experimental tests are performed for this research program. The detailed procedure of each test is described hereafter.

4.3.1 Hydration process

To measure the mortar's hydration process, isothermal calorimetry is conducted at 20°C (Figure 4.6). To ensure a temperature close to 20 °C at the mixing end, the binders are conditioned in the calorimeter for at least 12 hours prior to the test. After a manually mixing for two minutes, specimens (around 59 cm^3) are placed directly into the calorimeter and the hydration heat is measured till 72 hours.

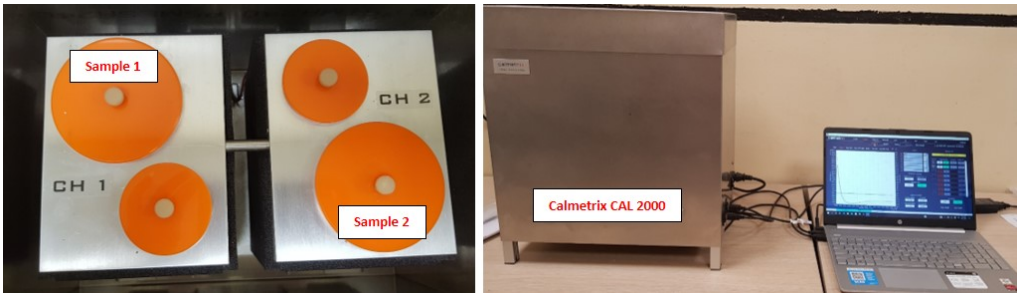

Figure 4.6 – The isothermal calorimeter "Calmetrix I-Cal 2000 HPC".

After, it is necessary to have an estimate of the heat released at a theoretical infinite time by a graphical extrapolation method. In this case, the cumulative heat evolution "$Q(t)$" -obtained by the isothermal calorimetry- is plotted on a graph as a function of "$\frac{1}{t}$". Then, $Q(\frac{1}{t})$ is extrapolated by an exponential function in the interval of $\frac{1}{t}$ = [0 - 0.05] (graphs shown in Figures A.2 and A.3 in Appendix A). So, the cumulative heat ad infinitum "$Q(\infty)$" can be obtained at the theoretical infinite time ($\frac{1}{t} = 0 \Leftrightarrow t = \infty$).

After that, the hydration advancement degree "x" is calculated using Eq. 4.1:

$$x = \frac{Q(t)}{Q(\infty)} \tag{4.1}$$

4.3.2 Hydration products

To determine the hydration products as well as the hydration rates of the different studied mortars, ThermoGravimetric Analysis (TGA) is performed at 3, 7, 28 and 90 days old specimens stored at RH = 95±5% and 20°C during the 28th days and cured in water beyond 28 days (Water Curing). Before testing, specimens are dried at 105°C for 24 hours to remove free water

existing in pores. The specimens are then crushed and ground. After, about 70 to 90 mg of powder is placed in a nitrogen environment and the temperature increases from 20 to 1000°C with a rate of 10°C/min. The main crystalline phases identified are brucite & hydrotalcite, portlandite and carbonates (e.g. $CaCO_3$, $MgCO_3$). These products decompose respectively in the temperature range of: [300-400]°C [109,110], [400-600]°C [92], [600-800]°C [72,111].

Moreover, X-ray diffractometer (XRD) analysis is performed on 28 days old specimens (Φ5xH10 cm^3 - 3 specimens/mixtures) stored at RH = 95±5% and 20°C. At 27 days old, the specimens are dried at 40°C into a vaccum oven to slightly remove the residual water that might affect the grounding process. After 24 hours, the specimens are ground to powders fine enough to pass the sieve with the mesh size of 8 μm. The XRD analysis is made in the range of 2Θ = [4-90]° and the source is copper.

4.3.3 Porosity

The pore radius of cementitious materials can be classified to three main groups according to [112]: micropores (r $\leq$ 1 nm), mesopores (1 nm < r $\leq$ 25 nm), and macropores (r > 25 nm). So, to evaluate the mortar's porosity, three techniques are used:

1. Water porosity: using water, this technique allows to estimates the total pores volume, i.e. micro, meso and macropores.

2. Gas permeability: using helium gas, this technique allows to estimate the connectivity between the pores.

3. Sorption analysis: using nitrogen gas, this technique allows to estimate the volume of mesopores for a pore radius ranging from 2 nm to 12 nm.

The water porosity and gas permeability are conducted according to the [EN – 18-459] European standard on 28 and 90 days old specimens stored at RH = 95±5% and 20°C (Φ4xH6 cm^3 - 3 specimens/mixtures). For the water porosity test, the specimens are placed in a vacuum desiccator for 4 hours. Then the water is filled into the desiccator and the vacuuming maintains for another 44 hours till saturation. After, the saturated air mass "M_{air}" and hydrostatic mass "M_{hyd}" are measured and the specimens are dried at 40°C until mass variation is inferior than 0.05%. Finally, the dried mass "M_{dry}" is measured and the water porosity is calculated using Equation 4.2.

$$\text{Water porosity} = \frac{M_{air} - M_{dry}}{M_{air} - M_{hyd}} \tag{4.2}$$

After the porosity test, gas permeability test is implemented on the same dried specimens in order to evaluate the connectivity between the pores. Specimens are placed in a permeability

cell where two pressures are applied: a confinement pressure fixed at 8 bars, and a percolation pressure varying from 1 to 7 bars (Figure 4.7). A flowmeter is used to record the gas flow rate and the gas permeability coefficient “K” is determined using Equation 4.3.

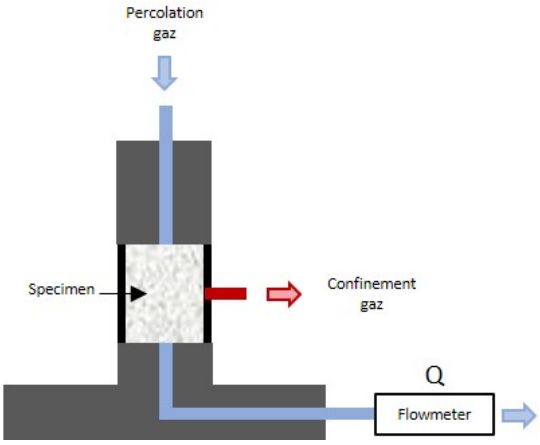

Figure 4.7 – Schematic of the permeability cell.

$$K = \frac{2QP_{\text{atm}}H\mu}{A\left(P_i^2 - P_{\text{atm}}^2\right)} \tag{4.3}$$

Where "Q" is the gas flowrate (m^3/s); "P_{atm}" the atmospheric pressure (Pa); "H" the specimen's height (m); "P_i" the input pressure (Pa); "A" the specimen section (m^2) and "μ" the dynamic viscosity of the helium gas (Pa.s).

In addition, nitrogen sorption analysis is made on 3, 7, 28 and 90 days old specimens stored at RH = 95±5% and 20°C during the 28th days and cured in water beyond 28 days (Water Curing). Before testing, powder samples (900 to 1000 mg) are dried at 105°C during 24 hours, then stored under vacuum at 105°C during 12 hours to remove any residual moisture into the powder. The mesoporal porosity is determined from nitrogen sorption curves.

4.3.4 Deformations

The understand the impact of EA ont the mortar's behavior, and to further explain the self-healing results, the mortar's deformation is monitored. The measurements are made on prismatic specimens (4x4x16 cm^3) stored under three types of curing at 20°C (3 specimens/curing): (1) autogenous curing on specimens sealed with a double layer of aluminum foil to prevent moisture loss, (2) curing under a high relative humidity (95±5% RH) during the 28th days followed by a Water Curing (WC) and (3) curing under a high relative humidity (95±5% of RH) during the 28th days followed by a Cycle Curing (CC) combining water and air curing at 95±5% RH for 3 days each. The last two curing conditions are chosen to be similar to those used for

self-healing evaluation (§4.3.7) in order to use them to explain the self-healing results. All these deformations are monitored from 1 day old using a retractometer with 1 µm of precision (Figure 4.8(a)). The exchanges between specimens and their environment are monitored by measuring their mass variation. The deformations "$\mathcal{E}(t)$" are calculated using Equation 4.4, and the mass variations "$\Delta m(t)$" using Equation 4.5.

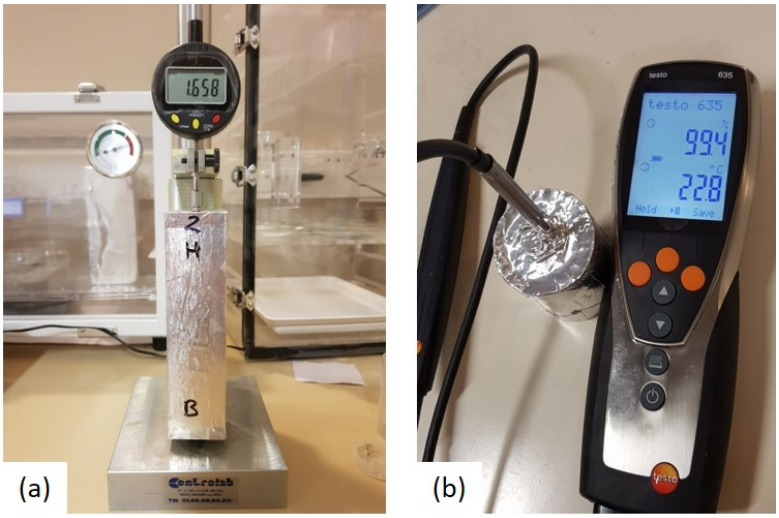

Figure 4.8 – Retractometer used to measure the deformation (a), IRH measurement (b).

$$\mathcal{E}(t) = \frac{L_i(t) - L_0}{L_0} \tag{4.4}$$

$$\Delta m(t) = \frac{m_i(t) - m_0}{m_0} \tag{4.5}$$

Where "L_0" and "m_0" are the initial length (mm) and mass (g) respectively measured on 1 day old specimens (just after demoulding). Similarly, "$L_i(t)$" and "m_i(t)" are the length (mm) and mass (g) respectively measured at time t.

In order to understand the autogenous deformation measurements, the Internal Relative Humidity (IRH) is monitored on two cylindrical specimens (Φ5xH6 cm^3). One measurement/week is made using a sensor of a thermo-hygrometer with an accuracy of 2%. The sensor is placed in a drill of 3.5 cm length in each specimen (Figure 4.8(b)).

4.3.5 Mechanical properties

The mechanical strengths (flexural and compressive strengths) are measured on three prismatic specimens (4x4x16 cm^3) at 3, 7, 28, 90 and 365 days according to [EN 196-1] European standard. First the bending test is carried out and the compressive test is secondly performed on the

two half-specimens resulting from the previous test. Before testing, specimens are stored in a humid chamber (RH = 95±5%) at 20°C.

In parallel, the dynamic Young's modulus is measured using a non-destructive method. It is based on the propagation of compressive ultrasonic waves on three prismatic specimens (4x4x16 cm^3) at 3, 7, 28, 90 and 365 days. This technique consists of subjecting the specimen to a wave signal and recording the response. The propagation of ultrasonic waves is affected by the size and orientation of pores and cracks, etc. When these last increase, the wave propagation is disturbed and its velocity decreases. In our work, the ultrasonic velocity is measured using two longitudinal wave transceivers of 25 mm diameter (Figure 4.9). Glycerin is used as a lubricant agent. Specimens are stored in a humid chamber (RH = 95 ± 5%, 20°C). The time required by the wave to pass through the specimen is recorded and the corresponding dynamic Young modulus is calculated using Equation 4.6.

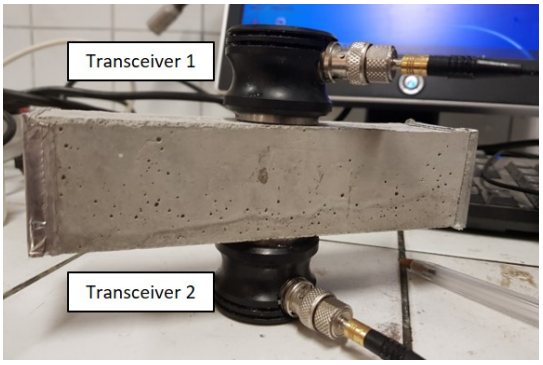

Figure 4.9 – The longitudinal wave transceivers used for the dynamic Young modulus.

$$E_{dyn}(t) = \rho \left(\frac{H}{t}\right)^2 \frac{(1+\gamma)(1-2\gamma)}{(1-\gamma)} \tag{4.6}$$

Where "t" is the recorded time (s), "γ" the Poisson ratio taking equal to 0.2 and "ρ" the material density (kg/m^3).

4.3.6 Cracking sensitivity

In order to estimate the sensitivity to cracking under restricted autogenous deformation conditions, the Cracking Sensitivity Index (CSI) is calculated by combining several mechanical properties: autogenous deformation, flexural or compressive strength and dynamic young modulus [113]. The second mechanical properties are used as they allow estimating the tensile or compressive stresses that can occur as a result of restricted or swelling deformations respectively. The third mechanical property is used as it can affect the magnitude of stresses associated with autogenous deformation.

This relation is given in Eq. (4.7) and (4.8) :

$$CSI(t_n) = \frac{\sigma(t_{n-1}) + \delta\sigma}{f_{t/c}(t_n)} \tag{4.7}$$

$$\delta\sigma = (\epsilon(t_n) - \epsilon(t_{n-1})) \frac{E_{dyn}(t_n) + E_{dyn}(t_{n-1})}{2} \tag{4.8}$$

where

$\epsilon(t_n)$ = Autogenous shrinkage at time t_n $(\mu m/m)$
$E_{dyn}(t_n)$ = Dynamic Young modulus at time t_n (GPa)
$f_{t/c}(t_n)$ = Tensile or compressive strength at time t_n (MPa)

Based on the experimental results, Eq. (4.9) and (4.10) are used to predict the evolution of these mechanical properties ($ft(t)$, $E_{dyn}(t)$, $\epsilon(t)$) as function of time. A second term (Eq. (4.11)) is added to Eq. (4.9) to take into account a possible reduction in the mechanical properties.

$$X(t) = X_\infty \beta(t)^{\eta_X} + \delta(1 - D) \tag{4.9}$$

$$\beta(t) = \exp\left(s\left(1 - \sqrt{28/(t - t_0)}\right)\right) \tag{4.10}$$

$$D = Y(1 - e^{\frac{t}{\tau}}) \tag{4.11}$$

where

X = Studied material property ($ft(t)$, $E_{dyn}(t)$, $\epsilon(t)$)
$\eta_X, X_\infty, s, Y, \tau$ = Parameters of the studied material properties calibrated on the experimental results
t_0 = Initial setting time determined from isothermal calorimetry (respectively for REF, MG5, MG10, CSA5, CSA10, BFS, BM5, BM10, BC5 and BC10: 9.5, 12.5, 14.5, 12.2, 12.5, 9.5, 11, 11.2, 9.5 and 9 hours

$$\delta = \begin{cases} 0, & \text{if no reduction of the mechanical properties at long term is considered} \\ 1, & \text{if reduction of the mechanical properties at long term is considered} \end{cases} \tag{4.12}$$

When swelling is detected, the above CSI model is no longer valid. In such case, the below equation is used:

$$\epsilon(t) = [\epsilon_{\text{swelling}} - \epsilon_\infty] \left[\left(\frac{\epsilon_\infty}{\epsilon_{\text{swelling}} - \epsilon_\infty} \right) + \sin\left(\frac{(1 - \xi_{\text{swelling}}) + (1 - t) - |(1 - \xi_{\text{swelling}}) - (1 - t)|}{1 - \xi_{\text{swelling}}} \cdot \frac{\pi}{4} \right)^\beta \right]$$

$$\cdot \left[1+\alpha\left(\frac{1-t-(1-\xi_{\text{swelling}})+|1-t-(1-\xi_{\text{swelling}})|}{2\xi_{\text{swelling}}}\right)^{4}\right]^{-1} - \left[\frac{\epsilon_{\text{swelling}}}{1+\alpha}\right](1-t)$$

Thus, a higher value of this index indicates a more important cracking sensitivity of the studied material. If the index reaches a value equal to 1, cracking should occur under fully restrained conditions. Nevertheless, this index does not take into account the beneficial effect of relaxation (decrease of internal stresses) which varies according to the studied material.

The approach chosen to evaluate the cracking sensitivity index in our case, is based on several assumptions such as: the use of the dynamic Young's modulus whose value is higher than the static Young's modulus, as well as the flexural strength whose value is higher than the tensile strength, hence an overestimation of the CSI. In addition, the setting time of the mixtures is estimated by isothermal calorimetry tests. This can lead to an inaccurate estimate of the crack sensitivity index, as the setting tests (via ultrasonic measurement using Vicasonics for example) give accurate values of the setting time of the mixtures. Finally, this calculation does not take into account the beneficial effect of relaxation (reduction of internal stresses) via creep tests, which reduces the CSI values.

4.3.7 Self-healing evaluation

To evaluate the self-healing capacity of the mixtures, Water Permeability (WP) tests are carried out in order to obtain a 3D monitoring of crack healing. Two cylindrical specimens (Φ11xH20 cm^3) are prepared for each composition. After demoulding, specimens are stored in a humid chamber (RH = 95±5%, 20°C) until the cracking age –28 days old. Three days before the test (at 25 days old), each cylindrical specimen is cut into 3 disks (Φ11xH5 cm^3). At 28 days old, all the disks are pre-cracked using a splitting test to obtain a crack width equal to 0.2 ± 0.05 mm.

The loading speed is fixed at 0.05 mm/min. During the splitting test, the crack opening is visually controlled using a specific ruler (Figure 4.10(a)). Before WP test, crack width is measured on the both disk surfaces using a reflective microscope (Figure 4.10(b)). The measurements are performed beyond 1 cm from the disk edges and on several points (from 3 to 10) over a 50 mm long area (Figure 4.10(c)). After crack width measurements, all specimens are stored at 40°C and 20% RH during 24 hours. This curing is applied to slightly dry mortar disks to ensure a good adhesion of the PVC tubes (Φ_{inner} = 100 mm, H = 200 mm) glued on the superior specimen face. Then, the disks are stored at 20°C and 60% RH during 24 hours to let dry the glue before the water permeability test. Note that these drying procedures (at 40°C and 20°C for 24 hours) may increase the possibility of crack carbonation, so they are not suggested for future works. After, PVC tubes are filled with 1.55 liters of tap water.

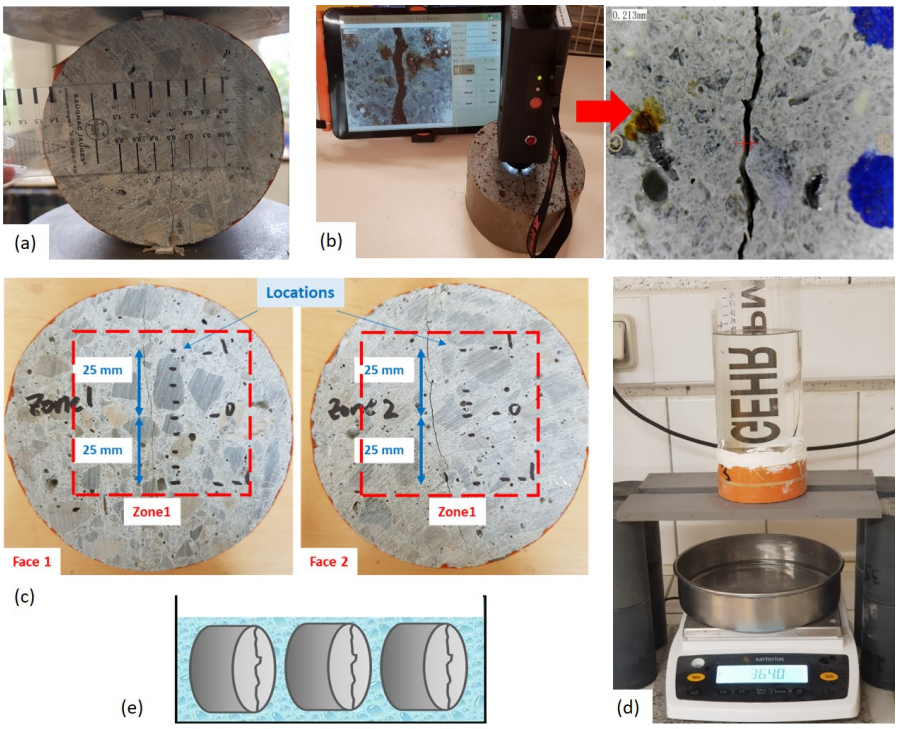

Figure 4.10 – Crack width controlled with a ruler during the splitting test (a), Crack width measurement device and its given optical microscope image (b), Location of zones where the crack width is measured on specimen surfaces (c), Water Permeability test (d), Disks position in the container (e).

To monitor the water flow through the crack, specimens are placed on a support above a balance (precision of 100 mg - Figure 4.10(d)). The flowed water quantity is measured after 5, 10, 15, 20, 25 and 30 minutes to quantify a water flow (l/m) on three disks/composition. Moreover, the water level is also monitored during 3 hours. The water permeability test is made just after cracking (0D), after 7 days (7D), 25 days (25D) and 112 days (112D) of curing. After WP test, all disks are stored vertically (Figure 4.10(e)) in a container (one container/mixture). Two types of curing are performed (WC and CC). For the WC, the water is renewed every month. From each curing condition, a Healing Rate (HR(t)) is calculated according to Equation 4.13.

$$HR(t) = \frac{W_{\text{unhealed}}\ (0\text{D}) - W_{\text{healing}}\ (t)}{W_{\text{unhealed}}\ (0\text{D})} \times 100 \tag{4.13}$$

Where $HR(t)$ is the Healing Rate at time t (%), $W_{unhealed}$ (0D) the initial water flow just after the cracking (at 0D) (l/min) and $W_{healing}(t)$ the water flow after a healing period t (l/min).

Moreover, the self-healing products formed within the crack are identified using Scanning Electron Microscope (SEM) analysis. At one year, the disks are cut around the crack into 2x2

cm cubes. After, the specimens are placed in a vacuum desiccator for 24 hours before the SEM analysis.

4.4 Conclusion

This preliminary study allowed the characterization of the different materials that will be used later: Sand, CEM I, BFS, MGO and CSA. These characterizations will help explain the results obtained in the following chapters (e.g. hydration of mortars).

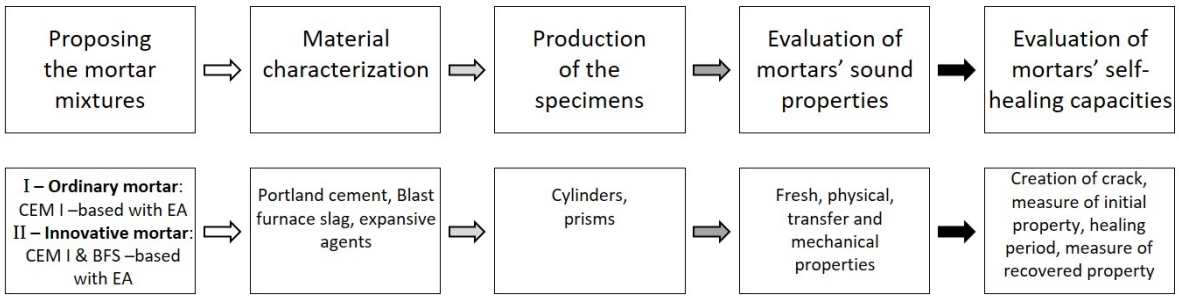

Figure 4.11 – Outline of the research program.

The experimental procedures necessary for this research program are explained to provide an overview of the program followed in our study (Figure 4.11). As shown in Figure 4.11, two reference mortar mixtures are proposed for this study: REF and BFS. They are compared to mortars containing MGO (MG5, MG10 and BM5, BM10 respectively), and to mortars containing CSA (CSA5, CSA10 and BC5, BC10 respectively). The first campaign consists in understanding the impact of EA on cement-based mortars in two states, sound and cracked. The objective is to propose a cement-based repair mortar with an interesting autonomous healing capacity. Then, the second campaign is planned in order to understand the impact of EA in the presence of blast furnace slag, on the mortar properties and its healing capacity. The objective is then to propose an innovative repair mortar with an interesting autonomous healing capacity.

Chapter 5

Effect of MGO and CSA-based EA on the behavior of Portland-cement mortars: microstructure, mechanical properties and healing capacity

Contents

5.1 Introduction

The main goal of this chapter is to determine the possibility to design a repair mortar with autonomous healing capacities by using Expansive Agents (EA) in the cement-based mortar mixtures. The present research focuses firstly on the effect of two types of EA based on MgO and CSA products on the properties of the sound mortars: their hydration process and microstructure evolution, as well as their mechanical properties and delayed deformations under three types of curing. This first step will allow us to determine the possibility to use this material in repair applications, in particular by taking into account their deformation compatibility with their support. Secondly, the benefit of the EA to promote the autonomous healing is investigated using the water permeability test following the methodology developed in the RRT as described in Chapter 3.

5.2 Hydration and microstructure of sound mortars with EA

The hydration process of the studied mortars is discussed below as well as their microstructure by evaluating their hydration products and porosity structure.

5.2.1 Hydration process

The hydration process is determined for all the studied mixtures at early age (before 3 days) using isothermal calorimetry and at long term (until 90 days) by ThermoGravimetric Analysis (TGA).

At early age: The heat flow, the cumulative heat and the hydration advancement degree are presented in Figures 5.1, 5.2 and 5.3 for all the studied mixtures. The heat flow curves of Portland cement mortars can be divided into four principal periods: (1) Pre-induction period; (2) Dormant period; (3) Acceleration period and (4) Post-acceleration period [114, 115] (Figure 5.1).

The dormant period of REF is shorter than that of other mixtures (3 hours -Table 5.1). The addition of 5% EA (MG5 and CSA5) slightly extends this period. It is equal to 3.5 hours for MG5 and 3.3 hours for CSA5 (Table 5.1). For mixtures containing 10% EA (MG10 and CSA10), this period is further extended and it is much longer for MG10 (5 hours) than for CSA10 (4.5 hours). The longer dormant period is partially related to the reduction of cement content due to the partial replacement of cement by EA in the mixtures. Moreover, it is related to the EA hydration kinetics (§4.2.3 - Chapter 4), as the CSA hydration is faster than MGO.

After the dormant period, mixtures with CSA (CSA5 and CSA10) continue with a fast hydration process as their second hydration peak appears after a smaller duration than that

Table 5.1 – Duration of period 2, time to reach the 2^{nd} and 3^{rd} peak and the value of the cumulative heat ad infinitum.

Hydration characteristics	REF	MG5	MG10	CSA5	CSA10
Duration of period 2 (h)	3.0	3.5	5.0	3.3	4.5
Time of the 2^{nd} peak (h)	12.0	12.5	14.5	12.2	12.5
Duration from period 2 to the 2^{nd} peak (h)	9.0	9.0	9.5	8.9	8.0
Time of the 3^{rd} peak (h)	15.5	16.5	17.5	17.0	-
Q_∞ (J/g)	328.7	330.4	336.2	332.4	332.9

of REF (Table 5.1). This duration is about 8.9 hours and 8 hours for CSA5 and CSA10 respectively, while it is equal to 9 hours for REF. This observation is consistent with their hydration advancement degree that is high before 9 hours (Figure 5.3). This behavior is more prominent by increasing the CSA content to 10%. It is related to the fact that the hydration kinetics of CSA is fast as it contains more than 50% CaO and 27% SO_3. This increases the formation of early ettringite in the mixture and accelerates the hydration process [81, 83, 84, 86]. After 9 hours, the hydration advancement degree of CSA5 and CSA10 become smaller than that of REF, indicating that the hydration of CSA might be completed. To ensure this hypothesis, the hydration process is evaluated at the long term.

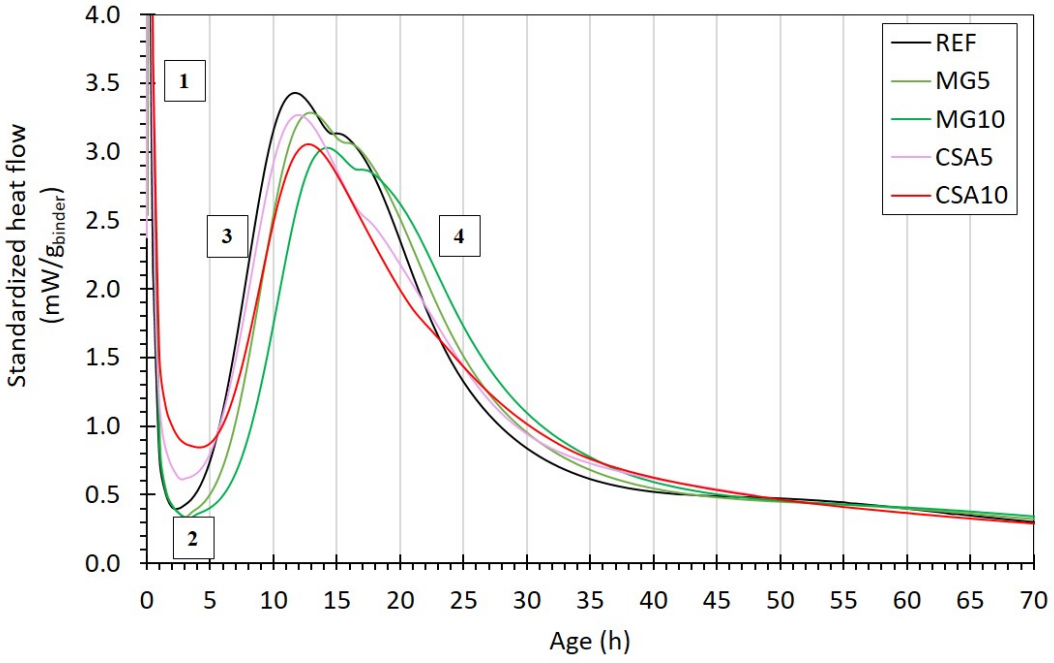

Figure 5.1 – Standardized heat flow for all the studied mixtures; *(1) Pre-induction period; (2) Dormant period; (3) Acceleration period and (4) Post-acceleration period*; and its cumulative heat (b).

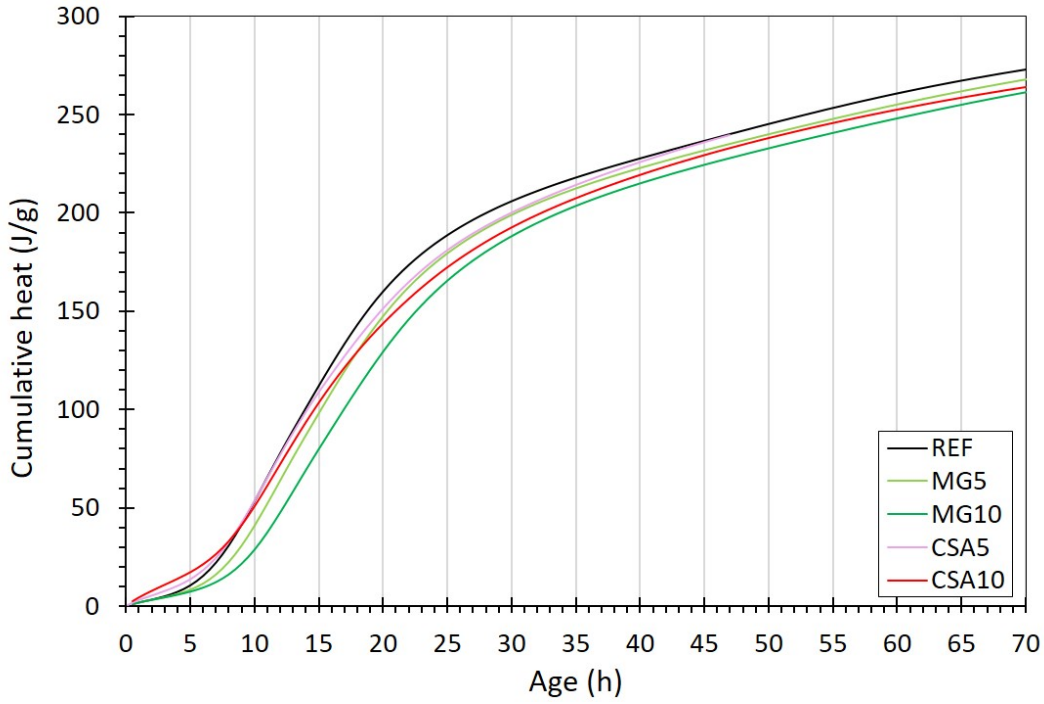

Figure 5.2 – Cumulative heat for all the studied mixtures.

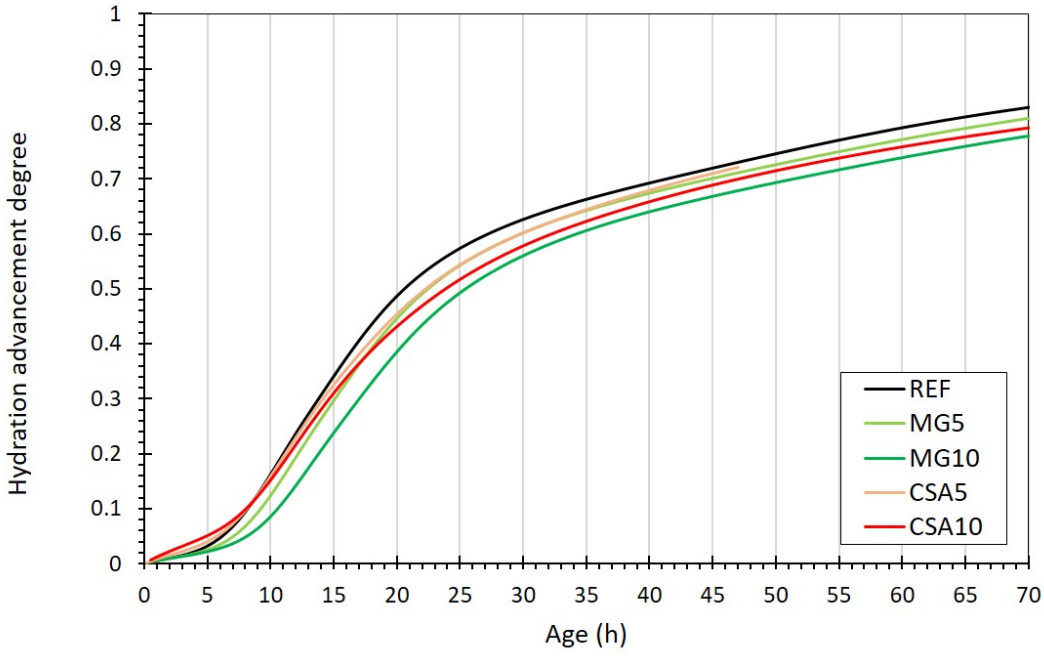

Figure 5.3 – Hydration advancement degree for all the studied mixtures.

In contrast, the addition of MGO (MG5 and MG10) delays the hydration process as shown by their time to reach the second peak (Table 5.1) as well as their hydration advancement degree (Figure 5.3). The addition of MGO increases the $[Mg^{2+}]$ concentration in the interstitial solution, which increases the pH to 12. This causes a delay in cement hydration [116]. The third hydration peak (Figure 5.1) is attributed to the secondary formation of ettringite (AFm) and thus, the sulfate depletion [117]. This peak appears clearly for REF and mixtures containing MGO. However, it appears slightly for CSA5 and it is absent for CSA10. It indicates that the sulfate is consumed during the ettringite formation at the early stage of hydration (second phase) [118], and this behavior is faster by increasing the CSA content.

At long term: From TGA analysis, the advancement of the hydration at long term is estimated through the mass loss of the sample in the temperature range of [105-1000]°C (Figure 5.4). This temperature range is chosen in order to take into account the overall mass loss related to the dehydration and decomposition of the hydration and the carbonation products respectively. In this analysis, the carbonation products are taken into account because they can be produced by the carbonation of some hydration products like portlandite. The mass losses in the temperature ranges of [105-300] °C and [105-600] °C will be presented in Appendix (C).

The mass loss of REF is the smallest at early age (3d). At this age, the mixtures with 5% EA (MG5 and CSA5) present higher mass losses compared to REF. Their values increases as a function of time for MG5, but not for CSA5. The addition of MGO allows the development of supplementary hydration products: brucite and M-S-H [83]. These supplementary hydration products increases the chemically bound water and thus, increases the total mass loss. The continuous increase in the mass loss till 90 days confirms that the hydration process of MG5 tends to the long term. The increase in MGO content to 10% (MG10) favors this behavior at long term. It indicates that this mixture presents additional hydration capacity at the long term, probably related to the higher MGO content in the mixture.

For CSA5, the mass loss decreases beyond 3 days until 28 days, then increases again at 90 days to a value close to that of REF. Increasing the CSA content to 10% (CSA10) further decreases the mass loss at early age (3d and 7d) compared to CSA5, but increases again at later age (28d and 90d). The addition of CSA increases the formation of AFt/AFm, although the mass of ettringite is not fully estimated in this case since it begins to decompose at 50°C, but these results highlight the stability of ettringite over time. It could transform into AFm which requires a slightly lower water content than AFt (12 water molecules). Furthermore, the hydration of CSA is rapid and could be complete before 14 days, indicating that no new AFt/AFm phase could be formed in the long term [83]. To test this hypothesis, XRD analyses are required. So, these results indicate that the addition of CSA accelerates the hydration process in the first few hours but does not tend to accelerate it in the long term. Finally, it should be noted that the mass variation in the temperature range [105-1000]°C of the anhydrous products (Portland cement, MGO and CSA) is negligible compared to the mortars.

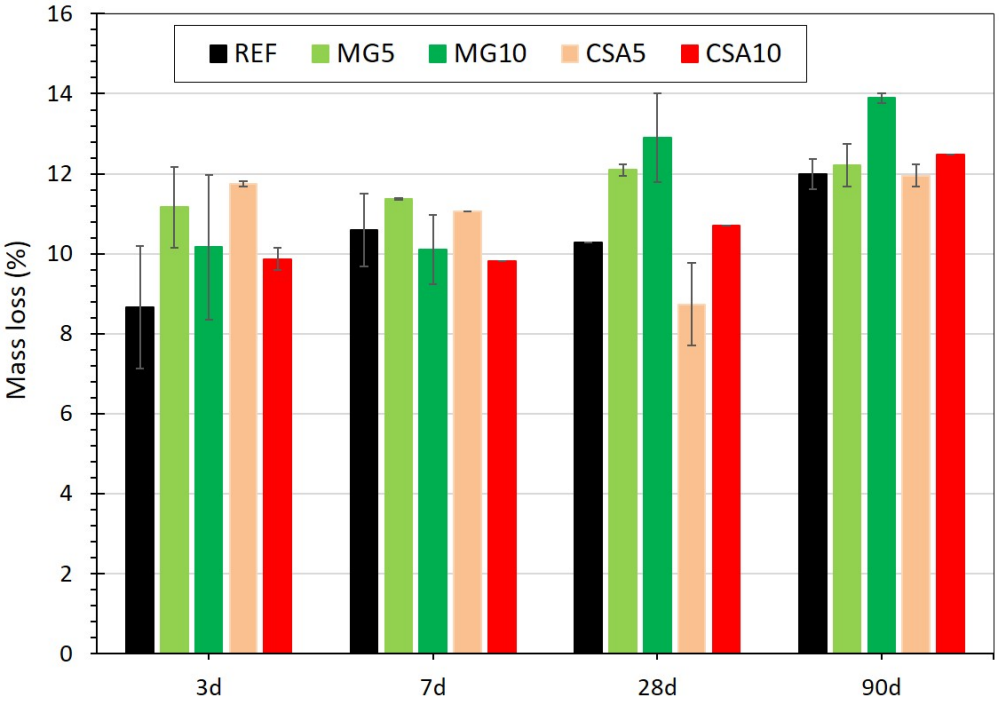

Figure 5.4 – Mass loss from 105°C to 1000°C from TGA at 3, 7, 28 and 90 days for all the studied mixtures.

5.2.2 Hydration products

From the TGA analysis, DTG curves are determined and presented for each mixture at 3, 7, 28 and 90 days (Figure 5.5). From these curves, it can be seen a first peak between 105°C to around 250°C for all the studied mixtures at each age. This peak is mostly associated to C-S-H that starts to decompose at 105°C. A second peak between [300-450]°C appears only for the mixtures containing MGO (MG5 and MG10). This peak is related to the brucite decomposition [110] and it mass variation increases gradually over time (Figure 5.6(a)). This peak appears more intense when increasing the MGO content to 10% (MG10), and its mass variation (Figure 5.6(a)). This confirms that brucite crystal growth is favored in solution rich in $[Mg^{2+}]$ [9, 88]. It also confirms the slower hydration kinetics observed for MG5 and MG10 in comparison to REF. A third peak is shown for all the studied mixtures and it is associated to the decomposition of portlandite that occurs between [450-550]°C [92]. Its mass variation varies from 3.6% and 5.5% at all ages for all the studied mixtures (Figure 5.6(b)). Finally, the decomposition of carbonates-containing phases (e.g. calcite, magnesian calcites, MgO carbonates, etc [119]) appears after 550°C for all the mixtures (Figure 5.5). Its mass variation is very small (between 0.9% and 2%) for all the studied mixtures (Figure 5.6(c)).

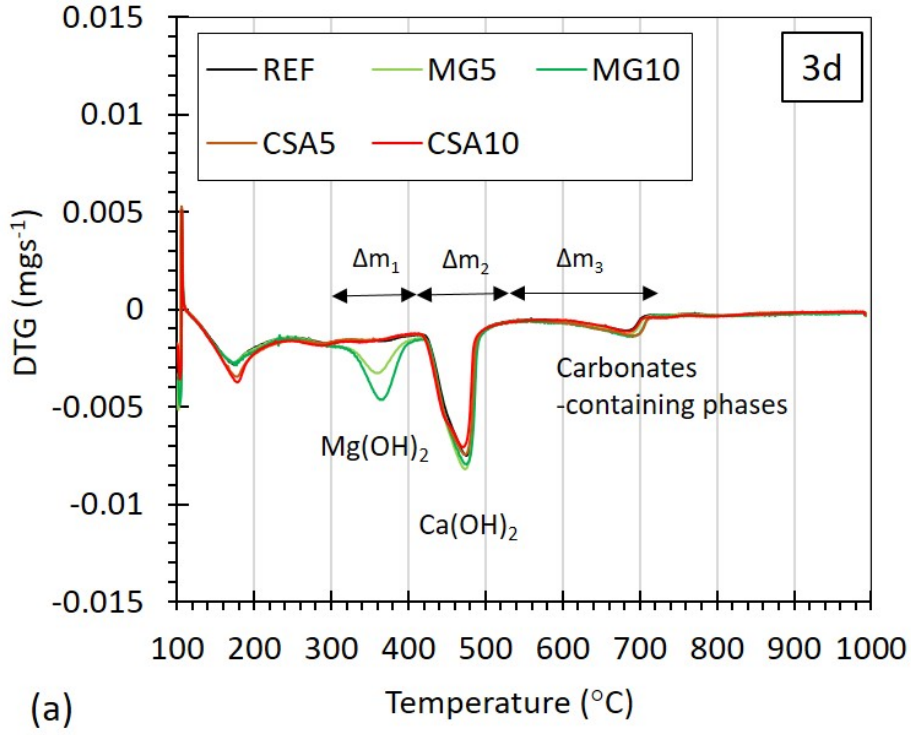
0.015
0.01
0.005
0
-0.005
-0.01
-0.015
DTG (mgs-1)
REF
MG5
MG10
CSA5
CSA10
3d
Δm1
Δm2
Δm3
Carbonates
-containing phases
Mg(OH)2
Ca(OH)2
100 200 300 400 500 600 700 800 900 1000
Temperature (°C)

(a)

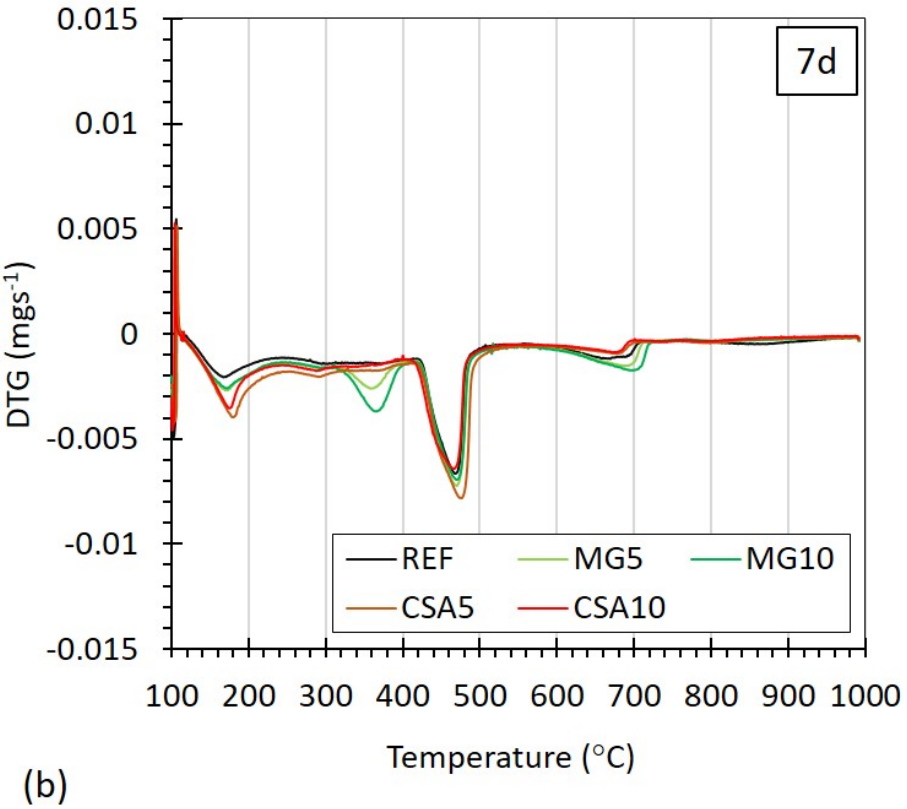
0.015
0.01
0.005
0
-0.005
-0.01
-0.015
DTG (mgs-1)
7d
REF
MG5
MG10
CSA5
CSA10
100 200 300 400 500 600 700 800 900 1000
Temperature (°C)

(b)

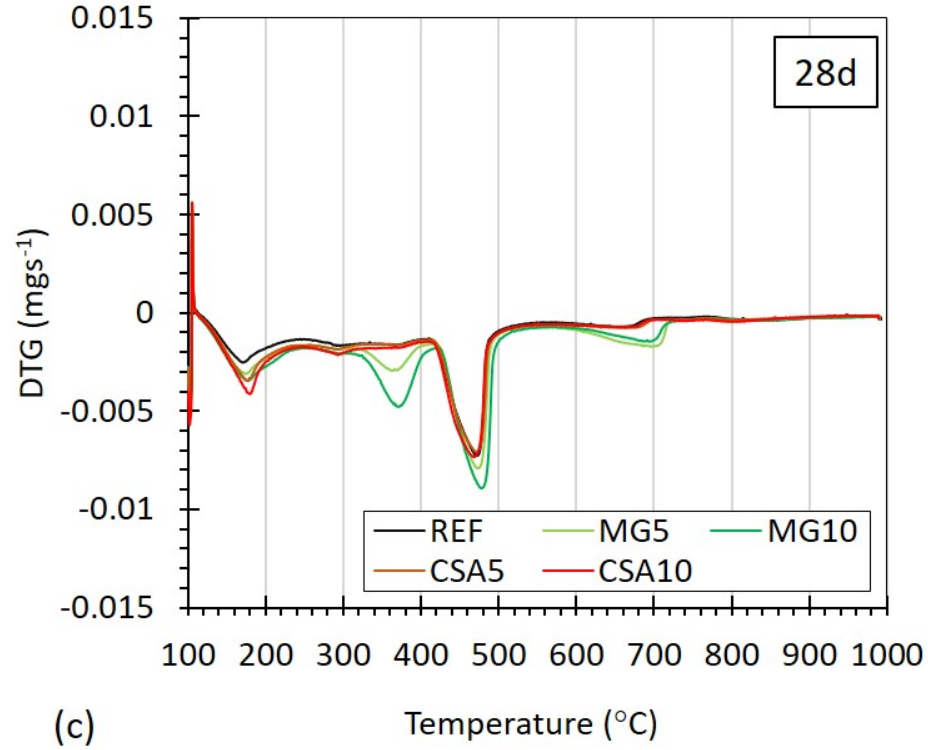

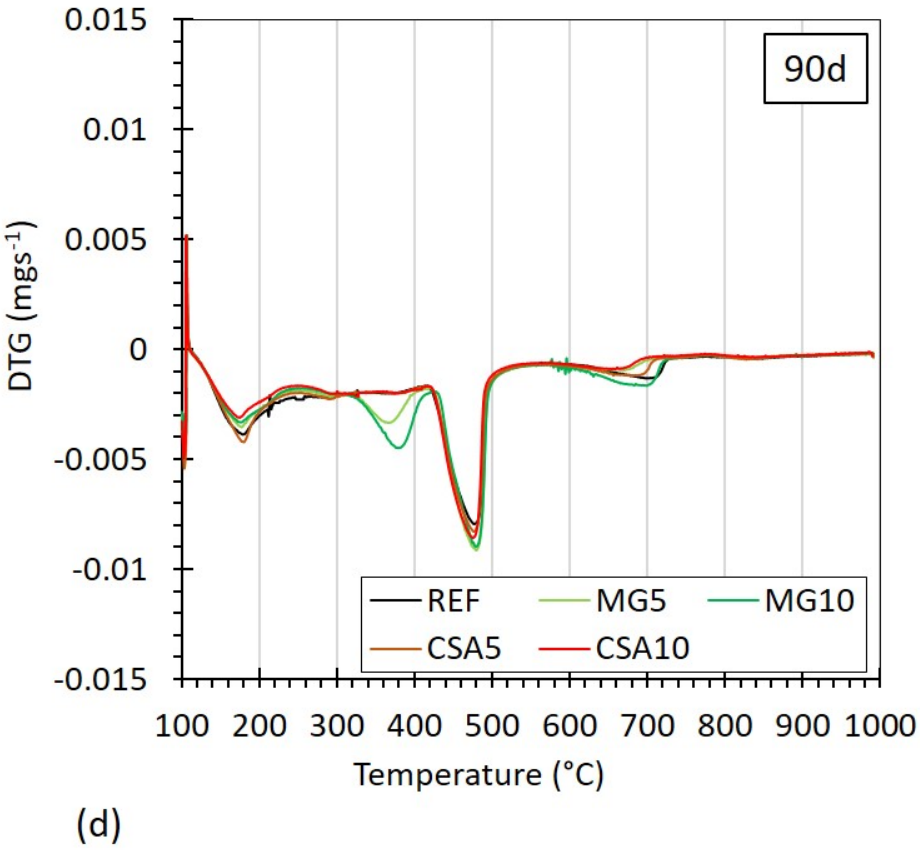

Figure 5.5 – DTG curves of the mixtures at 3 days (a), 7 days (b), 28 days (c) and 90 days (d).

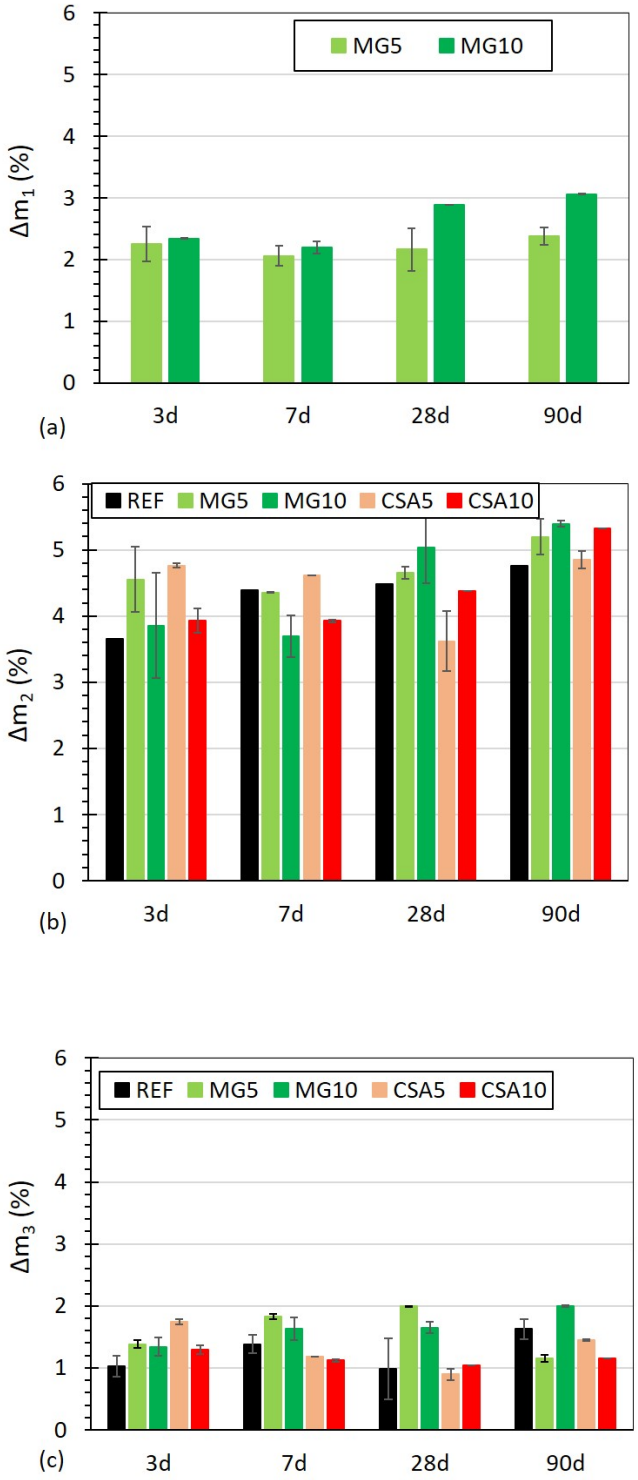

Figure 5.6 – Mass loss in the temperature range equal to [300-450]°C (Δm_1) related to brucite (a), [450-600]°C (Δm_2) related to portlandite (b) and [600-800]°C (Δm_3) related to carbonates-containing phases (c) at 3, 7, 28 and 90 days.

In order to clearly characterize the crystalline phases existing in the studied mixtures, XRD analysis was performed on paste because the quartz from mortar will interfere the results. So, paste of the same mixtures are proposed to analyze via XRD, and the water adsorption related to the sand was taken into account during calculation. But, firstly, it is important to determine if the degree of advancement of the hydration reaction for the paste mixtures is quite similar to that of mortars at 28 days. As shown in Figure 5.7, the pastes are characterized by similar peaks of mass losses in the following temperature ranges: [105-250]°C, [300-450]°C, [450-600]°C, [600-800]°C. Their values are also quite similar (Figure 5.8) as well as for the temperature ranges [105-1000]°C (Figure 5.9). So, the paste mixtures exhibit hydration behavior at 28 days quite similar to that of the mortar mixtures, which ensures that the XRD analysis done on the paste mixtures is valid in our case.

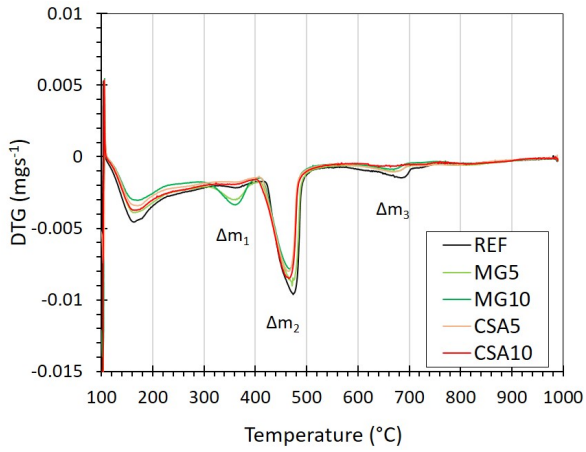

Figure 5.7 – DTG curves for paste mixtures at 28 days.

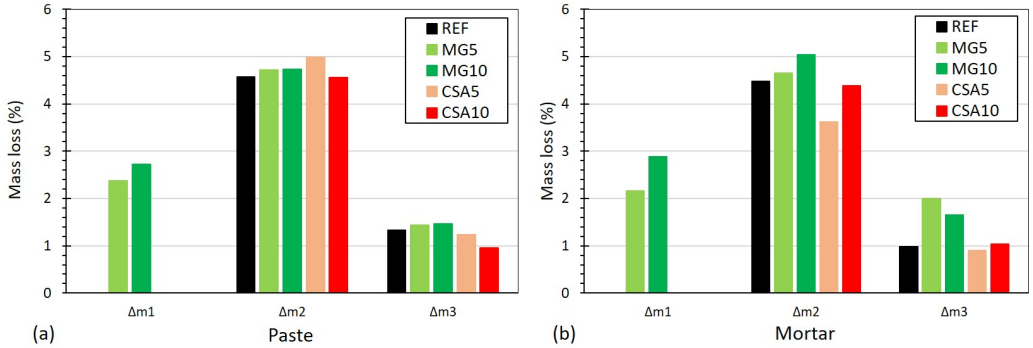

Figure 5.8 – Mass loss at 28 days in the temperature range equal to [300-450]°C (Δm_1), [450-600]°C (Δm_2) and [600-800]°C (Δm_3) for paste mixtures (b) and mortar mixtures (c).

The XRD results (Figure 1.11) show common phases between the studied mixtures such as: Ettringite (PDF #41-1451), portlandite (PDF #44-1481) and carbonates-containing phases (e.g calcite –PDF #5-586, dolomite –PDF #6-426 and magnesite –PDF #8-479).

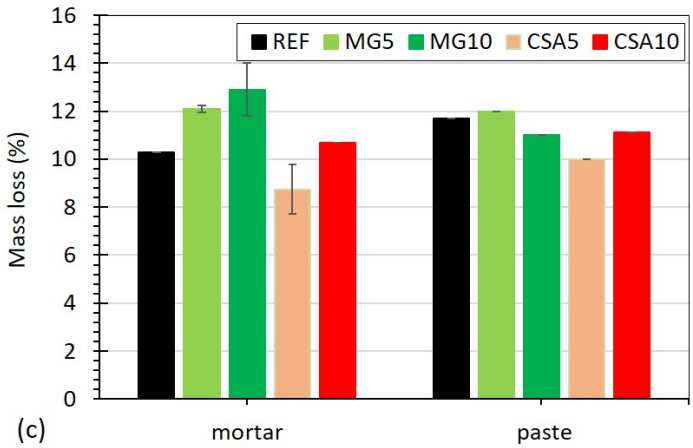

Figure 5.9 – Mass loss at 28 days in the temperature range equal to [105-1000]°C for mortar and paste mixtures (c).

The ettringite peaks found at 9.1°, 15.8°, 22.9° and 35° are more intense for mixtures containing CSA (CSA5 and CSA10) than for other mixtures. It confirms that the formation of ettringite is promoted in presence of CSA as explained earlier (§5.2.1). However, no monosulfoaluminate is detected for CSA5 and CSA10. It is probably related to the high sulfate content in these mixtures that favors the formation of ettringite rather than monosulfoaluminate [118]. It should be noted that the molar ratio of calcium sulfate over ye'elimite in CSA plays a key role in regulating the preference of hydration products in the matrix [118]. However, this molar ratio is not known for the CSA used in our study. Moreover, no anhydrous particles from the CSA (e.g. ye'elimite, calcium sulfate or calcium oxide) are found, which indicates that CSA hydration is complete before 28 days in CSA5 and CSA10. This explains that their mass losses in the temperature range [105-1000]°C that were quite close to REF after 28 days.

Some anhydrous particles are found in all the studied mixtures such as: Dicalcium silicate (C_2S –PDF #33-302) and tricalcium silicate (C_3S –PDF #31-301) and the intensity of their peaks is small. So, it indicates that the hydration process will continue after 28 days for all the studied mixtures. Moreover, anhydrous MgO (PDF #45-946) is found in mixture containing 5% MGO (MG5) at 42.9° and 62.3°. Their peak increases slightly with the addition of 10% MGO (MG10). These two peaks do not appear in REF, CSA5 and CSA10. Therefore, MG5 and MG10 exhibit an additional hydration capacity after 28 days more than other mixtures. It also explain their slightly higher mass losses in the temperature range [105-1000]°C than other mixtures.

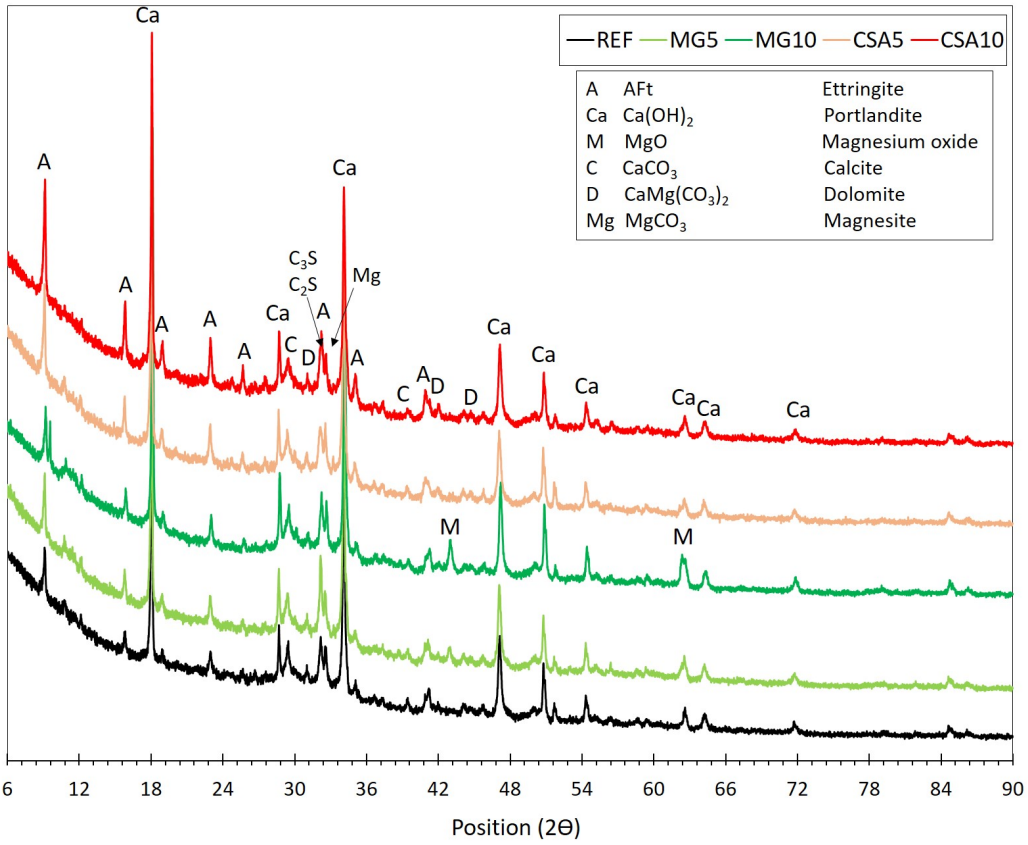

Figure 5.10 – XRD results for all the studied pastes.

5.2.3 Porosity

In order to study the effect of EA on the mortar's microstructure, the total porosity and the connectivity between the pores are determined for all the studied mixtures at 28 and 90 days. The volume of the mesopores is also determined at the pore radius ranging from 2 nm to 12 nm as well as the specific surface area for all the studied mixtures. The results are shown in Figures 5.11, 5.12 and 5.13 respectively.

After a drying at 40°C at 28d, the water porosity value of REF is equal to 14.3% (Figure 5.11(a)). At the same age, its intrinsic permeability coefficient is equal to $6.5E^{-17}$ m^2 (Figure 5.11(b)). The water porosity of mixtures with EA are slightly smaller (by 6%) compared to REF at 28d, except for MG10. In addition, the intrinsic permeability coefficient is smaller for all the mixtures containing EA (between 15% to 38%) compared to REF (Figure 5.11(b)). The addition of MGO and CSA forms additional brucite and ettringite respectively (§5.2.1), which might slightly decreases the mortar's porosity and the connectivity between the pores at 28d.

Thanks to the hydration advancement, the total porosity of all the mixtures slightly decreases at 90d. Similarly, the intrinsic permeability coefficient decreases at 90d for all the mixtures

(taking into account the standard deviations). So, these results indicate that the addition of 5% and 10% EA slightly decreases the total porosity and connectivity between the pores at 28d and 90d. From the gas permeability results, the Klinkenberg coefficient can be determined to obtain an information about the pore size. The results obtained are shown in Figure C.3 in Appendix C. However, no relevant information or conclusions can be drawn from this graph.

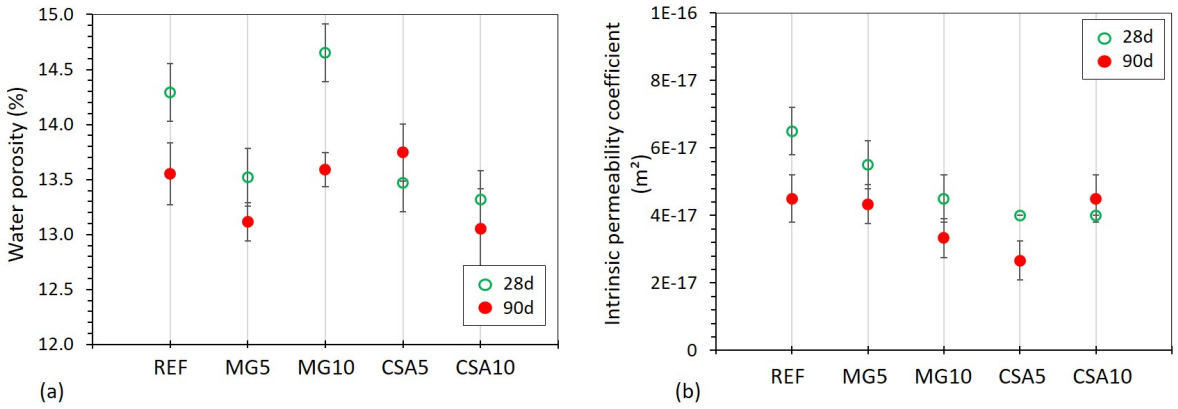

Figure 5.11 – Water porosity (a) and intrinsic permeability coefficient (b) for all the studied mixtures dried at 40°C.

The results of the mesopores volume and specific surface area are shown in Figure 5.12 and 5.13 respectively. The pore distribution curves as well as the cumulative pore volume for each mixture are presented in Appendix (C). At 3d, the volume of mesopores is between 2.2% and 3.1% for all the mixtures. This volume does not change significantly between 3d to 28d: it alternates between 1.8% and 3.1% for all the mixtures. Similarly, the S_{BET} values (Figure 5.13) alternate between 4.8 m^2/g and 8.8 m^2/g for the mixtures between 3d to 28d. At 90d, the mesopores volume slightly increases for REF (by 11%), while it increases significantly for MG5 and MG10 by 60% and for CSA10 by 40% compared to their mesopores volume at 28d. Meanwhile, the S_{BET} value of mixtures with EA is slightly smaller than that of REF at 90d. So, these observations indicate that the addition of EA does not significantly affect the mortar's porosity between 2 nm and 12 nm radius from 3 days to 90 days.

5.2.4 Summary

The main objective of this section is to evaluate the effects of adding EA on the hydration process and microstructure of the cement-based mortar. At early age, the cement-based mortar with MGO slows down the hydration process and increases the possibility of formation of additional hydration products (e.g. brucite). This behavior is more observed when the MGO content increases. An opposite behavior is shown by the cement-based mortar with CSA due to a fast hydration process at early age related to the formation of more ettringite. This behavior is more important when the CSA content increases. Brucite and ettringite are characterized by

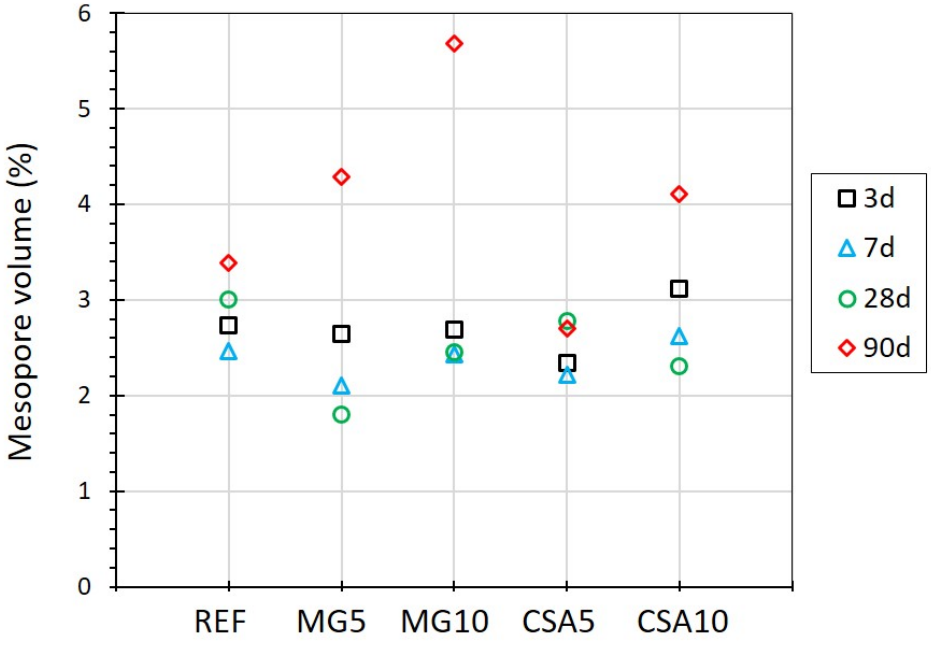

Figure 5.12 – Mesopore volume for all the studied mixtures at 3d, 7d, 28d and 90d.

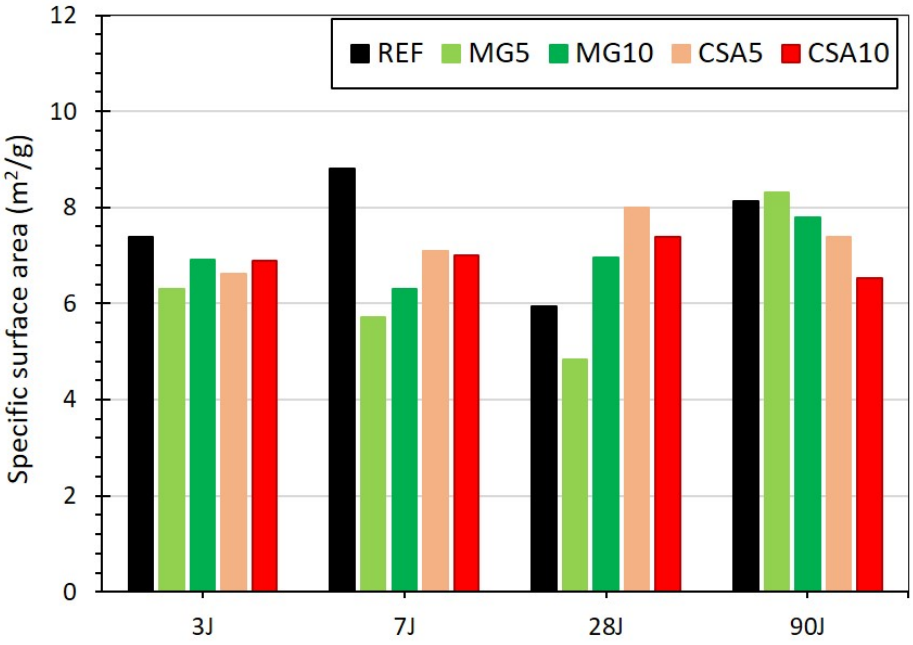

Figure 5.13 – Specific surface area S_{BET} derived from sorption analysis.

their swelling pressures in the pores. This mechanism can induce a swelling of the matrix at the macro scale, and therefore, promotes the self-healing process. Indeed, it can accelerate the closure of cracks over time, explaining the interest of adding EA.

At long term, the addition of EA (MGO and CSA) slightly reduces the porosity of the mortar. This is advantageous because finer porosity will require less products to generate macro-scale swelling. Additionally, the presence of C_2S and C_3S at 28 days increases the possibility of further hydration for all the mixtures. This mechanism can be further promoted by the addition of MGO which leads to the presence of additional anhydrous particles at 28 days (e.g. MgO). It also increases with increasing the content of MGO. Therefore, the results ensure the benefit of EA addition on the further hydration and matrix expansion mechanisms which may be promising for the self-healing process.

5.3 Mechanical properties and deformations of sound mortars with EA

As one of the main objectives of this research is to propose a repair mortar having mechanical performances adapted to the repair requirements (EN 1504-3) [10], the effects of EA on the mechanical performances have to be estimated. Firstly, the compressive strengths are determined at several ages and compared to the strength classes available for repair with cementitious materials. Secondly, parameters affecting the cracking sensitivity of the repair mortar when its delayed deformations are restrained by a support, are studied: flexural strength, dynamic Young's modulus and delayed deformations. For this last parameter, three curing conditions are investigated: autogenous curing, Water Curing "WC" and Cycle Curing "CC". These results will also give us an information on the swelling capacity of these mixtures to improve crack healing. In addition, drying can also affect the response of the repair material. For this purpose, shrinkage under drying condition (at 20°C and 60% RH) is also studied and the first results are given in Figure C.5 in Appendix C. Finally, all these parameters are coupled using a crack sensitivity index to compare the cracking risk of the studied mixtures.

5.3.1 Mechanical properties

The evolution of the mortars' mechanical strengths (flexural and compressive strength) are determined at 3, 7, 28 and 90 days and the results are presented in Figures 5.14 and 5.16.

During the first week, REF presents the highest compressive strength "f_c" (Figure 5.14) characterized by a value equal to 60 MPa at 7d. The "f_c" of REF are higher than those of MG5 by about 3% to 15% during the first week (56 MPa at 7d). Similarly, the addition of 5% CSA (CSA5) results in a significant reduction (by 30%, 37 MPa) in its compressive strength at 1d (26

MPa) in comparison to REF. But this reduction is progressively reduced and the compressive strength of CSA5 is similar to that of REF at 7d (60 MPa). Increasing the EA content to 10% (BM10 and BC10) results in a higher reduction in compressive strength (between 15% and 40%) compared to REF during the first week (50 MPa for MG10 and CSA10 at 7d). Due to the partial replacement of cement by 5% EA, the formation of C-S-H gel is reduced. This phenomenon is more important when increasing the EA content to 10%. Indeed, the addition of MGO and CSA leads to the formation of more brucite and ettringite respectively (§5.2.1) and less C-S-H gel [65,86,115]. Hence, the reduction in early age strength in the presence of EA could be attributed to the weaker chemical bonding (double bonding) presented by the brucite and ettringite when compared to the Van der Waals bonding presented by the C-S-H gels.

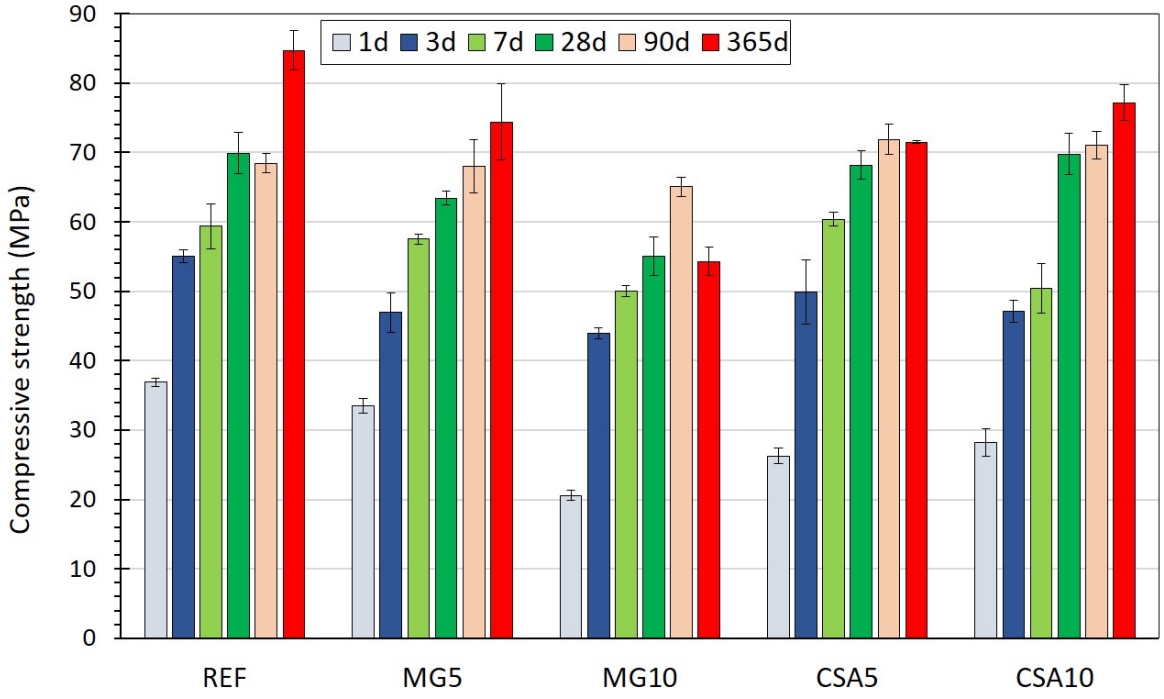

Figure 5.14 – Compressive strength evolution for all mixtures at 1, 3, 7, 28, 90 and 365 days.

On the other hand, all the mixtures present an increase in their compressive strength as a function of time except for MG10 at 365d. At 28 days, REF increases its compressive strength to 70 MPa till finally achieving the highest value (85 MPa) at 365d. The compressive strength of MG5 is 10% smaller than that of REF at 28d (63 MPa). The same behavior is observed beyond this age. However, the porosity of MG5 is slightly smaller than that of REF at 90d due to the continuous brucite formation as explained previously. The brucite is weaker than C-S-H. In addition, it could exhibit swelling pressures in the confined matrix as it continues to form over the long term and could exhibit poor matrix volume stability [8]. Indeed, this behavior is observed when increasing the MGO content to 10% (MG10). This mixture is characterized by

a drop in its compressive strength (smaller by 36% compared to REF at 365d) and the smallest f_c value at 1 year (54 MPa). On the other hand, the compressive strengths of the mixtures with CSA (CSA5 and CSA10) are quite close to those of REF at 28d and 90d (around 70 MPa). But at 1 year, their compressive strengths do not evolve significantly. They are smaller by 16% (71 MPa) and 9% (77 MPa) respectively due to the ettringite formed in these mixtures, which is weaker than the C-S-H [83, 86].

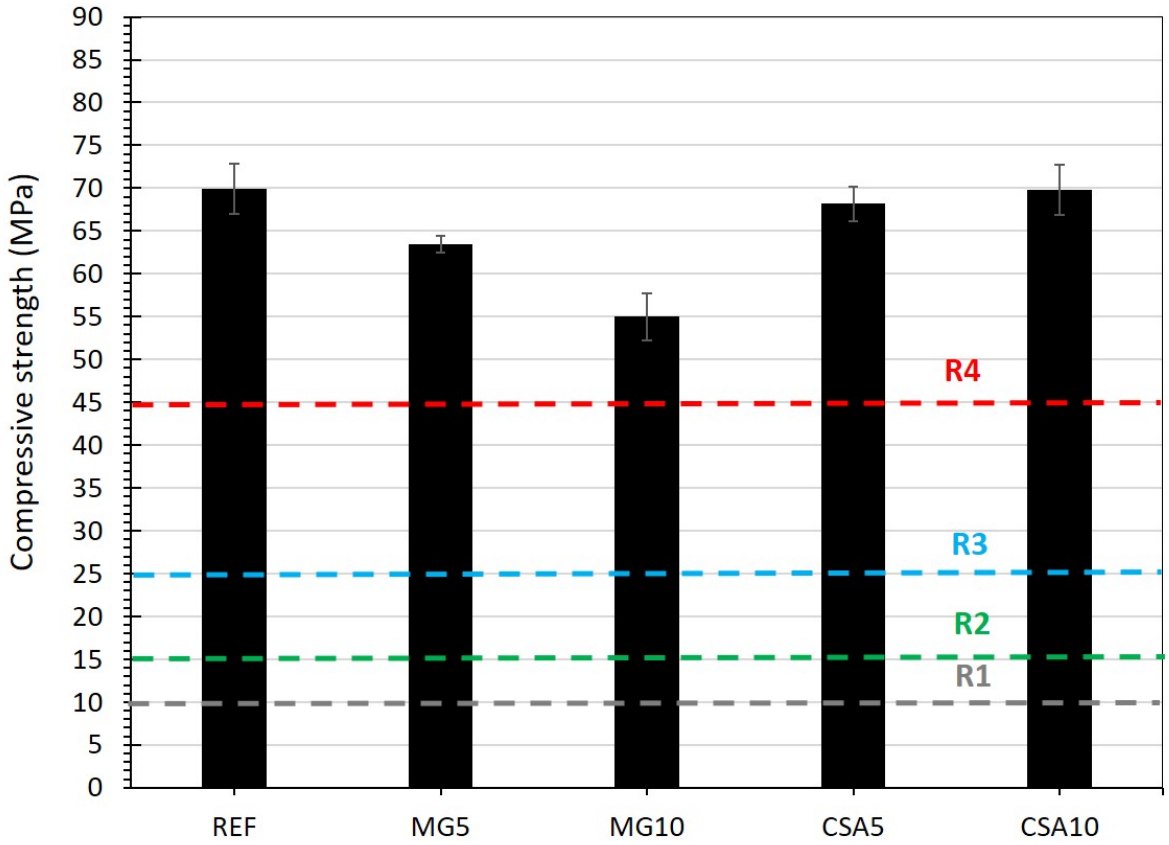

Figure 5.15 – Compressive strength at 28 days for all the studied mortars and the EN 1504-3 standard requirements: non structural (R1 $\geq$ 10 MPa and R2 $\geq$ 15 MPa) and structural (R3 $\geq$ 25 MPa and R4 $\geq$ 45 MPa) element.

Regardless of the different impacts shown by the addition of EA on the mortar's 28-day compressive strength, this strength is acceptable and comply with the requirements of the European standard "EN 1504-3" as shown in Figure 5.15. The EN 1504-3 standard proposes two requirements to identify the strength class for the tested mortar: non-structural (R1 and R2) and structural (R3 and R4) element. The mortars studied in this chapter are all classified in class R4 ($\geq$ 45 MPa).

The flexural strength "f_f" (Figure 5.16) of REF is equal to 7 MPa at 1d. Its value increases continuously until 10.2 MPa at 28d. Beyond this age, the flexural strength of REF slowly

improves until it reaches the highest value (11.2 MPa) at 365d. The addition of 5% MGO (MG5) decreases the flexural strength during the first week. Beyond this age, f_f of MG5 is quite constant around 9 MPa which is 19% inferior to REF's flexural strength at 365d. The increase in MGO content to 10% (MG10) amplifies the flexural strength reduction and MG10 is characterized by a drop in its flexural strength and the smallest value (7 MPa) at 365d. As the hydration advancement continues for the mixtures containing MGO, these observations confirm that brucite crystals are responsible for the strength reduction of the material. When there is no more space available in the pore for the new brucite crystals, the latter induces expansions and leads to a poor volume stability of the matrix [8]. This behavior will further increase the possibility of micro-cracks in the confined matrix and results in a drop of its strengths [8,86,88].

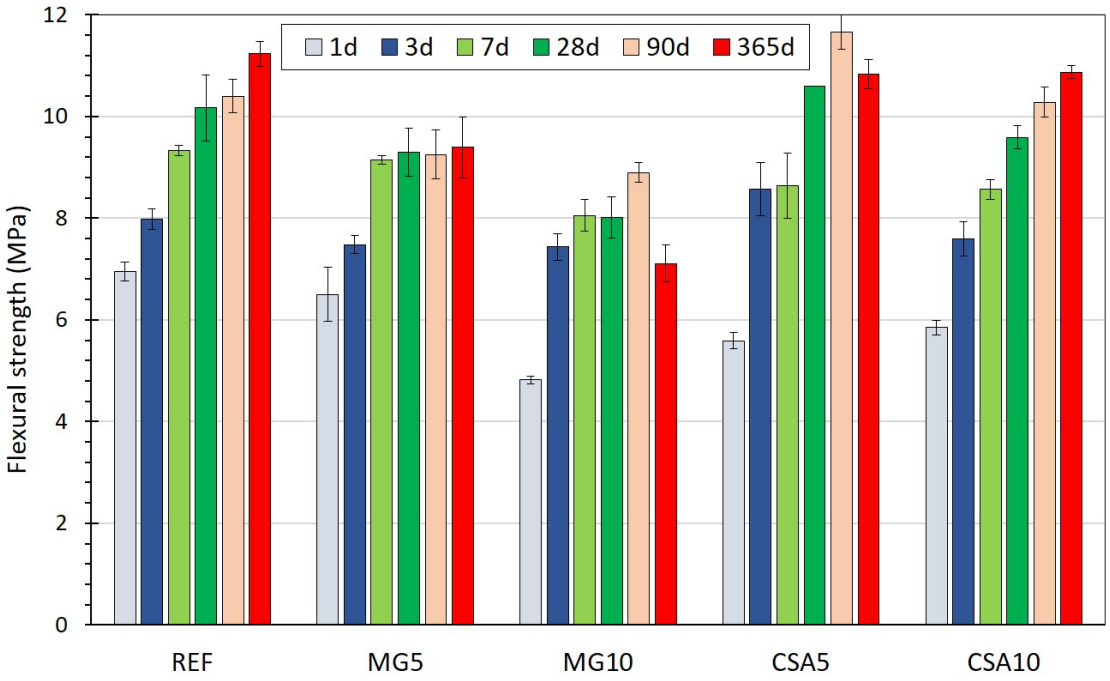

Figure 5.16 – Flexural strength evolution for all mixtures at 1, 3, 7, 28, 90 and 365 days.

On the other hand, the addition of CSA (CSA5 and CSA10) decreases the flexural strength at 1d (5.6 MPa and 5.8 MPa respectively) by 20% and 18% respectively in comparison to REF (7 MPa). Beyond this age, CSA5 and CSA10 gradually recover their flexural strength: CSA5 shows a higher strength than REF at 28d (10.6 MPa) and 90d (11.7 MPa), but it decreases at 365d (10.8 MPa) until it reaches a value 4% smaller than that of REF (11.2 MPa). CSA10 shows a continuous evolution of the flexural strength with values slightly smaller than those of REF. CSA10 is finally characterized by a flexural strength (10.9 MPa) 3% smaller than that of REF at 365d. The difference in mechanical behavior between the mixtures with MGO and those with CSA is due to their hydration characteristics. The addition of MGO leads to the formation of expansive brucite until the long term, while the formation of ettringite due to

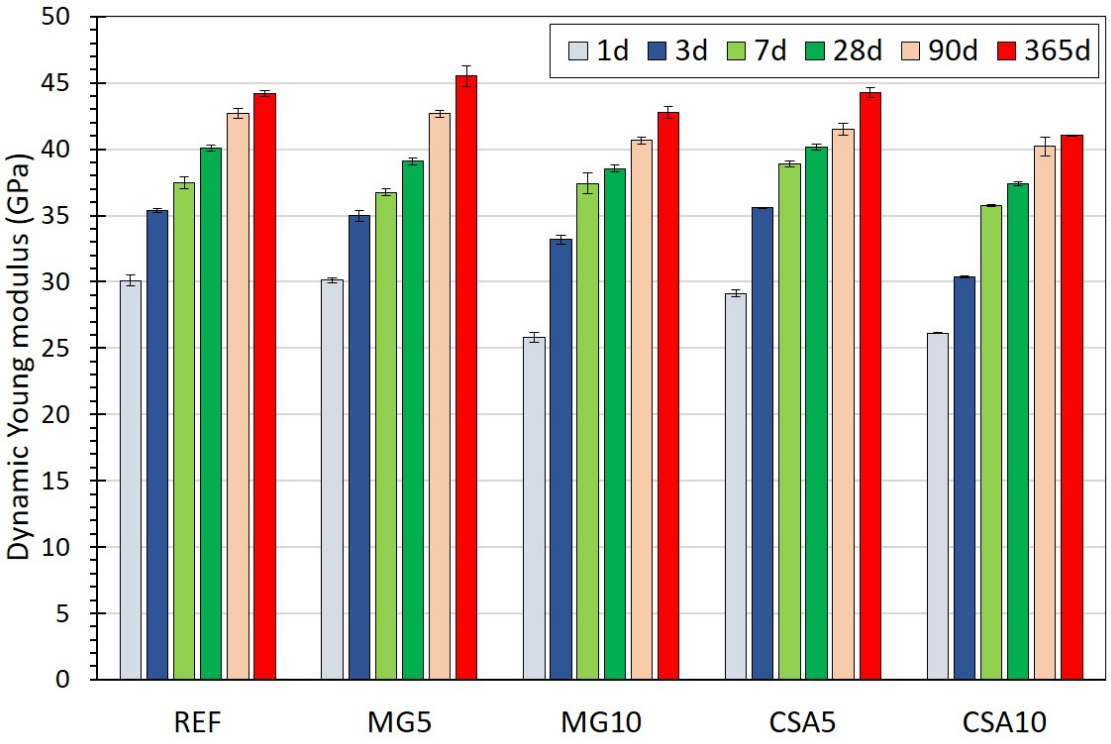

Figure 5.17 – E_{dyn} evolution for all mixtures at 1, 3, 7, 28, 90 and 365 days.

the CSA addition is complete before 28 days (§5.2.2). Although both hydration products are characterized by expansive behavior, the risk of new ettringite formation is lower than that of brucite. Therefore, CSA5 and CSA10 do not appear to exhibit poor volume stability of their matrices over time. This allows these mixtures to have higher compressive and flexural strengths than MG5 and MG10.

The dynamic Young's modulus Edyn (Figure 5.17) is quite similar at 1 day for REF, MG5 and CSA5 (around 30 GPa). The increase in EA content reduces its value. At 7 days, Edyn is quite similar for all the studied mixtures (around 37 GPa). At long term, mixtures with 5% of EA present the higher dynamic Young's modulus value (45 GPa and 44 GPa for MG5 and CSA5 respectively) close to that of REF (44 GPa). The lower Edyn value are presented by the mixtures with 10% of EA (43 GPa and 41 GPa for MG10 and CSA10 respectively).

5.3.2 Autogenous deformation

The results of autogenous deformation and Internal Relative Humidity (IRH) are presented in Figure 5.18 for all the studied mixtures. The mass variation of all the specimens is smaller than 0.02% (Appendix C). This confirms the autogenous conditions of the specimens. The evolution of the autogenous deformation as a function of log(IRH) is shown in Figure C.7 in Appendix C.

The REF's shrinkage evolves fast during the first 7 days and it reaches a deformation equal to -324 µm/m at this time (Figure 5.18(a)). During the same period, its IRH decreases very rapidly (Figure 5.18(b)) and presents the lower value during all the hydration process (84% at 7 days). From 28 days, the REF's shrinkage leads to a constant value (about -450 µm/m), and its IRH (84%). The addition of 5% EA reduces the autogenous shrinkage. Indeed, MG5 is characterized by a smaller autogenous shrinkage (-72 µm/m at 7 days) and higher IRH (92% at 7 days) compared to REF during the first week. It is related to the additional brucite formation in MG5, which requires a smaller water content than C-S-H and increases the IRH. This is in agreement with the Kelvin law, and thus, decreases the autogenous shrinkage for MG5. The addition of 5% CSA (CSA5) reduces the autogenous shrinkage (-165 µm/m at 7 days) and its IRH evolution is close to that of MG5 during the first week (92% at 7d). But, CSA5 shrinks faster than MG5. The hydration of CSA is fast and produces ettringite at early age, reducing the autogenous shrinkage of CSA5 at this time. Whereas the hydration of MGO is slow (Figure 4.5) and continues to form brucite in the long term. This behavior accelerates the reduction of autogenous shrinkage and MG5 is characterized by a quite constant autogenous shrinkage beyond 20 days (-105 µm/m) and its IRH decreases slowly (89% at 20 days). While CSA5 continues to shrink until 28 days (-300 µm/m). Then, its shrinkage and IRH are quite constant around -315 µm/m and 90% respectively beyond 28 days.

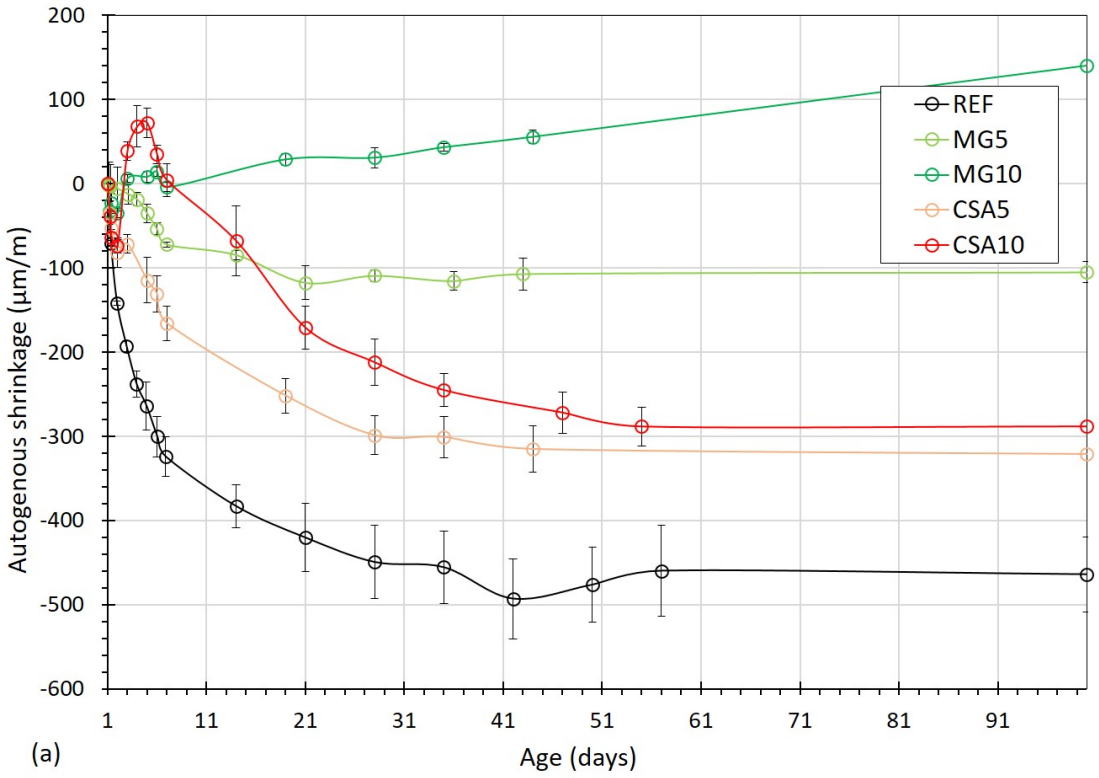

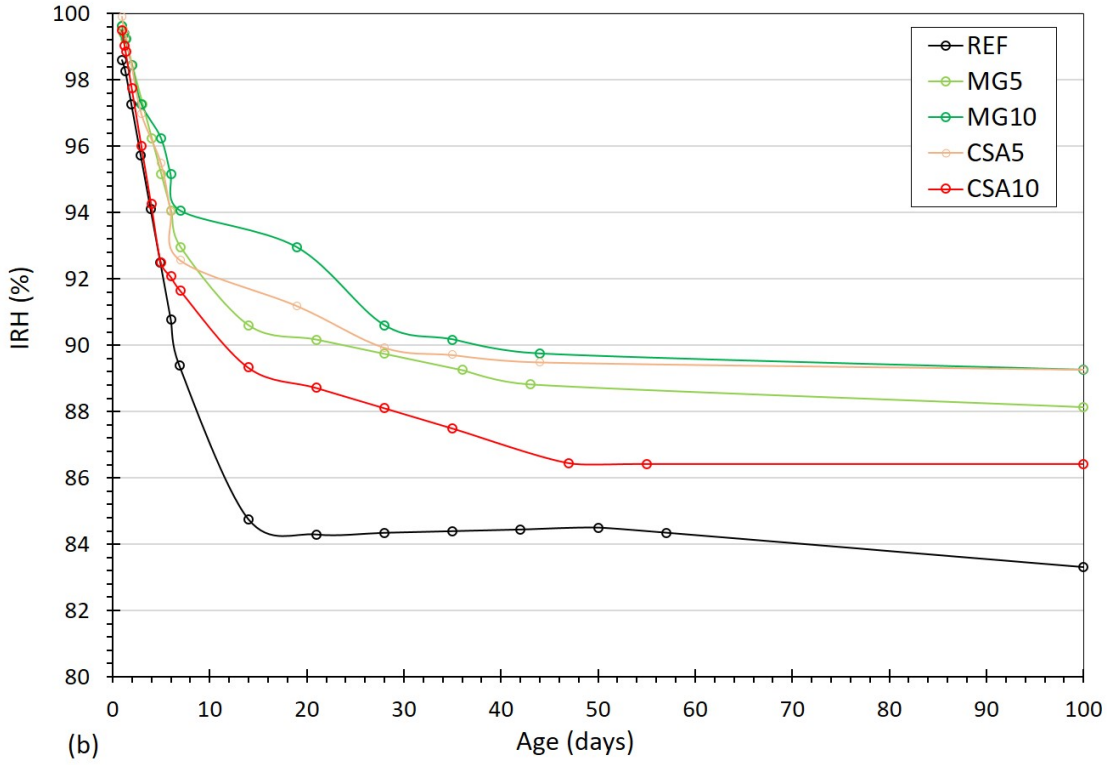

Figure 5.18 – Evolution of the autogenous deformation (a) and the IRH (b) for all the studied mixtures.

The increase in EA content allows balancing the autogenous shrinkage from the third day. Indeed, MG10 shrinks very little during the first two days. Its autogenous shrinkage is cancelled at 3 days and the matrix starts to swell after this age reaching a value equal to +4 µm/m at 7 days. Its IRH is close to that of MG5 during the first week. After, MG10 continues to swell rapidly and reach 30 µm/m at 28 days and more than 100 µm/m at 100 days. So, the increase in MGO content to 10% increases the formation of brucite which reduces the autogenous shrinkage faster thanks to a swelling of the matrix. On the other hand, CSA10's autogenous shrinkage evolve similarly to CSA5 during the first two days. In the period between 2 and 5 days, the initial autogenous shrinkage of CSA10 is followed by swelling with amplitude equal to +53 µm/m. Meanwhile, its IRH decreases rapidly and it is close to that of REF (92%). It is probably related to the excessive ettringite formation when 10% CSA is added to the mixture, which requires a large amount of water and generates a swelling of the matrix. After, CSA10 shrinks rapidly and reaches a shrinkage value equal to -212 µm/m at 28 days and -300 µm/m at 100 days. Its IRH continues to decreases but it is higher than that of REF (88% at 28 days and 86% at 100 days). This is probably due to the consumption of the CSA hydration at early age, which limits the formation of new ettringite phases at later ages.

5.3.3 Total deformation

The results of the total deformation are presented in Figures 5.19 and 5.20. All the mixtures are kept in the humidity room (RH = 95%) before 28 days. At two days, the specimens show a mass loss smaller than 0.5% at 2 days (Appendix C). This mass loss is due to the hydric exchanges between specimens and their environment (humidity room). After, they gradually start to regain their mass.

REF shrinks rapidly during the first 7 days (-330 µm/m) (Figure 5.19). After, its shrinkage decreases very slowly and reaches -280 µm/m at 28 days. The addition of 5% EA (MG5 and CSA5) reduces the shrinkage of the matrix. MG5 shrinks slowly during the first week and reaches a deformation equal to -150 µm/m at 7 days. Whereas CSA5 is characterized by a low shrinkage at 1 day (-16 µm/m), then its shrinkage is cancelled beyond this age thanks to a rapid swelling of the matrix (+54 µm/m at 7 days). In a very humid environment (RH=95%), the hydration of the CSA is very fast compared to the slow hydration of the MGO. Ettringite causes swelling pressures within the matrix, allowing for rapid reduction in its total shrinkage at early age. After 7 days, MG5 continues to decrease significantly its total shrinkage (-29 µm/m at 28 days) at a faster rate than CSA5 (+150 µm/m at 28 days). This phenomenon is related to the continuous formation of brucite by MGO hydration. Increasing the EA content to 10% (MG10 and CSA10) further accelerates the shrinkage reduction and the matrix expansion. Indeed, MG10 balances its shrinkage from the first day (+30 µm/m), and reaches a swelling value equal to +148 µm/m at 5 days. This is related to the excessive brucite formation due to the high MGO content [74]. While CSA10 is characterized by a low shrinkage at 1 day (-70 µm/m). Its shrinkage is cancelled beyond this age thanks to a swelling of its matrix (+162 µm/m at 5 days), with a slightly faster rate than MG10. After 5 days, both mixtures continue to swell, but the swelling kinetic is higher for MG10 than for CSA10. They reach swelling values equal to +500 µm/m and +320 µm/m respectively. This difference in behavior is related to the formation of ettringite which is faster at an early age, but slow in the long term, compared to the progressive formation of brucite over time [83, 86].

The same total deformation behaviors of these mixtures can be observed in Figure 5.20. The trends of the curves in Figure 5.20 are very similar to those in Figure 5.19 before 28 days, as all specimens were kept in the same humidity room (RH = 95%) before this age.

After WC (beyond 28 days) (Figure 5.19), the REF's total deformation does not change significantly. It can be seen in Figure 5.21 that the swelling of REF is quite negligible beyond 28 days (28d + 0d in WC). While the addition of 5% EA slightly promotes the continuous swelling for MG5 and CSA5. Meanwhile, the swelling behavior is more significant for the mixtures containing higher EA content (10%), and is faster for MG10 than for CSA10. These observations confirm the finer porosity exhibited by the mixtures containing EA compared to

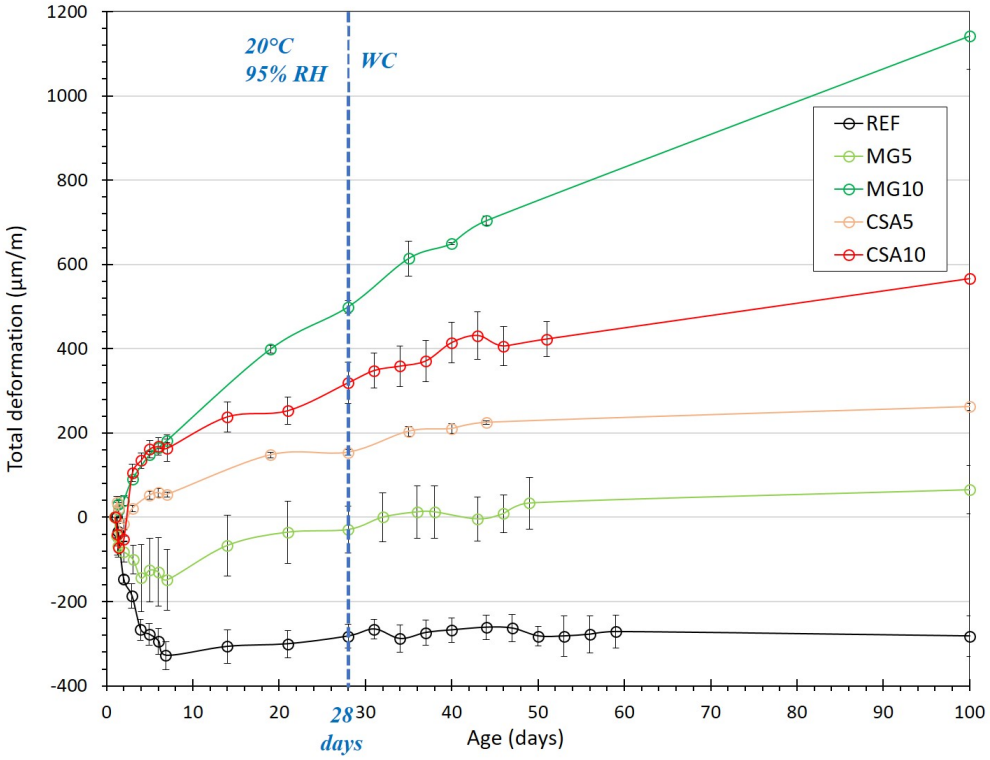

Figure 5.19 – Evolution of the total deformation for specimens kept in WC condition.

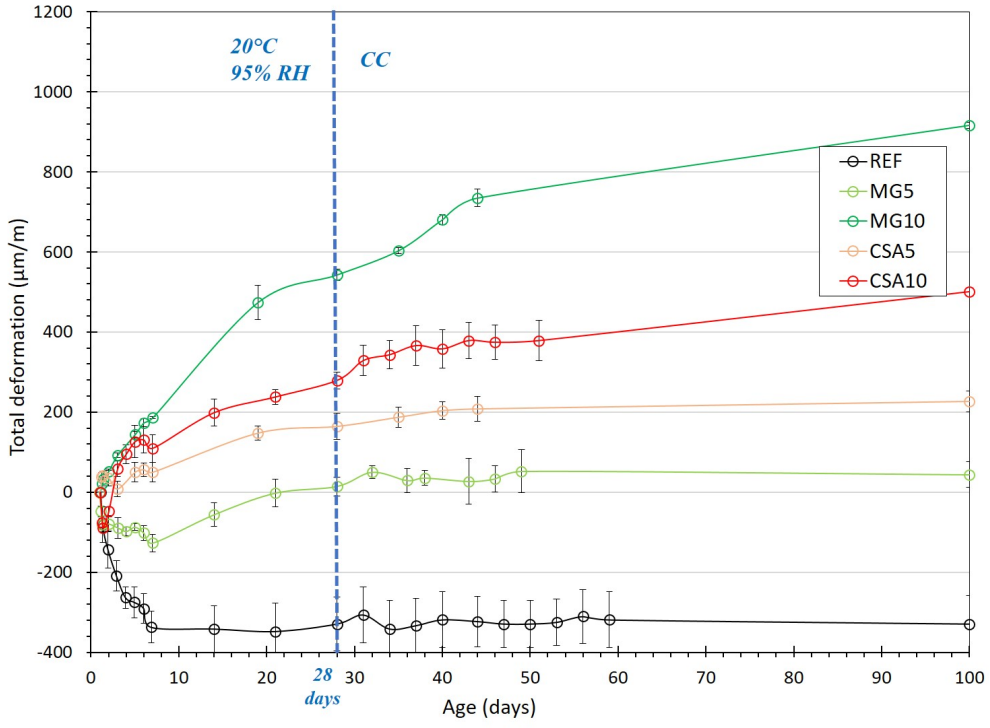

Figure 5.20 – Evolution of the total deformation for specimens kept in CC condition.

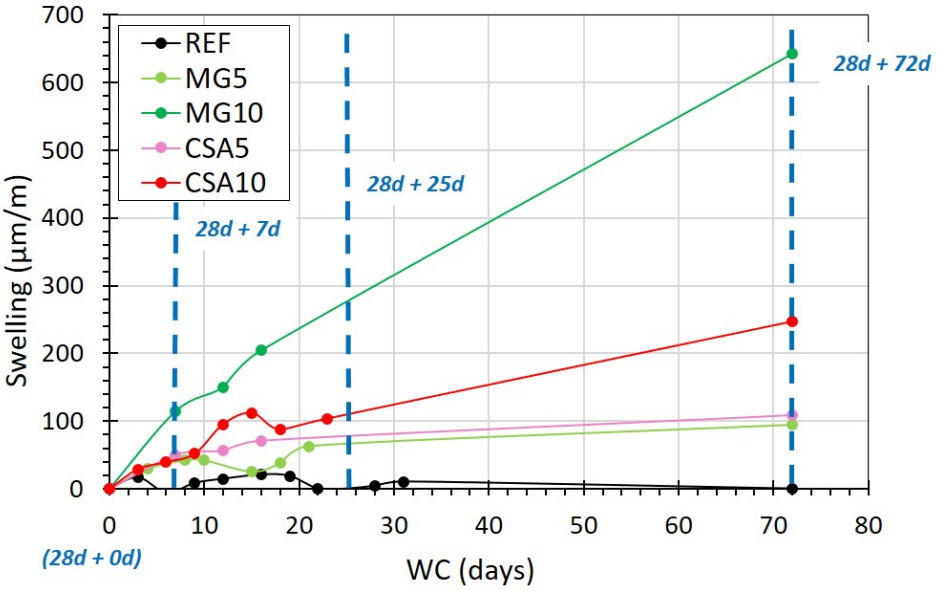

Figure 5.21 – Swelling values for all the studied mixtures from 28 days of WC.

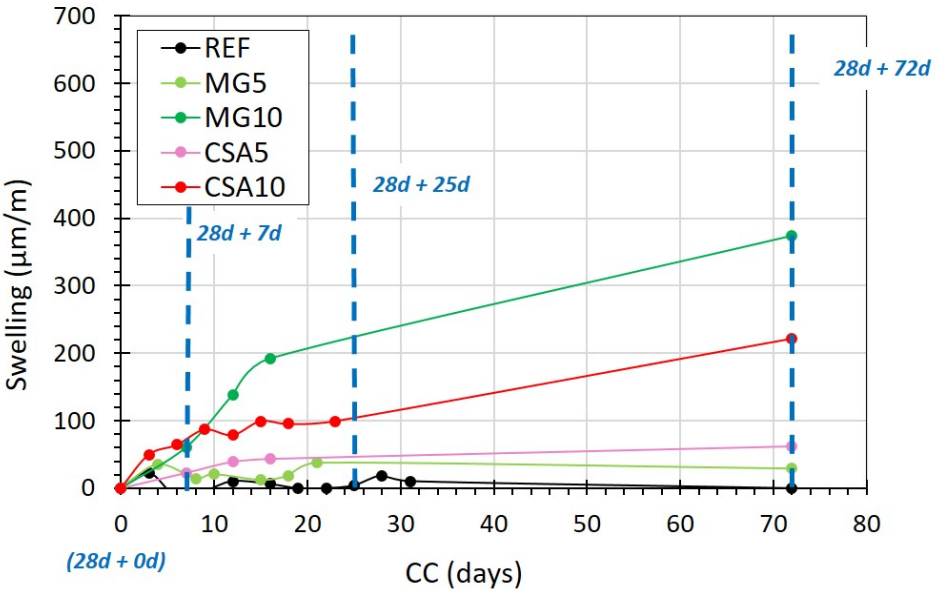

Figure 5.22 – Swelling values for all the studied mixtures from 28 days of CC.

REF. This indicates that the newly formed hydration products exhibit swelling pressures in the pores, which translates into a matrix swelling.

Similar observations can be seen when the specimens are cured in CC after 28 days (Figure 5.22). However, the swelling rate is smaller for all mixtures due to the drying cycles (RH = 95% at 20°C) that slightly reduce the continuous hydration for all mixtures.

5.3.4 Cracking sensibility

In order to estimate the sensitivity to cracking under restricted autogenous deformation conditions, the Cracking Sensitivity Index (CSI) is calculated by combining several mechanical properties: autogenous deformation, flexural or compressive strength and dynamic young modulus. The second mechanical properties are used as they allow estimating the tensile or compressive stresses that can occur as a result of restricted or swelling deformations respectively. The third mechanical property is used as it can affect the magnitude of stresses associated with autogenous deformation. Thus, a higher value of this index indicates a more important cracking sensitivity of the studied material. If the index reaches a value equal to 1, cracking should occur under fully restrained conditions. Nevertheless, this index does not take into account the beneficial effect of relaxation (decrease of internal stresses) which varies according to the studied material. The CSI for all the studied mixtures is presented in Figure 5.23 at 3d, 7d, 28d and 90d.

The addition of 5% MGO (MG5) significantly decreases the CSI: it is constant and smaller than 0.1 at early age and long term. This behavior is improved by increasing the MGO content to 10% (MG10): the CSI of MG10 is nearly zero until 28 days, and increases to 0.07 at 90d. These results indicate the safety of adding 5% and 10% MGO which significantly improves the cracking sensitibity of the cement-based mortar in a restricted autogenous condition. Similarly, the addition of 5% CSA decreases the CSI during the first week (0.57 at 7d) by 45% compared to REF. This behavior continues to the long term: the the CSI of CSA5 is 34% smaller than that of REF at 90d. The increase in CSA content to 10% (CSA10) decreases significantly the CSI during the first week, and CSA10 presents a similar CSI to that of CSA5 at 90d. The CSI value of these mixtures is slighlty higher than 1 at 90d. Although, this index does not take into account the beneficial effect of relaxation. Thus, these results ensure the safety of adding 5% and 10% CSA to improve the cracking sensitivity of the cement-based mortar in a restricted autogenous condition.

In order to evaluate the behavior and the cracking sensitivity of the cement-based mortars in a restricted condition, the evolution of their restricted deformations are determined using an autogenous ring test (Figure C.9 in Appendix C). The first results are presented in Figure C.10 in Appendix C. The graph shows that no cracks are detected for all the studied mixtures after 28 days, even up to 80 days for some mixtures (MG5 and MG10). For future work, the

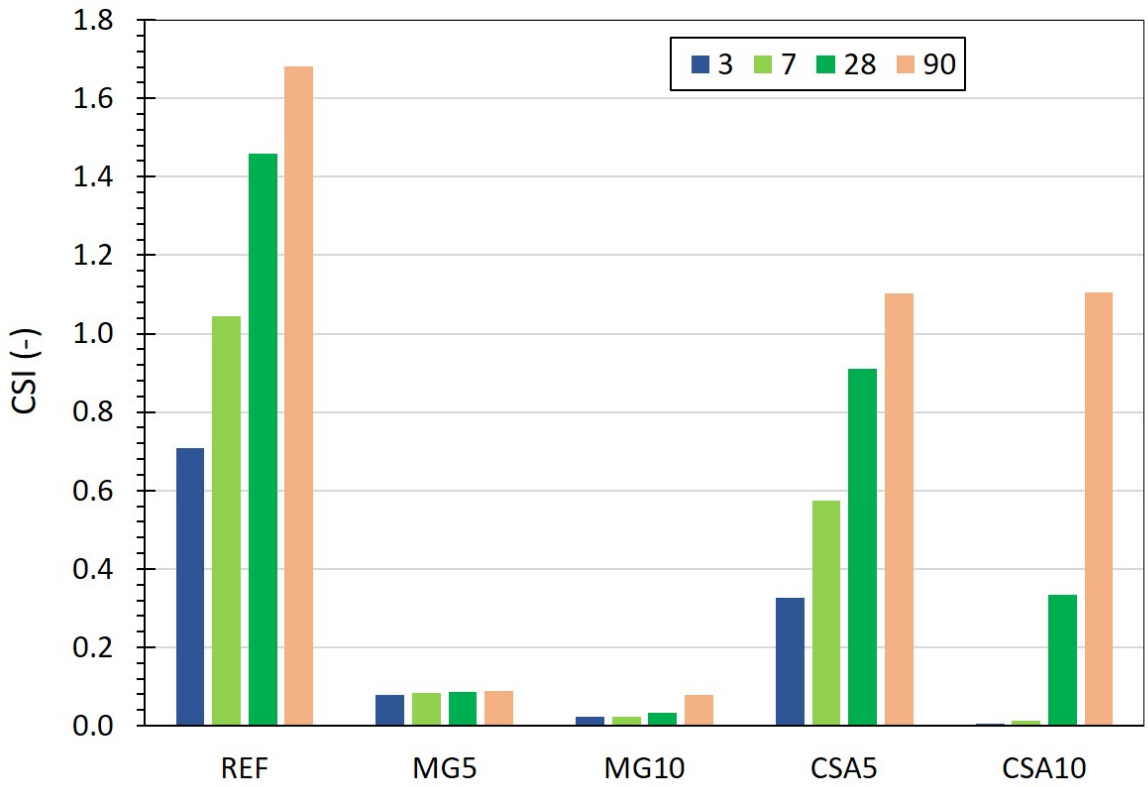

Figure 5.23 – Evolution of the Cracking Sensitivity Index (CSI) for all the studied mixtures.

restricted deformations of the mortars will be determined using a ring test under ambient conditions.

5.3.5 Summary

The main objective of this section is to evaluate the benefits of EA on the mechanical properties of cement-based mortar. The addition EA slightly decreases the compressive strengths of the mortar at early age and in the long term. However, despite this decrease, all the proposed mixtures have high compressive strengths at 28 days (greater than 45 MPa - Class R4), which confirms their compliance with the repair requirements. Furthermore, the addition of EA to the cement-based mortar significantly improves its cracking sensitivity in a restricted autogenous condition. Thus, cement-based mortar with EA constitute a promising mortar that can be used for repair application and limit the cracking sensitivity. Furthermore, the addition of EA increases the long-term swelling behavior of the mortar, which is a preferable mechanism to allow for autonomous healing.

5.4 Self-healing capacity

The self-healing capacity is evaluated through a crack width monitoring on the specimen surfaces (2D measurement) and a water permeability testing (3D measurement). To determine the healing kinetics, these measurements are performed on cracked specimens at the cracking age (0D), and after several curing duration: 7 days (7D), 25 days (25D) and 112 days (112D). As for the total deformation, the specimens are cured under Water Curing (WC) and Cycles Curing (CC). Moreover, the main healing products are identified on the crack surface and into the crack.

5.4.1 2D monitoring

For the different studied mixtures, the average residual Crack width "CW" obtained after the splitting test (at 0D) varies from 183 µm to 267 µm for the specimens kept under WC (Water Curing) and from 182 µm to 252 µm for the specimens kept under CC (Cycle Curing) respectively (Table 5.2). The evolution of CW as a function of their initial values (at 0D) is shown in Figure 5.24 for all the studied mixtures.

Table 5.2 – Average residual crack width (CW) measured after the splitting test at 0D.

Mixture	CW (μm)	
	WC	CC
REF	267 ± 25	248 ± 54
MG5	254 ± 4	241 ± 70
MG10	183 ± 34	190 ± 33
CSA5	213 ± 31	252 ± 2
CSA10	190 ± 72	182 ± 35

The kinetics of crack healing is influenced by the mixture and the initial CW. Indeed, in WC condition: mixtures with EA show complete healing of the majority of CW in the range [50-250] µm after 25 days (Figures 5.24(c, e, g, i)). In contrast, the majority of these CW heal after 112 days for REF (Figures 5.24(a)). Under CC condition: it appears that a larger number of CWs are healed after 25 days for all the studied mixtures (Figures 5.24(b, d, f, h, j)). The regular contact between the crack-water-CO_2 during CC condition, allows for the supplementary formation of carbonates on the crack surface, which further decreases the crack width [34, 120]. Furthermore, mixtures with EA (Figures 5.24(d, f, h, j)) show faster and higher crack healing than REF for CW in the range of [350-450] µm at 112D when kept under CC. Therefore, the addition of EA to cement-based mortar appears to increase the healing potential of large cracks.

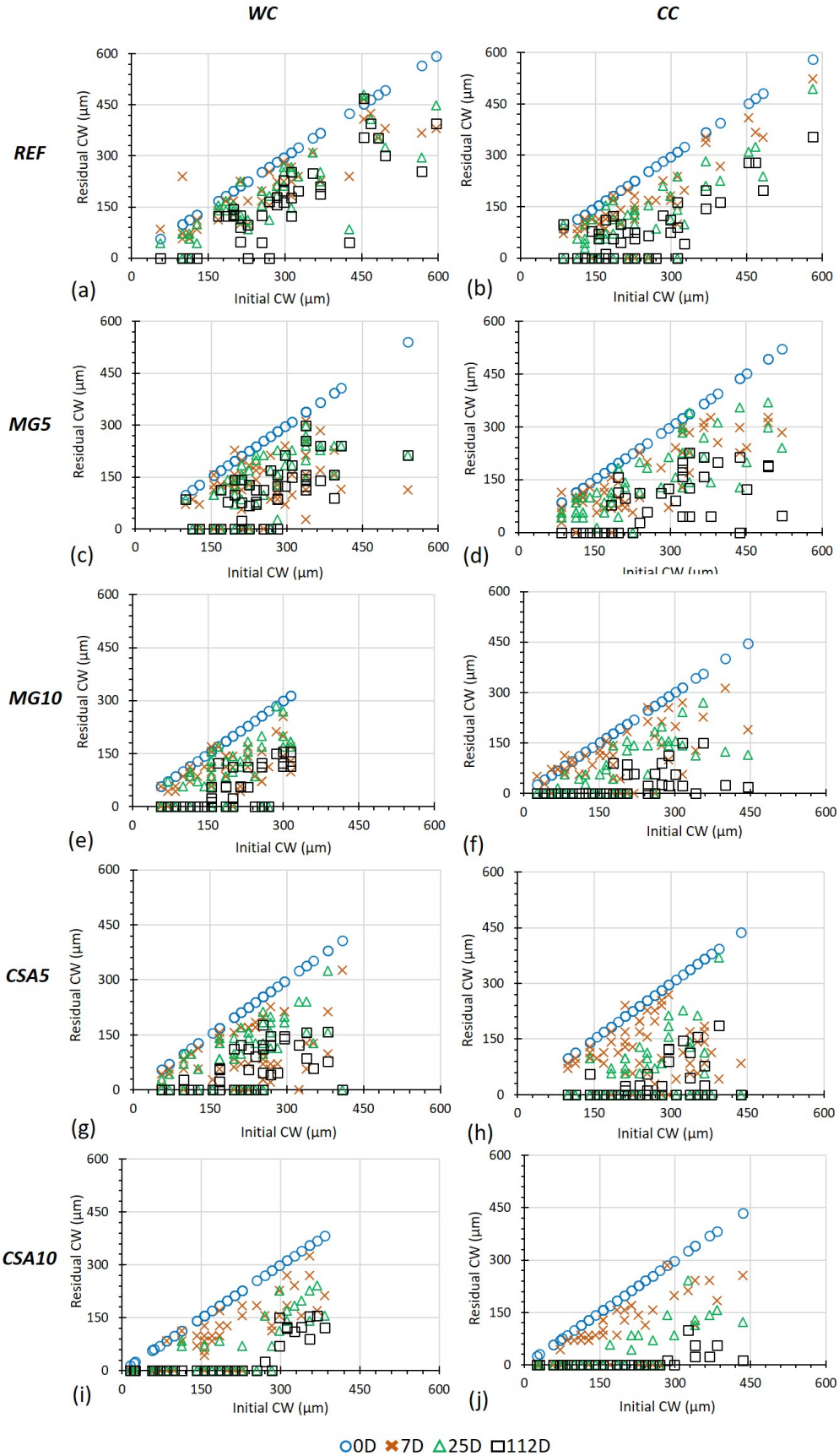

Figure 5.24 – Crack Width (CW) evolution for REF (a, b), MG5 (c, d), MG10 (e, f), CSA5 (g, h) and CSA10 (i, j) in WC and CC condition.

The mechanisms responsible for the crack healing potential are further hydration, carbonation and matrix expansion. These mechanisms change the dimensions of the crack throughout the specimen as a function of the studied mixture. It is therefore necessary to follow the healing process on all the crack depth by water permeability tests in order to evaluate the benefits of EA addition on the crack healing.

5.4.2 3D monitoring

In this paragraph, the Healing Rate (HR) is presented as function of the initial Crack Width (CW). Two initial WF ranges are selected: [0.001-0.03] l/min and [0.03-0.07] l/min. The CW corresponding to these WF ranges are giving in Table 5.3. So, For CW range, Figures 5.25 and 5.26 compare the HR evolution of all the studied mixtures cured under WC and CC.

Moreover, the HR is also calculated at a constant water pressure equal to 15 cm for all the specimens. The evolution of this HR as function of the initial CW is presented in Appendix C for all the studied mixtures.

Table 5.3 – Initial WF for specimens having a similar CW at 0D.

Initial WF (l/min)	[0.001-0.03]	[0.03-0.07]
Initial CW (μm)	[50-250]	[250-600]

For an initial CW = [50-250] µm of specimens stored under WC (Figure 5.25(a)): At 7 days of curing, mixtures with 10% EA (CSA10 and MG10) present the most important HR: 51% and 49% respectively. The other mixtures present a HR equal to 40%, 35% and 18% for CSA5, REF and MG5 respectively. After, the healing process continues and mixtures with 10% EA exhibit a quite similar healing rate: 70% and 69% respectively after 25 days of curing. Their HR are significantly higher than those of other mixtures at this time. So the addition of 10% EA is beneficial in accelerating crack healing during 25 days of curing. However, at 112 days, REF and MG10 achieve complete healing, slightly better than CSA10 (HR = 91%). While mixtures with 5% EA achieve the lowest HR (CSA5 and MG5) at 112 days (75% and 63% respectively). So, it appears that the benefit of 5% EA is limited in promoting the healing of cracks characterized by a width inferior to 250 µm. This is probably related to the limited further hydration in the presence of 5% EA. While REF and mixtures with 10% EA show quite similar healing behavior after 25 days. This confirms that the main healing mechanisms for these cracks are further hydration and carbonation.

For an initial CW = [50-250] µm of specimens stored under CC (Figure 5.25(b)): All the studied mixtures show a healing behavior quite similar to that of the specimens stored under WC (Figure 5.25(a)) at 7D and 25D: CSA10 and MG10 are characterized by the highest healing rates at 7d (56% and 45% respectively) and at 25D (82% and 78% respectively).

However, all the studied mixtures show a HR higher than 95% at 112D. Therefore, firstly, this confirms that the main healing mechanisms of cracks characterized by a width smaller than 250 µm are further hydration and carbonation. Second, this confirms that the CC condition increases long-term crack healing (at 112D), as explained previously.

For an initial CW = [250-600] µm of specimens stored under WC (Figure 5.26(a)): After 7 days of curing, the mixtures with 10% EA (MG10 and CSA10) show the highest HR values: 36% and 31% respectively. The HR of the other mixtures (REF, CSA5 and MG5) is equal to 23%, 23% and 13% respectively. So, the addition of 10% EA improves the self-healing of large cracks after one week of curing. As the curing period advances (up to 28 days), the addition of 10% EA (MG10 and CSA10) is consistently beneficial in promoting crack healing. The HR of these mixtures is equal to 50% and 41% respectively. On the other hand, the mixtures with 5% EA (CSA5 and MG5) show a quite similar healing behavior to that of REF. After 90 days of curing, the addition of 10% EA is continuously beneficial in promoting crack healing: MG10 and CSA10 reach HR values equal to 73% and 69% respectively. The HR of other mixtures is relatively low and varies between 44% and 56%. Therefore, this difference in behavior between mixtures with 10% EA and those with 5% EA is related to the fact that the addition of 10% EA contributes to a greater matrix expansion than a lower EA content (5%) as shown previously (Figure 5.21). This mechanism accelerates crack closure over time. Indeed, since 28 days (i.e. the age of cracking -Figure 5.21), REF and mixtures with 5% EA (CSA5 and MG5) show a negligible and small swelling rate respectively compared to the mixtures with 10% EA (MG10 and CSA10). Hence, the latter show a faster healing behavior at early and long term curing, which supports the autonomous healing. The anhydrous MGO present in MG10 further promotes this mechanism during water curing.

For an initial CW = [250-600] µm of specimens stored under CC (Figure 5.26(b)): All the studied mixtures show a healing behavior quite similar to that of the specimens stored under WC (Figure 5.26(a)) at 7D and 25D: MG10 and CSA10 are characterized by the highest healing rates at 7d (30% and 34% respectively) and at 25D (61% and 55% respectively). However, at 112D of CC, all the studied mixtures show higher HRs than when curing under WC (Figure 5.26(a)). This is related to their swelling rate which was lower in CC (Figure 5.22) than in WC (Figure 5.21), especially for the mixtures containing 10% EA. According to [8], the excessive matrix expansion could lead to poor volume stability, which could deteriorate the crack rather than heal it.

So, these observations confirm that three mechanisms are responsible for crack healing: further hydration, carbonation and matrix expansion. The first two mechanisms heal cracks smaller than 250 µm, while the last mechanism is involved when it is necessary to heal larger cracks (larger than 250 µm) through matrix expansion. The addition of 10% EA has a significant positive impact on the autonomous healing of cracks, and thus, on the third mechanism.

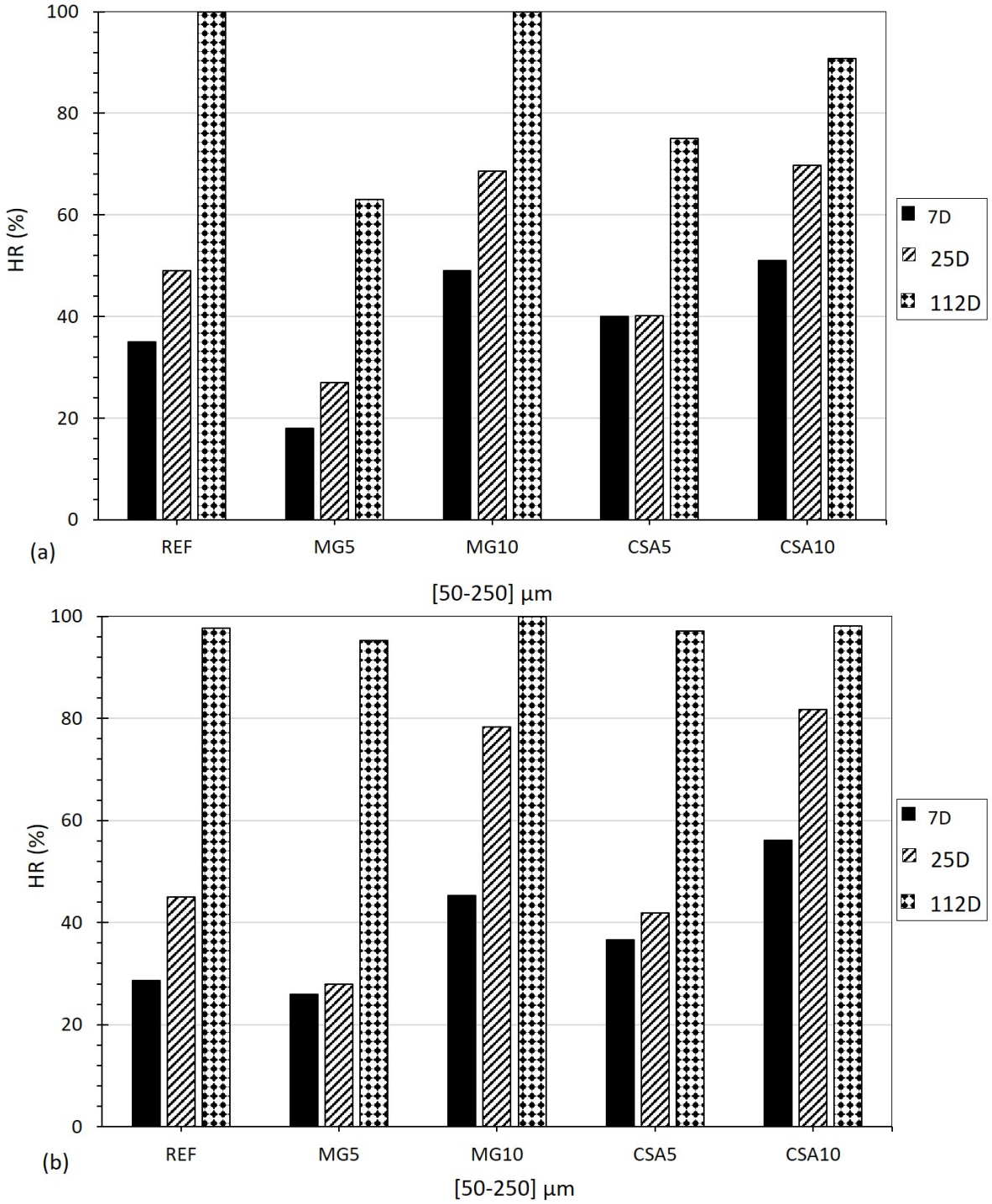

Figure 5.25 – HR evolution for specimens having an initial CW equal to [50-250] µm in WC (a) and CC (b).

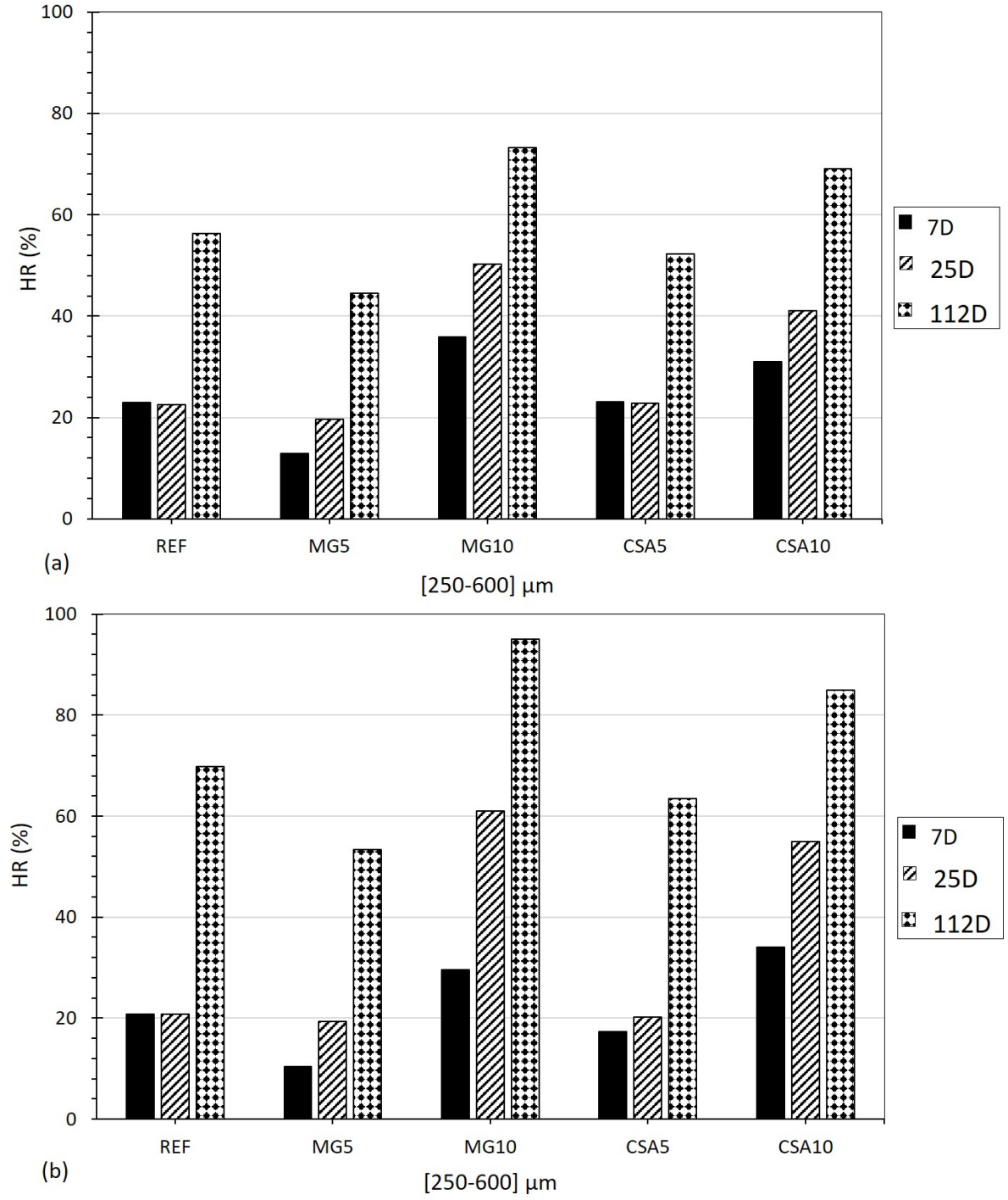

Figure 5.26 – HR evolution for specimens having an initial CW equal to [250-600] µm in WC (a) and CC (b).

5.4.3 Self-healing products on the crack surface

During the monitoring of the crack width on the specimen surfaces, the formation of white products were observed along the crack for all the studied mixtures (Figure 5.27). As shown in Figure 5.27, these products are mostly observed for mixtures containing EA than for REF. They are mainly carbonate-containing phases (Figure 5.28). Besides, a small amount of brucite is present among the white products of mixtures containing MGO (MG5 and MG10).

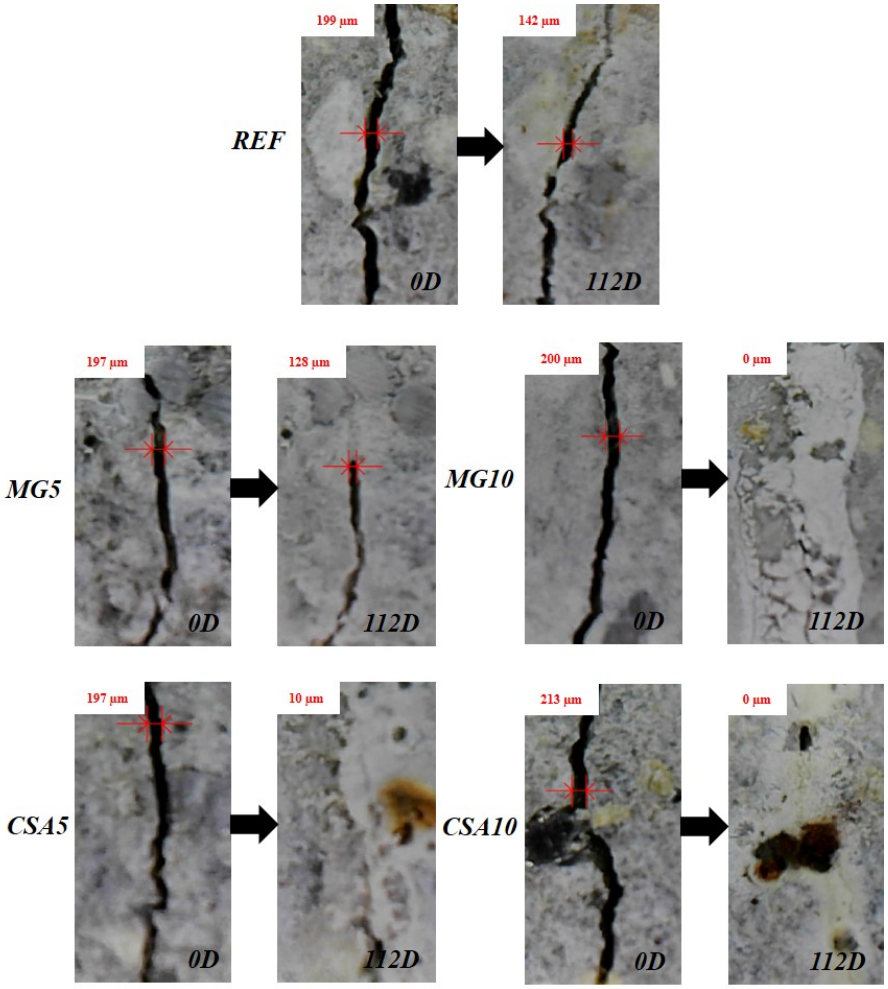

Figure 5.27 – Crack on the specimen surfaces at 0D and 112D for all the studied mixtures.

The morphology of the carbonates located on the crack surface is observed using SEM-EDX observations for REF, MG10 and CSA10. The EDX analysis is made at defined spots for each mixture. Different morphology of the carbonates are presented as a function of each mixture depending on several parameters, e.g. temperature, CO_2 pressure, pH, etc... [99, 119] . Based to the results obtained for REF (Figure 5.29), it shows products with cubic morphology formed along the crack, in which they contain magnesium (Figure 5.29(d)). According to [119, 121], these products are called magnesian calcites ($Mg_xCa_{(1-x)}CO_3$) where Mg partially

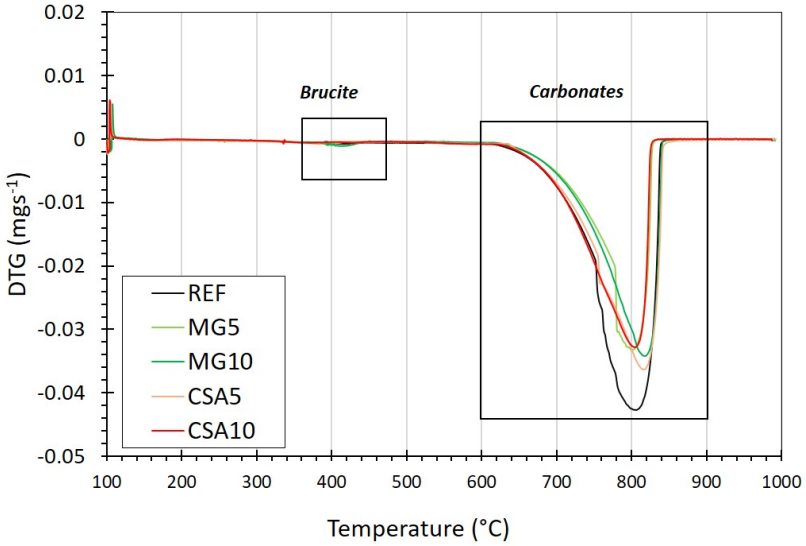

Figure 5.28 – DTG curves of the white products formed on the crack surface of each mixture.

substitutes Ca with a variable degree of replacement "x". Magnesian calcites are formed in the $CaO - MgO - CO_2 - H_2O$ system and "x" is the molar ratio of $[Mg^{2+}]/[Ca^{2+}]$ $(0 < x < 1)$. But, according to [119], when the ratio Mg/Ca is higher than 0.5, it can be an indication for the formation of other MgO containing phases like brucite. In our EDX analysis, the atomic ratio of Mg/Ca will be given hereafter.

Hence, In the case of REF, the atomic ratio of Mg/Ca is equal to 0.086, which confirms the presence of magnesian calcites on the crack of REF with a cubic morphology (Figure 5.29(d)). The magnesium comes from the Portland cement and/or the curing water. Cubic magnesian calcites are rarely seen on the MG10's crack as shown in Figure 5.30(a,b), and its Mg/Ca atomic ratio is so small (7.13E-3) (Figure 5.30(c)). Additionally, these magnesian calcites are formed on other magnesian calcite products (Figure 5.30(d,e)). The latter, having an Mg/Ca atomic ratio equal to 0.017 (Figure 5.30(f)), present a needle-like morphologies. They are therefore attributed to magnesian calcites of the aragonite type. As the concentration of $[Mg^{2+}]$ ions increases (due to the addition of 10% MGO), the aragonites formation is favored. This is observed by other research works [20,122]. For CSA10, also cubic magnesian calcites are formed on its crack with an atomic ratio Mg/Ca equal to 0.019 (Figure 5.31(a,c)). Another type of carbonates are also found (Figure 5.31(d)), but no magnesium is identified (Figure 5.31(f)). It can be attributed to the flower-like calcite [123]. This type of calcite is usually favored when the pH is around 13.0 due to the high concentration of $[Ca^{2+}]$ [123].

So, these results confirm the presence of magnesian calcites for REF, MG10 and CSA10. The addition of 10% MGO promotes the formation of additional hydration products on the crack surface: brucite.

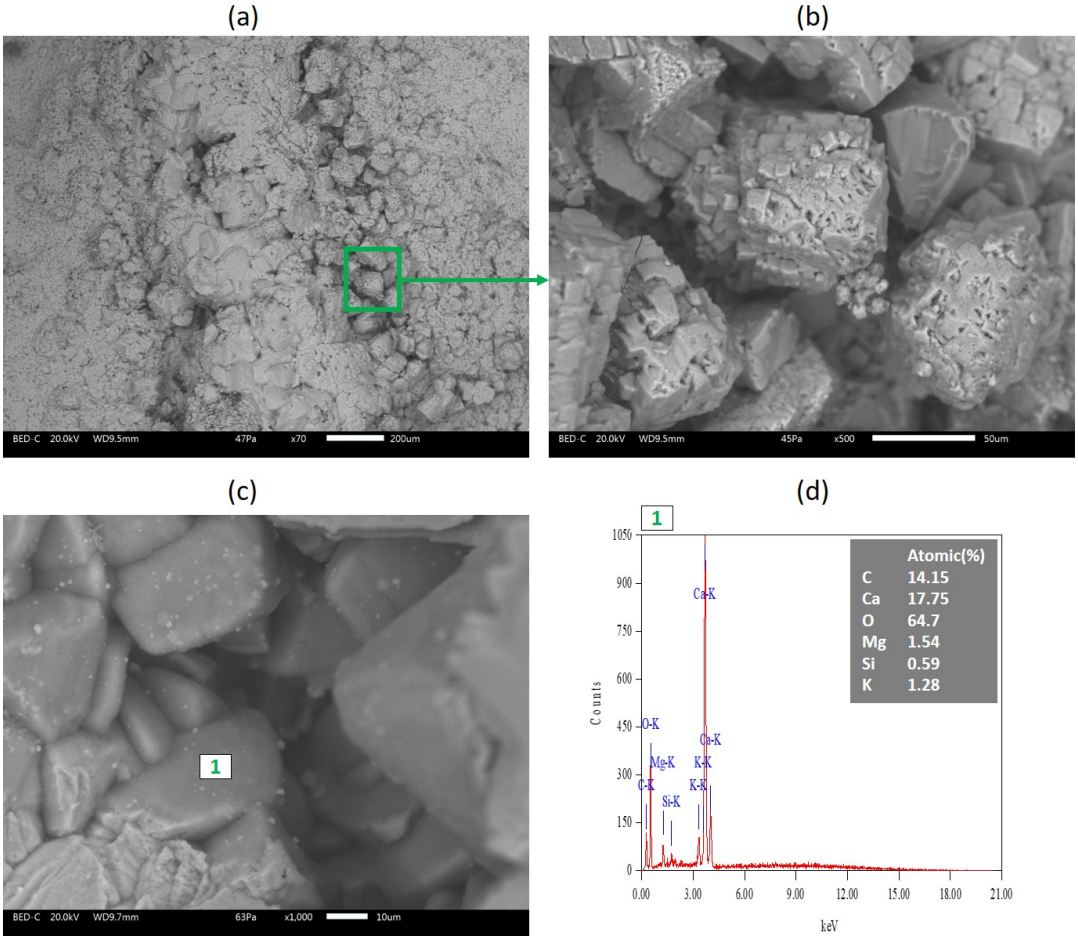

Figure 5.29 – SEM observation of self-healing products along the crack for REF and its EDX analysis.

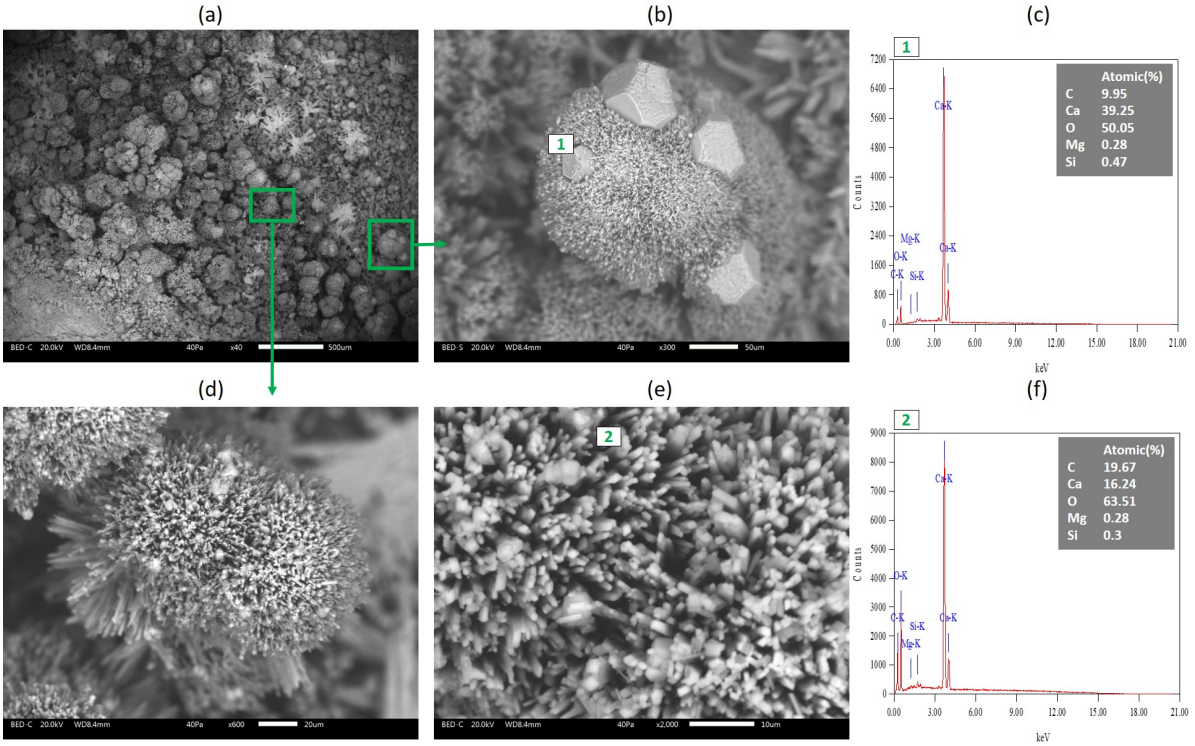

Figure 5.30 – SEM observation of self-healing products along the crack for MG10 and its EDX analysis.

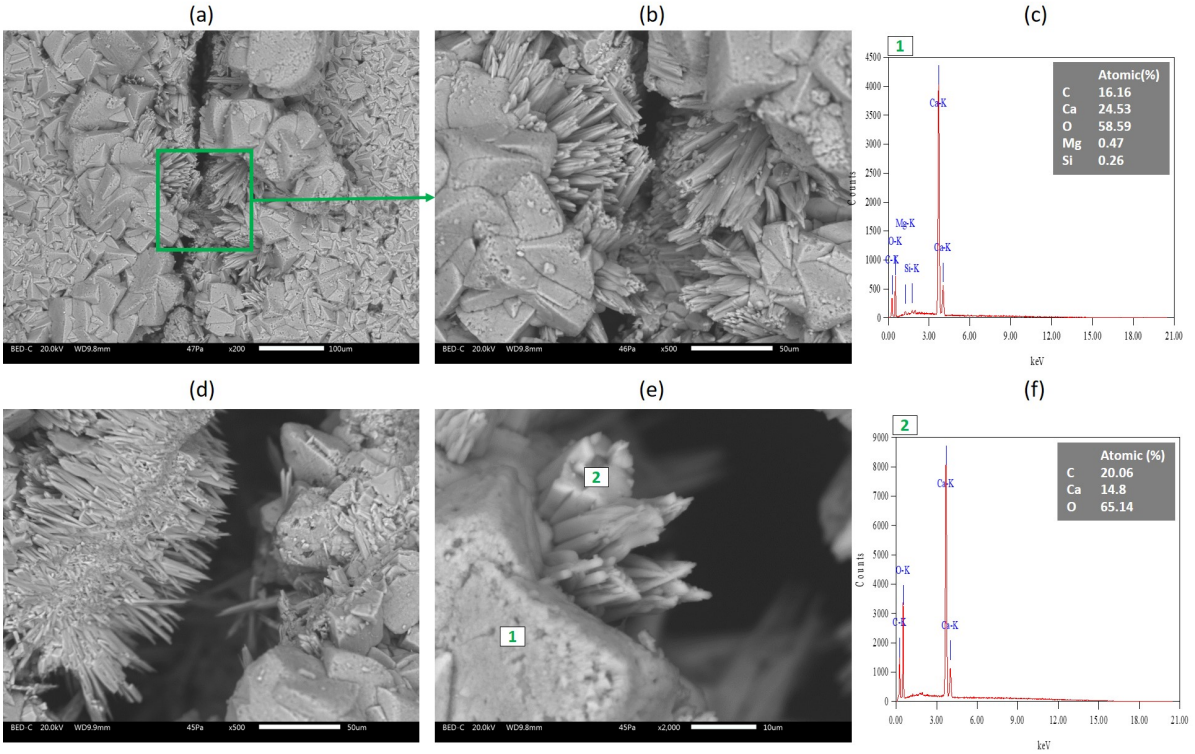

Figure 5.31 – SEM observation of self-healing products along the crack for CSA10 and its EDX analysis.

5.4.4 Self-healing products inside the crack

EDX observations are performed inside the crack for REF, MG10 and CSA10 to identify the internal self-healing products.

For REF, Figure 5.32 show self-healing products characterized by a Ca/Si = 0.56. According to [124], the C-S-H type gel has a Ca/Si atomic ratio that can vary between 0.2 and 1.7. It is therefore attributed to C-S-H gel. For MG10, the presence of ettringite is detected as shown in Figure 5.33(a-f). Another products are shown in Figure 5.33(g-k) having a significant Mg content, indicating that this product can be attributed to M-S-H. Indeed, a ratio of Mg/Al = 2.92 suggests the presence of additional Mg-rich phases such as M-S-H gel [119]. So, a high MGO content (10%) promotes the formation of Mg-rich phases such as M-S-H [125]. For CSA10, C-S-H gels are found located in the crack internal zone as shown in Figure 5.34. The Ca/Si is equal to 0.57. The Mg/Al ratio is small (0.16), so these products are associated to C-S-H gels.

These results confirm the presence of C-S-H as common healing products formed within the cracks of REF and CSA10, and M-S-H for MG10. These products are formed by the hydration of remaining unhydrated tricalcium and dicalcium silicate (C_3S and C_2S). Therefore, all mixtures present further hydration mechanism benefit for crack self-healing. The addition of 10% MGO is benefit to increase the further hydration due to the anhydrous MGO. The latter promotes the formation of additional healing products such as M-S-H gel.

5.4.5 Summary

The main objective of this section is to evaluate the benefits of adding EA on the self-healing process of cracks. It is concluded that the self-healing process is related to three mechanisms: carbonation, additional hydration and matrix expansion. The first two mechanisms are achieved by all the studied mixtures for the crack width in the range [50-250] µm. These two mechanisms are further enhanced for the mixture with 10% MGO due to the formation of different magnesian calcite morphologies on the crack surface and by the formation of M-S-H gels inside the crack. The third mechanism is achieved by the addition of 10% EA (MGO or CSA) allowing to increase the autonomous healing potential of the crack width ranging between [250-600] µm. This behavior is related to the type of hydration products formed in the presence of MGO and CSA (e.g. brucite and ettringite respectively).

So, these results highlight the use of the cement-based mortars containing 10% EA as a promising mortars characterized by an interesting autogenous and autonomous healing capacities.

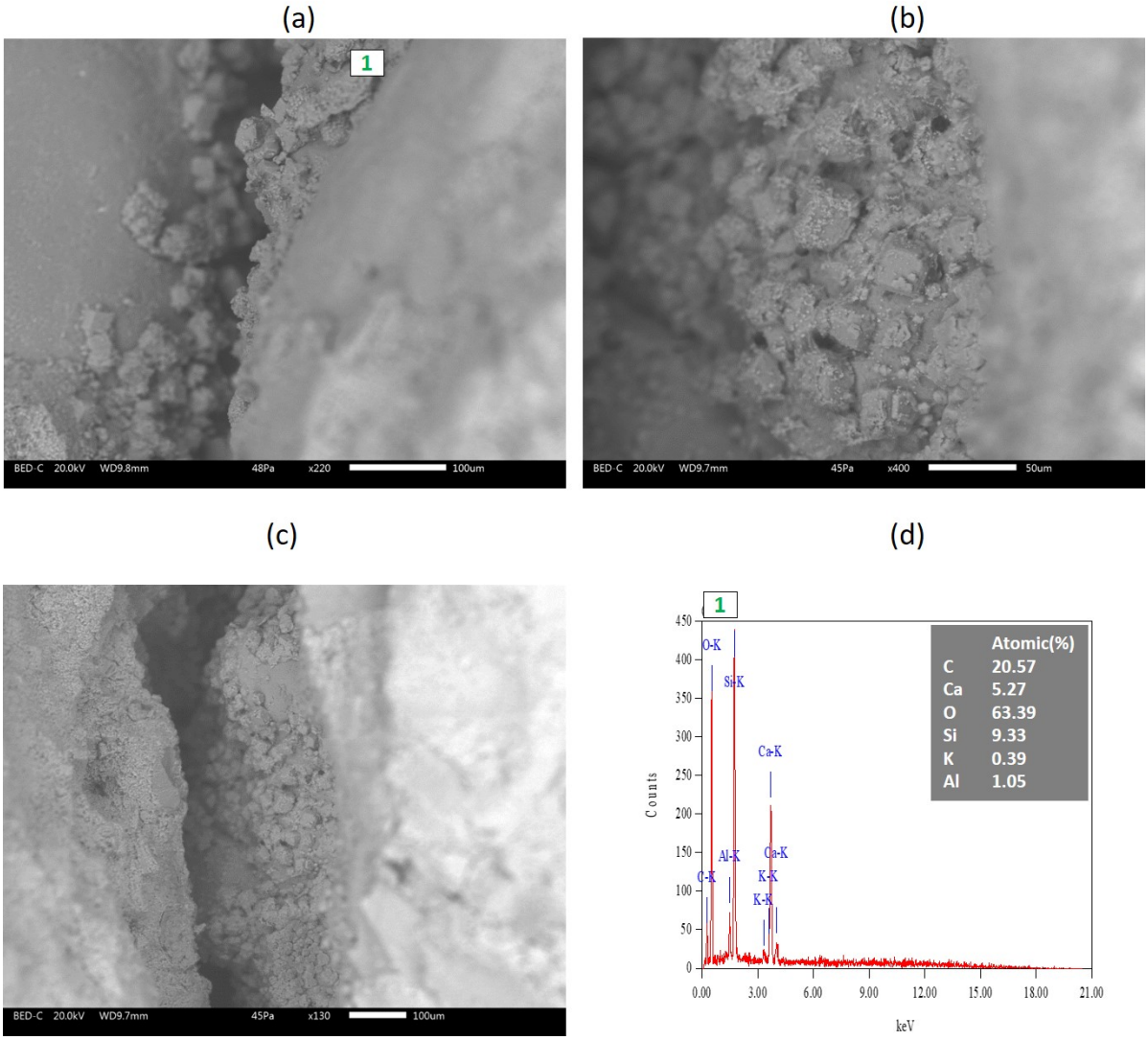

Figure 5.32 – SEM observation of self-healing products inside the crack for REF and its EDX analysis.

5.5 Conclusion

This chapter details the benefit of EA addition (MGO and CSA) on the properties of sound mortars and their self-healing capacity. The following mixtures are compared: REF, MG5, MG10, CSA5 and CSA10. The study is divided into three parts: (1) evaluation of mortar hydration and microstructure; (2) evaluation of mortar mechanical properties and delayed deformations and (3) evaluation of mortar self-healing capacity.

The experimental results show that the addition of an expansive agent type MGO or CSA leads to a significant decrease of the autogenous and total shrinkage due to the formation of additional products in the pore network, leading to crystallization pressures and a matrix swelling at macroscopic scale. This expansion accelerates crack closure and therefore increases

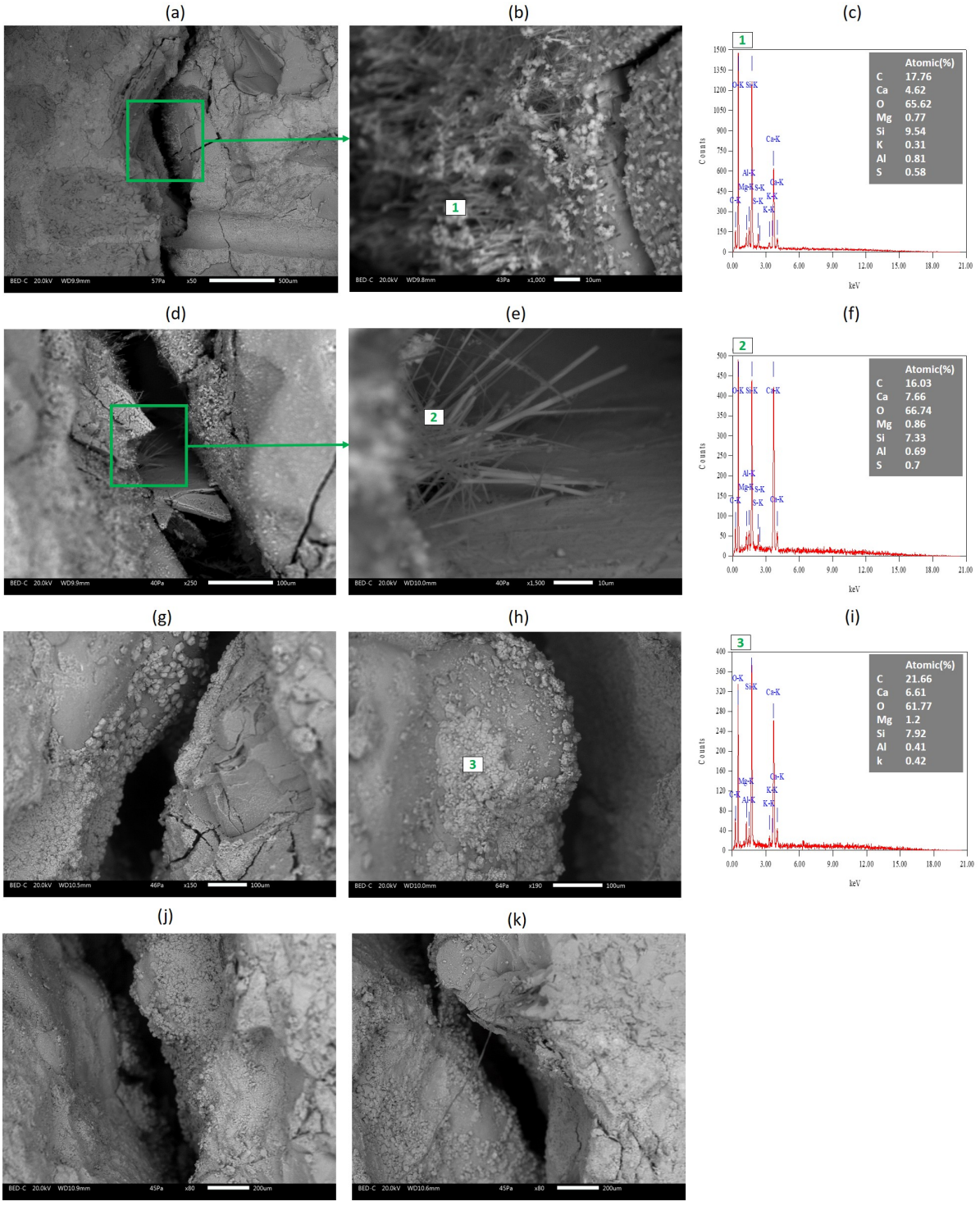

Figure 5.33 – SEM observation of self-healing products inside the crack for MG10 and its EDX analysis.

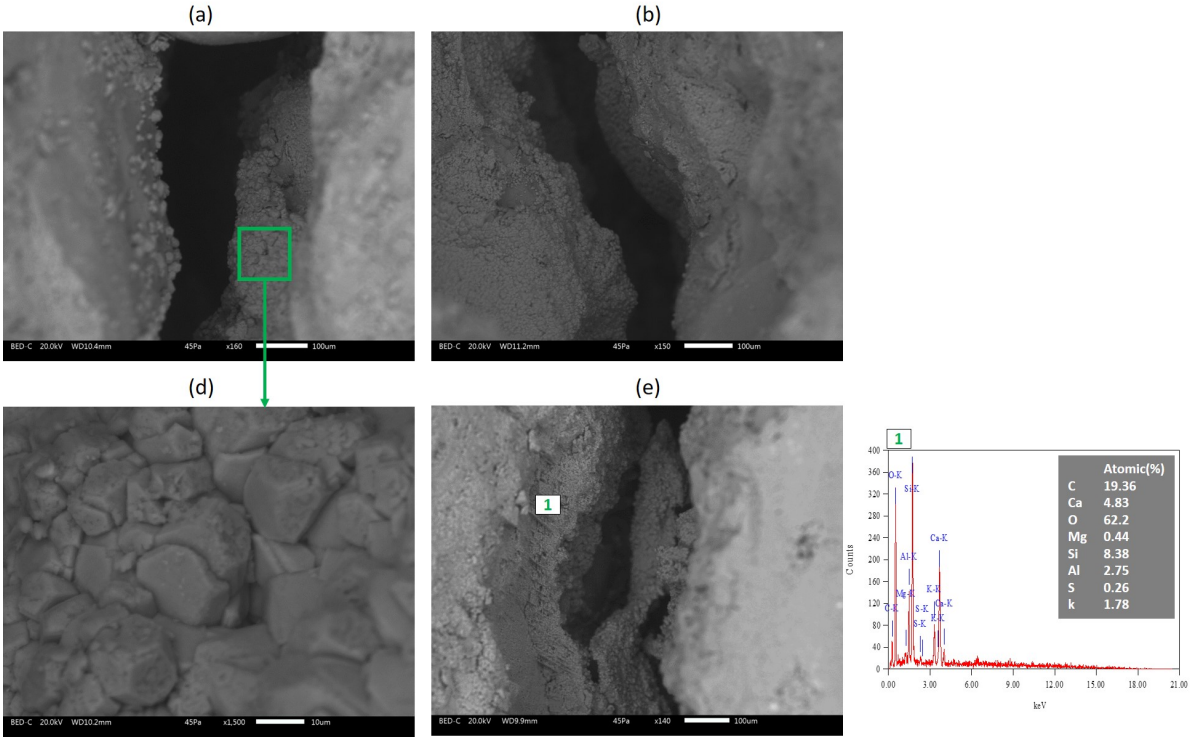

Figure 5.34 – SEM observation of self-healing products inside the crack for CSA10 and its EDX analysis.

the autonomous healing potential of mortars. These behaviors are more important by increasing the EA content into the mixture. On the other hand, the partial substitution of the cement mass by EA decreases the mechanical resistances (flexural and compressive) at early age and in the long term due to the lower C-S-H gels produced. This reduction is lower in the presence of CSA than in MGO, due to the CSA hydration that is completed at early age. Despite of this strength decrease, all the proposed mortars present high compressive strengths at 28 days. Therefore, it confirms their compliance to the repair standard requirements (EN 1504-3). Finally, the addition of EA significantly reduces the mortar's sensibility to cracking in a restricted autogenous condition. The presence of MGO in the mixture increases this behavior due to the moderate swelling of the matrix.

Therefore, this chapter proposes cement-based mixtures incorporating EA as promising mortars that can be used for repair applications, limiting cracking sensibility and characterized by interesting autogenous and autonomous healing capacities.

Chapter 6

Effect of MGO and CSA-based EA on the behavior of blast-furnace slag blended mortars: microstructure, mechanical properties and healing capacity

Contents

6.1 Introduction

The previous chapter (Chapter 5) evaluated the effect of EA on the cement-based mortar properties and its healing capacity. It was proved that the addition of 10% EA is beneficial to increase the autonomous healing capacities of the cement-based mortar. In this chapter, the benefit of incorporating EA (MGO and CSA) into a more environmentally-friendly mortar is investigated to propose an innovative mortar with autonomous healing capacities. So, the cement is partially substituted by a mineral addition: the blast-furnace slag. The interaction between MGO and blast furnace slag is a deep study that needs further attention due to the few results in the literature on this topic [119]. In addition, recent studies have investigated the use of CSA cement-slag binders as a novel combination of low CO_2 binders [118, 126, 127]. Hence, these are both interesting new research proposals that need further investigation. So, the effect of the coupling of mineral additions and EA (MGO and CSA) on the properties of the sound mortars is firstly investigated in focusing on their hydration and microstructure; their mechanical properties and their delayed deformations under two types of curing. Secondly, its benefit on the mortars self-healing capacity is estimated on cracked mortar using the water permeability test.

6.2 Hydration and microstructure of sound mortars

The hydration process of blast-furnace slag blended mortars is discussed below as well as their microstructure by evaluating their hydration products and porosity structure.

6.2.1 Hydration process

The hydration process is determined for all the studied mixtures at early age (before 3 days) using isothermal calorimetry and at long term (until 90 days) by ThermoGravimetric Analysis (TGA).

At early age: The heat flow, the cumulative heat and the hydration advancement degree are presented in Figures 6.1, 6.2 and 6.3 respectively for all the studied mixtures. The heat flow curves can be divided into four main periods: (1) Pre-induction period; (2) Dormant period; (3) Acceleration period and (4) Post-acceleration period [114, 115]. Comparing BFS to the mortar mixture containing only Portland cement (REF), it appears that the addition of blast furnace slag accelerates initially the hydration of Portland cement because the dormant period duration is smaller and the second hydration peak appears earlier for BFS (Figure 6.1 and Table 6.1). It appears at 9.5 h and 12 h for BFS and REF respectively (Table 6.1). This is also demonstrated by the faster hydration advancement degree for BFS compared to REF before 17 h (Figure 6.3). According to [128], this acceleration is due to the higher water/cement ratio in BFS.

This is known as the "dilution effect," which means that more water is available for the cement hydration in the blended mixture. Moreover, the addition of blast furnace slag results in a lower cumulative heat release as seen in Figure 6.2. It is because the hydration kinetics of slag is generally lower than that of Portland cement, and requires the presence of alkali that comes from the clinker dissolution in the pore solution [117,128,129]. The third hydration peak shown for BFS and REF is attributed to the secondary formation of ettringite and thus, the sulfate depletion [117]. This peak appears at 15.5 h and 13.3 h for REF and BFS respectively (Table 6.1). As the sulfate content of blast furnace slag is lower than that of Portland cement (Chapter 4), this peak appears very low for BFS (Figure 6.1). In addition, a fourth hydration peak is recorded only for BFS (Figure 6.1). Blast furnace slag is quite passive in a low pH environment because an impermeable coating of aluminosilicate forms on the surface of the slag particles within few minutes of exposure to water [117]. This prevents any further reaction of the slag with water. A strongly alkaline environment (pH = 12) serves as a chemical activator to break the glass structure of the blast furnace slag and accelerates its hydration [128]. This is thus evidenced by the appearance of the fourth peak at 17 h for BFS (Table 6.1). It corresponds to the acceleration of the blast furnace slag reaction by the available portlandite issued from the cement hydration.

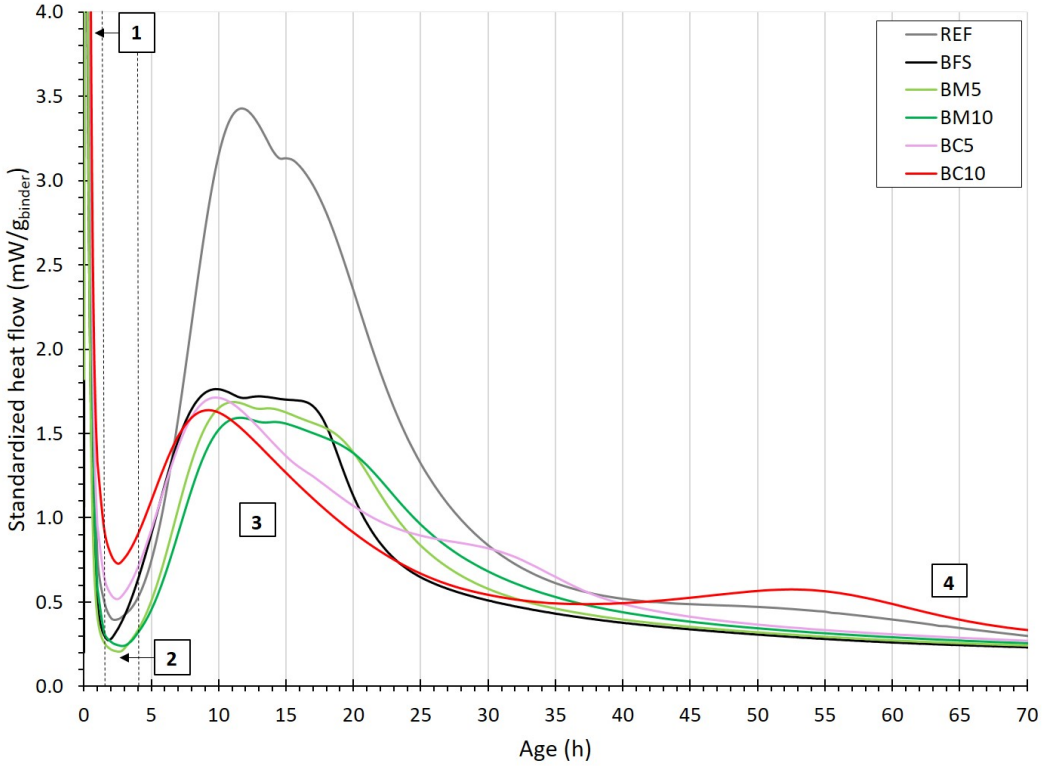

Figure 6.1 – Standardized heat flow for all the studied mixtures; *(1) Pre-induction period; (2) Dormant period; (3) Acceleration period and (4) Post-acceleration period*; and its cumulative heat (b).

Table 6.1 – Duration of period 2, time to reach the 2^{nd}, 3^{rd} and 4^{th} peak and the value of the cumulative heat ad infinitum.

Hydration characteristics	REF	BFS	BM5	BM10	BC5	BC10
Duration of period 2 (h)	3.0	1.5	3.0	3.0	1.5	1.5
Time of the 2^{nd} peak (h)	12.0	9.5	11.0	11.2	9.5	9.0
Time of the 3^{rd} peak (h)	15.5	13.3	14.3	14.5	-	-
Time of the 4^{th} peak (h)	-	17.0	19.0	20.0	32.0	54.0
Q_∞ (J/g)	328.7	201.5	206.7	219.9	220.2	234.2

The addition of MGO appears to delay the hydration process of BFS. Indeed, the dormant period is extended by 1.5 h for mixtures with MGO (Figure 6.1 and Table 6.1). In addition, the time to reach the second and third peaks is also delayed for these mixtures (BM5 and BM10). Several parameters can explain this hydration slow down. Due to binder substitution, the cement and mineral addition contents are lower for BM5 and BM10. The addition of MGO leads to the formation of brucite, which delays the cement hydration process [116]. The reaction of MGO with the blast furnace slag leads to the formation of hydrotalcite, which is believed to also retard the hydration process [130]. Furthermore, this induces a delay in the acceleration reaction of the blast furnace slag (the fourth peak). In the literature, several researchers [72, 131] used MgO to active blast furnace slag matrices as this product increases the pH of the pore solution. But its effect on the mineral addition activation depends on the reactivity and content of MGO used in the mixtures [72]. According to [72], an MGO content of less than 10% (of reactivity equal to 100.4 seconds, relatively close to the MGO used in our study $\backsim$127.7 seconds) in a blast furnace slag matrix lowers the pH of the pore solution below 12. Moreover, the effect of 50% cement in our mixtures tends to dominate and does not promote the slag activation by MGO (Figure 6.1). The delay in the hydration process is also evidenced by the cumulative heat and hydration advancement degree for BM5 and BM10 (Figures 6.2 and 6.3) and it increases with the MGO content.

In contrast, the hydration process is accelerated by the addition of CSA as shown by the dormant period and the time of the second peak for BC5 and BC10 (Table 6.1). This behavior is also shown by their cumulative heat and hydration advancement degree during the first 10 hours (Figures 6.2 and 6.3). The cement content is lower for BC5 and BC10 due to binder substitution and it might induce a delay in cement hydration. However, the ye'elimite ($C_4A_3\underline{S}$) present in CSA dissolves on contact with water and forms AFt/AFm phases at a faster rate than the hydration of C_3S [132], accelerating the hydration process of BC5 and BC10. It also explains the absence of a third hydration peak for these mixtures, indicating that sulfate is consumed during AFt/AFm formation at an early stage [118] (Figure 6.1 and Table 6.1). In addition, the hydration of CSA can also consume portlandite to form AFt according to [133]. Thus, the reaction of blast furnace slag with portlandite is delayed as a large content of portlandite is

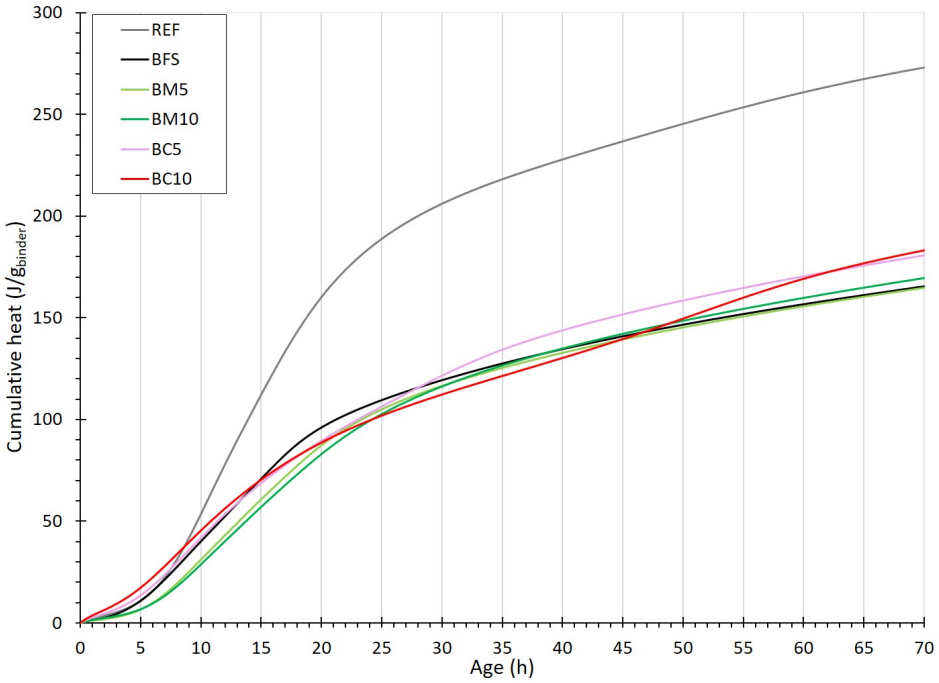

Figure 6.2 – Cumulative heat for all the studied mixtures.

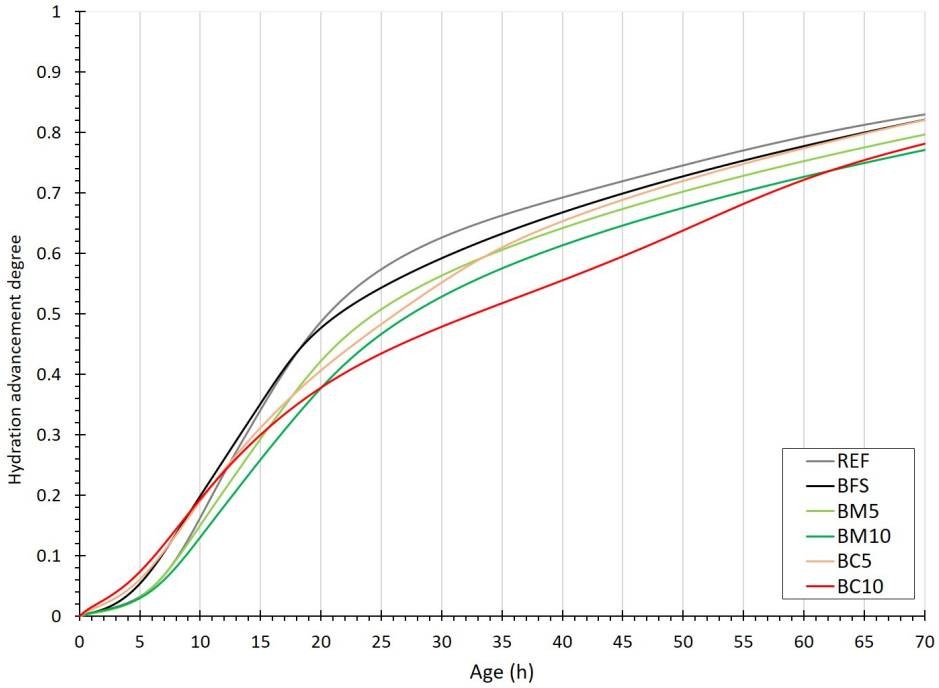

Figure 6.3 – Hydration advancement degree for all the studied mixtures.

consumed by CSA hydration. This is evidenced by the significant delay of the fourth peak for BC5 (at 32 h), which increases with the CSA content increases (BC10) (Figure 6.1). After the fourth peak, the cumulative heat for BC5 and BC10 increases again to reach a value superior to the cumulative heat of BFS (Figure 6.2). It is due to the exothermic activity of blast furnace slag [129].

At long term: From TGA analysis, the advancement of the hydration at long term is estimated through the mass loss of the sample in the temperature range of [105-1000] °C (Figure 6.4). This temperature range is chosen in order to take into account the overall mass loss related to the dehydration and decomposition of the hydration and the carbonation products respectively. In this analysis, the carbonation products are taken into account because they can be produced by the carbonation of some hydration products like portlandite. The mass losses in the temperature ranges of [105-300] °C and [105-600] °C will be presented in Appendix (D).

From Figure 6.4, it appears that the mass losses for BFS are lower than those for REF from 3d to 90d. But comparing the mass losses in the temperature range of [105-300]°C (Appendix (D)), from 28 days, they are quite similar for both mixtures. This is due to the delayed hydration of the blast furnace slag and the increase in C-A-S-H content with time for BFS. This behavior is consistent with the hydration advancement degree of BFS beyond 60 hours that is close to that of REF (Figure 6.3)).

The mixtures with MGO (BM5 and BM10) presents a higher mass loss than BFS during the first week. This mass loss increases slowly until 90 days. This might indicate that the mixtures with MGO form supplementary hydration products in comparison to the typical hydration products of BFS (e.g. C-S-H/C-A-S-H and hydrotalcite), such as: brucite and M-S-H [88] and more hydrotalcite [131]. In particular, this last product increases significantly the bound water content as the hydrotalcite contains relatively more water than C–S–H/C-A-S-H [131], which is consistent with the slightly higher mass losses presented by the mixtures with MGO compared to BFS. So, these results indicate that the addition of MGO forms additional hydration products (Figure 6.3).

The mixture with 5% CSA present mass losses quite close to those of BFS at early age and long term. This observation is consistent with their similar hydration advancement degree beyond 40 hours (Figure 6.3). However, the increase of CSA content to 10% (BC10) increases significantly the mass loss at 3 days. It is related to the AFt/AFm formation that require an important amount of water (32 and 12 molecules of water respectively). Beyond 3 days (at 7d), the mass loss of BC10 is lower than at 3d, but increases again at 28d and then decreases at 90d. This behavior highlights the stability of AFt over time. It could be related to the possibility of the transformation of some AFt to AFm which requires a slightly lower water content than AFt. In addition, hydration of CSA is fast and could be complete before 14 days, indicating that no new AFt/AFm phases could be formed at long term [83]. Eventually, these results indicate that

the addition of CSA accelerates the hydration process during the first hours (Figure 6.3) but does not tend to accelerate it at long term. Finally, it should be noted that the mass variation in the [105-1000]°C temperature range of anhydrous products (Portland cement, blast furnace slag, MGO and CSA) is negligible compared to mortars.

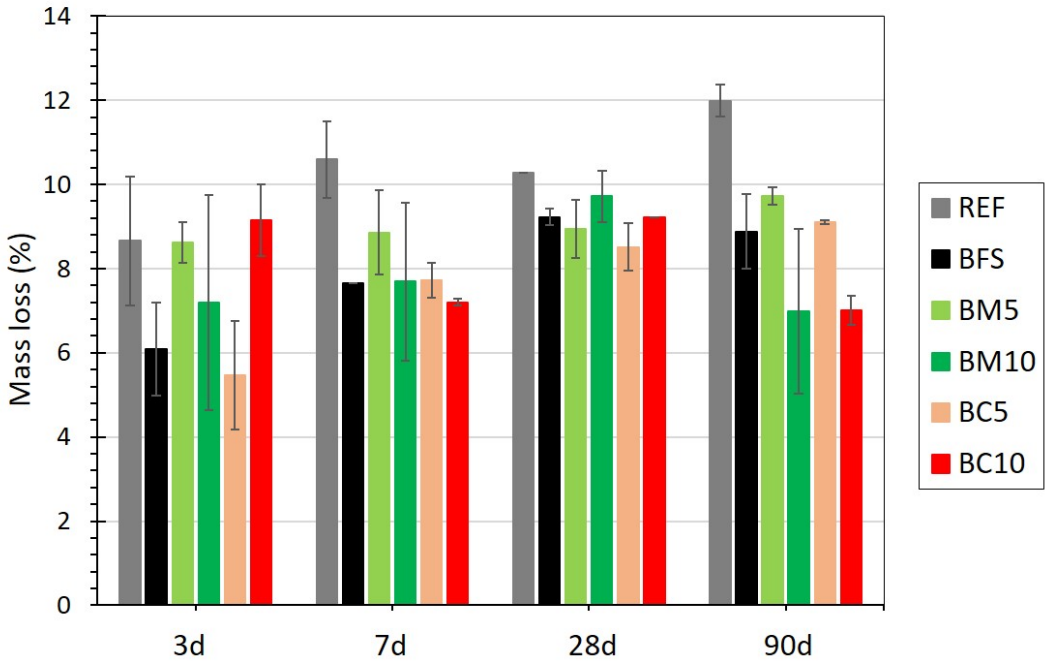

Figure 6.4 – Mass loss from 105°C to 1000°C from TGA at 3, 7, 28 and 90 days for all the studied mixtures.

6.2.2 Hydration products

From the TGA, DTG curves are determined and presented for each mixture at 3, 7, 28 and 90 days (Figure 6.5). From these curves, it can be seen a first peak between 105°C to around 250°C for all the studied mixtures. The C-S-H/C-A-S-H start to decompose at 105°C. At 160°C, it appears a slightly more intense peak for the mixtures containing CSA (BC5 and BC10) during the 28th days, associated to the dehydration of AFm as suggested by [118,126]. The AFm phase results from the ettringite reaction with C_3A [117]. This indicates that more ettringite may be formed and available for this reaction as CSA is added to the mixtures (BC5 and BC10). Other hydration products may also decompose partially at 200°C: stratlingite [118,126,127], and hydrotalcite [131]. The mass variation in the temperature range of [300-450]°C appears for all mixtures but with different intensities. For BFS, this mass variation increases over time (Figure 6.6(a)) and corresponds to the decomposition of hydrotalcite [110,131] since the blast furnace slag contains a sufficient amount of MgO to produce hydrotalcite (Chapter 4).

This mass variation shows a higher intensity for BM5 and BM10 at each age (Figure 6.5). This means that more hydrotalcite is formed over time by adding MGO as shown by Figure 6.6(a). This mass variation is more significant with the increase of the MGO content to 10% (BM10) (Figure 6.5 & Figure 6.6(a)). According to [131], slag pastes with 7% MgO content showed only hydrotalcite because the content of MgO was totally incorporated in hydrotalcite formation, while a higher MgO contents (up to 13%) was found to produce hydrotalcite and brucite. Other studies [119] also reported that AAS with high MGO content (13-16%) produce only hydrotalcite, while no brucite was found. It appears that in presence of hydrotalcite, the formation of brucite might not be favored. So, this suggests that mass variation in the temperature range of [300-450]°C is probably related to the hydrotalcite decomposition only. This hypothesis needs to be confirmed by the XRD analysis. The mixtures with CSA (BC5 and BC10) show mass losses in the [300-450]°C temperature range close to the mass losses of BFS, that fairly increase with time (Figure 6.6(a)). This also means that these mixtures produce hydrotalcite similarly as BFS.

The peak associated to the decomposition of portlandite is shown for all the mixtures (Figure 6.5). Its mass variation is lower for BFS compared to REF by about 30-40% at each age (Figure 6.6(b)), which clearly indicates the use of portlandite as an activator for the acceleration of blast furnace slag reaction in BFS mixture. However, its mass variation does not decrease with time due to the further hydration of the blast furnace slag. Two processes can take place at the same time: the formation of portlandite over a long time period by the cement hydration, and the consumption of a partial portlandite content by blast furnace slag reaction. Furthermore, the decomposition of other hydrates, e.g. C-S-H/C-A-S-H, is also possible in the temperature range of [450-600] °C. This explains the mass variation over time related to the decomposition of portlandite for all the studied mixtures (Figure 6.6(b)).

Finally, the decomposition of carbonates-containing phases appears after 600°C for all the mixtures (Figure 6.5) and their mass variation is very small (between 0.7% and 1.6%) (Figure 6.6(c)).

In order to clearly characterize the crystalline phases existing in the studied mixtures, XRD analysis was performed on paste because the quartz from mortar will interfere the results. So, paste of the same mixtures are proposed to analyze via XRD, and the water adsorption related to the sand was taken into account during calculation. But, firstly, it is important to determine if the degree of advancement of the hydration reaction for the paste mixtures is quite similar to that of mortars at 28 days. As shown in Figure 6.7, the pastes are characterized by similar peaks of mass losses in the following temperature ranges: [105-250]°C, [300-450]°C, [450-600]°C, [600-800]°C. Their values are also quite similar (Figure 6.8(a, b)) as well as for the temperature ranges [105-1000]°C (Figure 6.9). So, the paste mixtures exhibit hydration behavior at 28 days quite similar to that of the mortar mixtures, which ensures that the XRD analysis done on the paste mixtures is valid in our case.

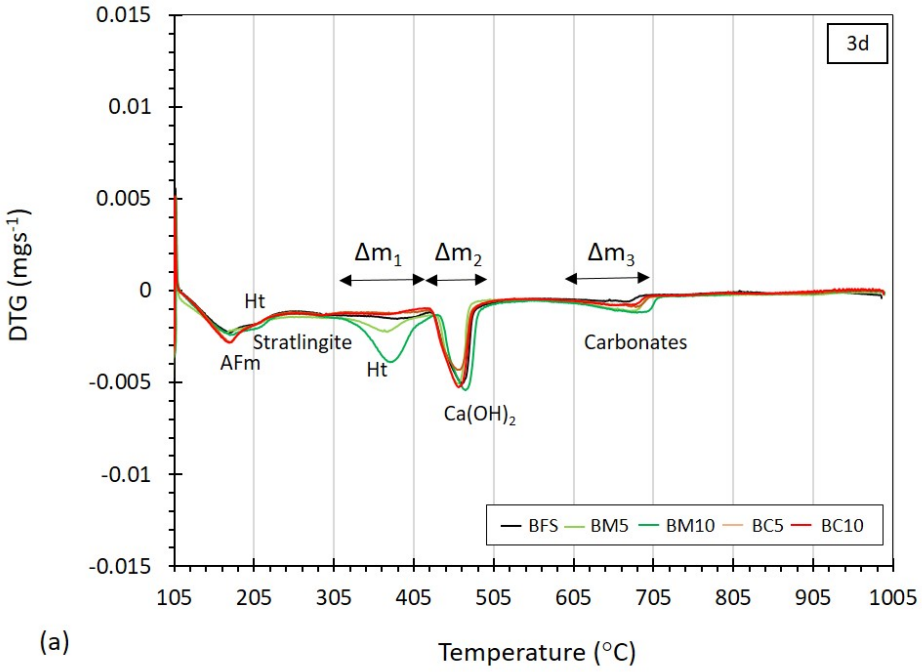
3d
DTG (mgs-1)
0.015
0.01
0.005
0
-0.005
-0.01
-0.015
Δm1
Δm2
Δm3
Ht
Stratlingite
AFm
Ht
Ca(OH)2
Carbonates
BFS
BM5
BM10
BC5
BC10
105
205
305
405
505
605
705
805
905
1005
Temperature (°C)

(a)

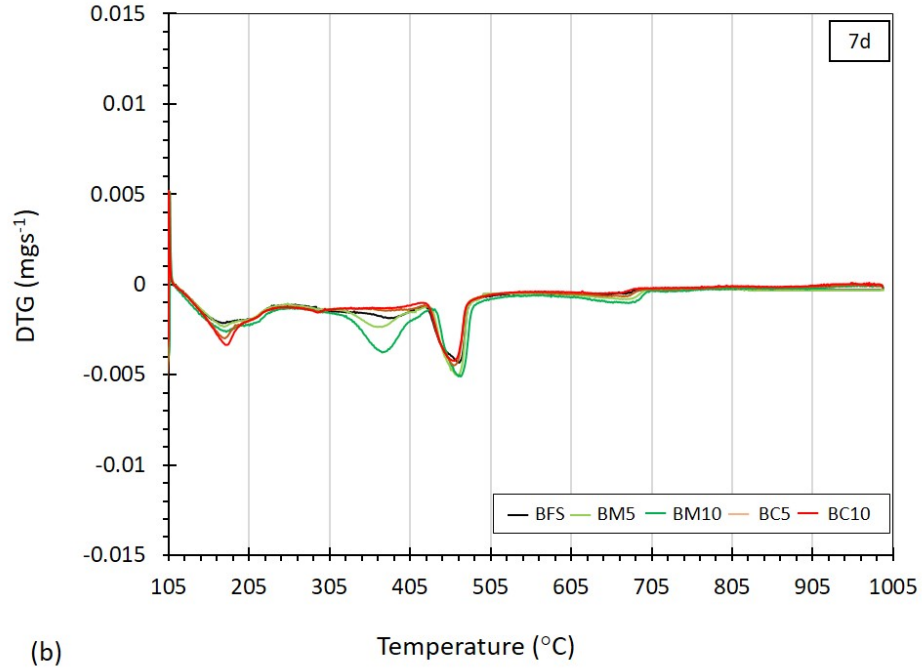
7d
DTG (mgs-1)
0.015
0.01
0.005
0
-0.005
-0.01
-0.015
BFS
BM5
BM10
BC5
BC10
105
205
305
405
505
605
705
805
905
1005
Temperature (°C)

(b)

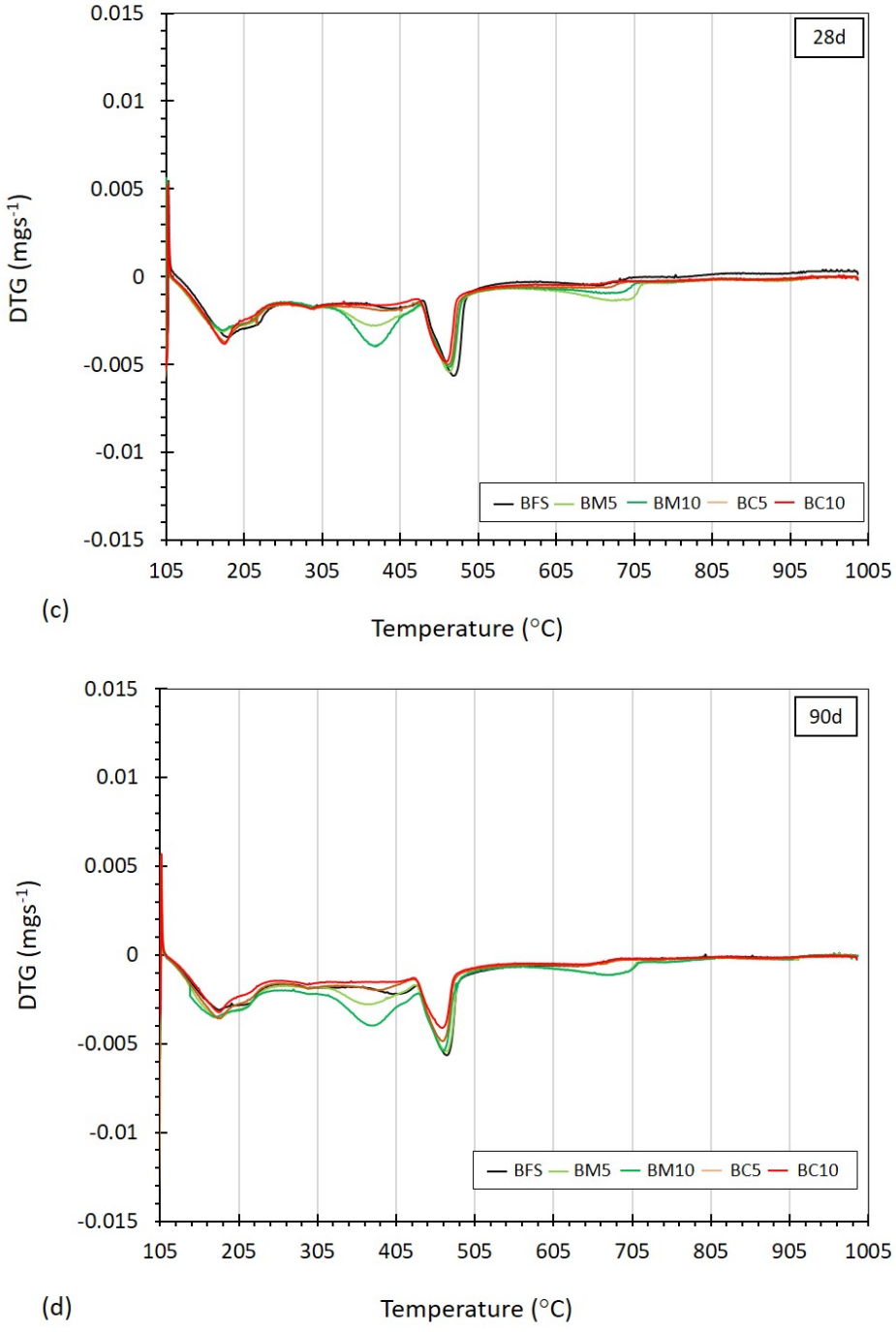

Figure 6.5 – DTG curves of the mixtures at 3 days (a), 7 days (b), 28 days (c) and 90 days (d).

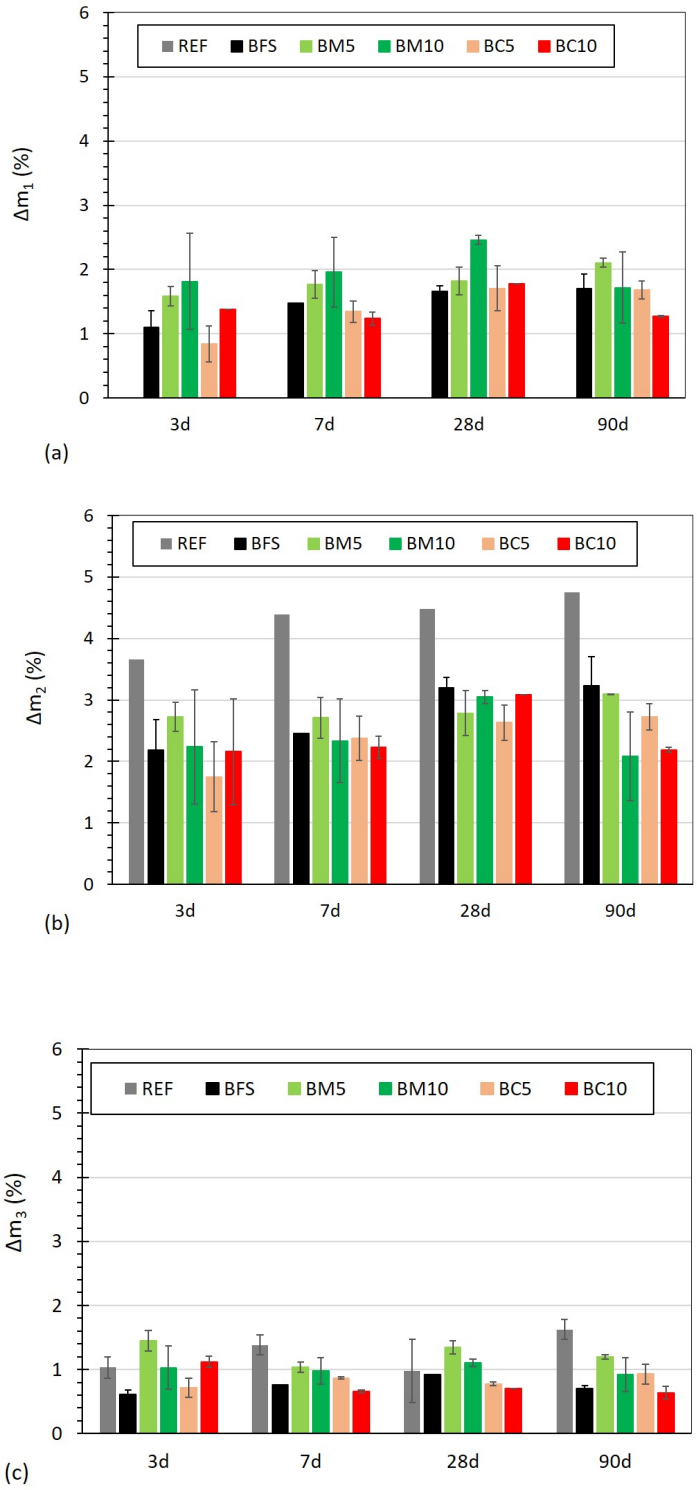

Figure 6.6 – Mass loss in the temperature range equal to [300-450]°C (Δm_1) related to hydrotalcite (a), [450-600]°C (Δm_2) related to portlandite (b) and [600-800]°C (Δm_3) related to carbonates-containing phases (c) at 3, 7, 28 and 90 days.

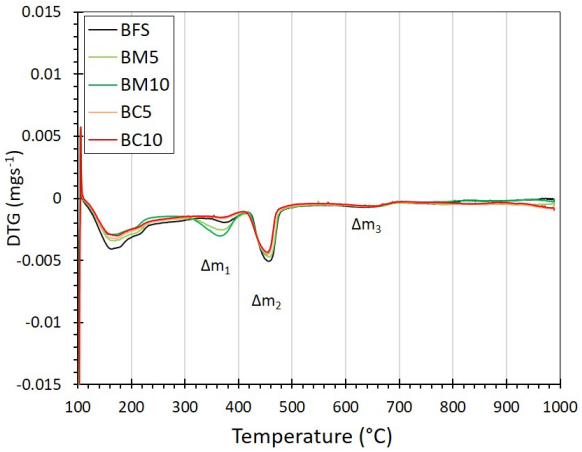

Figure 6.7 – DTG curves for paste mixtures at 28 days.

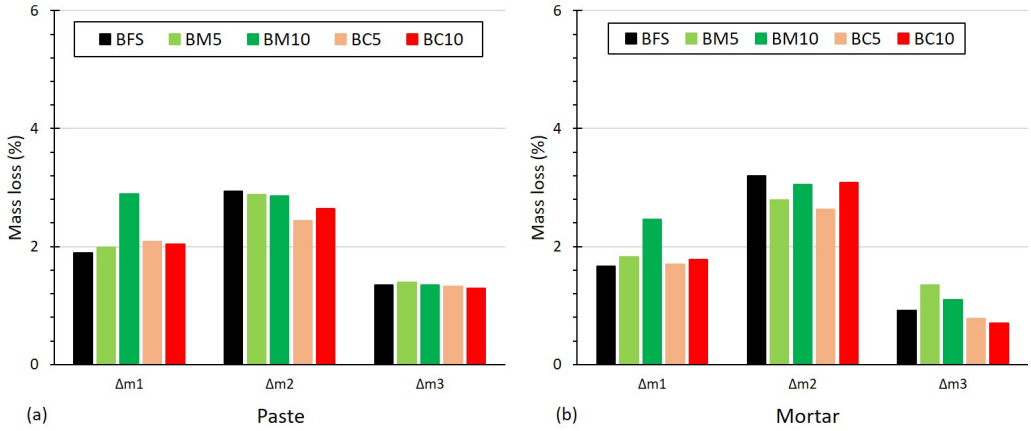

Figure 6.8 – Mass loss at 28 days in the temperature range equal to [300-450]°C (Δm_1), [450-600]°C (Δm_2) and [600-800]°C (Δm_3) for paste mixtures (a) and mortar mixtures (b).

The XRD results (Figure 6.10) show common phases between the studied mixtures such as: Ettringite (PDF #41-1451), hydrotalcite (PDF #41-1428), portlandite (PDF #44-1481) and carbonates-containing phases (e.g calcite –PDF# 5-586, dolomite –PDF #36-426 and magnesite –PDF #8-479).

The ettringite peaks found at 9.1° and 15.8° are more intense for mixtures containing CSA (BC5 and BC10) than for other mixtures. Moreover, the ettringite peak appears in several additional angles for BC5 and BC10 (at 22.9°, 25.6° and 35°). So, these results confirm that the formation of ettringite is promoted in presence of CSA as explained earlier (§6.2.1). However, no monosulfoaluminate is detected for BC5 and BC10. It is probably related to the high sulfate content in these mixtures that favors the formation of ettringite rather than monosulfoaluminate [118]. It should be noted that the molar ratio of calcium sulfate over ye'elimite in CSA plays a key role in regulating the preference of hydration products in the

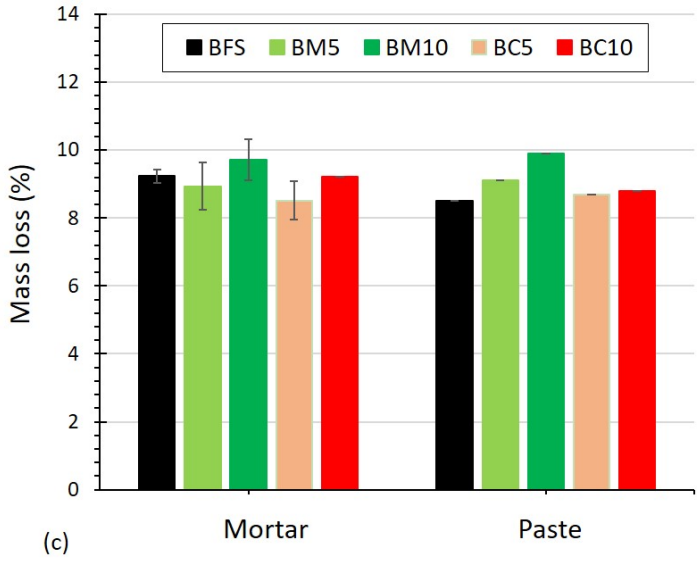

Figure 6.9 – Mass loss at 28 days in the temperature range equal to [105-1000]°C for mortar and paste mixtures.

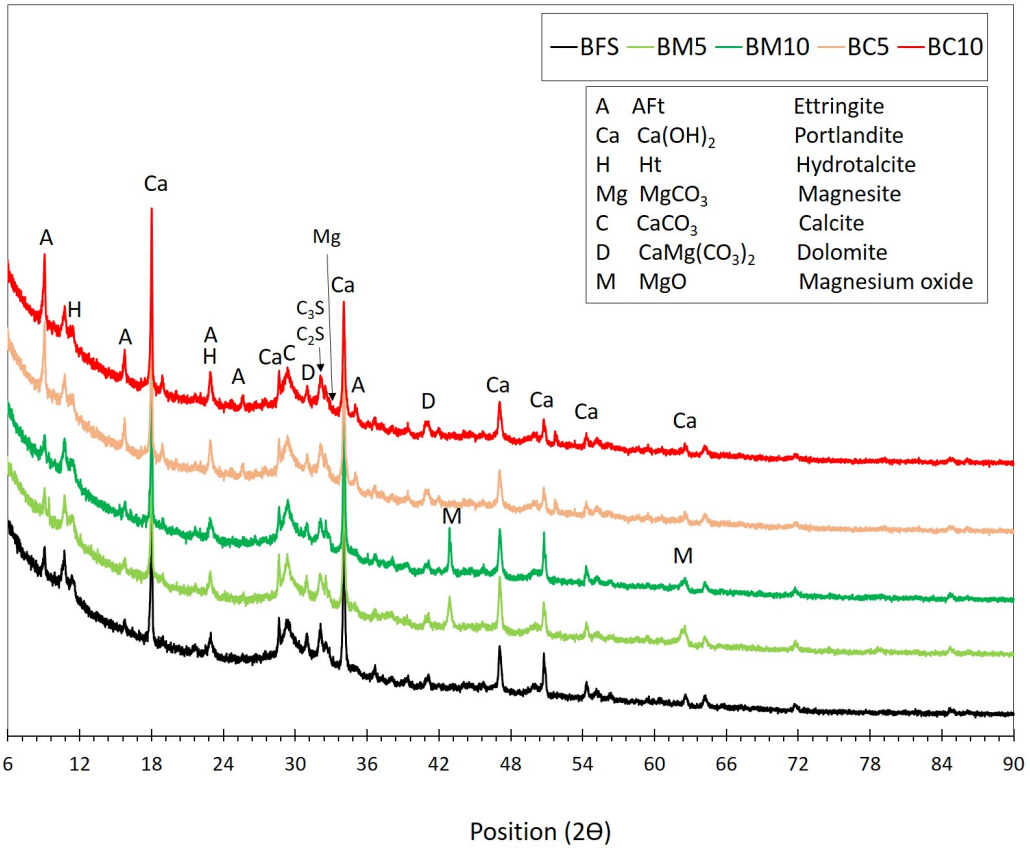

Figure 6.10 – -XRD results for all the studied pastes.

matrix [118]. However, this molar ratio is not known for the CSA that we used in our study. The hydrotalcite appears slightly higher for BM5 and BM10 on its first peak (at 11.3°), indicating that these mixtures form more hydrotalcite as suggested previously (§6.2.1. Moreover, no brucite is found. In addition, it appears that the peaks related to portlandite found at 47.1°, 50.8°, 54.4° and 62.6° are slightly smaller and shorter for the mixtures containing CSA than for other mixtures. It confirms that the portlandite can be used during CSA hydration to produce ettringite as indicated by [133]. However, no anhydrous particles from the CSA (e.g. ye'elimite, calcium sulfate or calcium oxide) are found, which indicates that CSA hydration is complete before 28 days in BC5 and BC10 .

Some anhydrous particles are found in all the studied mixtures such as: dicalcium silicate (C_2S –PDF #33-302) and tricalcium silicate (C_3S –PDF #31-301). The intensity of their peaks is small. So, it indicates that the hydration process can continue after 28 days for all the studied mixtures. Moreover, anhydrous MgO (PDF #45-946) is found in mixture containing 5% MGO (BM5) at 42.9° and 62.3°. Its peaks increase slightly with the addition of 10% MGO (BM10). These two peaks do not appear in BFS, BC5 and BC10. Therefore, BM5 and BM10 exhibit an additional hydration capacity after 28 days in comparison to the other mixtures.

6.2.3 Porosity

In order to study the effect of blast furnace slag and EA on the mortar's microstructure, the total porosity and the connectivity between the pores are determined for all the studied mixtures at 90 days. The volume of the mesopores is also determined at the pore radius ranging from 2 nm to 12 nm as well as the specific surface area for all the studied mixtures. The results are shown in Figures 6.11, 6.12 and 6.13 respectively.

After a drying at 40°C at 90d, the water porosity value of BFS is equal to 13.1%. It is 3% smaller than that of REF (Figure 6.11(a)). At the same age, the intrinsic permeability coefficient of BFS is 18% smaller than that of REF (Figure 6.11(b)). These results indicate that the substitution of 50% of cement weight by blast furnace slag decreases slightly the mortar's total porosity as well as the connectivity between the pores. This behavior is related to the delayed hydration of the blast furnace slag which promote the formation of further C-A-S-H gel in the pores at long term resulting in a smaller pore network. The addition of MGO seems to increase slightly the total pore volume (by 3% and 4% respectively for BM5 and BM10) compared to BFS at 90d (Figure 6.11(a)). This behavior is probably related to their mass losses presented previously that suggest the additional hydrotalcite formation and less C-S-H [131]. Thus, this could slightly increase the total pore volume when the MGO content increases. However, BM5 and BM10 present a smaller intrinsic permeability that are 18% and 36% respectively smaller than that of BFS at 90d (Figure 6.11(b)). It means that the connectivity between their pores is significantly smaller than that of BFS at 90d. The addition of 5% CSA (BC5) leads to a similar

total pore volume to that of BFS (Figure 6.11(a)). It is related to the similar hydration process presented by BFS and BC5 at 90d (§6.2.1), and thus quite similar hydration products except their content of AFt. It seems also that the additional formation of ettringite at early age leads to a denser structure at long term, which can explain the smaller connectivity between the pores presented by the BC5: its intrinsic permeability coefficient is 27% smaller than that of BFS (Figure 6.11(b)). However, these observations are not consistent with the behavior of BC10. The increase in CSA content to 10% (BC10), increases slightly (1.8%) its total pore volume compared to BFS, while the connectivity between the pores is so similar to that of BFS. As explained previously, it could be related to the stability of ettringite over time [134, 135].

Moreover, from the gas permeability results, the Klinkenberg coefficient can be determined to obtain an information about the pore size. The results obtained are shown in Figure D.3 in Appendix D. However, no relevant information or conclusions can be drawn from this graph.

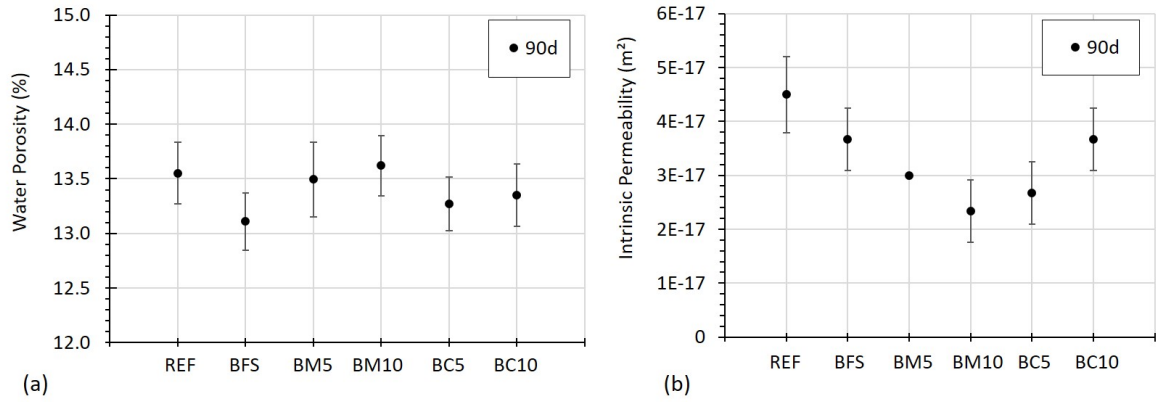

Figure 6.11 – Water porosity (a) and intrinsic permeability coefficient (b) for all the studied mixtures dried at 40°C.

The results of the mesopore volume are shown in Figure 6.12. They are calculated from the cumulative pore volume curves determined by sorption analysis (Appendix (D)). At 3d, the volume of mesopores is slightly larger (4% and 3.5%) for the mixtures with 10% EA (BM10 and BC10 respectively). But this volume decreases over time (3.3% and 2.8% respectively at 90d), while it increases for REF and BC5 at 90d (3.4% and 3.6% respectively). On the other hand, BFS and BM5 show variations in their mesopores volumes over time, but their values at 90d are close to those at 3d (2% and 2.6% respectively). Eventually, the mesopores volume for each mixture alternates between 2% and 4% from 3d to 90d. Similar observations for the results of S_{BET} shown in Figure 6.13. The S_{BET} values alternate between 5.9 m^2/g and 10 m^2/g for the mixtures. These observations indicate that the addition of 50% blast furnace slag and EA does not significantly affect the mortar's porosity between 2 nm and 12 nm radius from 3 days to 90 days.

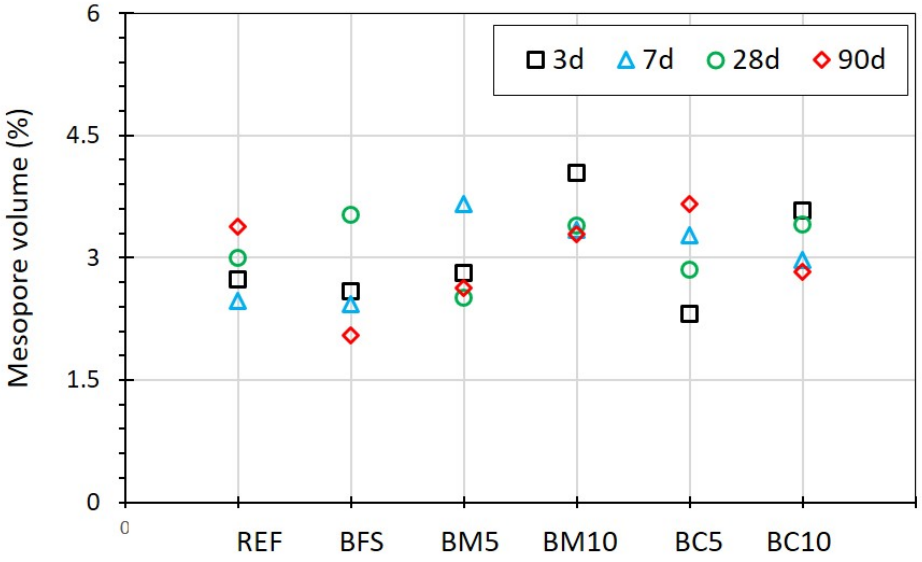

Figure 6.12 – Mesopore volume for all the studied mixtures at 3d, 7d, 28d and 90d.

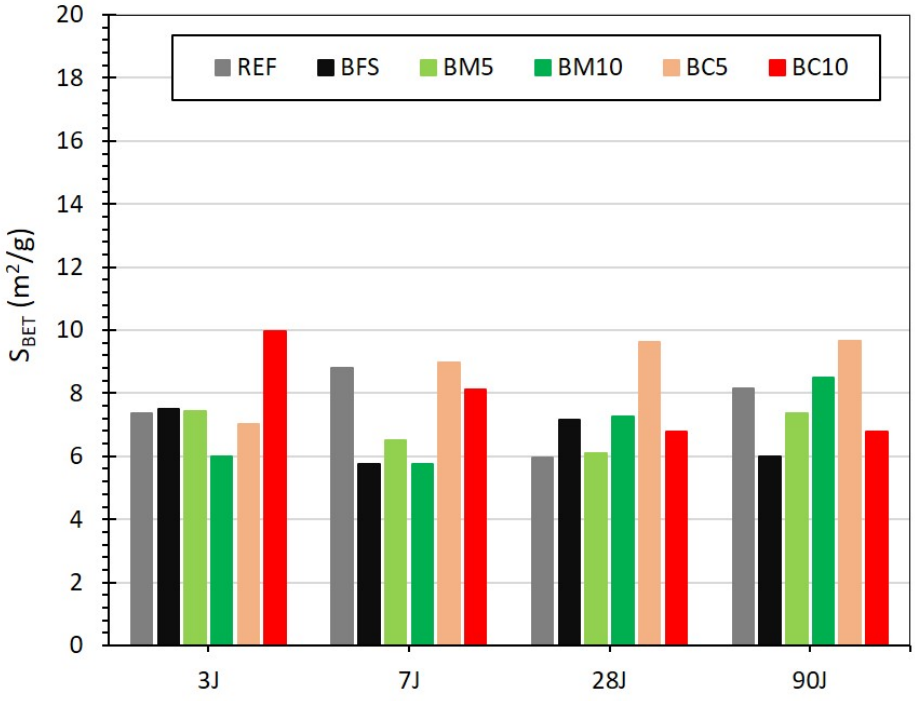

Figure 6.13 – Specific surface area S_{BET} derived from sorption analysis.

6.2.4 Summary

The main objective of this section is to evaluate the effects of adding blast furnace slag and EA on the hydration process and microstructure of the cement-based mortar. At early age, the ternary mixture of cement-blast furnace slag-MGO slows down the hydration process and increases the possibility of formation of additional hydration products (e.g. more hydrotalcite). This behavior is more observed when the MGO content increases. An opposite behavior is shown by the ternary mixture of cement-blast furnace slag-CSA due to a fast hydration process at early age related to the formation of more ettringite. This behavior is more important when the CSA content increases. Hydrotalcite and ettringite are characterized by their swelling pressures in the pores. This mechanism can induce a swelling of the matrix at the macro scale, and therefore, promotes the self-healing process. Indeed, it can accelerate the closure of cracks over time, explaining the interest of adding EA.

At long term, the addition of blast furnace slag and CSA slightly reduces the porosity of the mortar. This is advantageous because finer porosity will require less products to generate macro-scale swelling. Additionally, the presence of blast furnace slag in all of these mixtures increases the possibility of further hydration. This mechanism can be further promoted by the addition of MGO which leads to the presence of additional anhydrous particles at 28 days (e.g. MgO). This will increase with increasing the content of MGO. Therefore, the results ensure the benefit of blast furnace slag and EA addition on the further hydration mechanism which may be promising for the self-healing process.

6.3 Mechanical properties

As one of the main objectives of this research is to propose a repair mortar having mechanical performances adapted to the repair requirements (EN 1504-3) [10], the effects of blast furnace slag and EA on the mechanical performances have to be estimated. Firstly, the compressive strengths are determined at several ages and compared to the strength classes available for repair with cementitious materials. Secondly, parameters affecting the cracking sensitivity of the repair mortar when its delayed deformations are restrained by a support, are studied: flexural strength, dynamic Young's modulus and delayed deformations. For this last parameter, two curing conditions are investigated: autogenous and water curing. These results will also give us an information on the swelling capacity of these mixtures to improve crack healing. In addition, drying can also affect the response of the repair material. For this purpose, shrinkage under drying condition (at 20°C and 60% RH) is also studied and the first results are given in Figure D.6 in Appendix D. Finally, all these parameters are coupled using a crack sensitivity index to compare the cracking risk of the studied mixtures.

6.3.1 Mechanical strength

The evolution of the mortars' mechanical strengths (flexural and compressive strength) are determined at 3, 7, 28 and 90 days and the results are presented in Figures 6.14 and 6.16.

At 3 days, the compressive strength "f_c" of BFS is equal to 32 MPa, which is 42% smaller than that of REF at the same age (55 MPa). The "f_c" of BFS increases at 7d to 43 MPa, but this value is still smaller than that of REF at the same age (59 MPa). This behavior is mainly related to the substitution of the cement weight by blast furnace slag. The latter presents a slower hydration reaction compared to Portland cement (as confirmed previously by its mass loss §6.2.1), and therefore, reduces the formation of the C-A-S-H gel responsible for improving the compressive strength of the mortar at early age.

The "f_c" of BFS (Figure 6.14) are higher than those of BM5 (34 MPa at 7d) by about 20% during the first week. Similarly, the addition of 5% CSA (BC5) decreases the compressive strengths by 18% at 3d (25 MPa) and by 10% at 7d (39 MPa) compared to BFS. Increasing the EA content to 10% (BM10 and BC10) results in a higher reduction in compressive strength (between 30% and 40%) compared to BFS during the first week. Their "f_c" is about 31 MPa at 7d. Due to the partial replacement of cement and blast furnace slag by 5% EA, the formation of C-S-H/C-A-S-H gel is reduced. This phenomenon is more important when increasing the EA content to 10%. Indeed, the addition of MGO and CSA leads to the formation of more hydrotalcite and ettringite respectively and less C-S-H/C-A-S-H gel [74, 131, 132]. Hence, the reduction in early age strength in the presence of EA can be attributed to the weaker chemical bonding presented by Ht and AFt when compared to the Van der Waals bonding presented by the C-S-H/C-A-S-H gels.

On the other hand, all the mixtures present an increase in their compressive strength as a function of time. At 28 days, BFS significantly increases its compressive strength (57 MPa) till finally achieving a value equal to 73 MPa at 90d, higher by 6% than that of REF (68 MPa). This behavior is due to the delayed hydration of blast furnace slag and the continuous formation of C-A-S-H gels at the long term. While BM5 continues to show smaller compressive strengths than BFS at the long term. The compressive strength of BM5 is 8% (52 MPa) and 17% (60 MPa) smaller than that of BFS at 28d and 90d. At 90 days, BM5 is slightly coarser than BFS (§6.2.3). This behavior is amplified by the addition of higher MGO content (BM10). So, the reduction of the compressive strengths at the long term of mixtures containing MGO is directly influenced by their total porosity. However, the compressive strength of BC5 increases continuously until it reaches values close to those of BFS at 28d (61 MPa) and 90d (73 MPa). This can be explained by the total porosity of BC5 being close to that of BFS at 90 days (§6.2.3) which is related to their close hydration process (§6.2.1). But, increasing the CSA content to 10% (BC10) further decreases the compressive strengths: BC10 is characterized by

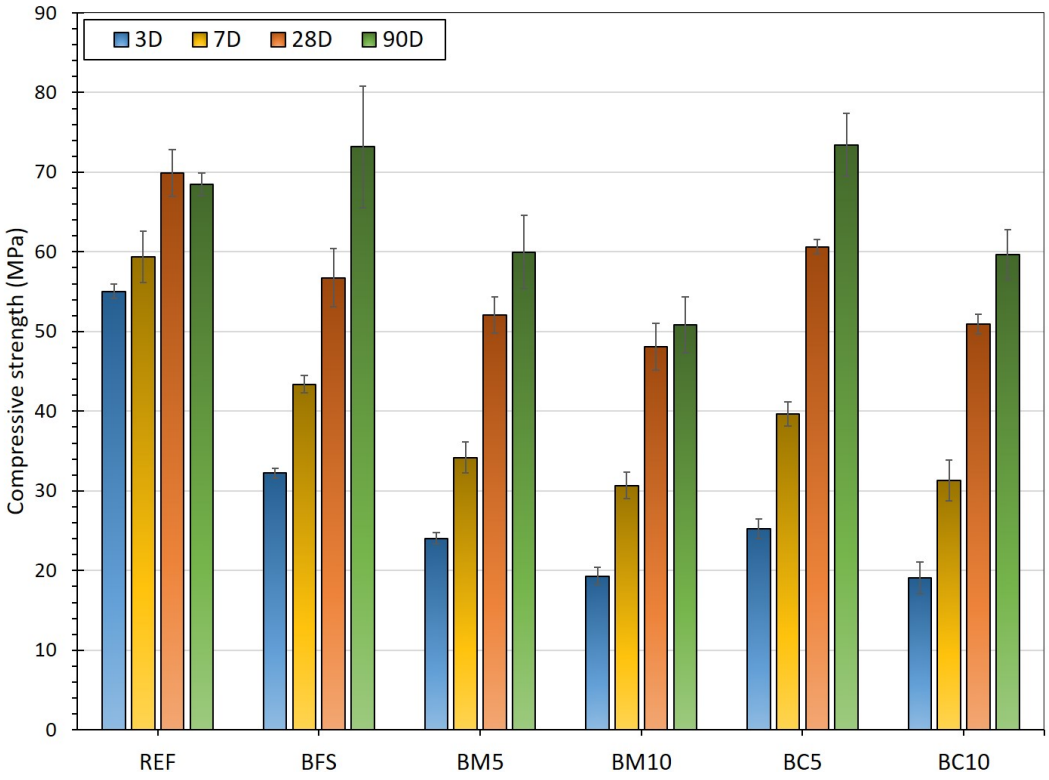

Figure 6.14 – Compressive strength evolution for all mixtures at 3, 7, 28 and 90 days.

a "f_c" values 11% (51 MPa) and 18% (60 MPa) lower than those of BFS at 28d and 90d. This behavior is influenced by the total porosity shown by BC10 at 90 days (§6.2.3).

Regardless of the different impacts shown by the addition of blast furnace slag and expansive agents on the mortar's 28-day compressive strength, this strength is acceptable and comply with the requirements of the European standard "EN 1504-3" as shown in Figure 6.15. The [EN 1504-3] standard proposes two requirements to identify the strength class for the tested mortar: non-structural (R1 and R2) and structural (R3 and R4) element. The mortars studied in this chapter are all classified in class R4 ($\geq$ 45 MPa).

The flexural strength "f_f" (Figure 6.16) of BFS is smaller by 14% (8.6 MPa at 7d) than that of REF (10 MPa at 7d) during the first week. The slow hydration of blast furnace slag could result in higher porosity for BFS than for REF at early age, resulting in lower flexural strength for BFS. The flexural strength of BM5 is about 16% (5.7 MPa and 6.5 MPa) lower than that of BFS at 3d and 7d respectively. This strength reduction can be explained by the slower hydration process of BM5 compared to BFS, which also results in higher porosity at early age. While at the same ages (3d and 7d), the addition of 5% CSA (BC5) improves the mortar's flexural strength (6.6 MPa and 8.6 MPa respectively). It is quite close to that of BFS at 3d and higher by 10% compared to BFS at 7d. The addition of 10% EA (BM10 and BC10) significantly decreases the flexural strength at 3d by 29% (4.8 MPa) and 25% (5.1

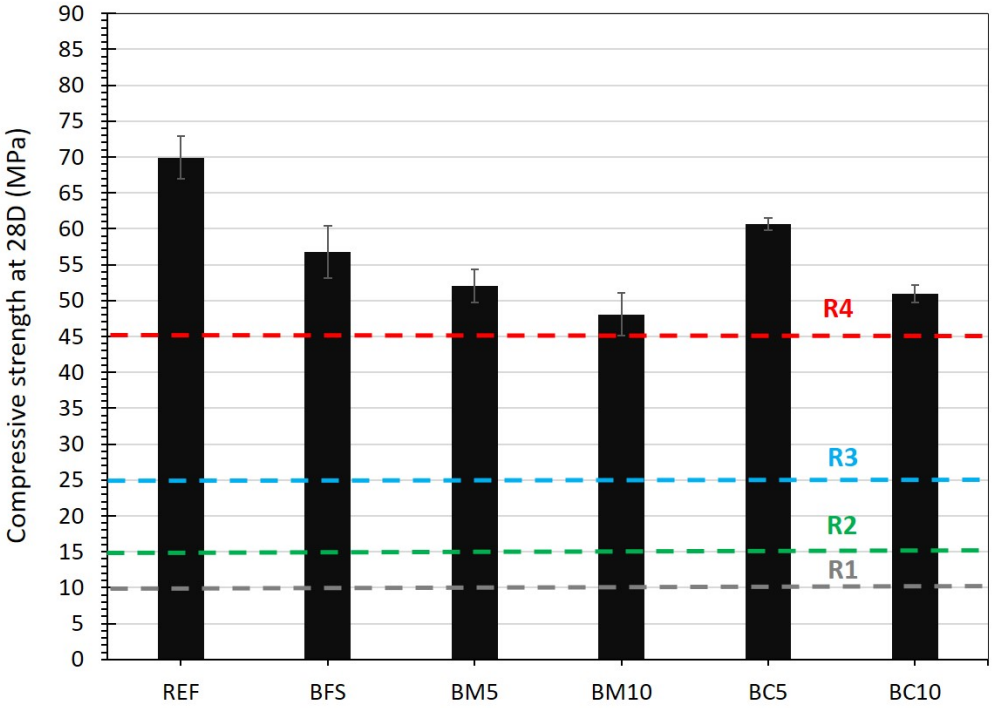

Figure 6.15 – Compressive strength at 28 days for all the studied mortars and the EN 1504-3 standard requirements: non structural (R1 $\geq$ 10 MPa and R2 $\geq$ 15 MPa) and structural (R3 $\geq$ 25 MPa and R4 $\geq$ 45 MPa) element.

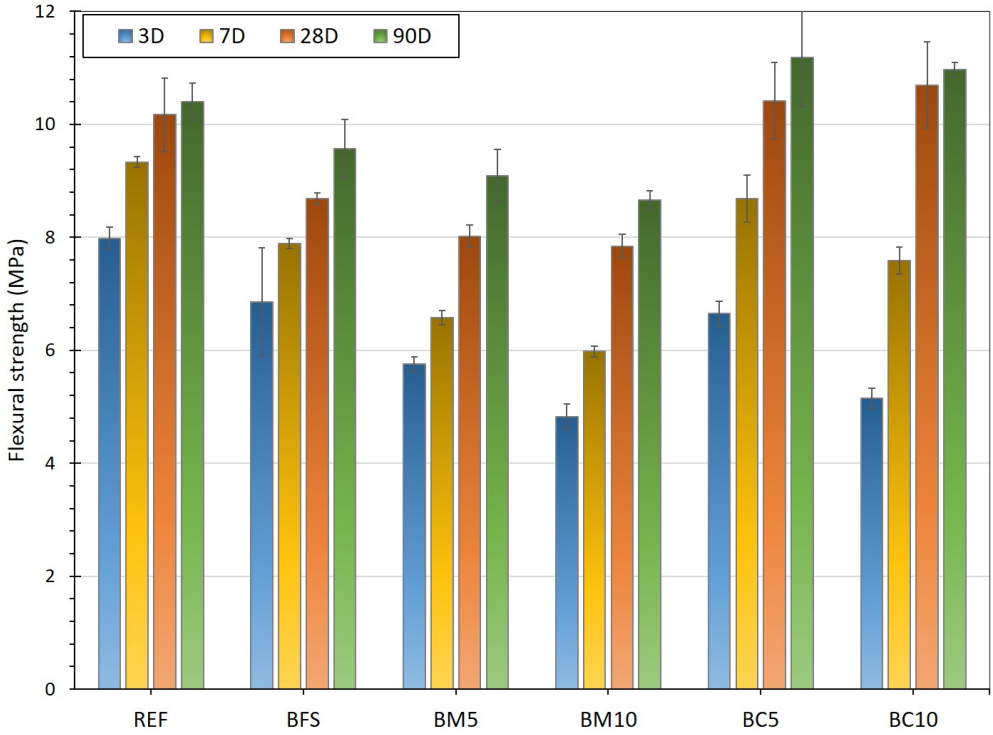

Figure 6.16 – Flexural strength evolution for all mixtures at 3, 7, 28 and 90 days.

MPa) respectively compared to BFS. At 7d, this behavior continues for BM10 (6 MPa), while BC10 regains its strength (7.6 MPa) and reaches a close value to that of BFS at the same age. Afterwards, mixtures with MGO (BM5 and BM10) continue to show flexural strength smaller than those of BFS at the long term (by 8% to 30%). Their "f_f" are equal to 9 MPa and 8.7 MPa at 90d respectively. While the mixtures with CSA (BC5 and BC10) show flexural strength values higher by 15% to 20% than those of BFS at 28d (10.4 and 10.7 MPa respectively) and 90d (11.2 MPa and 10.9 MPa respectively). So, these results confirm that the addition of MGO promote the formation of hydrotalcite more than C-A-S-H which reduces the flexural and compressive strength of the mortar at early age and the long term. This is evidenced by the anhydrous MGO found in these mixtures, and thus, the continuous formation of hydrotalcite more than C-A-S-H. While the addition of CSA forms excessive ettringite at early age that decreases the compressive strengths. After, the hydration of CSA is completed before 28 days, and the mixtures containing CSA can regain their flexural strength progressively. But, it is not the case for the compressive strength when increasing the CSA content to 10%.

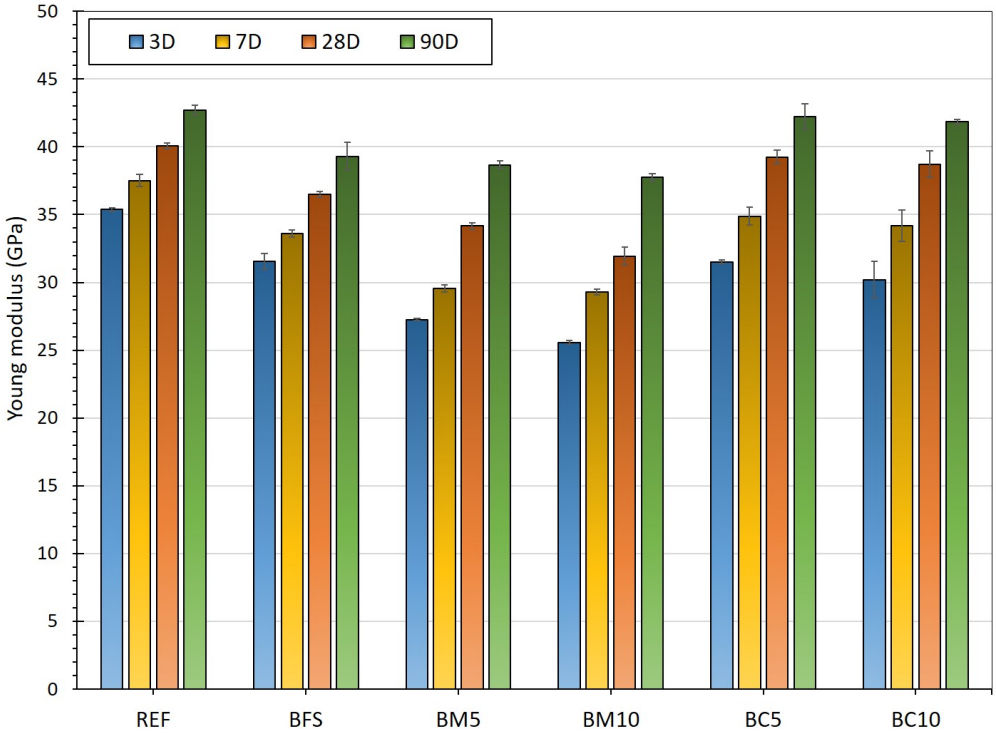

Figure 6.17 – E_{dyn} evolution for all mixtures at 3, 7, 28 and 90 days.

The dynamic Young's modulus is determined for all the studied mixtures at 3, 7, 28 and 90 days (Figure 6.17). For each mixture, the mortar's "E_{dyn}" evolution is quite similar to the evolution of its flexural strength. The results confirm that BFS has a higher porosity than REF at 3d, 7d and 28d, resulting in a smaller "E_{dyn}" at these ages (31.5 GPa, 33.6 GPa and 36.5 GPa respectively). However, this behavior continues at 90d (39.3 GPa) and it is not consistent

with the compressive strength and porosity of BFS compared to REF at this age. BFS, BC5 and BC10 present quite close "E_{dyn}" values at 3d (31 GPa). The addition of CSA (BC5 and BC10) increases gradually the "E_{dyn}" reaching higher values than those of BFS over time (42.2 GPa and 41.8 GPa respectively, at 90d). This might be related to the ettringite than can help the wave propagation during the velocity measurement used to calculate "E_{dyn}". This can explains the enhanced "E_{dyn}" values for these mixtures (BC5 and BC10). As for their flexural strength evolution, the addition of MGO decreases slightly the Edyn values compared to BFS (38.6 GPa for BM5 at 90d), and this behavior is amplified by the increase in MGO content (37.7 GPa for BM510 at 90d).

6.3.2 Autogenous deformation

The autogenous deformation results are presented in Figure 6.18 for all the studied mixtures. The average mass variation of all mixtures is equal to about 0.01% (Appendix (D)). This confirms the autogenous condition for all specimens.

Directly after demolding, BFS shrinks and reaches a value equal to -60 µm/m at 7 days. This value increases gradually to -150 µm/m at 28 days. The substitution of 50% of the cement weight by blast furnace slag has clearly reduced the mortar's autogenous shrinkage over time (BFS compared to REF). It is related to the slower hydration of blast furnace slag compared to Portland cement, resulting in a higher porosity at early age and reduced decappillary pressures in the pores. Moreover, the formation of hydrotalcite in BFS reduces the autogenous shrinkage due to its voluminous type [136]. However, the autogenous shrinkage of BFS continues up to 100 days, in contrast to the steady autogenous shrinkage behavior of REF since 40 days. The BFS continues its long-term hydration process and forms additional hydration products. This further refines its pore network and continues its autogenous shrinkage over time.

The addition of 5% EA allows reducing shrinkage thanks to a swelling of the matrix. It appears directly for BC5 and it is equal to +55 µm/m at 5 days. This behavior is associated with the additional ettringite that forms with the addition of 5% CSA (BC5) as explained previously (§6.2.1). The ettringite is characterized by its expansive behavior, generating swelling pressure into the matrix. On the other hand, after a low shrinkage during the first day (-30 µm/m) for BM5, this mixture swells during the first week (+70 µm/m). This behavior is related to the slower hydration process presented by BM5 compared to BFS (§6.2.1), resulting in reduced decappilary pressures in the pores during the first day. After, the addition of 5% MGO increases the formation of additional hydration products (§6.2.1), which might decreases the autogenous shrinkage faster than BFS by a swelling of the matrix. After the first week, the swelling kinetics of BM5 slows down and the deformation tends to a constant value equal to about +100 µm/m. It seems that in autogenous condition, the formation of hydrotalcite is relatively low after 7 days due to the limited water supply. BM5 also showed anhydrous MgO at

28 days when cured at HR=95% (§6.2.2). Even in a humid curing, there is still anhydrous MgO in the matrix. So, in an autogenous condition, it is evident that the formation of hydrotalcite is low because it requires a lot of water. A different behavior is observed for BC5. After 5 days, it shrinks rapidly till reaching a shrinkage equal to -55 µm/m at 28 days and -120 µm/m at 100 days. It is due to the CSA hydration that is fast and can be complete before 28 days as confirmed previously (§6.2.2). In autogenous condition, it seems that the addition of 5% CSA can produce ettringite till 5 days, reducing the autogenous shrinkage during this period, but afterwards, the autogenous shrinkage increases again.

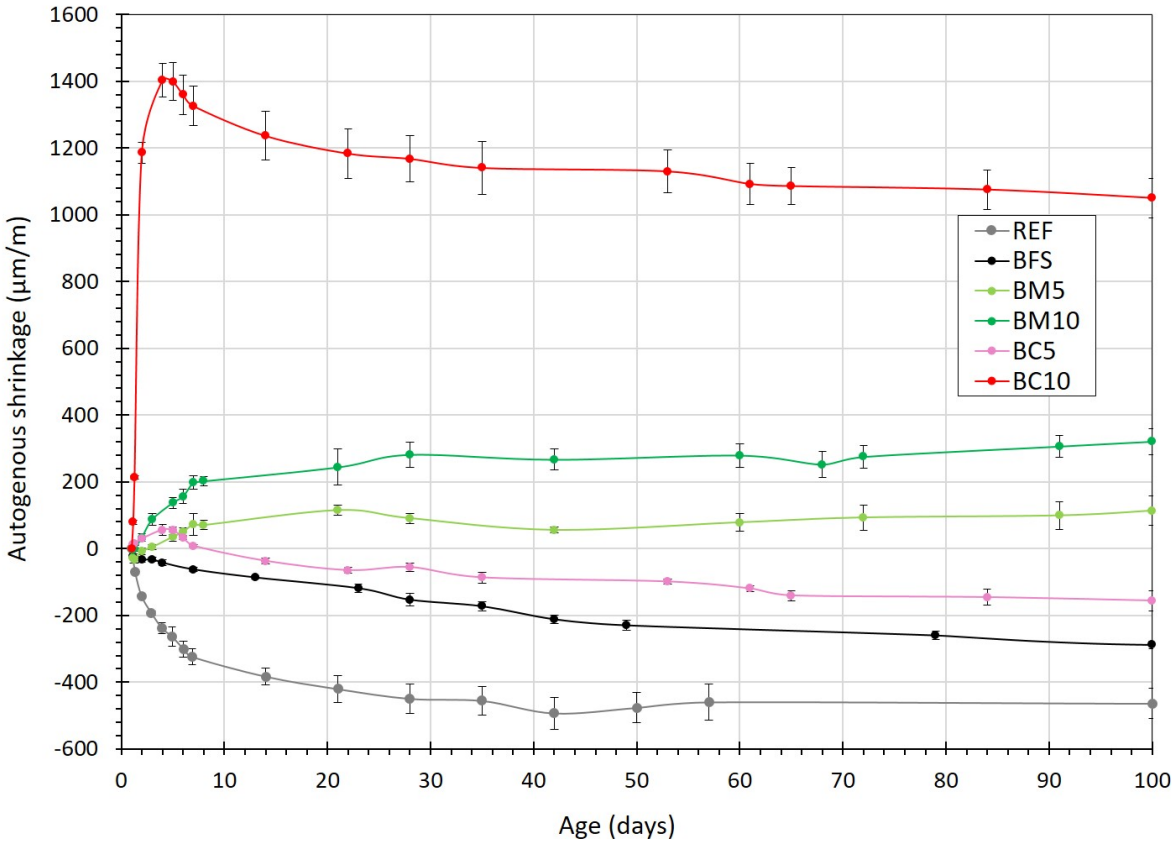

Figure 6.18 – Evolution of the autogenous deformation for all the studied mixtures.

The increase in EA content to 10% allows balancing the autogenous shrinkage from the first day for BM10 and its matrix swells to +200 µm/m at 7 days and tends to a constant value beyond 28 days (about +300 µm/m). Thus, the addition of 10% MGO offsets the shrinkage more quickly and the matrix swells through 28 days due to the larger amounts of hydrotalcite that have formed. For BC10, an important and rapid swelling is observed with a maximal value equal to +1400 µm/m at 5 days. This behavior is associated with the excessive production of ettringite that occurred at an early age, generating swelling pressures to the matrix [137, 138]. Therefore, the matrix shrinkage is effectively offset at early age. After, it shrinks rapidly and

reaches a deformation value equal to +1170 µm/m at 28 days and +1050 µm/m at 100 days. Its behavior is similar to that of BC5 and is due to the fast hydration of the CSA addition and the production of ettringite at early age reducing the autgenous shrinkage. But afterwards, the autogenous shrinkage increases again.

6.3.3 Total deformation

The results of total deformation for the specimens are presented in Figure 6.19. All the mixtures show a mass loss equal to 0.5% at 4 days (Appendix (D)). This mass loss is due to the hydric exchanges between specimens and their environment (RH = 95% in the humidity room). After, they gradually regain their mass and the initial shrinkage is balanced since the first day (except REF and BFS) (Figure 6.19).

Contrary to REF, BFS shrinks very slowly during the first week until 13 days and reach a deformation equal to -37 µm/m at this time. The slow hydration of blast furnace slag helps in reducing the total shrinkage at early age due to the progressive formation of C-A-S-H and hydrotalcite into the pores. Then, BFS's shrinkage is offset and it reaches a deformation equal to +20 µm/m at 28 days. After the WC, it starts to swell progressively until +160 µm/m at 100 days. The substitution of 50% of the cement by blast furnace slag reduces effectively the total shrinkage of the mortar. It produces C-A-S-H and hydrotalcite that are two voluminous hydration products [131].

The addition of 5% EA (BM5 and BC5) offsets the matrix shrinkage from the first day (+5 µm/m and +50 µm/m respectively) thanks to a matrix shrinkage. Its kinetic is faster for BC5 than for BM5. It is related to the faster ettringite formation when the RH=95% compared to the hydrotalcite, leading to an excessive matrix expansion since the first day. Then, their swelling is increasing and it reaches a value equal to +110 µm/m and +75 µm/m respectively at 7 days. These values reach +210 µm/m and +130 µm/m respectively at 28 days. In a high-humidity environment (RH=95%), the hydration of CSA is very fast and seems to be consumed quickly (contrary to the behavior of CSA in autogenous condition). Hence, beyond 3 days, given the similar mass losses between BFS and BC5, this means that no new ettringite phase can be formed beyond 3 days. This leads to a slow swelling kinetic for BC5 and close to that of BFS. This may also explain the evolution of the mechanical strengths of BC5 in the long term where no ettringite can be formed to reduce its strengths due to its expansive behavior.

Increasing the EA content to 10% (BM10 and BC10) further accelerates the shrinkage reduction and the matrix expansion. Indeed, BM10 present a swelling value equal to +240 µm/m at 7 days, which is related to the excessive hydrotalcite formed by the addition of 10% MGO. This is supported by [131] that confirms that high MGO content increases the formation of more hydrotalcite and less C-S-H. On the other hand, this can explain the evolution of the mechanical strength of BM10. While BC10 is characterized by the highest swelling value at 2

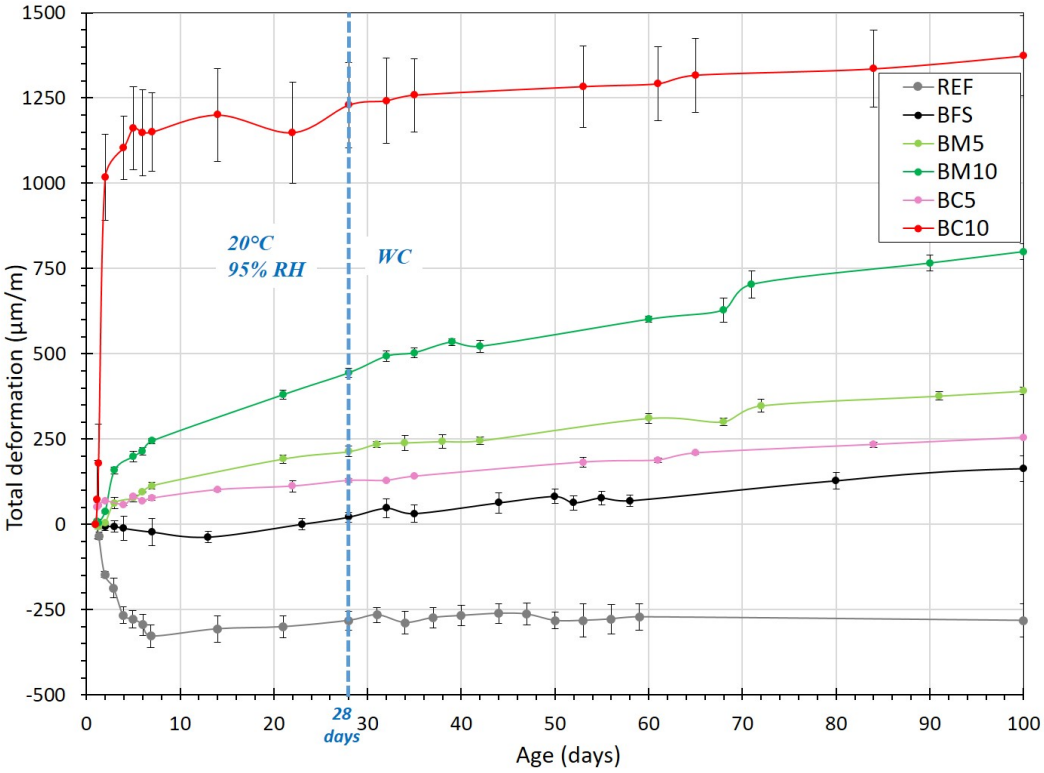

Figure 6.19 – Evolution of the total deformation for all the studied mortars.

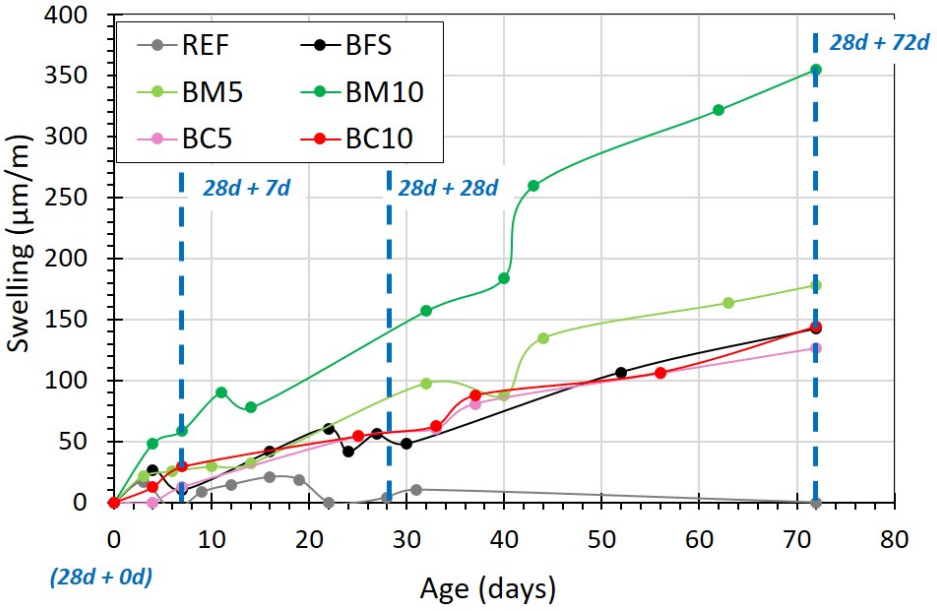

Figure 6.20 – Swelling values for all the studied mixtures from 28 days of WC.

days (+1000 µm/m), which is related to its excessive ettringite formation. After, its swelling kinetic is quite slow and close to that of BFS (+1230 µm/m at 28 days), while it is fast for BM10 (+440 µm/m at 28 days). This difference of behavior is related to the early consumption of the CSA addition, while MGO addition tends to continue its hydration process and the hydrotalcite formation more than 28 days (§6.2.2).

After the WC (at 28 days) (Figure 6.20), the swelling continues to increase for BM5 and BC5 until reaching values equal to +390 µm/m and +250 µm/m respectively at 100 days. Similarly, BM10 and BC10 reach swelling values equal to +800 µm/m and +1400 µm/m respectively. The swelling behavior of the mixtures with CSA is so similar to that of BFS, as confirmed earlier. The water curing does not amplify the swelling mechanism of BC5 and BC10 since the hydration of CSA is completed before 28 days. Their swelling mechanism is due to the delayed hydration of blast furnace slag, C_2S and C_3S. However, mixture with 5% MGO (BM5) present a more important swelling values due to the continuous hydration of anhydrous MgO, producing more hydrotalcite. This behavior is amplified by increasing the MGO content to 10% (BM10).

6.3.4 Cracking sensibility

In order to estimate the sensitivity to cracking under restricted autogenous deformation conditions, the Cracking Sensitivity Index (CSI) is calculated by combining several mechanical properties: autogenous deformation, flexural or compressive strength and dynamic young modulus. The second mechanical properties are used as they allow estimating the tensile or compressive stresses that can occur as a result of restricted or swelling deformations respectively. The third mechanical property is used as it can affect the magnitude of stresses associated with autogenous deformation. Thus, a higher value of this index indicates a more important cracking sensitivity of the studied material. If the index reaches a value equal to 1, cracking should occur under fully restrained conditions. Nevertheless, this index does not take into account the beneficial effect of relaxation (decrease of internal stresses) which varies according to the studied material. The CSI for all the studied mixtures is presented in Figure 6.21 at 3d, 7d, 28d and 90d.

The addition of blast furnace slag (BFS) results in a significant decrease in its CSI during the first week: the CSI is equal to 0.22, 80% lower than that of the REF at 7 days. This behavior continues in the long term, but BFS reaches a CSI close to 1 at 90 days. On the other hand, the addition of MGO (BM5 and BM10) leads to a CSI value below 0.1 at 3 days. Furthermore, the CSI of BM5 decreases with time due to its reduced autogenous shrinkage compared to BFS. While the CSI of BM10 increases very slowly with time but remains less than 0.2 at 90d. These results indicate the safety of adding 5% and 10% MGO which significantly improves the cracking sensitivity of the blended mortar in a restricted autogenous condition.

Similar observations can be made for mixtures containing CSA (BC5 and BC10). BC5 shows a rather zero CSI value during the first week, related to its slight swelling behavior during this period. After 7 days, its CSI increases until it reaches 0.56 at 90 days. BC10 shows higher CSI values than BFS during the first week (0.45 at 7 days), mainly due to its excessive swelling behavior at this time. However, beyond 7 days, its CSI value decreases significantly, consistent with its swelling behavior, until it reaches 0.14 at 90 days. Thus, these results ensure the safety of adding 5% and 10% CSA to improve the cracking sensitivity of the blended mortar in a restricted autogenous condition.

Consequently, these results indicate that the ternary blend of cement-blast furnace slag-EA is a promising mixture to limit the cracking sensitivity, much more than a mixture with 100% Portland cement and the cement-blast furnace slag mixture.

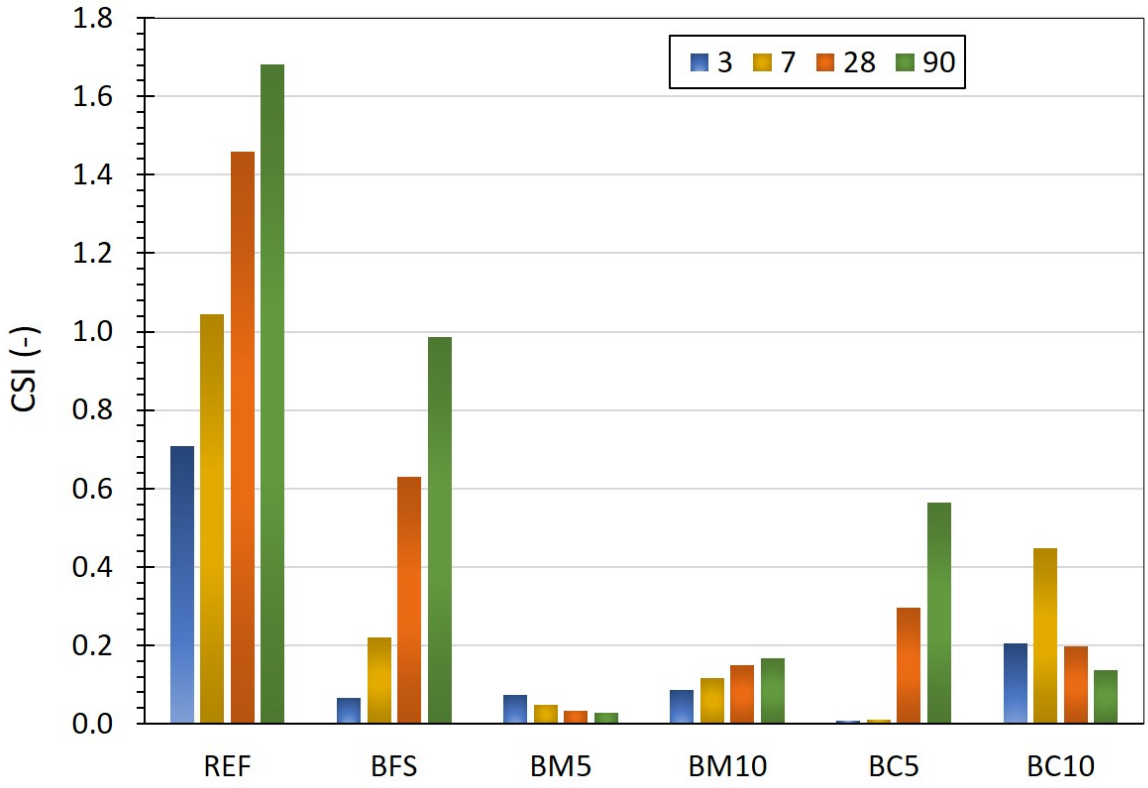

Figure 6.21 – Evolution of the Cracking Sensitivity Index (CSI) for all the studied mixtures.

6.3.5 Summary

The main objective of this section is to evaluate the benefits of adding blast furnace slag and EA on the mechanical properties of cement-based mortar. The addition of blast furnace slag and EA slightly decreases the compressive strengths of the mortar at early age and in the long term. However, despite this decrease, all the proposed mixtures have high compressive

strengths at 28 days (greater than 45 MPa - Class R4), which confirms their compliance with the repair requirements. Furthermore, the addition of EA to the blended mortar significantly improves its cracking sensitivity in a restricted autogenous condition. Thus, ternary mixtures of cement-blast furnace slag-EA constitute a promising mortar that can be used for repair application and limit the cracking sensitivity. Furthermore, the addition of blast furnace slag increases the long-term swelling behavior of the mortar, which is a preferable mechanism to allow for autonomous healing. This mechanism is further promoted by the mixtures containing MGO thanks to their hydration process and additional hydration products that allow for a higher long-term swelling behavior than other mixtures.

6.4 Self-healing capacity

The self-healing capacity is evaluated through a crack width monitoring on the specimen surfaces (2D measurement) and a water permeability testing (3D measurement). To determine the healing kinetics, these measurements are performed on cracked specimens at the cracking age (0D), and after several curing duration: 7 days (7D), 28 days (28D) and 90 days (90D). In this chapter, the specimens are cured only under Water Curing (WC). Moreover, the main healing products are identified on the crack surface and into the crack.

6.4.1 2D monitoring

For the different studied mixtures, the average residual Crack Width "CW" obtained after the splitting test (at 0D) varies from 215 µm to 239 µm (Table 6.2). The evolution of CW as a function of their initial values (at 0D) is shown in Figure 6.22 for all the studied mixtures.

Moreover, the HR is also calculated at a constant water pressure equal to 15 cm for all the specimens. The evolution of this HR as function of the initial CW is presented in Appendix D for all the studied mixtures.

CW (μm)	Min	Max	**Average**
BFS	112	450	**237**
BM5	113	441	**236**
BM10	95	454	**239**
BC5	113	435	**222**
BC10	100	410	**215**

Table 6.2 – Minimal, maximal and average Crack Width (CW) measured after the splitting test at 0D.

As for the Portland cement mortars (Figure 5.24), the kinetics of crack healing is influenced by the initial CW [96]. Indeed, the majority of the specimens with an initial CW ranging

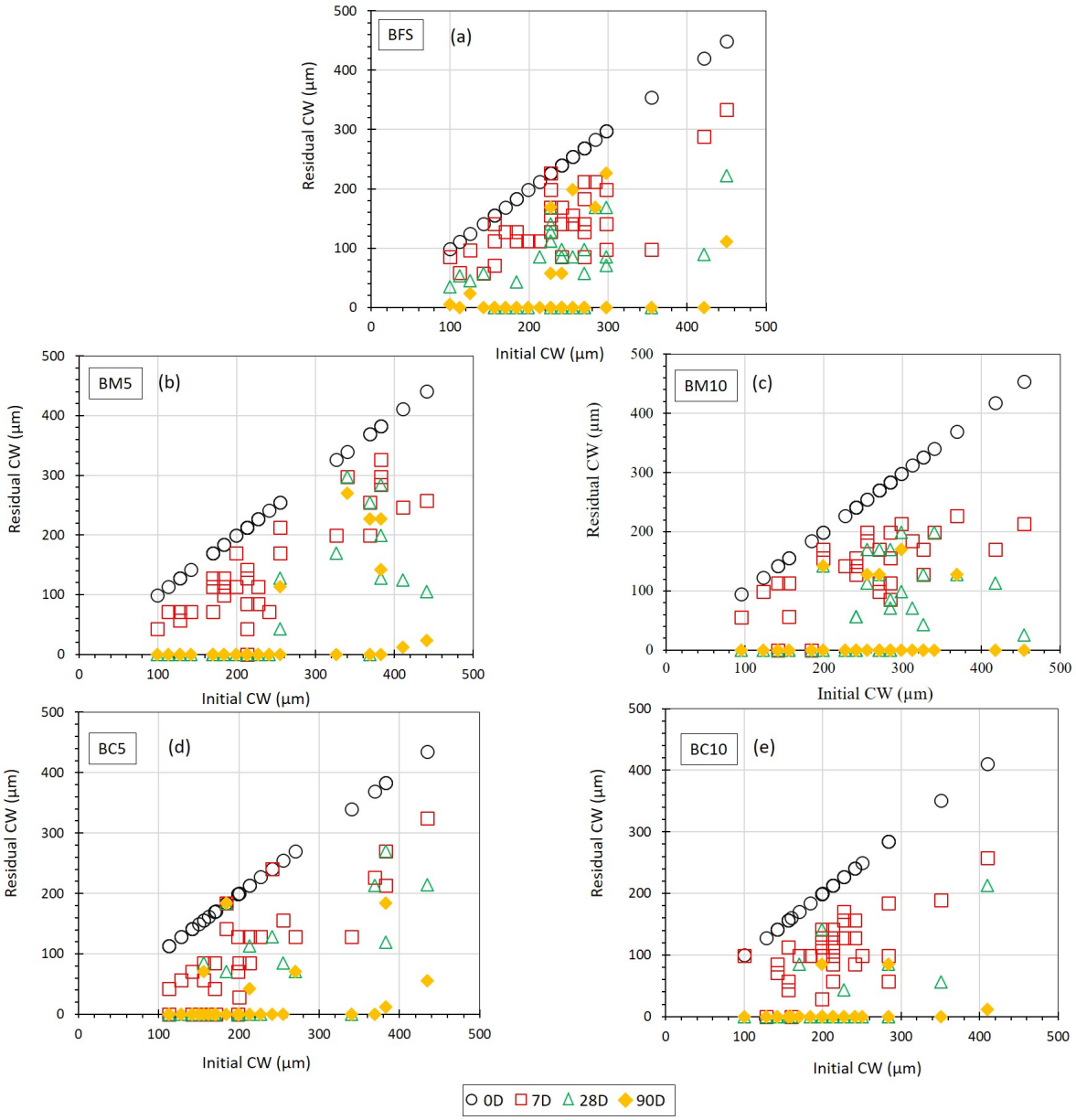

Figure 6.22 – Crack Width (CW) evolution for BFS (a), BM5 (b), BM10 (c), BC5 (d) and BC10 (e) cured under WC.

from 100 µm to 250 µm are completely healed after a curing duration equal to 28 days under WC (Figure 6.22). This observation is available for all the studied mixtures. In addition, the majority of large CW ([250-500] µm) are completely healed after a longer WC duration (at 90 days) for all the studied mixtures. But, it appears that mixtures with MGO (BM5 and BM10, Figures 6.22(b, c)) show a crack healing that is slightly faster than that of other mixtures (BFS, BC5 and BC10, Figures 6.22(a, d, e)), when the initial CW is equal to [300-500] µm. This is because the majority of these CW are decreased to less than 150 µm after 28 days (Figures 6.22(b, c)) compared to the CW of other mixtures. For the studied mixtures, the mechanisms responsible to the crack healing potential are further hydration, carbonation and matrix expansion. These mechanisms modify the crack dimensions through all the specimen. So it is necessary to monitor the healing process on all the crack depth thanks to a water permeability tests.

6.4.2 3D monitoring

In this paragraph, the healing rate is presented as function of the initial Crack Width (CW). Two initial WF ranges are selected: [0.01-0.02] l/min and [0.02-0.04] l/min. The CW corresponding to these WF ranges are giving in Table 6.3. So, for each CW range, Figure 6.23 compares the HR evolution of all the studied mixtures cured under WC.

Table 6.3 – Initial WF for specimens having a similar CW at 0D.

Initial WF (l/min)	[0.01-0.02]	[0.02-0.04]
Initial CW (μm)	[100-250]	[250-500]

For an initial CW = [100-250] µm: At 7 days of curing, BM5 and BFS present the most important HR: 40% and 39% respectively. The other mixtures present a HR equal to 35%, 35% and 32% for BM10, BC10 and BC5 respectively. So the healing rate is superior to 30% for all the studied mixtures after one week curing. After, the healing process slows down and all mixtures exhibit a quite similar healing rate varying from 47% to 52% after 28 days of curing. Finally, the healing rate is slightly more important for the mixtures with 5% of EA after 90 days of curing: 100% and 95% for BC5 and BM5 respectively. But the difference with the other mixtures is low. Their HR is equal to 93%, 91% and 92% for BFS, BM10 and BC10 respectively. So, the benefit of EA is limited to promote the healing crack characterized by width inferior to 250 µm. That confirms that the main mechanisms of healing for these crack healing is further hydration and carbonation.

For an initial CW = [250-500] µm: At 7 days of curing, the mixtures with MGO (BM10 and BM5) and the one with 5% CSA (BC5) show the highest HR values: 20%, 18% and 17% respectively. The HR of the other mixtures (BFS and BC10) is equal to 14% and

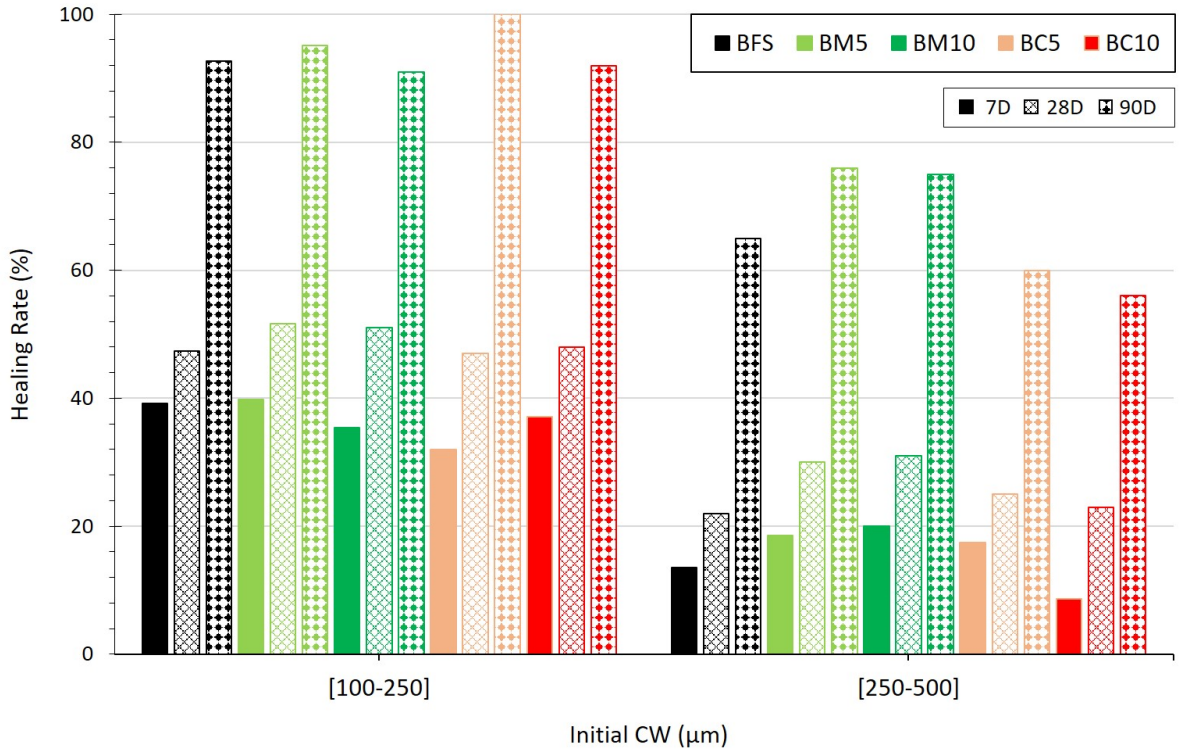

Figure 6.23 – HR evolution for specimens having an initial WF of [0.01-0.02] l/min and [0.02-0.04] l/min for all the studied mixtures.

9% respectively. Thus, the addition of two contents of MGO (5% and 10%), as well as 5% of CSA improves the self-healing after one week of curing. As the curing period advances (up to 28 days), the addition of MGO (BM10 and BM5) is consistently beneficial in promoting crack healing. The HR of these mixtures is equal to 31% and 30% respectively. On the other hand, the mixtures with CSA (BC5 and BC10) present a relatively lower HR than the mixtures with MGO (25% and 23% respectively), but is slightly higher than that of BFS (22%). Thus, it appears that the effect of CSA content (5% and 10%) on crack healing decreases with the curing time. After 90 days of curing, the addition of MGO is continuously beneficial: BM5 and BM10 reach HR values equal to 76% and 75% respectively. BC5 and BC10 reach the lowest HR values (60% and 56% respectively), comparing with BFS (HR = 65%). Therefore, both EA (MGO and CSA) have a beneficial effect on crack healing during the first days of curing. But in the long term, only the addition of MGO shows a significant positive impact on the crack autonomous healing. This difference in behavior is related to the fact that the addition of EA is advantageous when it is necessary to promote the autonomous healing for large cracks through matrix expansion (Figure 6.20). This mechanism accelerates the crack closure over time.

Indeed, BFS and mixtures with CSA (BC5 and BC10) show similar matrix expansion since 28 days (i.e. the age of cracking -Figure 6.20), which may explain their relatively close healing

behavior over time. Their matrix expansions are smaller than those of the mixtures with MGO (BM5 and BM10). Thus, the latter show a faster healing behavior at early and long term curing, which is supported by the autonomous healing. The anhydrous MGO present in their mixtures further promotes this mechanism during water curing.

6.4.3 Self-healing products on the specimen surface

During the monitoring of the crack width on the specimen surfaces, the formation of white products were observed along the crack for all the studied mixtures (Figure 6.24). These products are mainly carbonate-containing phases (Figure 6.25).

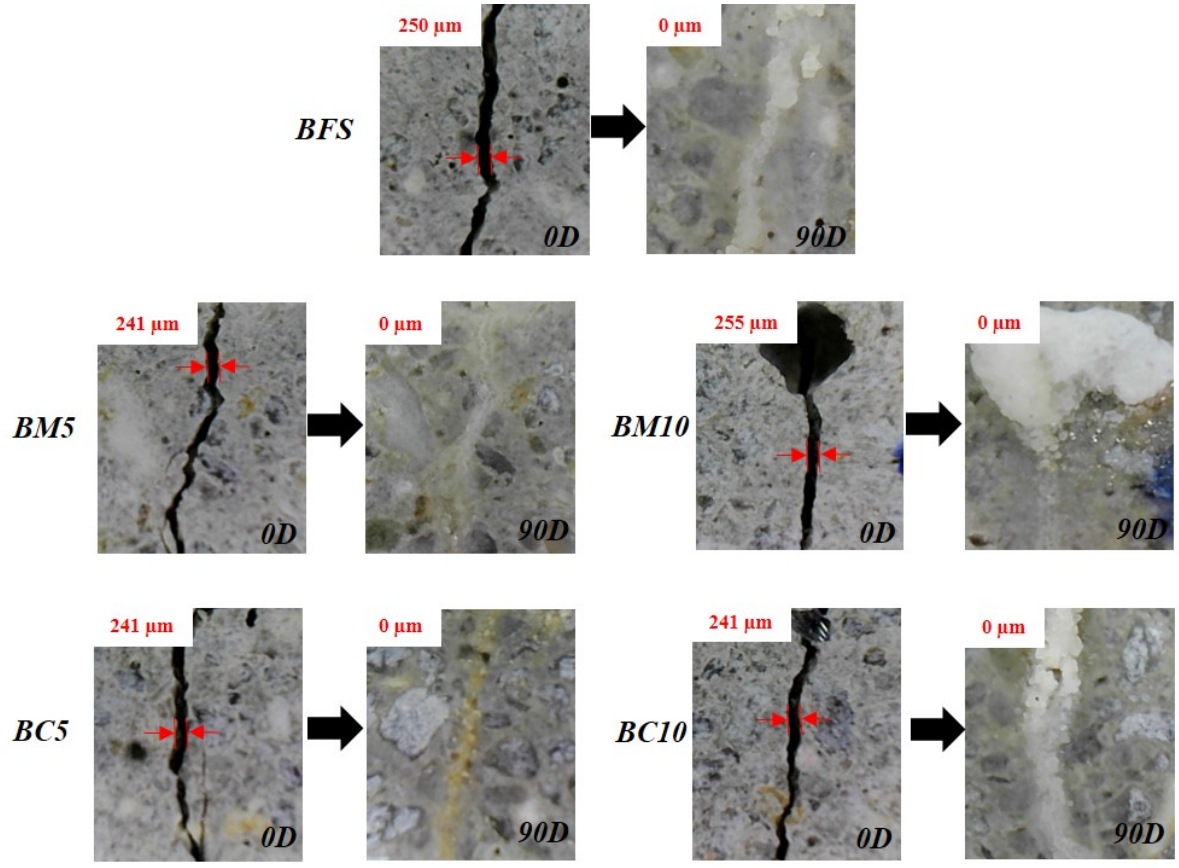

Figure 6.24 – Crack on the specimen surfaces at 0D and 90D for all the studied mixtures.

The morphology of the carbonates located on the crack surface is observed using SEM-EDX observations for BFS, BM10 and BC10. The EDX analysis is made at defined spots for each mixture. Different morphology of the carbonates are presented as a function of each mixture depending on several parameters, e.g. temperature, CO_2 pressure, pH, etc... [20, 119].

Based to the results obtained for BFS (Figure 6.26), it shows products with cubic morphology formed along the crack, in which they contain magnesium (Figure 6.26(d)). According to

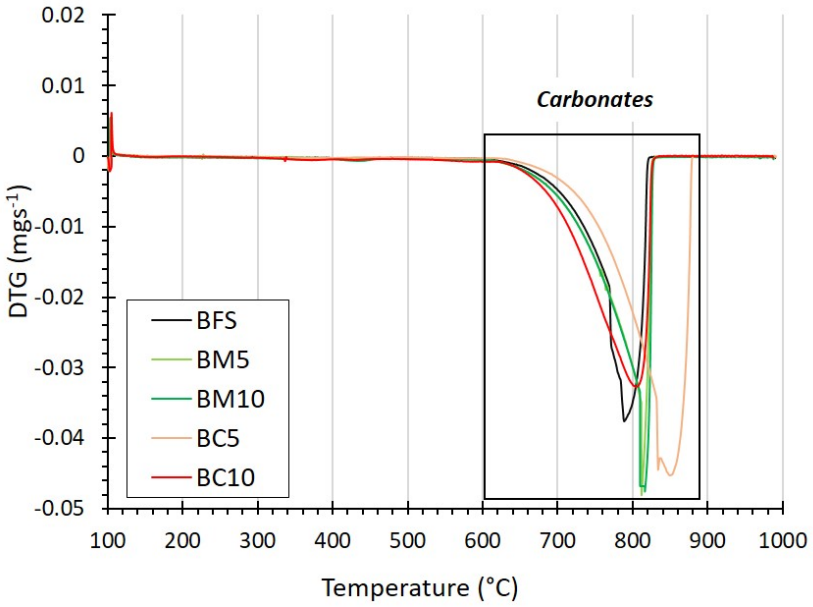

Figure 6.25 – DTG curves of the white products formed on the crack surface of each mixture.

[119, 121], these products are called magnesian calcites ($Mg_xCa_{(1-x)}CO_3$) where Mg partially substitutes Ca with a variable degree of replacement "x". Magnesian calcites are formed in the $CaO - MgO - CO_2 - H_2O$ system and "x" is the molar ratio of $[Mg^{2+}]/[Ca^{2+}]$ ($0 < x < 1$). But, according to [119], when the ratio Mg/Ca is higher than 0.5, it can be an indication for the formation of brucite, hydromagnesite and even hydrotalcite. In our EDX analysis, the atomic ratio of Mg/Ca will be given hereafter. Hence, In the case of BFS, the atomic ratio of Mg/Ca is equal to 0.033, which confirms the presence of magnesian calcites on the crack of BFS with a cubic morphology (Figure 6.26(c)).

Cubic magnesian calcites are also presented on the BM10's crack as shown in Figure 6.27(a). Furthermore, its Mg/Ca atomic ratio is greater (0.057) than in the case of BFS. This ensures that as the concentration of $[Mg^{2+}]$ ions increases (due to the addition of 10% MGO), the replacement of Ca by Mg increases. Additionally, these magnesian calcites appear to be formed and clustered on other magnesian calcite products (Figure 6.27(b,d)). The latter, having a very small atomic ratio of Mg/Ca ($\sim 9\text{x}10^{-3}$), present a needle-like morphologies. They are therefore attributed to magnesian calcites of the aragonite type. For BC10 (Figure 6.28), also cubic magnesian calcites are formed on its crack with an atomic ratio Mg/Ca equal to 0.033 ((Figure 6.28(c)). So, these results confirm the presence of magnesian calcites for BFS, BM10 and BC10. The addition of 10% MGO promote the formation of different morphology of the magnesian calcites.

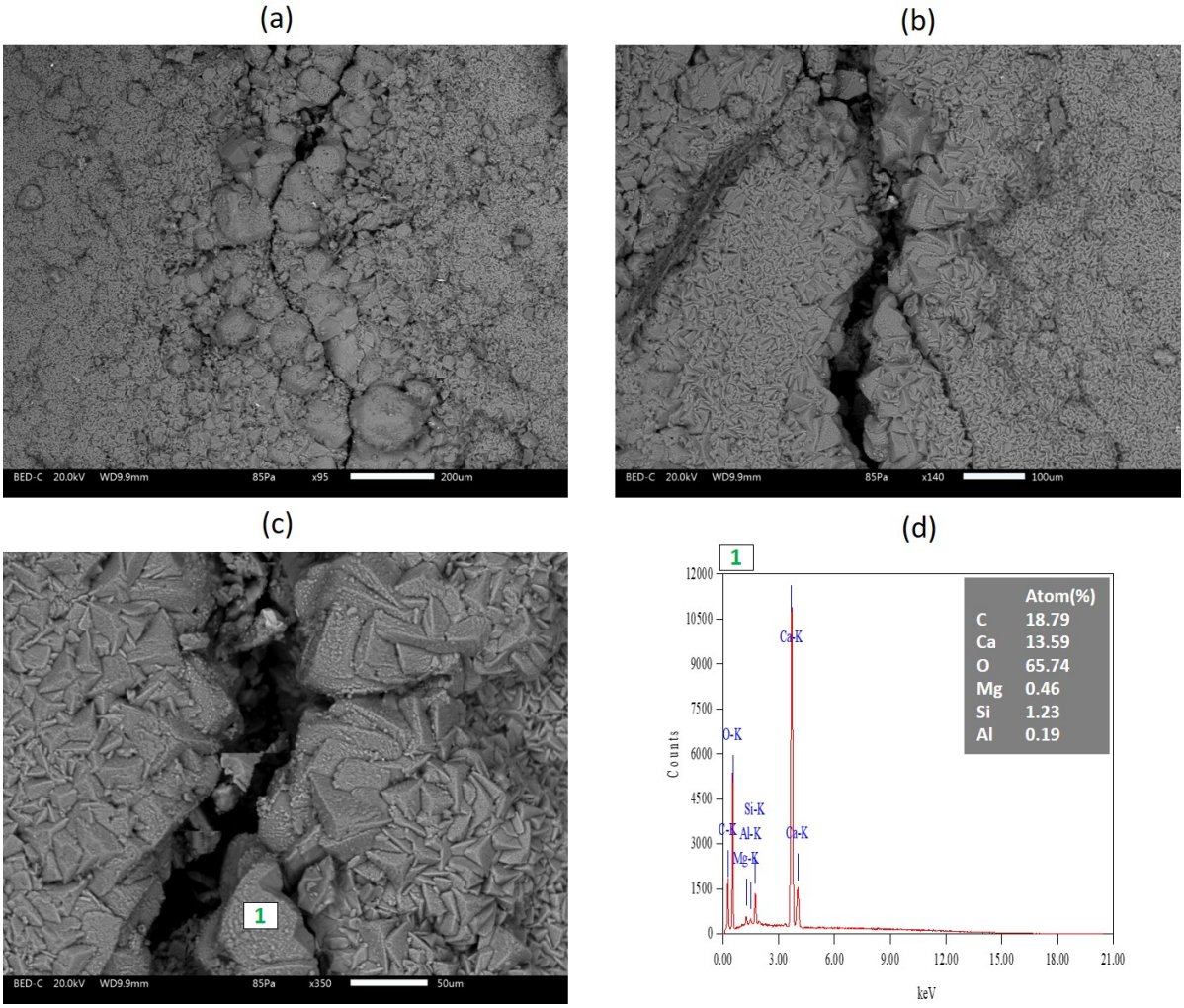

Figure 6.26 – SEM observation of self-healing products along the crack for BFS and its EDX analysis.

6.4.4 Self-healing products inside the crack

SEM-EDX observations are performed inside the crack for BFS, BM10 and BC10 to identify the internal self-healing products. For BFS, Figures 6.29(a-c) show products characterized by a Ca/Si = 0.89, Al/Si = 0.12 and a small Mg/Si = 0.08 ratio. According to [124], the C-S-H type gel has a Ca/Si atomic ratio that can vary between 0.2 and 1.7. In addition, the aluminum content (Al/Si) is significant, indicating that this type of gel is C-A-S-H [139]. The Al/Si ratio in the C-A-S-H gel cannot exceed 0.25 according to [139]. Another C-S-H gel admits a Ca/Si ratio equal to 0.29 and a very low Al/Si ratio = 0.02 (Figure 6.29(d-f)). It is therefore attributed to the C-S-H gel.

For BM10, the presence of C-A-S-H gel is detected in Figure 6.30(b,c), and its Ca/Si, Al/Si and Mg/Si ratios are respectively equal to 1.48, 0.19 and 0.21. Another product (Figure 6.30(c))

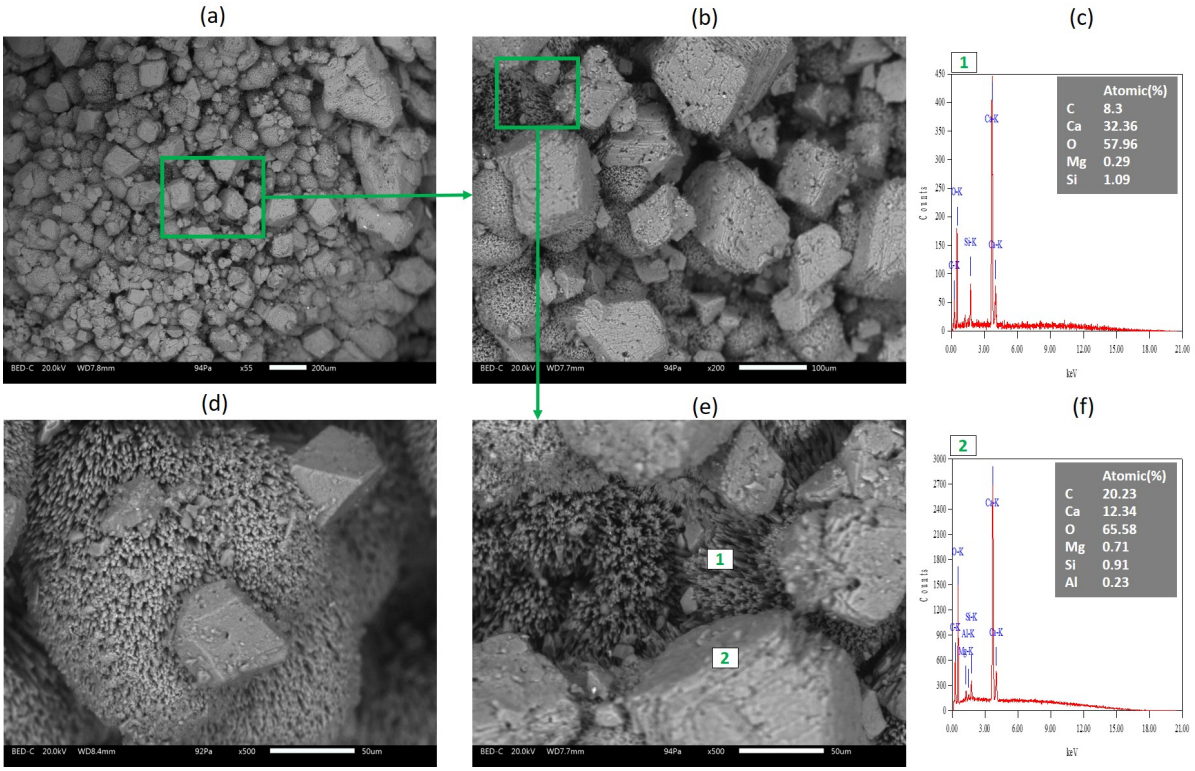

Figure 6.27 – SEM observation of self-healing products along the crack for BM10 and its EDX analysis.

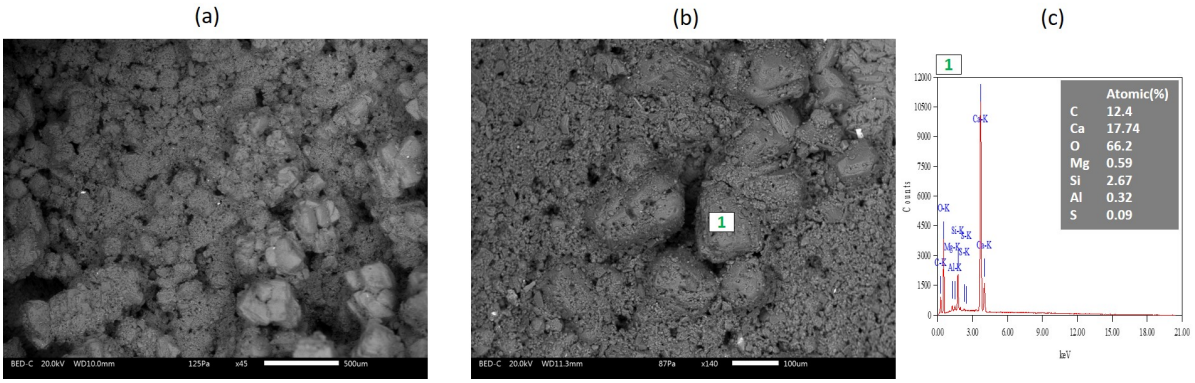

Figure 6.28 – SEM observation of self-healing products along the crack for BC10 and its EDX analysis.

shows a significant Mg content, indicating that this product can be attributed to M-S-H. Indeed, a ratio of Mg/Al = 5.2 suggests the presence of additional Mg-rich phases such as M-S-H gel [119]. Another hypothesis is that an Mg/Ca ratio greater than 0.5 (in this case is equal to 0.57) indicates the formation of hdyrotalcite [119]. However, the presence of a significant amount of Si confirms the presence of M-S-H. So, a high MGO content (10%) promotes the formation of Mg-rich phases such as M-S-H [125]. While for BC10, C-A-S-H is found as shown in Figure 6.31. Its EDX analysis (Figure 6.31(c,f)) show Al/Si ratios equal to 0.12 and 0.13 respectively.

So, these results confirm the presence of C-A-S-H as common healing products formed within the cracks of BFS, BM10 and BC10. These products are formed by the hydration of remaining unhydrated tricalcium and dicalcium silicate (C_3S and C_2S), as well as the delayed hydration of the blast furnace slag. Therefore, the addition of blast furnace slag and 10% EA is benefit to increase the further hydration mechanism, and thus, the self-healing capacity. Furthermore, the anhydrous MgO present in BM10 promotes the formation of additional healing products such as M-S-H gel. This observation is consistent with its higher healing capacity compared to BFS and BC10 as shown previously. Therefore, the addition of 10% MGO increases the self-healing process through further hydration, carbonation and matrix expansion.

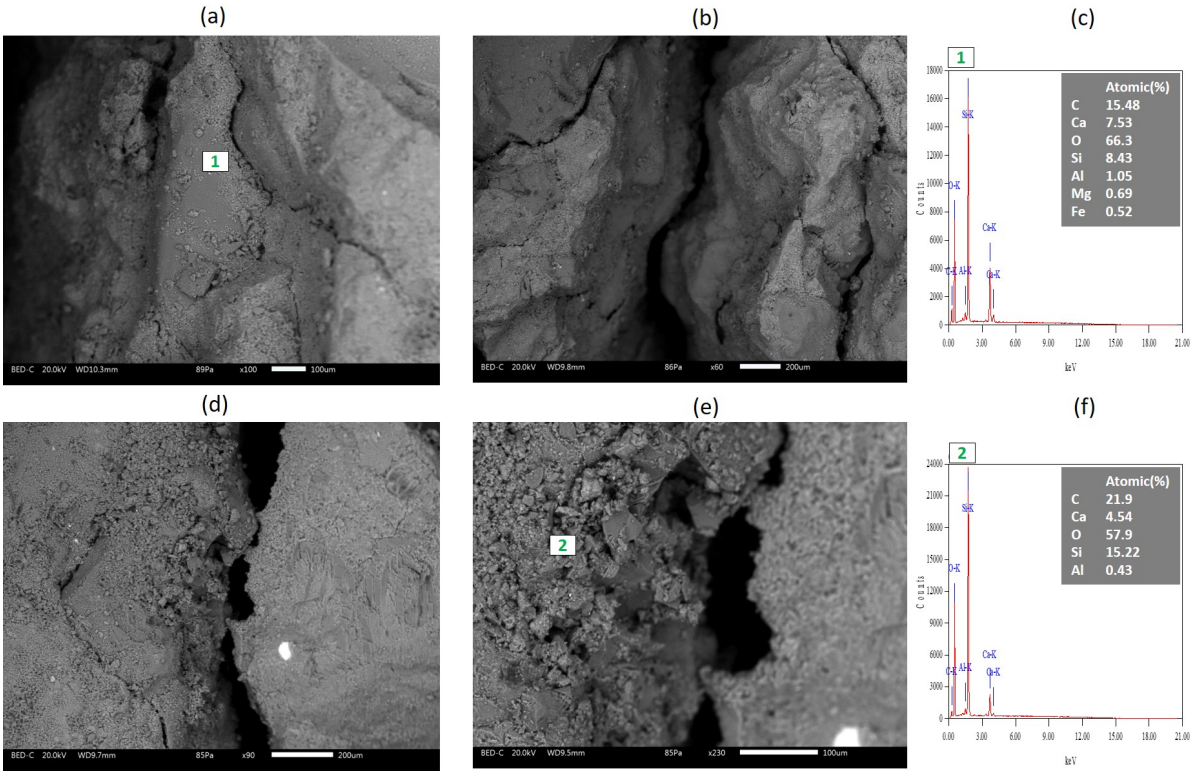

Figure 6.29 – SEM observation of self-healing products inside the crack for BFS and its EDX analysis.

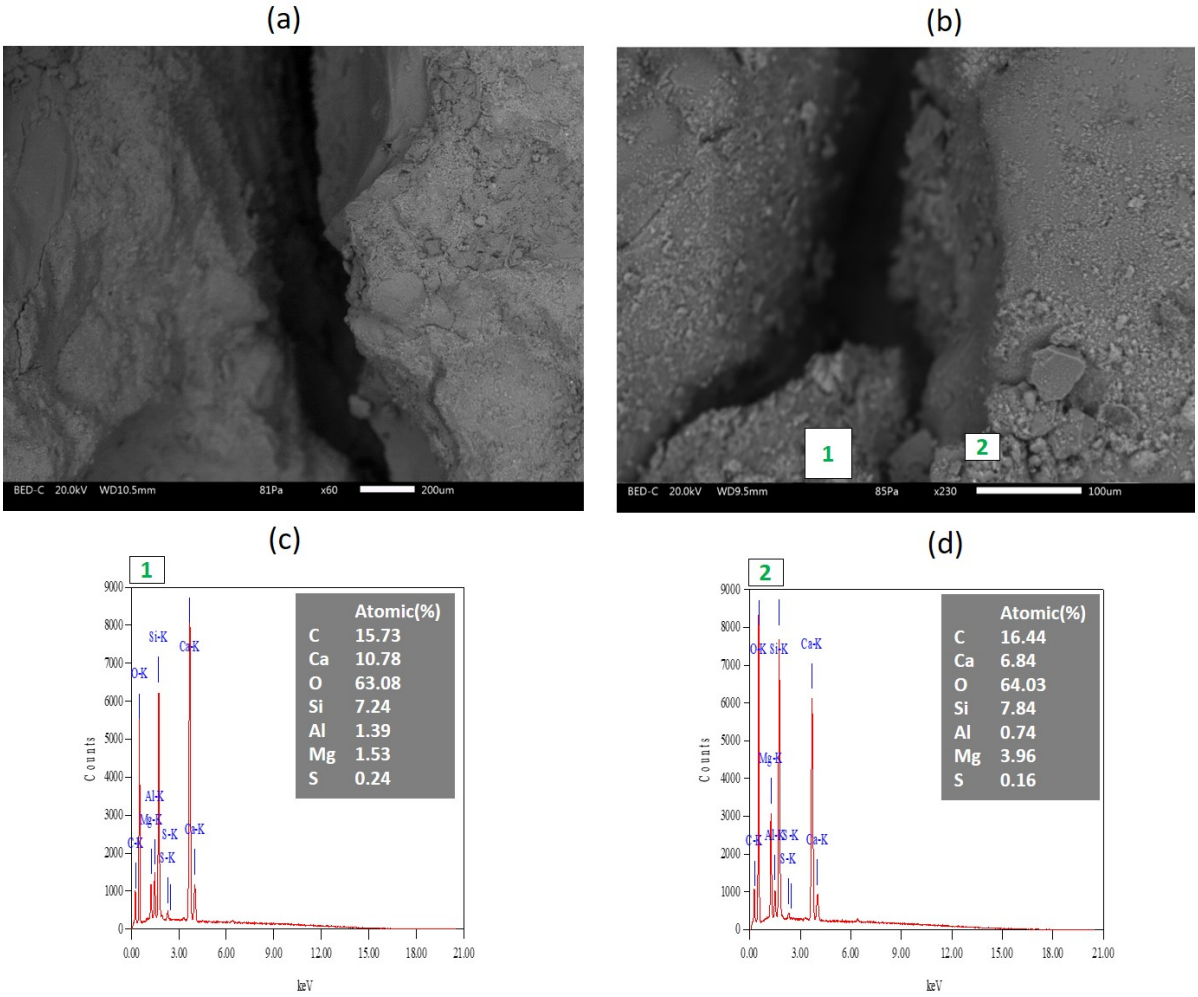

Figure 6.30 – SEM observation of self-healing inside the crack for BM10 and its EDX analysis.

6.4.5 Summary

The main objective of this section is to evaluate the benefits of adding blast furnace slag and EA on the self-healing process of cracks. It is concluded that the self-healing process is related to three mechanisms: carbonation, additional hydration and matrix expansion. The first two mechanisms are achieved by all the studied mixtures for the crack width in the range [100-250] µm. These two mechanisms are further enhanced for the mixture with 10% MGO due to the formation of different magnesian calcite morphologies on the crack surface and by the formation of C-A-S-H and M-S-H gels inside the crack. The third mechanism is also obtained with this mixture allowing to increase its autonomous healing capacity to heal the crack width of [250-500] µm. This mechanism is also obtained by the mixture containing 5% MGO. This behavior is related to the slow hydration process exhibited by these mixtures and the type of hydration products formed in the presence of MGO (e.g. hydrotalcite).

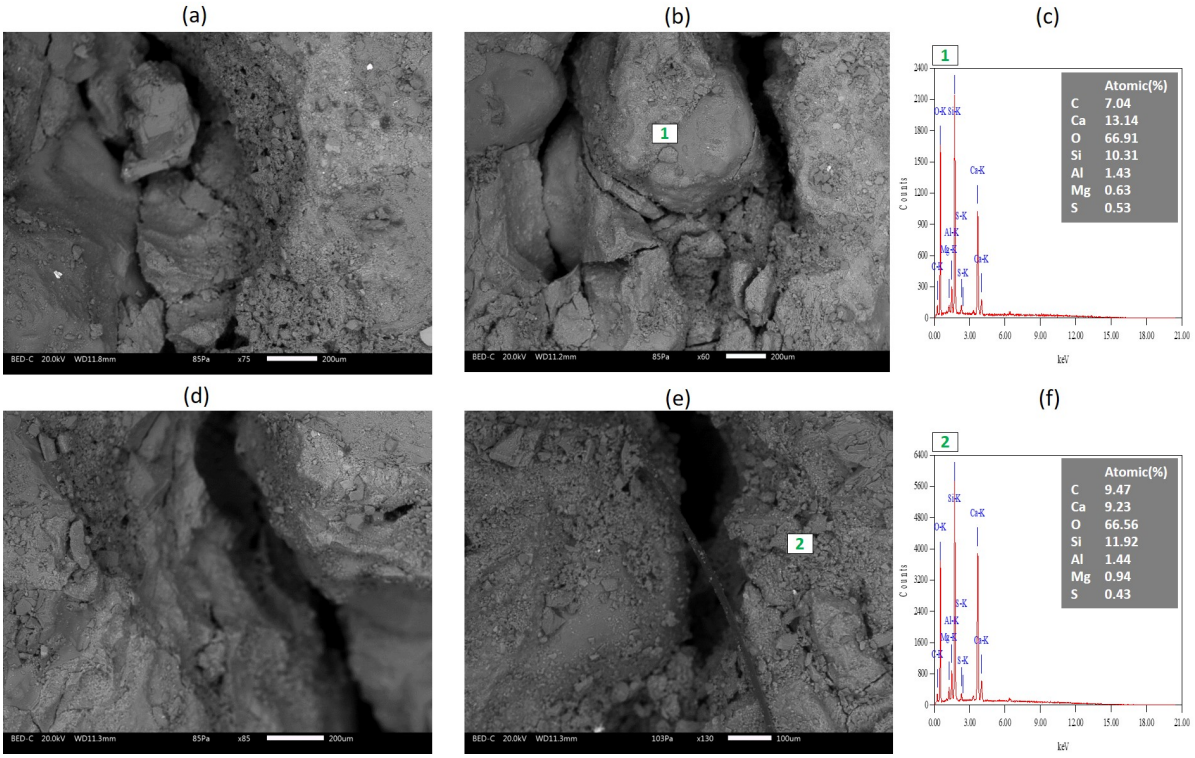

Figure 6.31 – SEM observation of self-healing products inside the crack for BC10 and its EDX.

So, these results highlight the use of the ternary blend of cement-blast furnace slag-EA (CSA or MGO) as a promising mortar with an interesting autogenous healing capacity, and the use of the ternary blend of cement-blast furnace slag-10% MGO as a promising mortar characterized by an interesting autogenous and autonomous healing capacities.

6.5 Conclusion

This chapter details the benefit of coupling mineral additions and EA (MGO and CSA) on the properties of sound mortars and their self-healing capacity. The following mixtures are compared: REF, BFS, BM5, BM10, BC5 and BC10. The study is divided into three parts: (1) evaluation of mortar hydration and microstructure; (2) evaluation of mortar mechanical properties and delayed deformations and (3) evaluation of mortar self-healing capacity.

The experimental results show that the addition of an expansive agent type MGO or CSA leads to a significant decrease of the autogenous and total shrinkage due to the formation of additional products in the pore network, leading to crystallization pressures and a matrix swelling at macroscopic scale. This expansion accelerates crack closure and therefore increases the autonomous healing potential of mortars. These behaviors are observed to be more important in the presence of EA type MGO due to its slow hydration that tends to the long term. Moreover,

it increases the formation of supplementary self-healing products inside the crack by autogenous healing. On the other hand, the partial substitution of the cement mass by EA decreases the mechanical resistances (flexural and compressive) at early age and in the long term due to the lower C-A-S-H gels produced. This reduction is lower in the presence of CSA than in MGO, due to the CSA hydration that is completed at early age. Despite of this strength decrease, all the proposed mortars present high compressive strengths at 28 days. Therefore, it confirms their compliance to the repair standard requirements (EN 1504-3). Finally, the addition of EA significantly reduces the mortar's sensibility to cracking in a restricted autogenous condition.

Therefore, this chapter proposes ternary blend of cement-blast furnace slag-EA as promising mortars that can be used for repair applications, limiting cracking sensibility and characterized by interesting autogenous and autonomous healing capacities.

Chapter 7

General Conclusion

The work presented in this dissertation fits into a wide body of research that has been looking for novel repair mortars to enhance the lifespan of the concrete structures. In particular, this PhD thesis studies the possibility of designing repair mortars with self-healing capacities. However, the developed self-healing repair mortar must be carefully designed to avoid future repairing demands. Here, we recognized the importance of designing a durable repair mortar. In the following sections, we summarize the contributions of this thesis and present a list of conclusions that can be drawn from the results.

Main results and finding of the thesis

Healing monitoring

For cementitious materials with Expansive Agents "EA", the mechanisms responsible for the crack healing potential are further hydration, carbonation, and matrix expansion. In order to take these three mechanisms into account when monitoring the self-healing of cracks, a 3D monitoring technique must be used. We select a water permeability test as it provides a good approach to monitor self-healing on all the crack surfaces. From this test, the healing rates of the cracked specimens were estimated by monitoring a parameter affecting the crack throughout its depth (e.g., water flow rate). Furthermore, with this test, it is possible to take into account several crack characteristics, i.e., connectivity, tortuosity, geometric dimensions, variation of its opening along its length, etc. In this case, this approach allows a 3D assessment of the healing process. Thanks to all these benefits, it is possible to estimate the crack healing rates in the case of these three healing mechanisms.

Proposing cement-based mortars and blended mortars containing EA and validating their self-healing capacities

The conventional repair mortars, e.g., the cement-based mortars, may experience cracking problems over time, shortening the structure's service life and increasing the maintenance cost. Lately, the sustainable development concept that aims at optimizing the repair operation cost has gained a lot of attention, promoting the use of self-healing mortars in future reparations. In this context, we have used two types of expansive agents, one is based on magnesium oxide and the second based on calcium sulfoaluminate. Then, we propose cement-based mortars and blended mortars containing theses expansive agents and we validate their self-healing capacities.

The experimental tests carried out on the mixtures with EA have shown that a mortar with MGO presents a slowing down of its hydration process at a young age, due to the formation of hydration products containing Mg (e.g., brucite or hydrotalcite). An opposite behavior is shown by the mortar with CSA which accelerates the hydration process at an early age due to the formation of more ettringite. These hydration behaviors in the presence of EA are more important by increasing their content. In the presence of cement and anhydrous blast furnace slag, further hydration was possible in the long term. However, the addition of CSA appears to consume its hydration capacity at a young age. Nonetheless, the addition of MGO promotes the presence of additional anhydrous particles at 28 days (e.g., MgO) which also increases with increasing MGO content.

In a second step, it was shown that the hydration of EA produces expansive hydration products that exert swelling pressures in the pores. This mechanism is further promoted by increasing the EA content when the environmental conditions are favorable for EA hydration (high Relative Humidity "RH"). Since CSA hydrates rapidly at an early age, the reduction of autogenous shrinkage is very important at this period. CSA addition has also shown greater reactivity in the presence of blast furnace slag due to its high aluminates content, thus promoting excessive ettringite formation and matrix expansion at a very young age. At long-term, the benefits of CSA addition on shrinkage reduction are not significant. In the presence of MGO, however, autogenous shrinkage reduction occurs at a young age and at the long term, and matrix expansion continues until the long term. Therefore, the initial experimental results ensure the benefit of EA addition on early and long-term hydration, which is a promising phenomenon to limit mortar shrinkage.

Following the impact of EA on the mechanical resistances, it was demonstrated that the partial substitution of the cement mass by EA decreases the mechanical resistances (flexural and compressive) at an early age and in the long term due to the lower C-S-H gels produced. On the other hand, this reduction is lower in the presence of CSA than in MGO, due to the difference between their hydration processes. It is thus shown that a reactive EA (CSA), after completing its hydration at an early age, the mortar increases its strength progressively to

reach slightly smaller strength values to those of 100% Portland cement mortar. However, in spite of this decrease, all the proposed mortars present high compressive strengths at 28 days. Therefore, these findings confirm the compliance of mortars with expansive agents with the compressive strength required by the repair standard (EN 1504-3).

In a second approach, different mechanical parameters are coupled to evaluate the cracking sensitivity of the mortar in a restricted autogenous condition. The results prove that the addition of slow or fast reactive EA (MGO or CSA) was found to significantly reduce the mortar's sensibility to cracking in a restricted autogenous condition. The presence of MGO in the mixture amplifies this behavior due to the moderate swelling of the matrix in comparison to the mixture with CSA. Therefore, the experimental results allow cement-based mortars and blended mortars with MGO to effectively limit the mortar's cracking sensibility.

The most important contribution of this PhD thesis can be summarized by the benefit of EA additions to the mortar on the self-healing process. The experimental results showed that a mixture characterized by high swelling behavior after the expected cracking date (at 28 days), can exhibit significant self-healing behavior in the long term due to the autonomous healing mechanism. In addition, the addition of a low-reactivity EA (MGO) further promotes the autogenous healing process through the formation of more healing products within the crack. Finally, it should be noted that water curing can sometimes lead to slightly lower healing capacity when using high EA content. This is mainly related to the expansion of the matrix which can be excessive and therefore, produces instability of the matrix volume reducing slightly its autonomous healing capacity.

Combining all these results, this research work presents several durable repair mortar formulations made with environmentally-friendly materials. We propose then, cement-based mortars or blended mortars with expansive agents featuring by an interesting autogenous and autonomous healing potential and good mechanical performances. Among the various proposed mixtures, we classify the most interesting blended mortars with blast furnace slag and expansive agent (based on magensium oxide or calcium sulfoaluminate): BM5 > BM10 > BC5 > BC10. These findings shed the light on the importance of the self-healing to increase the lifespan of the repair mortar and limit the reparation works in the future.

Challenging and future lines

This research work proved the benefit of adding blast furnace slag and expansive agents for the self-healing process and mechanical properties. However, to further improve this work, other studies can be pursued, such as:

1. Development of a statistical approach for the water permeability test to consider the variability in the initial crack geometry of the specimens. This will allow for more reliable and comparable water flow results between specimens.

2. Improvement of the water permeability test by developing a system that maintains a constant water pressure above the specimen during the test.

3. Evaluation of mortar porosity at the micro-pore scale. This will provide a better understanding of the swelling behavior of MGO and CSA if linked to smaller porosity filled by the expansive products for example.

4. Performing X-ray tomography images to provide information regarding the connectivity, tortuosity, or permeability associated with a pore network (3D analysis). This will allow verifying whether the swelling mechanism of the EA-containing mixtures could lead to micro-cracks.

5. Monitoring the hydration process by XRD analysis and quantification of the hydration products over time. This allows a better understanding of the effect of EA on the hydration advancement, and the stability of the hydration products formed over time.

6. Investigation of the visco-elastic behavior of mortars. The mechanical strength of the mortar affects the magnitude of the expansion. Since we observed larger expansions for mixtures having lower mechanical strengths compared to the 100% Portland cement mixture, this study will allow us to understand if this behavior is related to low porosity, stress relaxation capacity for example, etc. In particular, this last parameter is beneficial to give a good indication of the cracking sensibility index because it takes into account the decrease of internal stresses related to the material.

Furthermore, several future lines can be drawn from this thesis:

- Evaluation of the self-healing process through mechanical testing to monitor the impact of self-healing on mechanical strength recovery. This will allow evaluating the bond and strength of the self-healing products formed on the crack surface and inside the crack.

- Adding two types of magnesium oxide to the mixture: one that reacts quickly and one that reacts slowly. This allows for both a reduction in shrinkage and incompatibility of the mortar with its substrate in the short term and self-healing in the long term. To ensure long-term hydration, the fast-reacting EA will be encapsulated to promote the formation of additional hydration products and rapid matrix expansion and ensure optimal use of the magnesium oxide, when needed.

- Investigation of the durability of a repair mortar containing blast furnace slag: its sensitivity to carbonation and chloride penetration. Blast furnace slag based-products require an optimal curing to limit carbonation and chloride penetration.
- Study of the behavior of the interface between the repair mortar and its support: physical and chemical incompatibilities, tensile stresses, etc.

These last two investigations are currently in progress within the framework of the DEcoMat project - Sustainability of Eco-Materials: Interfaces Issues at INSA Rennes.

Appendix A

Raw materials: CEM I, BFS, MGO, CSA

A.1 TGA analysis for raw materials

The DTG curves obtained from TGA analysis for the Portland cement, blast furnace slag, MGO and CSA-based expansive agents:

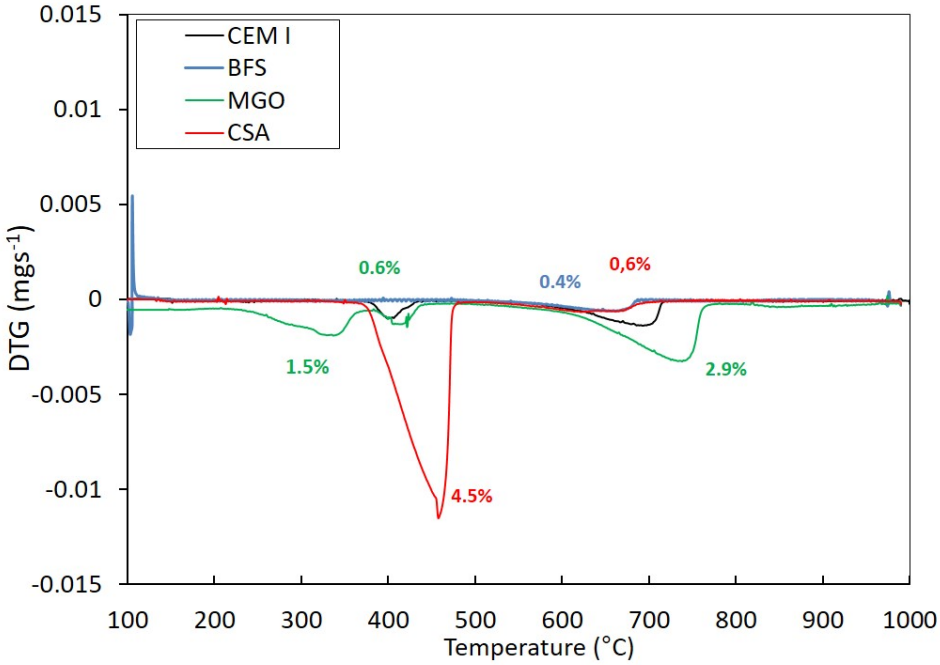

Figure A.1 – DTG curves of CEM I, BFS, MGO and CSA.

A.2 Determination of the cumulative heat ad infinitum from isothermal calorimetry

The cumulative heat $Q(t)$ determined from isothermal calorimetry is plotted on a graph as a function of $\frac{1}{t}$. Then, $Q(\frac{1}{t})$ is extrapolated by an exponential function in the interval of $\frac{1}{t}$ = [0 - 0.05]. The cumulative heat ad infinitum "$Q(\infty)$" is obtained at the theoretical infinite time ($\frac{1}{t} = 0$) for each mixture as shown in Figure A.2 and A.3.

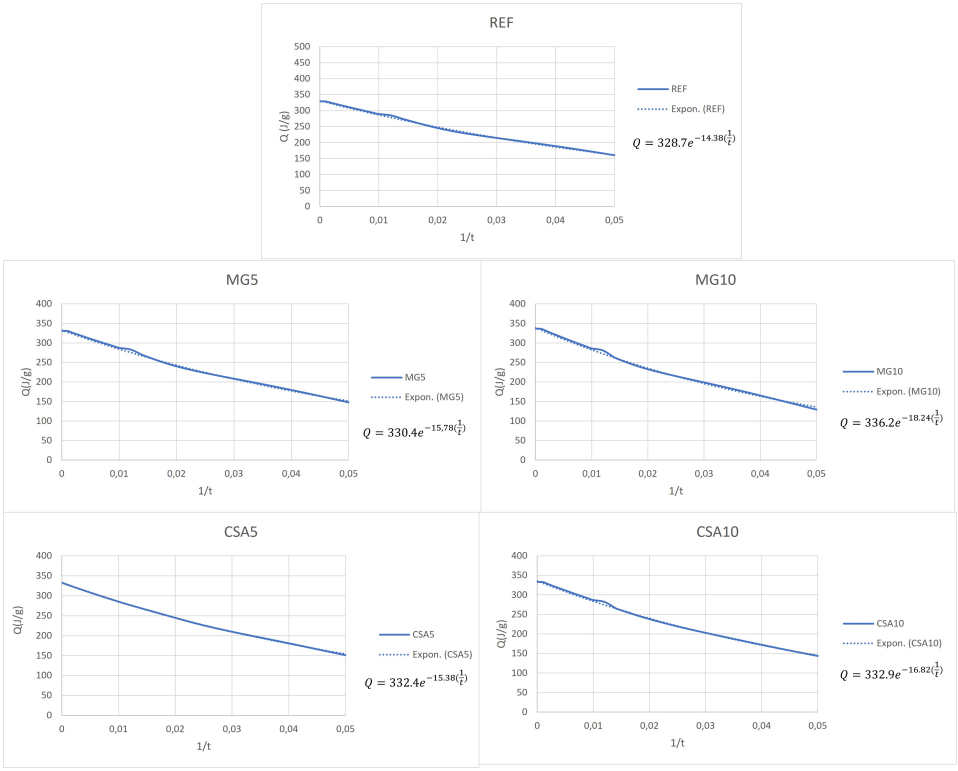

Figure A.2 – The cumulative heat evolution as a function of $\frac{1}{t}$ in the interval: [0 - 0.05] for all the cement-based mortars.

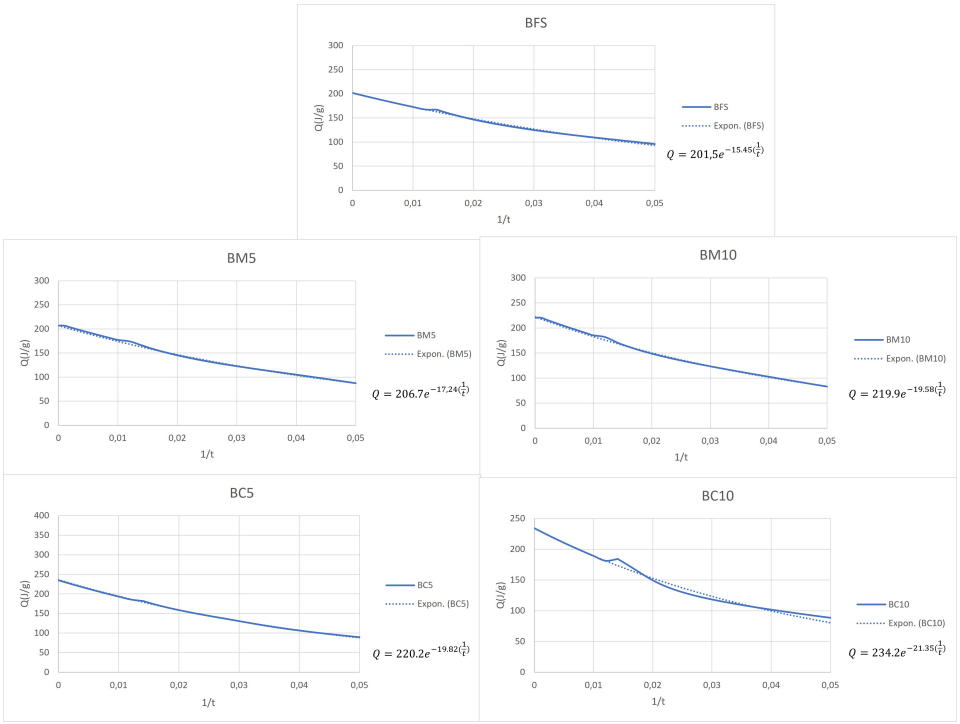

Figure A.3 – The cumulative heat evolution as a function of $\frac{1}{t}$ in the interval: [0 - 0.05] for all the blended mortars.

Appendix B

Round Robin Tests

B.1 Polynomial relationship between water flow and crack width

Relationship between the water flow and the crack width for REF and CA (Figure B.1).

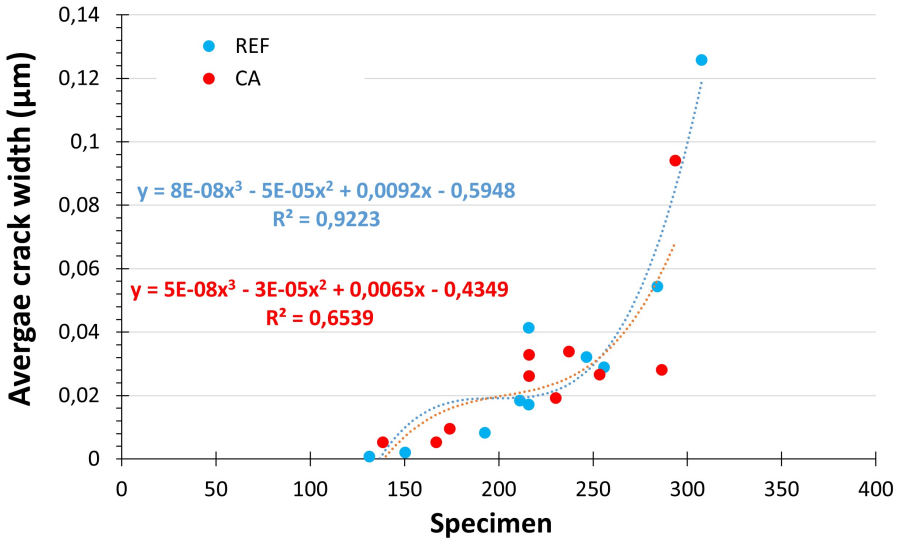

Figure B.1 – Relationship between the water flow and the crack width for REF and CA (10 specimens/composition).

B.2 Sorption coefficient as a function of square root of time

1. The SC evolution as a function of square root of time for REF and SLAG (Figure B.2).

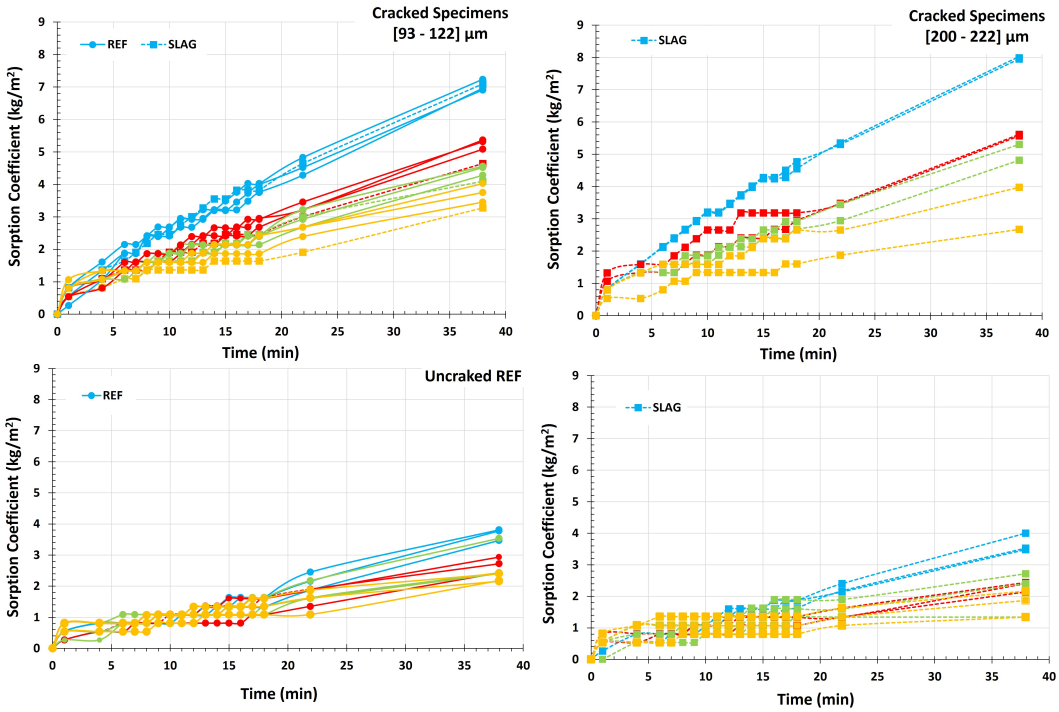

Figure B.2 – SC evolution as a function of square root of time for REF and SLAG.

2. The SC evolution as a function of square root of time for REF and CA (Figure B.3).

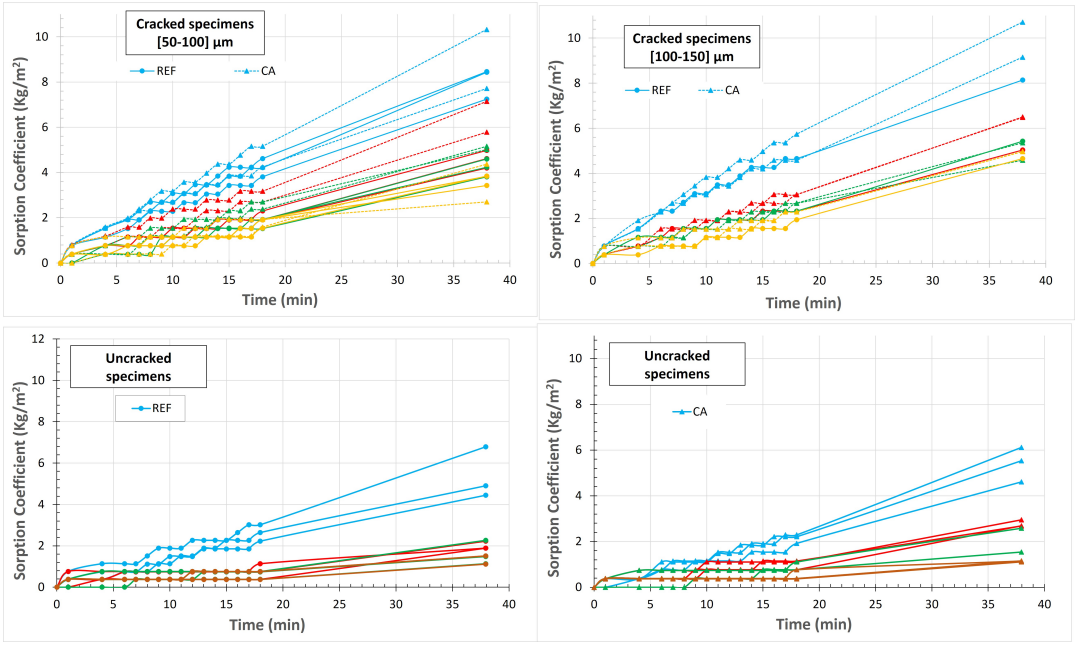

Figure B.3 – SC evolution as a function of square root of time for REF and CA.

Appendix C

Cement-based mortars with EA

C.1 Hydration and microstructure

1. Mass loss in the temperature of [105-300]°C related to the C-S-H decomposition (Figure C.1).

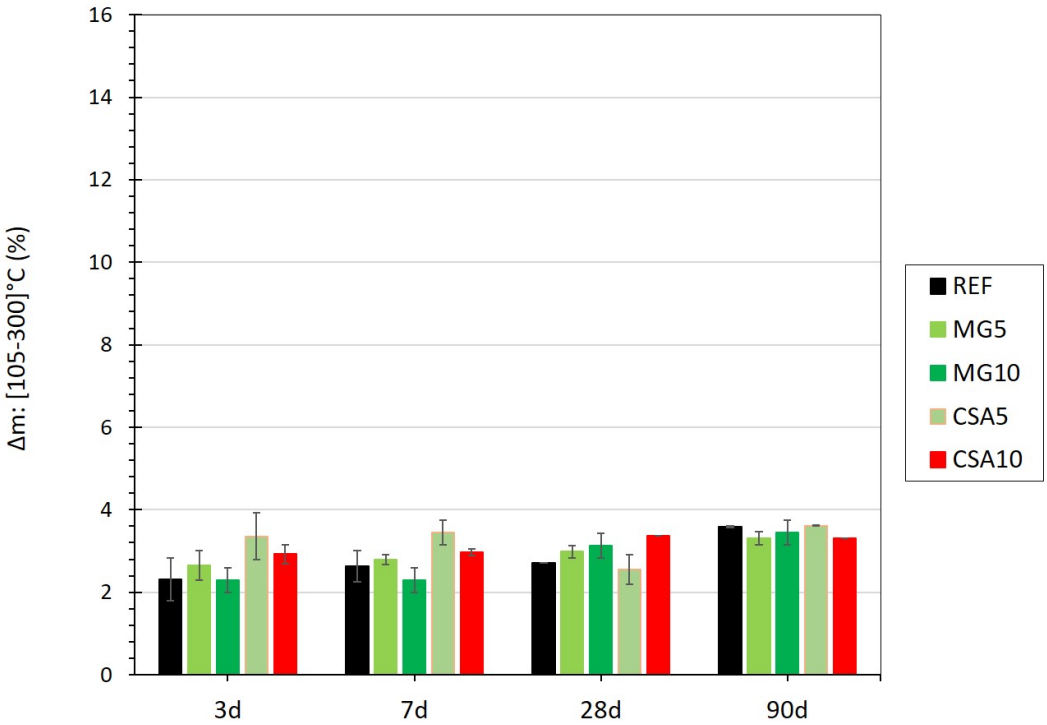

Figure C.1 – Mass loss in the temperature range of [105-300]°C for all the cement-based mortars.

2. Mass loss in the temperature of [105-600]°C related to the chemically bound water (Figure C.2).

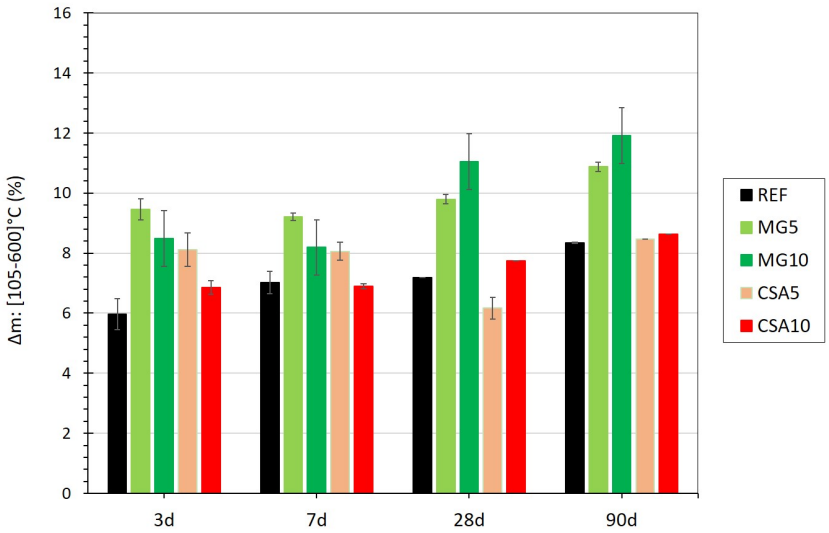

Figure C.2 – Mass loss in the temperature range of [105-600]°C for all the cement-based mortars.

3. Klinkenberg coefficient determined from gas permeability results using Eq. C.1 [140] (Figure C.3).

$$K_a = K_v(1 + \frac{\beta}{P_m}) \tag{C.1}$$

Where "K_a" is the apparent permeability (m^2), "K_v" is the intrinsic permeability (m^2), "β" is the Klinkenberg coefficient (Pa), "$P_m = \frac{P_i + P_{atm}}{2}$" and "$P_i$" and "$P_m$" are the input and the atmospheric pressure respectively (Pa).

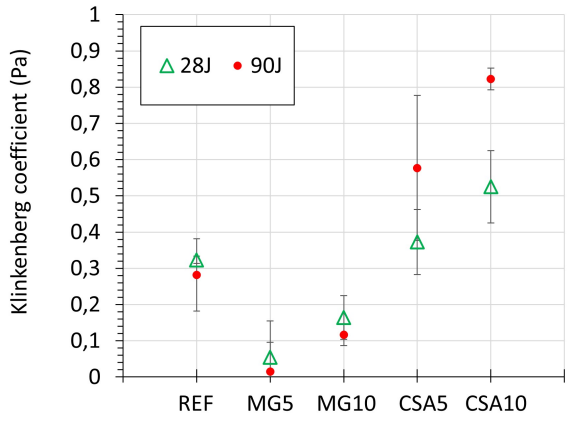

Figure C.3 – Klinkenberg coefficient determined from gas permeability results for all the cement-based mortars at 28 and 90 days.

4. Pore distribution and cumulative pore volumes determined from sorption analysis (Figure C.4).

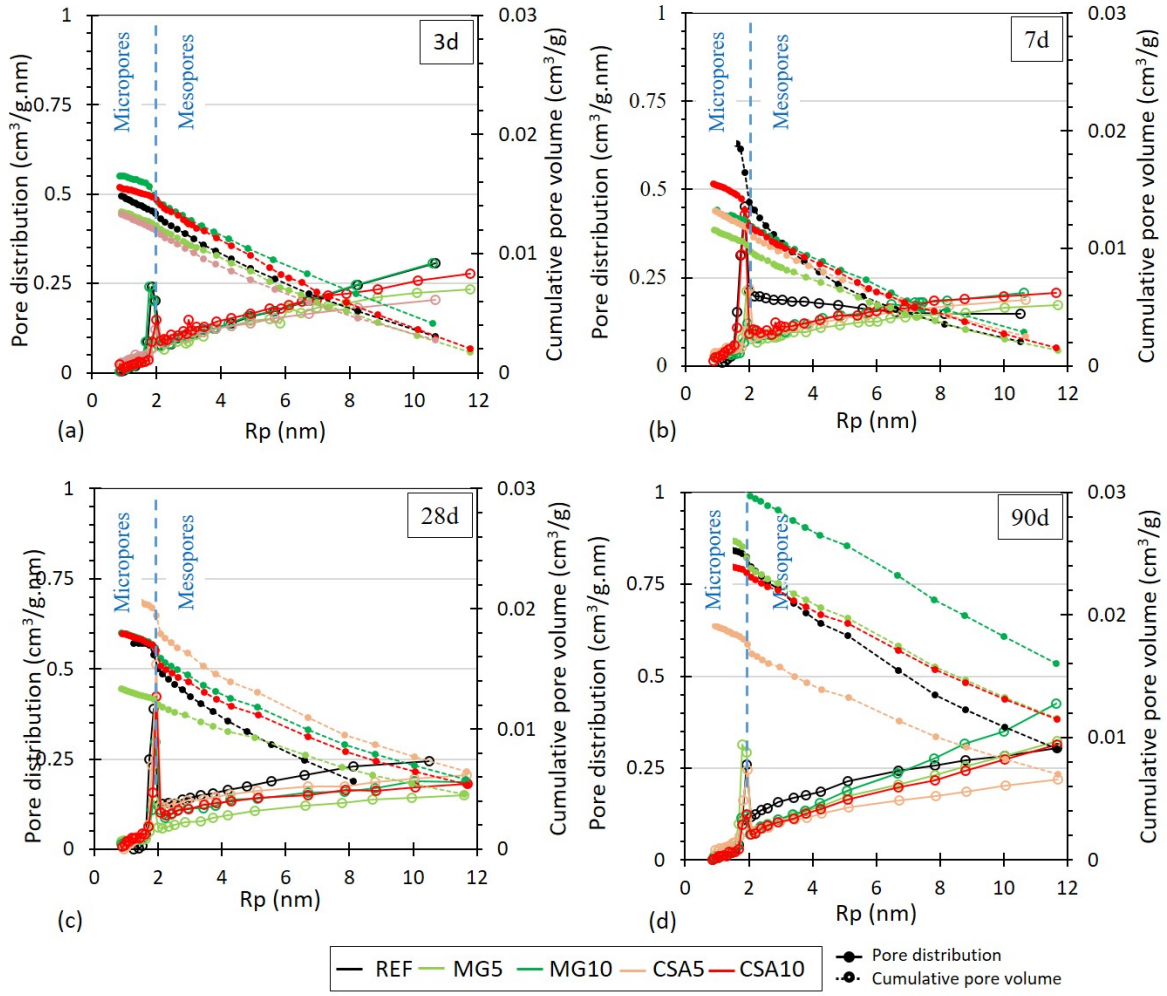

Figure C.4 – Pore distribution and cumulative pore volumes determined from sorption analysis for all the cement-based mortars.

C.2 Mechanical properties

1. The evolution of the drying deformation as a function of time for all the cement-based mortars (Figure C.5).

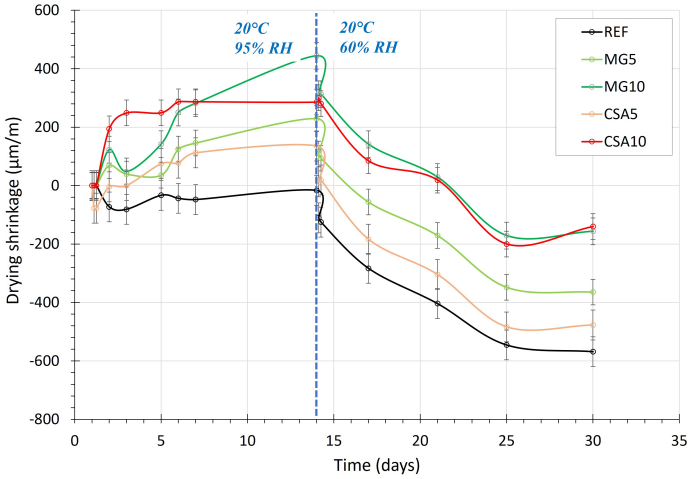

Figure C.5 – The evolution of the drying deformation as a function of time for all the cement-based mortars.

2. Mass variation of the specimens stored in autogenous curing for all the cement-based mortars (Figure C.6).

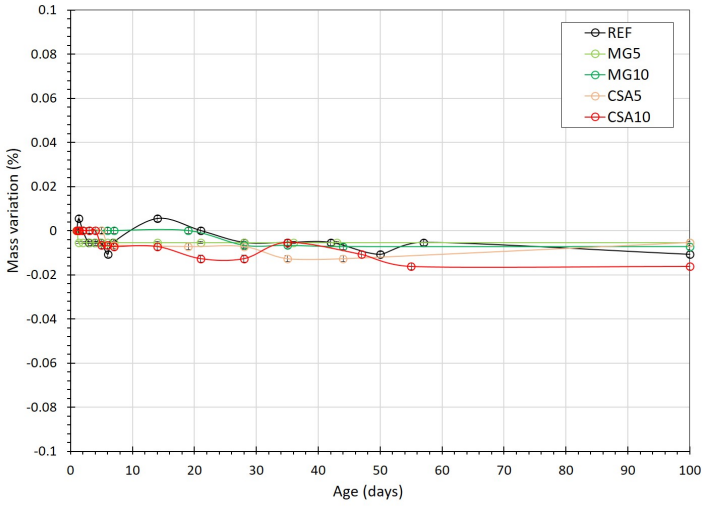

Figure C.6 – Mass variation of the specimens kept in autogenous curing for all the cement-based mortars.

3. The evolution of the autogenous deformation as a function of log(IRH) (Figure C.7).

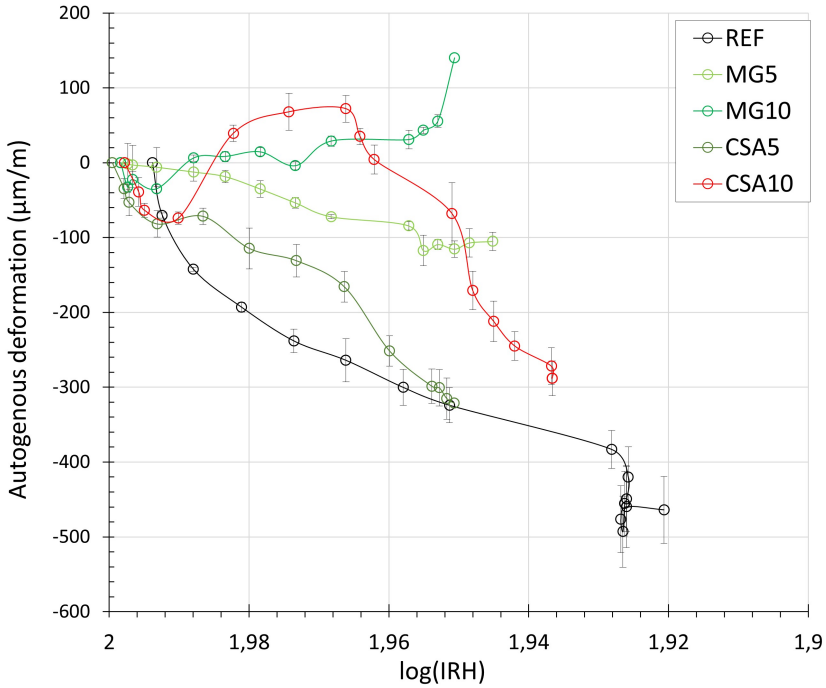

Figure C.7 – The evolution of the autogenous deformation as a function of log(IRH) for all the cement-based mortars.

4. Mass variation of the specimens kept in Water Curing (WC) and Cycle Curing (CC) for all the cement-based mortars (Figure C.8).

5. The evolution of the restricted deformations for all the cement-based mortars are determined using a ring test in an autogenous condition and no cracks are detected for all the studied mixtures (Figure C.10). The ring test consists in casting the mixture between two steel rings, where three strain gauges are fixed on the inner ring (Figure C.9(a)). After demolding, the specimens are covered with several layers of aluminum foil to avoid any drying effect (Figure C.9(b)), and stored at 20°C and 60 ± 5% R.H. In parallel, two thermocouples are used to record the ambient temperature as a function of time. One of them is embedded in a 1 year old specimen of the same mixture (to record $T_1(t)$ in the hardened mixture), and the other is placed near the ring (to record $T_2(t)$ in the room). The deformations of the mortar are then only of thermal and autogenous origin. The test is performed for a minimum duration of 50 days. The collected data allow to calculate the restricted deformations "$\mathcal{E}_r(t)$" by using Equation C.2.

$$\mathcal{E}_r(t) = \mathcal{E}(t) - \alpha(T_1(t) - T_2(t)) \tag{C.2}$$

Where $\mathcal{E}(t)$ is the gauge deformation recorded at time t.

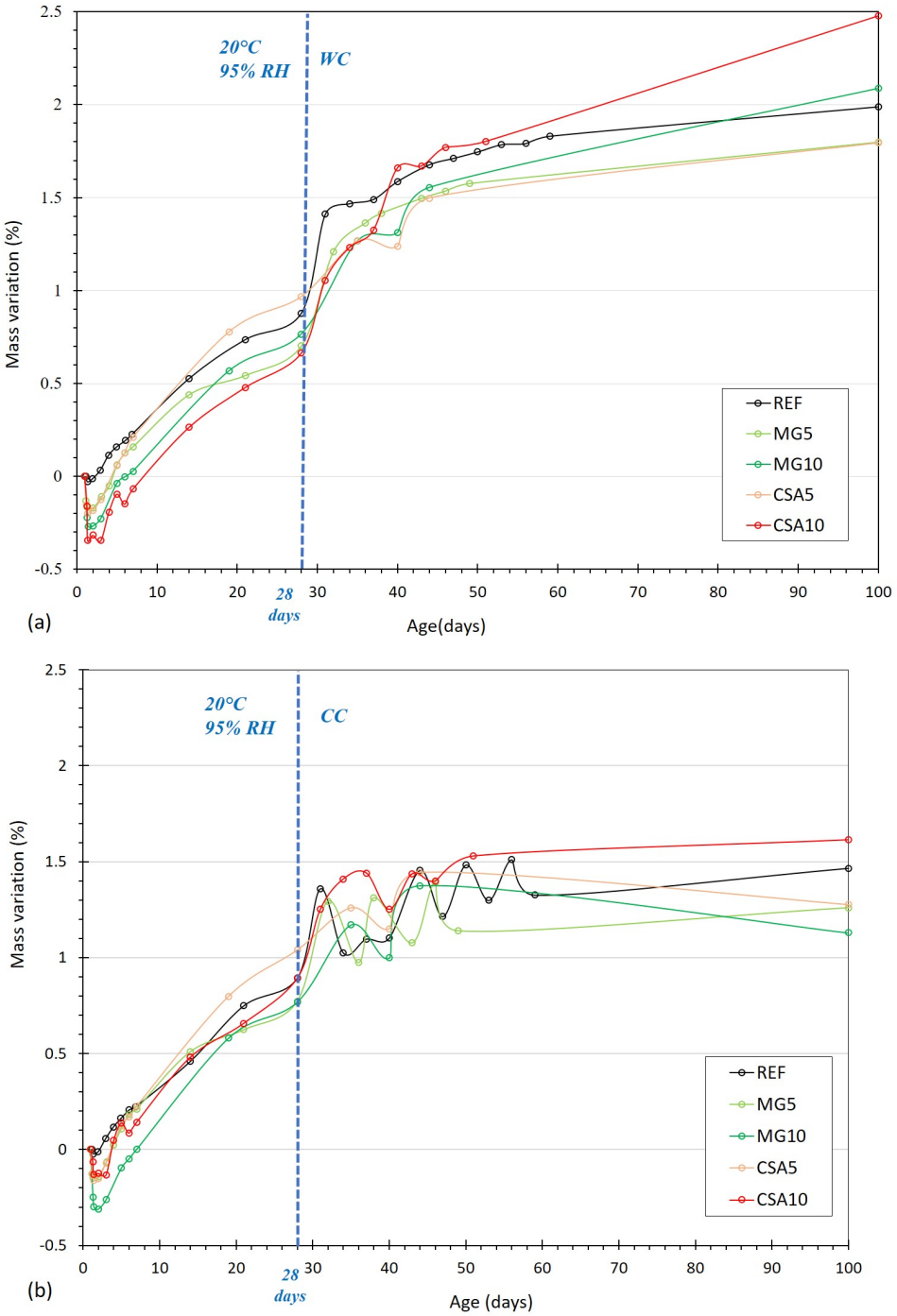

Figure C.8 – Mass variation of the specimens kept in WC (a) and CC (b) for all the cement-based mortars.

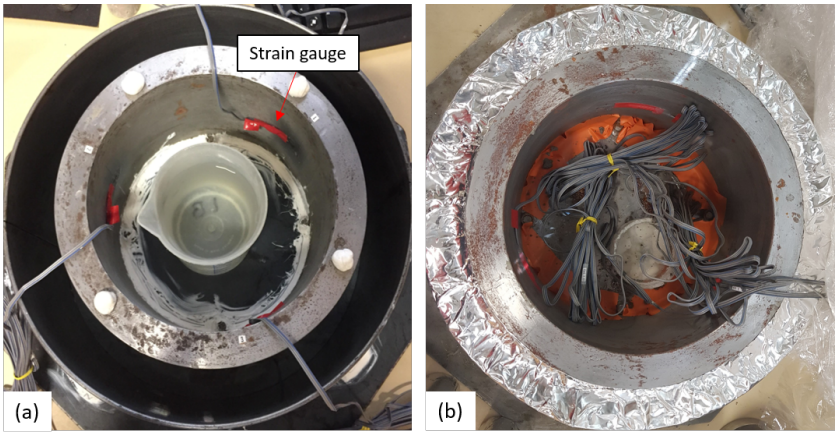

Figure C.9 – (a): The steel ring with the strain gauges fixed on its inner; (b): Specimen covered with aluminum foils after demoulding.

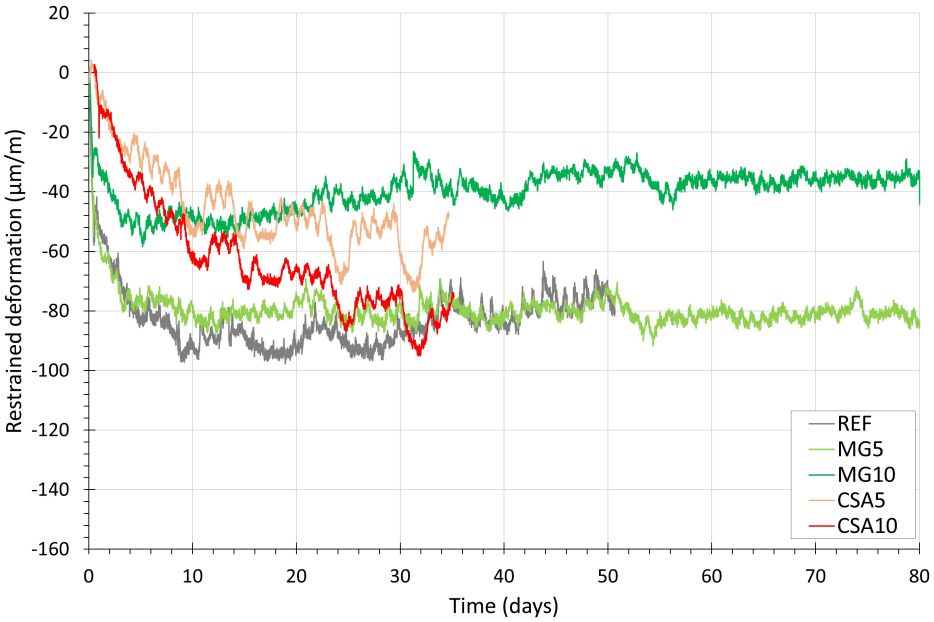

Figure C.10 – The evolution of the restricted deformations for all the cement-based mortars.

C.3 Self-healing capacity

Average Healing Rate (HR) calculated at constant water pressure (15 cm) for all the cement-based mortars at 7d, 28d and 90d (Figure C.11 and C.12).

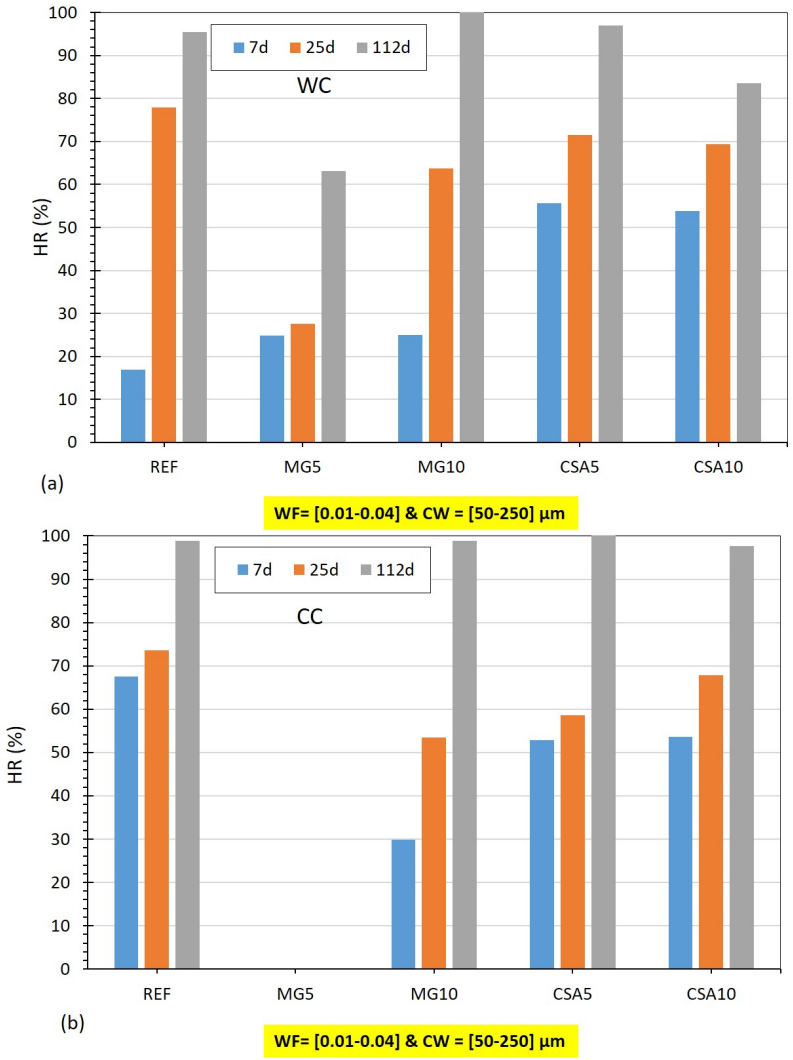

Figure C.11 – Average HR at a water pressure = 15 cm for all the cement-based mortars having an initial WF = [0.01-0.04] l/min cured under WC (a) and CC (b).

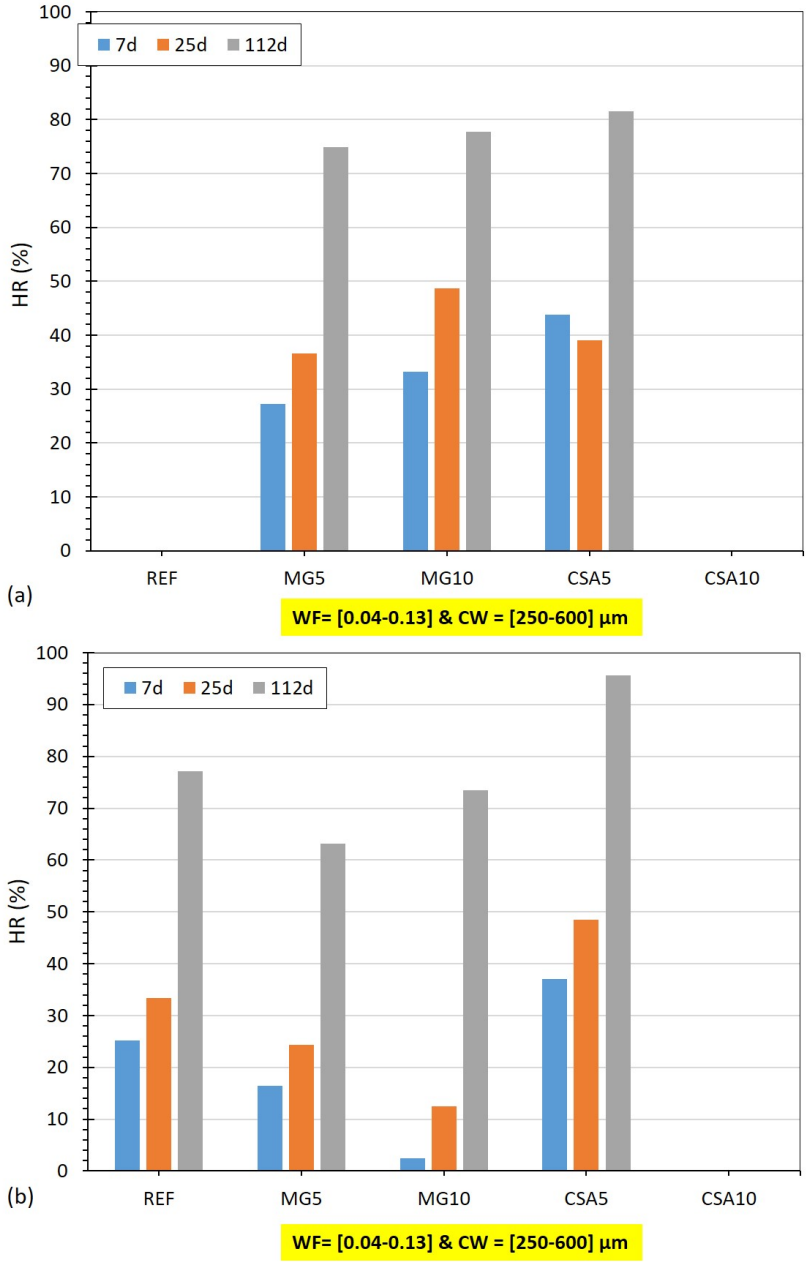

Figure C.12 – Average HR at a water pressure = 15 cm for all the cement-based mortars having an initial WF = [0.04-0.13] l/min cured under WC (a) and CC (b).

Appendix D

Blended mortars with EA

D.1 Hydration and microstructure

1. Mass loss in the temperature of [105-300]°C related to the C-S-H decomposition (Figure D.1).

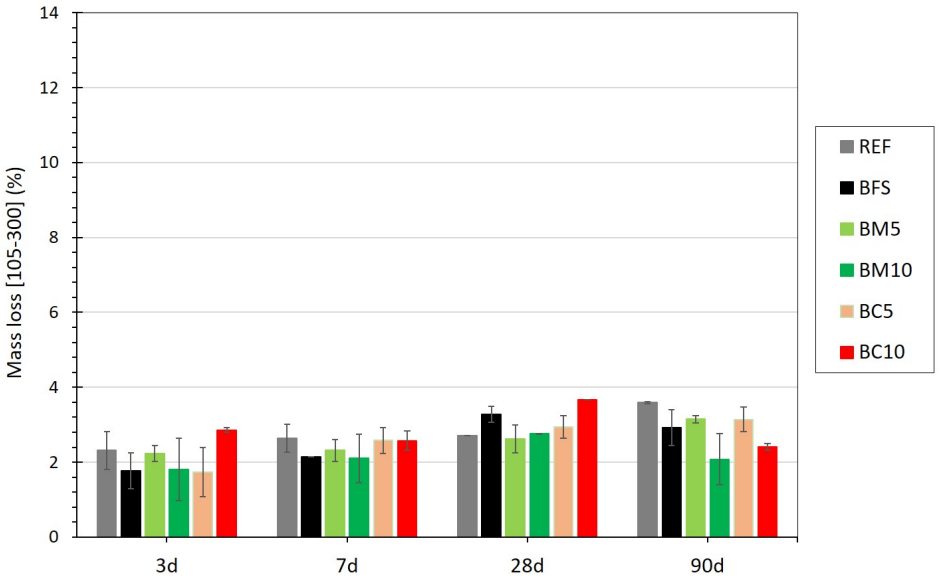

Figure D.1 – Mass loss in the temperature range of [105-300]°C for all the blended mortars.

2. Mass loss in the temperature of [105-600]°C related to the chemically bound water (Figure D.2).

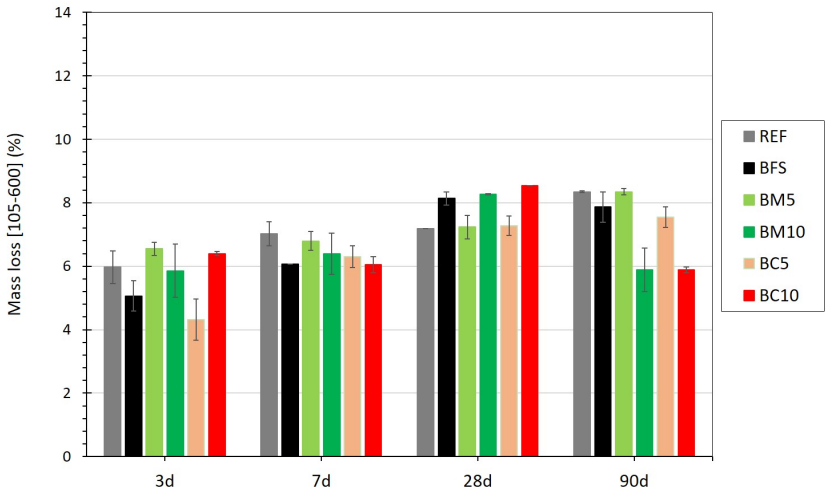

Figure D.2 – Mass loss in the temperature range of [105-600]°C for all the blended mortars.

3. Klinkenberg coefficient determined from gas permeability results using Eq. C.1 [140] (Figure D.3).

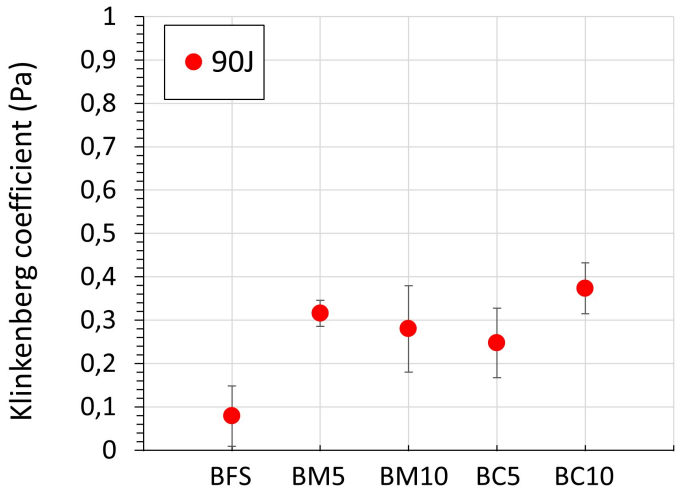

Figure D.3 – Klinkenberg coefficient determined from gas permeability results for all the blended mortars at 90 days.

4. Pore distribution and cumulative pore volumes determined from sorption analysis (Figure D.4).

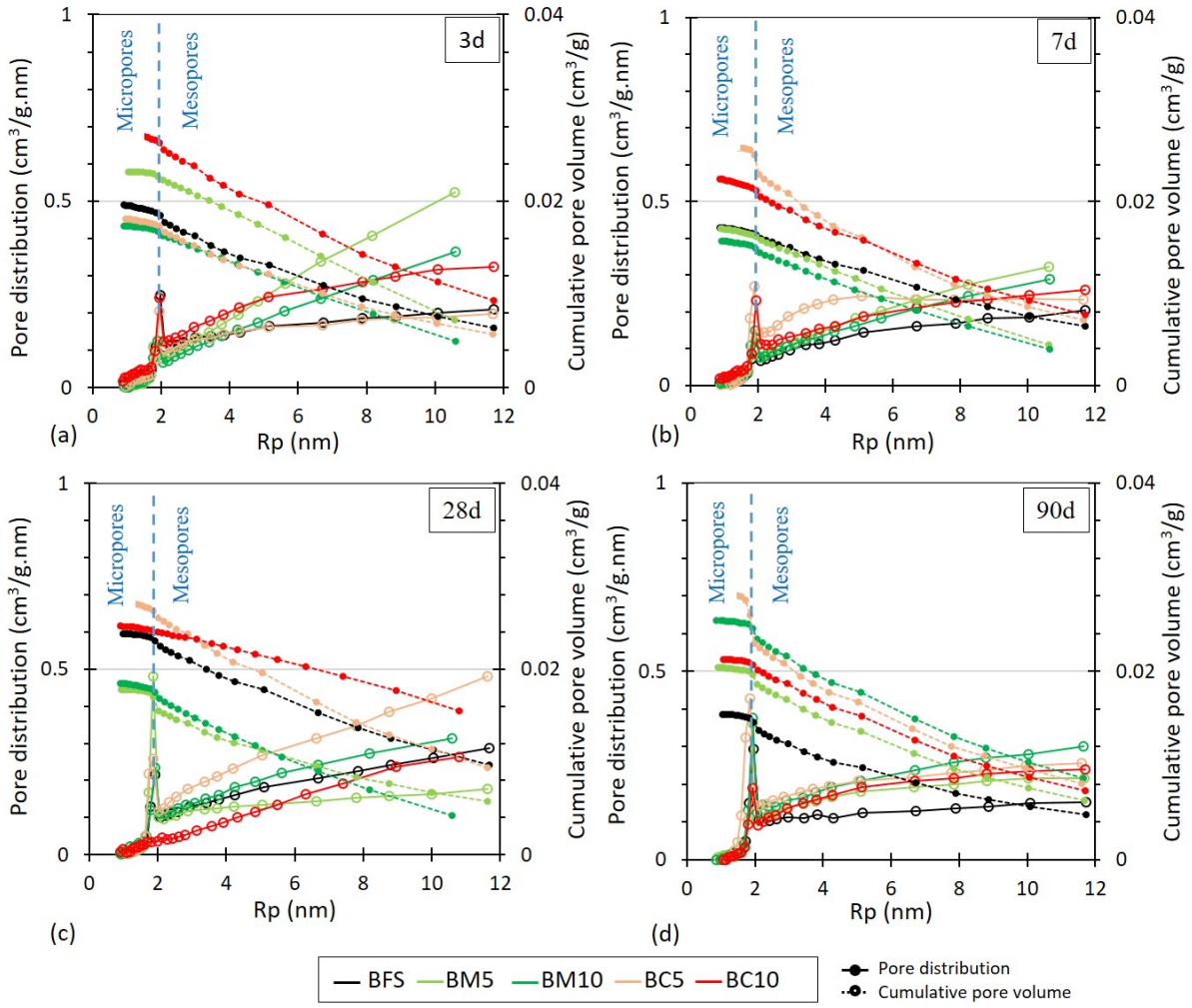

Figure D.4 – Pore distribution and cumulative pore volumes determined from sorption analysis for all the blended mortars.

D.2 Mechanical properties

1. Mass variation of the specimens kept in autogenous and water curing for all the blended mortars (Figure D.5).

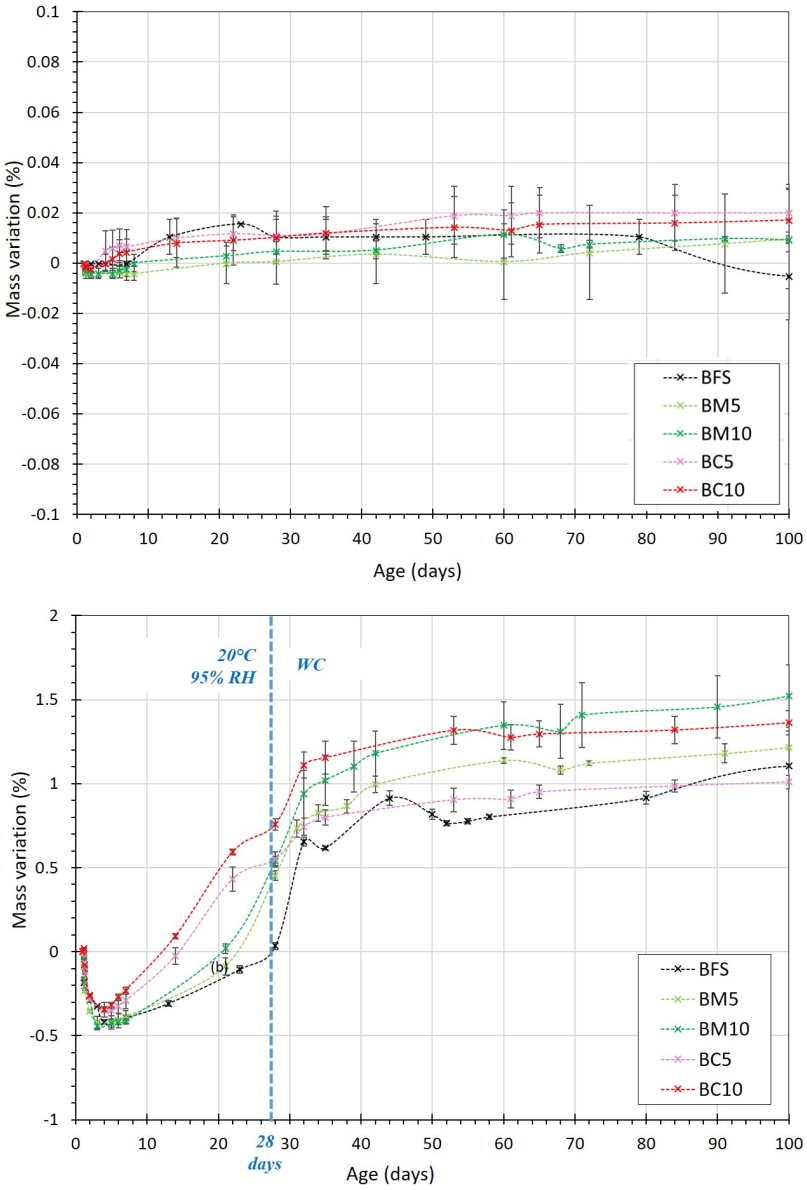

Figure D.5 – Mass variation of the specimens kept in autogenous curing (a) and water curing (b) for all the blended mortars.

2. Evolution of the drying shrinkage determined for all the blended mortars (Figure D.6).

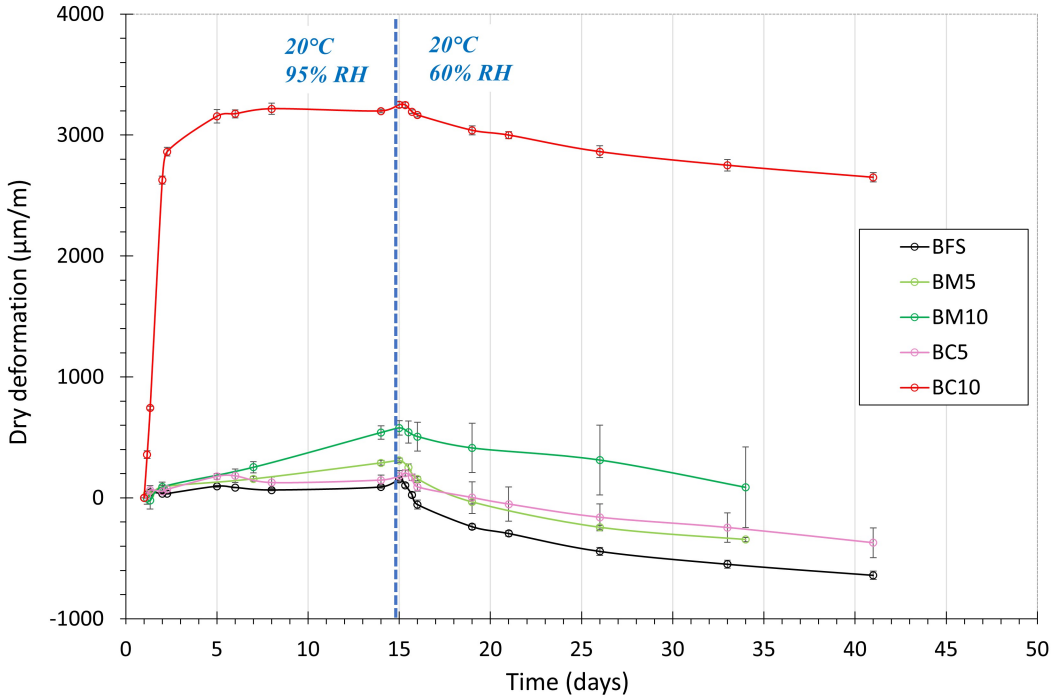

Figure D.6 – Evolution of the drying shrinkage determined for all the blended mortars.

3. Average Healing Rate (HR) calculated at constant water pressure (15 cm) for all the blended mortars at 7d, 28d and 90d (Figure D.7).

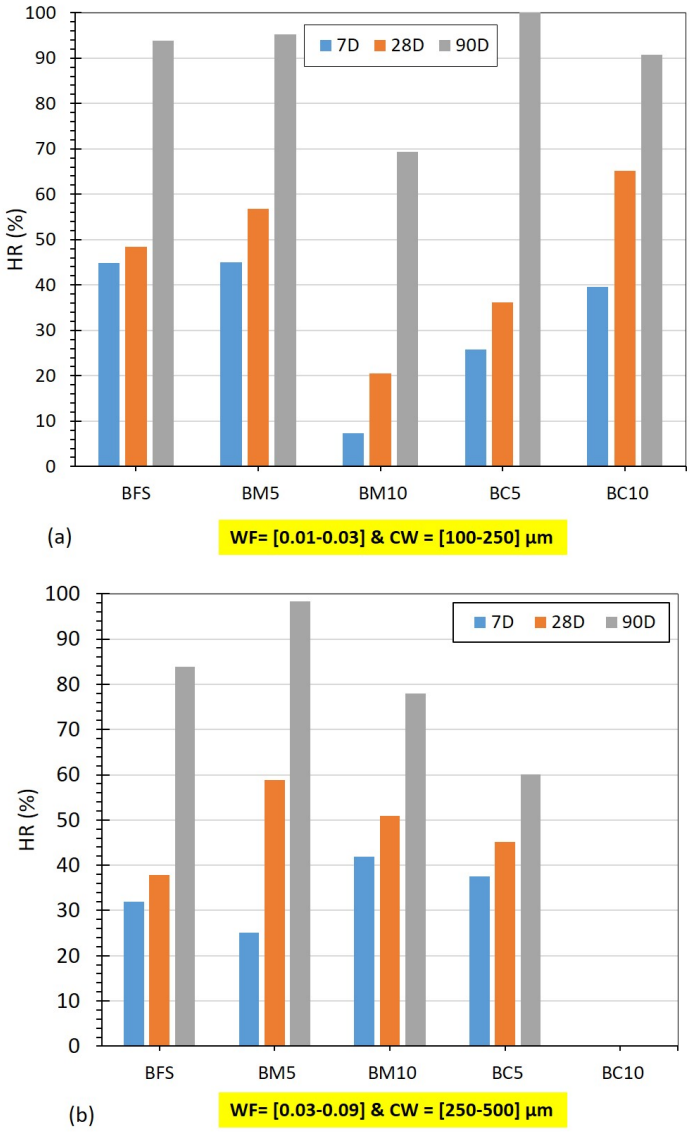

Figure D.7 – Average HR at a water pressure = 15 cm for all the blended mortars having an initial WF = [0.01-0.03] l/min (a) and [0.03-0.09] l/min (b).

Bibliography

[1] D. Breysee, *Introduction à la problématique des risques en Génie Civil, [online] Available:http://www.unit.eu/cours/cyberrisques/rdc/res/Polycopie$_r$dc.pdf*, 2009.

[2] M. Lechani, S. kenai, and N. E. Hannachi, *Diagnostic des causes de dégradation des ouvrages en béton armé, [online] Available:http://www.entp.edu.dz/revue/files/article/15/article%207.pdf.*

[3] F. Benboudjema and A. Darquennes, "Fissuration par retrait gêné dans les ouvrages en béton armé," *Construction et travaux publics, Vieillissement, pathologies et réhabilitation du bâtiment*, May 2015.

[4] P. Mounanga, *Etude expérimentale du comportement de pâtes de ciment au très jeune âge: hydratation, retraits, propriétés thermophysiques.* PhD thesis, Nantes, 2003.

[5] M. Roig-Flores, S. Moscato, P. Serna, and L. Ferrara, "Self-healing capability of concrete with crystalline admixtures in different environments," *Construction and Building Materials*, vol. 86, pp. 1–11, 2015.

[6] T. Qureshi and A. Al-Tabbaa, "The effect of magnesia on the self-healing performance of portland cement with increased curing time," in *1st International Conference on Ageing of Materials & Structures*, pp. 635–642, 2014.

[7] T. Qureshi, A. Kanellopoulos, and A. Al-Tabbaa, "Autogenous self-healing of cement with expansive minerals-i: Impact in early age crack healing," *Construction and Building Materials*, vol. 192, pp. 768–784, 2018.

[8] P. Zhang, Y. Dai, W. Wang, J. Yang, L. Mo, W. Guo, and J. Bao, "Effects of magnesia expansive agents on the self-healing performance of microcracks in strain-hardening cement-based composites (shcc)," *Materials Today Communications*, vol. 25, p. 101421, 2020.

[9] M. A. Sherir, K. M. Hossain, and M. Lachemi, "The influence of mgo-type expansive agent incorporated in self-healing system of engineered cementitious composites," *Construction and Building Materials*, vol. 149, pp. 164–185, 2017.

[10] NF EN 1504-3, *Produits et systèmes pour la protection et la réparation des structures en béton - Définitions, exigences, maîtrise de la qualité et évaluation de la conformité - Partie 3 : réparation structurale et réparation non structurale, [online] Available: https://viewerbdc.afnor.org/pdf/viewer/sF$_y$cAEC2H01*, 2006.

[11] A. SHREM, *Self-Healing Repair Eco-Mortar, INSA Rennes.*, 2022-2026.

[12] L. Yang, C. Shi, and Z. Wu, "Mitigation techniques for autogenous shrinkage of ultra-high-performance concrete–a review," *Composites Part B: Engineering*, vol. 178, p. 107456, 2019.

[13] M. Roig Flores, *Self-healing concrete: efficiency evaluation and enhancement with crystalline admixtures*. PhD thesis, Universitat Politècnica de València, 2018.

[14] M. De Rooij, K. Van Tittelboom, N. De Belie, and E. Schlangen, *Self-healing phenomena in cement-Based materials: state-of-the-art report of RILEM technical committee 221-SHC: self-Healing phenomena in cement-Based materials*, vol. 11. Springer, 2013.

[15] E. Cuenca, A. Tejedor, and L. Ferrara, "A methodology to assess crack-sealing effectiveness of crystalline admixtures under repeated cracking-healing cycles," *Construction and Building Materials*, vol. 179, pp. 619–632, 2018.

[16] A. Neville, "Autogenous healing—a concrete miracle?," *Concrete international*, vol. 24, no. 11, pp. 76–82, 2002.

[17] N. Hearn, "Self-sealing, autogenous healing and continued hydration: what is the difference?," *Materials and structures*, vol. 31, no. 8, pp. 563–567, 1998.

[18] S. Jacobsen, J. Marchand, and H. Hornain, "Sem observations of the microstructure of frost deteriorated and self-healed concretes," *Cement and Concrete Research*, vol. 25, no. 8, pp. 1781–1790, 1995.

[19] K. Olivier, *Étude expérimentale et modélisation de l'auto-cicatrisation des matériaux cimentaires avec additions minérales*. PhD thesis, Université Paris-Saclay; Université de Sherbrooke. Département de physique, 2016.

[20] P. Escoffres, C. Desmettre, and J.-P. Charron, "Effect of a crystalline admixture on the self-healing capability of high-performance fiber reinforced concretes in service conditions," *Construction and Building Materials*, vol. 173, pp. 763–774, 2018.

[21] K. Van Tittelboom, E. Gruyaert, H. Rahier, and N. De Belie, "Influence of mix composition on the extent of autogenous crack healing by continued hydration or calcium carbonate formation," *Construction and Building Materials*, vol. 37, pp. 349–359, 2012.

[22] H. Deng and G. Liao, "Assessment of influence of self-healing behavior on water permeability and mechanical performance of ecc incorporating superabsorbent polymer (sap) particles," *Construction and Building Materials*, vol. 170, pp. 455–465, 2018.

[23] Y. S. Lee and W. Park, "Current challenges and future directions for bacterial self-healing concrete," *Applied microbiology and biotechnology*, vol. 102, no. 7, pp. 3059–3070, 2018.

[24] K. Sisomphon, O. Copuroglu, and E. Koenders, "Self-healing of surface cracks in mortars with expansive additive and crystalline additive," *Cement and Concrete Composites*, vol. 34, no. 4, pp. 566–574, 2012.

[25] R. Gagné and M. Argouges, "A study of the natural self-healing of mortars using air-flow measurements," *Materials and structures*, vol. 45, no. 11, pp. 1625–1638, 2012.

[26] L.-L. Kan, H.-S. Shi, A. R. Sakulich, and V. C. Li, "Self-healing characterization of engineered cementitious composite materials.," *ACI Materials Journal*, vol. 107, no. 6, 2010.

[27] H.-W. Reinhardt and M. Jooss, "Permeability and self-healing of cracked concrete as a function of temperature and crack width," *Cement and concrete research*, vol. 33, no. 7, pp. 981–985, 2003.

[28] B. Hilloulin, *Méthodes avancées et analyses multi-échelles pour l'étude de l'autocicatrisation des fissures dans les matériaux cimentaires*. PhD thesis, Ecole Centrale de Nantes (ECN); Université de Gand, 2015.

[29] Z. Jiang, W. Li, and Z. Yuan, "Influence of mineral additives and environmental conditions on the self-healing capabilities of cementitious materials," *Cement and Concrete Composites*, vol. 57, pp. 116–127, 2015.

[30] N. ter Heide and E. Schlangen, "Self-healing of early age cracks in concrete," in *Proceedings of the First international conference on Self Healing Materials*, pp. 18–20, 2007.

[31] Y. Yang, E.-H. Yang, and V. C. Li, "Autogenous healing of engineered cementitious composites at early age," *Cement and concrete research*, vol. 41, no. 2, pp. 176–183, 2011.

[32] L. Ferrara, V. Krelani, and M. Carsana, "A "fracture testing" based approach to assess crack healing of concrete with and without crystalline admixtures," *Construction and Building Materials*, vol. 68, pp. 535–551, 2014.

[33] M. Roig-Flores, F. Pirritano, P. Serna, and L. Ferrara, "Effect of crystalline admixtures on the self-healing capability of early-age concrete studied by means of permeability and crack closing tests," *Construction and Building Materials*, vol. 114, pp. 447–457, 2016.

[34] K. Sisomphon, O. Copuroglu, and E. Koenders, "Effect of exposure conditions on self healing behavior of strain hardening cementitious composites incorporating various cementitious materials," *Construction and Building Materials*, vol. 42, pp. 217–224, 2013.

[35] C.-C. Hung, Y.-F. Su, and Y.-M. Su, "Mechanical properties and self-healing evaluation of strain-hardening cementitious composites with high volumes of hybrid pozzolan materials," *Composites Part B: Engineering*, vol. 133, pp. 15–25, 2018.

[36] S. Qian, J. Zhou, M. De Rooij, E. Schlangen, G. Ye, and K. Van Breugel, "Self-healing behavior of strain hardening cementitious composites incorporating local waste materials," *Cement and Concrete Composites*, vol. 31, no. 9, pp. 613–621, 2009.

[37] P. Termkhajornkit, T. Nawa, Y. Yamashiro, and T. Saito, "Self-healing ability of fly ash–cement systems," *Cement and concrete composites*, vol. 31, no. 3, pp. 195–203, 2009.

[38] M. Şahmaran, S. B. Keskin, G. Ozerkan, and I. O. Yaman, "Self-healing of mechanically-loaded self consolidating concretes with high volumes of fly ash," *Cement and Concrete Composites*, vol. 30, no. 10, pp. 872–879, 2008.

[39] K. Olivier, A. Darquennes, F. Benboudjema, and R. Gagné, "Etude de l'auto-cicatrisation des matériaux cimentaires avec additions minérales après fissuration au jeune âge par retrait gêné," *Rencontres universitaires de l'AUGC*, 2013.

[40] M. J. Miah, M. K. Ali, S. C. Paul, A. John Babafemi, S. Y. Kong, and B. Šavija, "Effect of recycled iron powder as fine aggregate on the mechanical, durability, and high temperature behavior of mortars," *Materials*, vol. 13, no. 5, p. 1168, 2020.

[41] B. A. Tayeh and D. M. Al Saffar, "Utilization of waste iron powder as fine aggregate in cement mortar," *journal of engineering research and technology*, vol. 5, no. 2, 2018.

[42] S. I. Ghazanlou, M. Jalaly, S. Sadeghzadeh, and A. H. Korayem, "A comparative study on the mechanical, physical and morphological properties of cement-micro/nanofe 3 o 4 composite," *Scientific reports*, vol. 10, no. 1, pp. 1–14, 2020.

[43] M. V. Kiamahalleh, A. Alishah, F. Yousefi, S. H. Astani, A. Gholampour, and M. V. Kiamahalleh, "Iron oxide nanoparticle incorporated cement mortar composite: correlation between physico-chemical and physico-mechanical properties," *Materials Advances*, vol. 1, no. 6, pp. 1835–1840, 2020.

[44] Z. Z. Ismail and E. A. Al-Hashmi, "Reuse of waste iron as a partial replacement of sand in concrete," *Waste Management*, vol. 28, no. 11, pp. 2048–2053, 2008.

[45] P. Helmand, S. Saini, *et al.*, "Mechanical properties of concrete in presence of iron filings as complete replacement of fine aggregates," *Materials Today: Proceedings*, vol. 15, pp. 536–545, 2019.

[46] S. Said, S. Mikhail, and M. Riad, "Recent processes for the production of alumina nano-particles," *Materials Science for Energy Technologies*, vol. 3, pp. 344–363, 2020.

[47] H. Shokravi, S. E. Mohammadyan-Yasouj, S. S. R. Koloor, M. Petr, and M. Heidarrezaei, "Effect of alumina additives on mechanical and fresh properties of self-compacting concrete: A review," *Processes*, vol. 9, no. 3, p. 554, 2021.

[48] L. Moutei, Y. Benbrahim, A. Bouih, S. Labied, T. Guedira, O. Benali, *et al.*, "The effect of the addition of alumina powder on the confinement properties of a cement mortar," in *MATEC Web of Conferences*, vol. 149, p. 01055, EDP Sciences, 2018.

[49] N. Farzadnia, A. A. A. Ali, and R. Demirboga, "Characterization of high strength mortars with nano alumina at elevated temperatures," *Cement and Concrete Research*, vol. 54, pp. 43–54, 2013.

[50] B. J. Zhan, D. X. Xuan, and C. S. Poon, "The effect of nanoalumina on early hydration and mechanical properties of cement pastes," *Construction and Building Materials*, vol. 202, pp. 169–176, 2019.

[51] M. Heikal, M. Ismail, and N. Ibrahim, "Physico-mechanical, microstructure characteristics and fire resistance of cement pastes containing al2o3 nano-particles," *Construction and Building Materials*, vol. 91, pp. 232–242, 2015.

[52] S. E. Mohammadyan-Yasouj, N. Heidari, and H. Shokravi, "Influence of waste alumina powder on self-compacting concrete resistance under elevated temperature," *Journal of Building Engineering*, vol. 41, p. 102360, 2021.

[53] J. Szymanowski and Ł. Sadowski, "The development of nanoalumina-based cement mortars for overlay applications in concrete floors," *Materials*, vol. 12, no. 21, p. 3465, 2019.

[54] H. A. Abdel-Gawwad, M. S. Mohammed, and T. Alomayri, "Single and dual effects of magnesia and alumina nano-particles on strength and drying shrinkage of alkali activated slag," *Construction and Building Materials*, vol. 228, p. 116827, 2019.

[55] A. Hoteit, *Etude expérientale des mécanismes de capture de Co^2 par cycle calcium en lit fluidisé circulant.* PhD thesis, Mulhouse, 2006.

[56] J. Valverde, P. Sanchez-Jimenez, and L. A. Pérez-Maqueda, "Limestone calcination nearby equilibrium: kinetics, cao crystal structure, sintering and reactivity," *The Journal of Physical Chemistry C*, vol. 119, no. 4, pp. 1623–1641, 2015.

[57] R. Rubiandini, S. Siregar, N. Suhascaryo, and D. Efrial, "The effect of cao and mgo as expanding additives toimprove cement isolation strength under hphtexposure," 2005.

[58] M. Deng, D. Hong, X. Lan, and M. Tang, "Mechanism of expansion in hardened cement pastes with hard-burnt free lime," *Cement and concrete research*, vol. 25, no. 2, pp. 440–448, 1995.

[59] S. W. Yoo, S.-J. Kwon, and S. H. Jung, "Analysis technique for autogenous shrinkage in high performance concrete with mineral and chemical admixtures," *Construction and Building Materials*, vol. 34, pp. 1–10, 2012.

[60] S. Treesuwan and K. Maleesee, "Effects of shrinkage reducing agent and expansive additive on mortar properties," *Advances in Materials Science and Engineering*, vol. 2017, 2017.

[61] J. Seo, S. Park, H. N. Yoon, and H.-K. Lee, "Effect of cao incorporation on the microstructure and autogenous shrinkage of ternary blend portland cement-slag-silica fume," *Construction and Building Materials*, vol. 249, p. 118691, 2020.

[62] M. Gruszczyński and G. Bajorek, "The possibility of shrinkage strain reduction in cements mortars," in *MATEC Web of Conferences*, vol. 174, p. 02013, EDP Sciences, 2018.

[63] S. Z. Zhang, Q. Tian, and A. Q. Lu, "Influence of cao-based expansive agent on the deformation behavior of high performance concrete," in *Applied Mechanics and Materials*, vol. 438, pp. 113–116, Trans Tech Publ, 2013.

[64] C. Maltese, C. Pistolesi, A. Lolli, A. Bravo, T. Cerulli, and D. Salvioni, "Combined effect of expansive and shrinkage reducing admixtures to obtain stable and durable mortars," *Cement and concrete research*, vol. 35, no. 12, pp. 2244–2251, 2005.

[65] F. Cao, M. Miao, and P. Yan, "Hydration characteristics and expansive mechanism of mgo expansive agents," *Construction and Building Materials*, vol. 183, pp. 234–242, 2018.

[66] H. Kabir and R. Hooton, "Evaluating soundness of concrete containing shrinkage-compensating mgo admixtures," *Construction and Building Materials*, vol. 253, p. 119141, 2020.

[67] L. Chen, L. Jiang, H. Chu, P. Xu, W. Jin, C. Chen, F. Zhi, and X. Ben, "Effect of retarder on hydration properties of light-burned magnesia," *Construction and Building Materials*, vol. 263, p. 119762, 2020.

[68] P. W. Gao, F. Geng, and X. L. Lu, "Hydration and expansion properties of novel concrete expansive agent," in *Key Engineering Materials*, vol. 405, pp. 267–271, Trans Tech Publ, 2009.

[69] F. Cao and P. Yan, "The influence of the hydration procedure of mgo expansive agent on the expansive behavior of shrinkage-compensating mortar," *Construction and Building Materials*, vol. 202, pp. 162–168, 2019.

[70] L. Mo, M. Deng, and M. Tang, "Effects of calcination condition on expansion property of mgo-type expansive agent used in cement-based materials," *Cement and Concrete Research*, vol. 40, no. 3, pp. 437–446, 2010.

[71] H. Zhao, Y. Xiang, D. Xie, W. Xu, Y. Wang, H. Li, Q. Tian, and J. Liu, "Effects of cao-based and mgo-based expansion agent, curing temperature and restraint degree on pore structure of early-age mortar," *Construction and Building Materials*, vol. 257, p. 119572, 2020.

[72] F. Jin, K. Gu, and A. Al-Tabbaa, "Strength and hydration properties of reactive mgo-activated ground granulated blastfurnace slag paste," *Cement and Concrete Composites*, vol. 57, pp. 8–16, 2015.

[73] S. Park, H. M. Park, H. Yoon, J. Seo, C.-M. Yang, J. L. Provis, and B. Yang, "Hydration kinetics and products of mgo-activated blast furnace slag," *Construction and Building Materials*, vol. 249, p. 118700, 2020.

[74] L. Mo, M. Liu, A. Al-Tabbaa, M. Deng, and W. Y. Lau, "Deformation and mechanical properties of quaternary blended cements containing ground granulated blast furnace slag, fly ash and magnesia," *Cement and concrete Research*, vol. 71, pp. 7–13, 2015.

[75] H. Zhao, Y. Xiang, X. Chen, J. Huang, W. Xu, H. Li, Y. Wang, and P. Wang, "Mechanical properties and volumetric deformation of early-age concrete containing cao-mgo blended expansive agent and temperature rising inhibitor," *Construction and Building Materials*, vol. 299, p. 123977, 2021.

[76] H. Zhao, X. Li, X. Chen, C. Qiao, W. Xu, P. Wang, and H. Song, "Microstructure evolution of cement mortar containing mgo-cao blended expansive agent and temperature rising inhibitor under multiple curing temperatures," *Construction and Building Materials*, vol. 278, p. 122376, 2021.

[77] H. Li, Y. Wang, Y. Wang, J. Liu, and Q. Tian, "Effect of cao and mgo based expansive agent on deformation and mechanical properties of concrete-filled steel tubes," *Construction and Building Materials*, vol. 250, p. 118723, 2020.

[78] S.-W. Yoon and J.-S. Rho, "Preparation and application of csa expansive additives using industrial wastes," *Journal of the Korea Concrete Institute*, vol. 16, no. 3, pp. 369–374, 2004.

[79] S. Nagataki and H. Gomi, "Expansive admixtures (mainly ettringite)," *Cement and concrete composites*, vol. 20, no. 2-3, pp. 163–170, 1998.

[80] S. J. Huang, Z. C. Ge, L. Zhou, and J. L. Zhou, "Effect of fly ash on expansion properties of concrete added with expansive agents," in *Advanced Materials Research*, vol. 393, pp. 684–687, Trans Tech Publ, 2012.

[81] D.-Y. Yoo, B. Chun, and J.-J. Kim, "Effect of calcium sulfoaluminate-based expansive agent on rate dependent pullout behavior of straight steel fiber embedded in uhpc," *Cement and Concrete Research*, vol. 122, pp. 196–211, 2019.

[82] M. Miao, Q. Liu, J. Zhou, and J. Feng, "Effects of expansive agents on the early hydration kinetics of cementitious binders," *Materials*, vol. 12, no. 12, p. 1900, 2019.

[83] J. Guo, S. Zhang, C. Qi, L. Cheng, and L. Yang, "Effect of calcium sulfoaluminate and mgo expansive agent on the mechanical strength and crack resistance of concrete," *Construction and Building Materials*, vol. 299, p. 123833, 2021.

[84] P. Shen, L. Lu, Y. He, F. Wang, J. Lu, H. Zheng, and S. Hu, "Investigation on expansion effect of the expansive agents in ultra-high performance concrete," *Cement and Concrete Composites*, vol. 105, p. 103425, 2020.

[85] J. Shao, H. Zhu, G. Xue, Y. Yu, S. M. Borito, and W. Jiang, "Mechanical and restrained shrinkage behaviors of cement mortar incorporating waste tire rubber particles and expansive agent," *Construction and Building Materials*, vol. 296, p. 123742, 2021.

[86] J. Guo, S. Zhang, T. Guo, and P. Zhang, "Effects of uea and mgo expansive agents on fracture properties of concrete," *Construction and Building Materials*, vol. 263, p. 120245, 2020.

[87] W. Nocuń-Wczelik, Z. Konik, and A. Stok, "Blended systems with calcium aluminate and calcium sulphate expansive additives," *Construction and Building Materials*, vol. 25, no. 2, pp. 939–943, 2011.

[88] T. Qureshi, A. Kanellopoulos, and A. Al-Tabbaa, "Autogenous self-healing of cement with expansive minerals-ii: Impact of age and the role of optimised expansive minerals in healing performance," *Construction and Building Materials*, vol. 194, pp. 266–275, 2019.

[89] M. A. Sherir, K. M. Hossain, and M. Lachemi, "Self-healing and expansion characteristics of cementitious composites with high volume fly ash and mgo-type expansive agent," *Construction and Building Materials*, vol. 127, pp. 80–92, 2016.

[90] M. A. Sherir, K. M. Hossain, and M. Lachemi, "Development and recovery of mechanical properties of self-healing cementitious composites with mgo expansive agent," *Construction and Building Materials*, vol. 148, pp. 789–810, 2017.

[91] B. Park and Y. C. Choi, "Self-healing capability of cementitious materials with crystalline admixtures and super absorbent polymers (saps)," *Construction and Building Materials*, vol. 189, pp. 1054–1066, 2018.

[92] C. Alonso and L. Fernandez, "Dehydration and rehydration processes of cement paste exposed to high temperature environments," *Journal of materials science*, vol. 39, no. 9, pp. 3015–3024, 2004.

[93] R. D. Cody, A. Cody, P. Spry, and H. Lee, "Expansive mineral growth and concrete deterioration," *Iowa State University, Ames, Final Report, Iowa DT HR-384*, 1997.

[94] J. Wang, O. Novaro, X. Bokhimi, T. Lopez, R. Gomez, J. Navarrete, M. Llanos, and E. Lopez-Salinas, "Characterizations of the thermal decomposition of brucite prepared by sol–gel technique for synthesis of nanocrystalline mgo," *Materials letters*, vol. 35, no. 5-6, pp. 317–323, 1998.

[95] Q. Zhou and F. P. Glasser, "Thermal stability and decomposition mechanisms of ettringite at< 120 c," *Cement and Concrete Research*, vol. 31, no. 9, pp. 1333–1339, 2001.

[96] K. Olivier, A. Darquennes, F. Benboudjema, and R. Gagné, "Early-age self-healing of cementitious materials containing ground granulated blast-furnace slag under water curing," *Journal of Advanced Concrete Technology*, vol. 14, no. 11, pp. 717–727, 2016.

[97] D. J. Kim, S. H. Kang, and T.-H. Ahn, "Mechanical characterization of high-performance steel-fiber reinforced cement composites with self-healing effect," *Materials*, vol. 7, no. 1, pp. 508–526, 2014.

[98] B. Park and Y. C. Choi, "Prediction of self-healing potential of cementitious materials incorporating crystalline admixture by isothermal calorimetry," *International Journal of Concrete Structures and Materials*, vol. 13, no. 1, pp. 1–14, 2019.

[99] P.-C.-R. Escoffres, *Effet de l'utilisation d'ajouts cristallins sur le potentiel de cicatrisation de bétons à hautes performances en condition de service.* PhD thesis, École Polytechnique de Montréal, 2017.

[100] E. T. M. Stefanidou, *RRT1 - Concrete with mineral additions*, Aristotle University of Thessaloniki (AUTH) 2019.

[101] M. R. P. Serna, *RRT3 - Concrete with crystalline admixture*, Universitat Politècnica de València 2020.

[102] T. Van Mullem, *SARCOS RRT: Guidelines for crack width measurement - Preliminary description*, Internal document, 16^{th} April 2019.

[103] E. Tziviloglou, V. Wiktor, J. Wang, K. Paine, M. Alazhari, A. Richardson, M. Gueguen, N. De Belie, E. Schlangen, and H. Jonkers, "Evaluation of experimental methodology to asses the sealing efficiency of bacteria based self healing concrete: Round robin test," 2016.

[104] T. N. d. C. Moreira, S. R. Ferreira, and R. Dias, "Investigation of self-healing phenomenon in high performance fiber reinforced microconcrete with steel and sisal fibers,"

[105] H. Ulugöl, M. F. Günal, İ. Ö. Yaman, G. Yıldırım, and M. Şahmaran, "Effects of self-healing on the microstructure, transport, and electrical properties of 100% construction- and demolition-waste-based geopolymer composites," *Cement and Concrete Composites*, vol. 121, p. 104081, 2021.

[106] Y. Zhao, J. Qiu, S. Zhang, Z. Guo, Z. Ma, X. Sun, and J. Xing, "Effect of sodium sulfate on the hydration and mechanical properties of lime-slag based eco-friendly binders," *Construction and Building Materials*, vol. 250, p. 118603, 2020.

[107] A. Darquennes, M. Khokhar, E. Rozière, A. Loukili, F. Grondin, and S. Staquet, "Early age deformations of concrete with high content of mineral additions," *Construction and Building Materials*, vol. 25, no. 4, pp. 1836–1847, 2011.

[108] A. Darquennes, S. Staquet, M.-P. Delplancke-Ogletree, and B. Espion, "Effect of autogenous deformation on the cracking risk of slag cement concretes," *Cement and Concrete Composites*, vol. 33, no. 3, pp. 368–379, 2011.

[109] F. L. Theiss, G. A. Ayoko, and R. L. Frost, "Thermogravimetric analysis of selected layered double hydroxides," *Journal of thermal analysis and calorimetry*, vol. 112, no. 2, pp. 649–657, 2013.

[110] R. Trittschack, B. Grobéty, and P. Brodard, "Kinetics of the chrysotile and brucite dehydroxylation reaction: a combined non-isothermal/isothermal thermogravimetric analysis and high-temperature x-ray powder diffraction study," *Physics and Chemistry of Minerals*, vol. 41, no. 3, pp. 197–214, 2014.

[111] Y. Pei, *Effets du chauffage sur les matériaux cimentaires-impact du «self-healing» sur les propriétés de transfert.* PhD thesis, Ecole centrale de Lille, 2016.

[112] J. Rouquerol, D. Avnir, C. Fairbridge, D. Everett, J. Haynes, N. Pernicone, J. Ramsay, K. Sing, and K. Unger, "Recommendations for the characterization of porous solids (technical report)," *Pure and applied chemistry*, vol. 66, no. 8, pp. 1739–1758, 1994.

[113] A. Darquennes and F. Benboudjema, "Behavior of activated ternary binders under autogenous condition," *Special Publication*, vol. 326, pp. 22–1, 2018.

[114] L. Frølich, L. Wadsö, and P. Sandberg, "Using isothermal calorimetry to predict one day mortar strengths," *Cement and Concrete Research*, vol. 88, pp. 108–113, 2016.

[115] P. Hewlett and M. Liska, *Lea's chemistry of cement and concrete*. Butterworth-Heinemann, 2019.

[116] X. Li, Z. Shui, T. Sun, K. Liu, and X. Wang, "The hydration mechanism of cement-based materials served in marine environment during early-age magnesium precipitation," *Construction and Building Materials*, vol. 230, p. 117010, 2020.

[117] Q. T. Phung, E. Ferreira, S. Seetharam, J. Govaerts, E. Valcke, *et al.*, "Understanding hydration heat of mortars containing supplementary cementitious materials with potential to immobilize heavy metal containing waste," *Cement and Concrete Composites*, vol. 115, p. 103859, 2021.

[118] J. Seo, S. Kim, H. Yoon, and H.-K. Lee, "Effect of the molar ratio of calcium sulfate over ye'elimite on the reaction of csa cement/slag blends under an accelerated carbonation condition," *Journal of Building Engineering*, vol. 46, p. 103785, 2022.

[119] M. Shand, A. Al-Tabbaa, J. Qian, L. Mo, and F. Jin, *Magnesia Cements: From Formulation to Application*. Newnes, 2020.

[120] S. Qian, J. Zhou, and E. Schlangen, "Influence of curing condition and precracking time on the self-healing behavior of engineered cementitious composites," *Cement and concrete composites*, vol. 32, no. 9, pp. 686–693, 2010.

[121] J. Xu, C. Yan, F. Zhang, H. Konishi, H. Xu, and H. H. Teng, "Testing the cation-hydration effect on the crystallization of ca–mg–co3 systems," *Proceedings of the National Academy of Sciences*, vol. 110, no. 44, pp. 17750–17755, 2013.

[122] D. Wang, L. Hamm, A. Giuffre, T. Echigo, J. D. Rimstidt, J. De Yoreo, J. Grotzinger, and P. Dove, "Revisiting geochemical controls on patterns of carbonate deposition through the lens of multiple pathways to mineralization," *Faraday Discussions*, vol. 159, no. 1, pp. 371–386, 2012.

[123] Ç. M. Oral and B. Ercan, "Influence of ph on morphology, size and polymorph of room temperature synthesized calcium carbonate particles," *Powder technology*, vol. 339, pp. 781–788, 2018.

[124] M. B. Haha, G. Le Saout, F. Winnefeld, and B. Lothenbach, "Influence of activator type on hydration kinetics, hydrate assemblage and microstructural development of alkali activated blast-furnace slags," *Cement and Concrete Research*, vol. 41, no. 3, pp. 301–310, 2011.

[125] T. Qureshi and A. Al-Tabbaa, "Self-healing of drying shrinkage cracks in cement-based materials incorporating reactive mgo," *Smart Materials and Structures*, vol. 25, no. 8, p. 084004, 2016.

[126] H. N. Yoon, J. Seo, S. Kim, H.-K. Lee, and S. Park, "Hydration of calcium sulfoaluminate cement blended with blast-furnace slag," *Construction and Building Materials*, vol. 268, p. 121214, 2021.

[127] J. Seo, S. Kim, S. Park, H. N. Yoon, and H.-K. Lee, "Carbonation of calcium sulfoaluminate cement blended with blast furnace slag," *Cement and Concrete Composites*, vol. 118, p. 103918, 2021.

[128] J. Zhou, G. Ye, and K. van Breugel, "Hydration of portland cement blended with blast furnace slag at early stage," in *2nd international symposium on advances in concrete science and engineering, Quebec City, Canada. RILEM Publications (on CD)*, 2006.

[129] B. Kolani, L. Buffo-Lacarrière, A. Sellier, G. Escadeillas, L. Boutillon, and L. Linger, "Hydration of slag-blended cements," *Cement and concrete composites*, vol. 34, no. 9, pp. 1009–1018, 2012.

[130] A. Lozano-Lunar, J. I. Álvarez, Í. Navarro-Blasco, J. R. Jiménez, and J. M. Fernández-Rodriguez, "Optimisation of mortar with mg-al-hydrotalcite as sustainable management strategy lead waste," *Applied Clay Science*, vol. 212, p. 106218, 2021.

[131] M. B. Haha, B. Lothenbach, G. Le Saout, and F. Winnefeld, "Influence of slag chemistry on the hydration of alkali-activated blast-furnace slag—part i: Effect of mgo," *Cement and Concrete Research*, vol. 41, no. 9, pp. 955–963, 2011.

[132] G.-S. Ryu, S. Choi, K.-T. Koh, G.-H. Ahn, H.-Y. Kim, and Y.-J. You, "A study on initial setting and modulus of elasticity of aam mortar mixed with csa expansive additive using ultrasonic pulse velocity," *Materials*, vol. 13, no. 19, p. 4432, 2020.

[133] Y. Liao, G. Jiang, K. Wang, S. Al Qunaynah, and W. Yuan, "Effect of steel slag on the hydration and strength development of calcium sulfoaluminate cement," *Construction and Building Materials*, vol. 265, p. 120301, 2020.

[134] H. Taylor, C. Famy, and K. Scrivener, "Delayed ettringite formation," *Cement and concrete research*, vol. 31, no. 5, pp. 683–693, 2001.

[135] C. Famy and H. F. Taylor, "Ettringite in hydration of portland cement concrete and its occurrence in mature concretes," *Materials Journal*, vol. 98, no. 4, pp. 350–356, 2001.

[136] F. Jin, K. Gu, and A. Al-Tabbaa, "Strength and drying shrinkage of reactive mgo modified alkali-activated slag paste," *Construction and Building Materials*, vol. 51, pp. 395–404, 2014.

[137] J. Sharp, C. Lawrence, and R. Yang, "Calcium sulfoaluminate cements—low-energy cements, special cements or what?," *Advances in Cement Research*, vol. 11, no. 1, pp. 3–13, 1999.

[138] F. Winnefeld, L. H. Martin, C. J. Müller, and B. Lothenbach, "Using gypsum to control hydration kinetics of csa cements," *Construction and Building Materials*, vol. 155, pp. 154–163, 2017.

[139] J. Haas and A. Nonat, "From c–s–h to c–a–s–h: Experimental study and thermodynamic modelling," *Cement and Concrete Research*, vol. 68, pp. 124–138, 2015.

[140] S. Medjigbodo, A. Darquennes, C. Aubernon, A. Khelidj, and A. Loukili, "Effects of the air–steam mixture on the permeability of damaged concrete," *Cement and concrete research*, vol. 54, pp. 98–105, 2013.

Titre : Capacité d'auto-cicatrisation des matériaux cimentaires: Amélioration avec des agents expansifs et des additions minérales

Mots clés : Agents expansifs, cicatrisation, gonflement, laitier de haut fourneau, matériaux cimentaires, mortier de réparation

Résumé : Suite à leur vieillissement, les structures actuelles en béton armé nécessitent de plus en plus de travaux de maintenance et de réparation. Ayant une durée de vie limitée, les matériaux de réparation peuvent également présenter précocement des fissures dues à des facteurs environnementaux, à des incompatibilités déformationnelles et physico-chimiques entre le matériau de réparation et le substrat, etc. Dans le cadre du développement durable, il devient essentiel d'éviter les opérations de maintenance et de réparation coûteuses, et de développer des matériaux plus durables et plus respectueux de l'environnement. La réparation de structures à l'aide d'un mortier auto-cicatrisant apparaît comme une solution s'inscrivant pleinement dans cette démarche. Ce mortier présentera la capacité de cicatriser ses propres fissures de manière autonome. Pour atteindre cet objectif, une large campagne expérimentale a été mise en œuvre afin d'évaluer l'impact de l'ajout d'additifs expansifs à différents pourcentages et d'additions minérales sur le comportement mécanique et la capacité d'auto-cicatrisation de mortiers. Les résultats expérimentaux montrent que l'ajout d'un additif expansif de type MgO ou CSA entraîne une diminution significative du retrait endogène en raison de la formation de produits supplémentaires dans le réseau poral, générant des pressions de cristallisation et un gonflement de la matrice à l'échelle macroscopique. Cette expansion permet d'accélérer la fermeture des fissures et augmente ainsi le potentiel de cicatrisation autonome des mortiers. Une substitution partielle du ciment par du laitier de haut-fourneau est également bénéfique pour réduire le retrait endogène, et en présence de MgO pour augmenter la capacité de cicatrisation autonome des fissures.

Title : Self-healing capacity of cementitious materials: Enhancement with expansive agents and mineral additions

Keywords : Blast furnace slag, cementitious materials, expansive agents, repair mortar, self-healing, swelling

Abstract : As the reinforced concrete structures are aging, they require more and more maintenance and repair works. Having a limited life span, repair materials may also show an early cracking due to environmental factors, deformational and physico-chemical incompatibilities between the repair material and the substrate, etc. In the context of sustainable development, it becomes essential to avoid costly maintenance and repair operations, and to develop more durable and environmentally-friendly materials. The repair of structures using a self-healing mortar appears to be a solution in favor of this approach. This mortar will be able to heal autonomously its cracks. To achieve this objective, a large experimental campaign was performed to evaluate the effect of the addition of expansive at different contents and mineral additions on the mechanical behavior and self-healing capacity of mortars. The experimental results show that the addition of an expansive agent type MgO or CSA leads to a significant decrease of the autogenous shrinkage due to the formation of additional products in the pore network, leading to crystallization pressures and a matrix swelling at macroscopic scale. This expansion accelerates crack closure and therefore increases the autonomous healing potential of mortars. A partial substitution of cement by blast furnace slag is also beneficial to reduce autogenous shrinkage, and in the presence of MgO to increase the autonomous healing capacity of cracks.